R88-08

THREE-DIMENSIONAL FLOW IN RANDOM POROUS MEDIA

Vol. 2

by
RACHID ABABOU
LYNN W. GELHAR
and
DENNIS McLAUGHLIN

RALPH M. PARSONS LABORATORY
HYDROLOGY AND WATER RESOURCE SYSTEMS

Report Number 318

Prepared under the support of the
Nuclear Regulatory Commission, Contract NRC-04-83-174
National Science Foundation, Grant ECE-8311786

March, 1988

MIT

DEPARTMENT
OF
CIVIL
ENGINEERING

SCHOOL OF E
MASSACHUSETTS INSTIT
Cambridge, Massa

CHAPTER 6
THREE-DIMENSIONAL SINGLE-REALIZATION SIMULATIONS OF SATURATED FLOW IN RANDOM POROUS MEDIA

6.1 Scope, Model Problems, and Methodology

This Chapter is devoted to the physical interpretation and statistical analysis of large realizations of steady state saturated flow fields in three-dimensional random porous media. In the single-realization approach, the hydraulic conductivity $K(\underline{x})$ is generated as a particular replica of a statistically homogeneous random field in 3D space. In view of reproducing a relatively wide range of natural conditions, two main types of model problems (isotropic/anisotropic) were selected, with different subcases corresponding to various degrees of conductivity variability. In all cases, the random field conductivity was assumed *locally* isotropic, although the spatial structure could be *statistically* anisotropic as well as isotropic. This will be explained in more detail shortly.

[a] Model Problems.

The single-realization flow problems to be examined in this Chapter are listed in Table 6.1, with a summary of numerical and statistical input data in each case (problems A, B, E and F, to be analyzed in Sections 6.3, 6.2, 6.4, respectively).

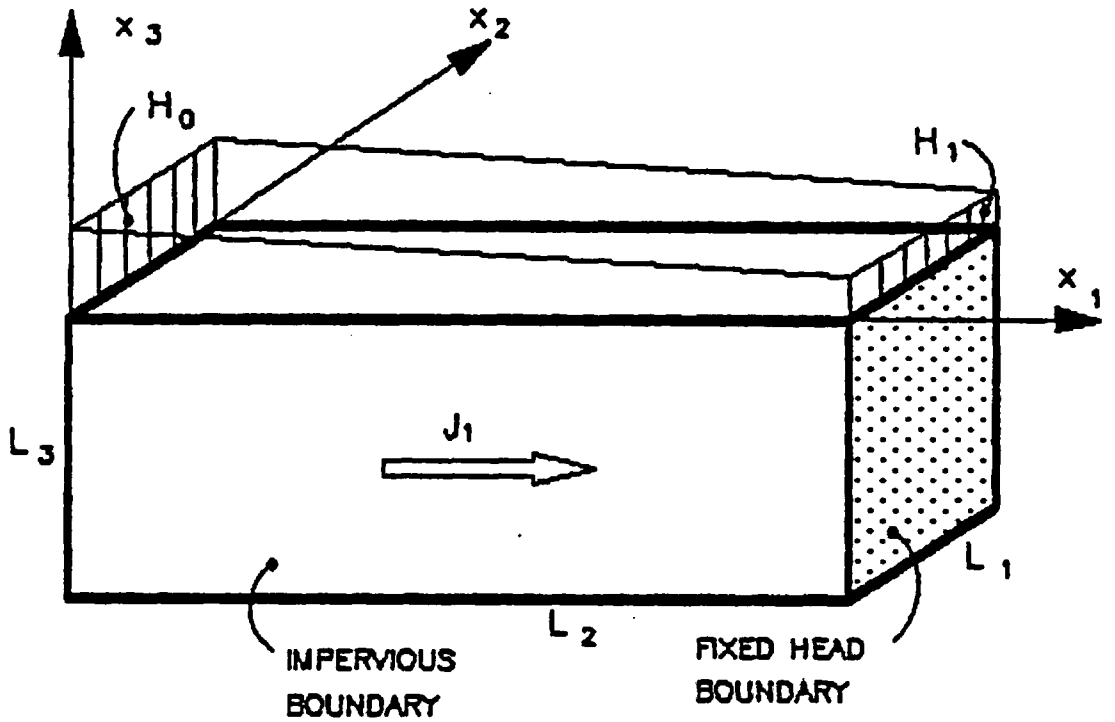

Figure 6.1 Schematic representation of flow domain geometry and boundary conditions used for single-realization simulations of steady-state saturated flow.

as part of the solution. However, there was no provision to do this in the *saturated* flow simulator developed in this work. To be fair, note that the flow simulator could also be run in the *partially saturated* mode to simulate unconfined flow, provided that the vadose zone above the water table be included in the flow domain. However, we have not tried this cumbersome approach. Instead, the case of unconfined flow could be approximated in the purely saturated flow regime by assuming a fixed, horizontal water table, through which some distributed recharge flux could be prescribed. The regional hydraulic gradient should be taken horizontal, and equal to the mean slope of the water table as measured in the field. In our view, the simulated flow fields obtained in this way could be fairly representative of natural unconfined groundwater flow systems, at least far enough below the water table. Thus, the model flow problem of Figure 6.1 could be interpreted alternatively as a confined flow system or as an unconfined flow system with zero recharge at the water table.

Let us now discuss our particular choice of boundary conditions (Figure 6.1) in the context of the single-realization approach to stochastic flow. We have indicated earlier that the flow was assumed to be driven at the large scale by some regional hydraulic gradient. This type of condition was modeled in an

indirect fashion by prescribing constant head conditions on two opposite faces of the flow domain, and zero flux conditions on all other lateral faces.

As a consequence, the regional or "mean" hydraulic gradient will be approximately aligned with the horizontal axis x_1, which also coincides exactly with the mean flow direction.

This property can be expressed more precisely by defining "regional" or "mean" quantities as three-dimensional spatial averages, e.g.:

$$\underline{\text{Mean Hydraulic Gradient:}} \quad \overline{J}_i = -\frac{1}{L_1 L_2 L_3} \cdot \iiint \frac{\partial H}{\partial x_i} \cdot d\underline{x} \qquad (6.1)$$

$$\underline{\text{Mean Flux:}} \quad \overline{Q}_i = \frac{1}{L_1 L_2 L_3} \cdot \iiint Q_i \, d\underline{x} \, .$$

Due to the particular geometry and boundary conditions (impervious lateral boundaries), the mean transverse flux components necessarily vanish ($\overline{Q}_2 = \overline{Q}_3 = 0$) and the mean flow is exactly horizontal. On the other hand, a simple manipulation of the triple volume integral defining $\overline{J}_i$ shows that the longitudinal component $\overline{J}_1$ is exactly equal to:

$$\boxed{\overline{J}_1 = -\frac{H_1 - H_0}{L_1}} \tag{6.2}$$

and the other gradient components are expected to vanish for sufficiently large domains ($\overline{J}_2 \simeq \overline{J}_3 \simeq 0$). Note that the boundary conditions are such that the transverse components of the mean hydraulic gradient are only approximately null in a heterogeneous medium, whereas the mean transverse flux components are exactly zero by construction. It does not seem possible to ensure both conditions exactly with a consistent set of boundary conditions. Attempts to do so will lead to an ill-posed boundary value problem.

Equation (6.2) defines in a simple manner the longitudinal "mean" hydraulic gradient imposed on the flow in terms of the prescribed heads H_0 and H_1 at the left and right boundaries. One may conceptually relate this quantity to the ensemble mean hydraulic gradient that would obtain by taking L_1 infinite while $(H_1 - H_0)/L_1$ remains constant. Furthermore, we have seen that the average flux over the flow domain is necessarily aligned with the horizontal axis (x_1), since all lateral boundaries are impervious. This property of the finite-domain flow field is consistent with the predictions of the infinite domain spectral theory in the special case where the log-conductivity field is *statistically isotropic* or has its

principal axis of anisotropy aligned with the mean gradient (horizontal axis x_1).

Accordingly, the anisotropic model problems listed in Table 6.1 (E and F) were restricted to the case of horizontally stratified aquifers, with a zero dip angle between the mean flow and the principal axis of statistical anisotropy of the log-conductivity field. In the more general case of a non-zero dip angle (sloping stratification) the mean flux will not be aligned with the mean hydraulic gradient in general. Future work on this complex case should focus on the design of boundary conditions compatible with the infinite domain and ergodicity assumptions of the spectral theory. Briefly, there are at least two different ways in which a global flow condition can be prescribed over a finite domain of rectangular shape with a dip angle. A regional hydraulic gradient can be ascribed by assuming a linear head variation outside the computational domain (i.e., on all sloping boundaries). Alternatively, a regional discharge rate vector can be ascribed by assuming a constant discharge rate outside the computational domain. The first of these approaches is a generalization of the boundary conditions chosen in this work for the case of isotropic or horizontally stratified formations. It is not clear at this point which one of the two approaches will be the most advantageous for the simulation of groundwater flow in *sloping* stratified formations: we leave this

problem for future research.

[b] Random Conductivity Fields:

The random *log-conductivity field* used for each single-realization problem was a normally distributed three-dimensional Markov field. In short hand notation, the probability distribution function of $\ell n\ K(\underline{x})$ can be defined as:

$$\text{pdf} = \mathcal{N}(\ell n\ K_G, \sigma_f^2) \tag{6.3a}$$

where $\mathcal{N}$ indicates the standard normal distribution, K_G is the geometric mean conductivity:

$$K_G = \exp\langle \ell n\ K \rangle \tag{6.3b}$$

and σ_f^2 is the variance of the log-conductivity perturbation f:

$$f(\underline{x}) = \ell n\ (K(\underline{x})/K_G)$$

$$\sigma_f^2 = \langle f(\underline{x})^2 \rangle. \tag{6.3c}$$

The spectral density $S_{ff}(k)$ of the Markov field was given in Table 3.1 of Chapter 3 under the designation "3D Ellipsoidal

Markov". The covariance function of this random field is exponential, of the form:

$$R_{ff}(\xi) = \langle f(\underline{x}) \cdot f(\underline{x}+\xi) \rangle$$
$$= \sigma_f^2 \cdot \exp(-\sqrt{\sum_i \xi_i^2/\lambda_i^2}) \qquad (6.3d)$$

where ξ_i is the separation vector, and λ_i is the integral correlation scale of the log-conductivity along the principal axis x_i (i = 1,2,3). In the special isotropic case ($\lambda_1=\lambda_2=\lambda_3$), the covariance function takes the simple form:

$$R_{ff}(\xi) = \sigma_f^2 \cdot e^{-\xi/\lambda} \qquad (6.3.e)$$

where ξ is the separation distance, and λ the isotropic correlation length (same in all directions). For illustration, we show in Figure (6.2) a contour map of a three-dimensional isotropic Markov log-conductivity field in a two-dimensional slice. Only the low contour values (from $K = K_G$ to $K = K_G/100$) are represented. The size of the slice is about 43 correlation scales in each direction, the grid resolution is one third of the correlation scale, and there are 129 nodes on each side (about 16,600 grid points on the slice). Note the large number of very small regions of extreme conductivity. The areas devoid of contour lines indicate high permeability "pathways" for the flow:

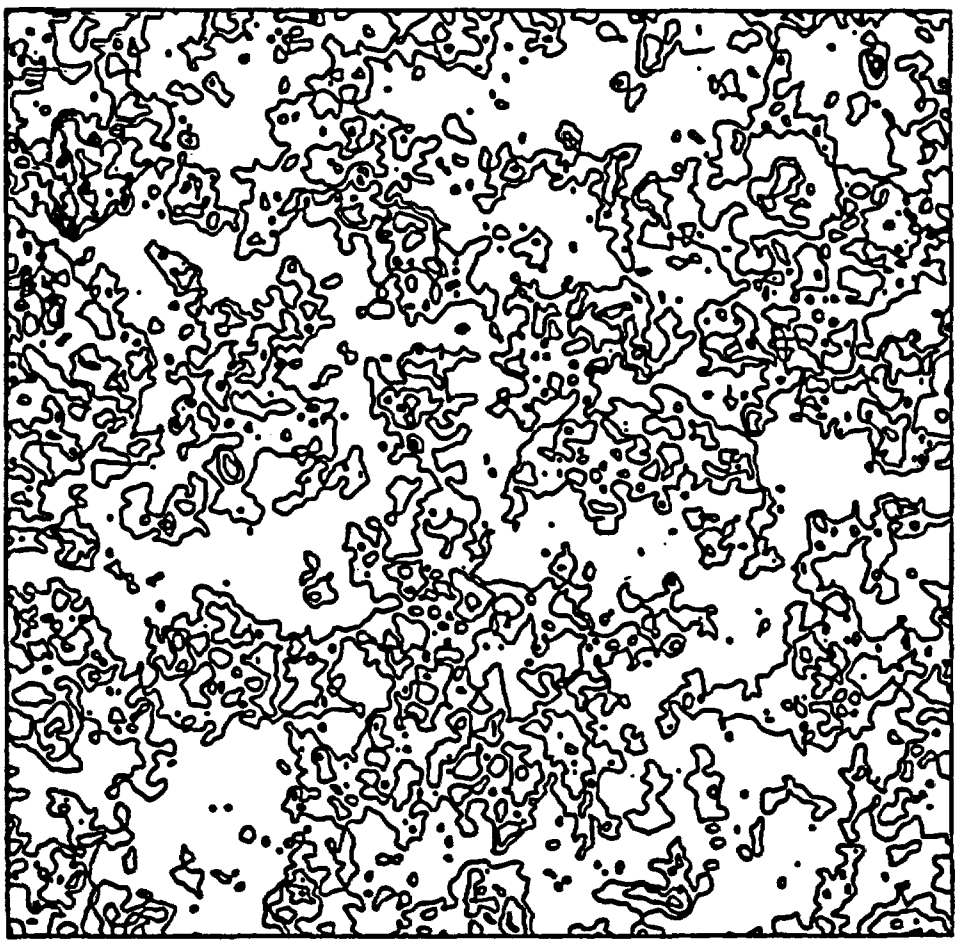

Figure 6.2 Typical high-resolution contour map of three-dimensional isotropic Markov log-conductivity field in a square two dimensional slice. Only the low contour values $K/K_G = 1$ to $1/100$ are represented ($\sigma_f = 1.$, $\Delta x_i/\lambda_i = 1/3$, $L_i/\lambda_i = 43$)

there is no preferential direction for these pathways since the field is statistically isotropic in this example.

It is important to note that the log-conductivity field just defined is, by construction, statistically homogeneous and ergodic in the strict sense. In other words, all n-point moments up to arbitrary order are statistically invariant by translation. Ergodicity guarantees the equivalence of infinite-domain spatial average with the ensemble means. For instance, the fact that:

$$\lim_{\|\underline{\xi}\| \to \infty} R_{ff}(\underline{\xi}) = 0$$

suffices to guarantee ergodicity in the first and second order moments (cf. Yaglom, 1962, 1.4). This is a desirable property to have in the context of the single-realization approach. In essence, ergodicity guarantees that, for sufficiently large domains ($L_i \gg \lambda_i$) a single spatial realization of the log-conductivity field will carry almost all the information contained in an infinite number of replicas of the random field obtained in ensemble space. This will be illustrated later, by comparing in a specific case the ensemble and spatial moments of the input log-conductivity fields generated by the Turning Band Method (problem A, section 6.3).

[c] Statistical Analysis Methodology

Our methodology for estimating the statistical properties (moments) of single realizations of random fields was based on standard spatial average estimators applicable under the assumptions of spatial homogeneity and ergodicity. The precise procedure we used was not exactly the same for different types of random fields (input log-conductivity, output hydraulic head and output flux vector). The exact procedure used in each case is explained in more detail below.

The spatial moments of the prescribed homogeneous/ergodic log-conductivity field were computed by using standard unbiased estimators. Let $\ell n(K_{i,j,k})$ be the discrete realization of the log-conductivity field over the grid. The mean and variance were computed by three-dimensional discrete averages as follows:

Mean: $$\ell n\, \hat{K}_G = \frac{1}{N} \cdot \sum_{i,j,k} \ell n\, K_{i,j,k} \qquad (6.4a)$$

Perturbation: $$f_{i,j,k} = \ell n\, (K_{i,j,k} / \hat{K}_G) \qquad (6.4b)$$

Variance: $$\hat{\sigma}_f^2 = \frac{1}{N} \cdot \sum_{i,j,k} (f_{i,j,k})^2 \qquad (6.4c)$$

where N is the total number of nodes on the grid ($N = n_1 n_2 n_3$).

The two-point covariance functions along each of the axes (x_1, x_2, x_3) were computed for discrete values of the separation distance $(\xi_1 = i_1\Delta x_1,\ \xi_2 = i_2\Delta x_2,\ \xi_3 = i_3\Delta x_3)$ in a similar fashion. Note however that the fully three-dimensional function $R_{ff}(\xi_1, \xi_2, \xi_3)$ was not directly computed. For example, the unidirectional covariance along x_1 was evaluated by:

$$\hat{R}_{ff}(i_1, 0, 0) = \frac{1}{N(i_1)} \sum_{j_1, j_2, j_3} f(j_1, j_2, j_3) \cdot f(j_1 - i_1, j_2, j_3) \quad (6.4d)$$

where $N(i_1)$ represents the number of pair of points with separation vector $\underline{\xi} = (i_1\Delta x_1, 0, 0)$ on the grid, that is:

$$N(i_1) = (n_1 - i_1) \cdot n_2 \cdot n_3$$

Note that $0 \leq i_1 \leq n_1 - 1$. The triple index (j_1, j_2, j_3) in equation (6.4d) was from (1,1,1) through $(n_1 - i_1, n_2, n_3)$. The formulas used to compute the covariance function in the other directions are analogous.

For the particular single-realization problems examined in this work, it was found that the spatial moments (6.4) of the log-conductivity fields generated by the Turning Band Method were fairly close to the prescribed ensemble moments. More details will be given in later sections. Let us just mention here that the agreement was particularly good for the isotropic flow

problem A which had the finest resolution ($\Delta x_i/\lambda_i = 1.3$) and the largest sample size ($L_i/\lambda_i \simeq 33.$). The reader is referred to Tompson, Ababou, and Gelhar (1987) for an evaluation of the capabilities of the Turning Band random field generator and a systematic comparison of ensemble versus spatial moments in a variety of cases.

The statistical properties of the simulated flow field ($H(\underline{x}), Q_i(\underline{x})$) were evaluated in a similar fashion, for comparison with the ensemble moments predicted by the spectral theory. Note that the spectral theory itself is only approximate. In particular there is no guarantee that the variables H and Q_i describing the flow share the properties of homogeneity and ergodicity satisfied by the input log-conductivity field. Indeed, the hydraulic head field is obviously not homogeneous in the mean, since there is a non-vanishing mean head gradient in the longitudinal direction. Moreover, the zero-mean head perturbation:

$$h = H - \langle H \rangle$$

may not be second order stationary/ergodic as the spectal theory assumes, except perhaps asymptotically as $\sigma_f \to 0$ (Chapter 4, Section 4.1). Finally, the correlation range of the head perturbation appears to be significantly larger than the

conductivity correlation scale λ (Chapter 3). As a consequence, to obtain a statistically meaningful realization of the hydraulic head field may require a domain much larger than what is needed for a representative realization of the conductivity field. The effect of boundary conditions renders this problem even more accute, as the deterministic constraint on the head near a boundary will tend to propagate towards the interior, in proportion to the correlation range of the hydraulic head.

Accordingly, our strategy for evaluating the statistical properties of the flow field was based on the premise that the flow variables of interest are not necessarily fully homogeneous in three-dimensional space. More precisely, we have found empirically that the preferential direction of spatial inhomogeneity for the finite-domain hydraulic head field was the longitudinal direction parallel to the mean flow. It should not be surprising that the flow be more nearly homogeneous in the direction transverse to the driving force. This was confirmed directly from the numerical solutions by examining the spatial variations of the cross-flow average of the head field as a function of the longitudinal coordinate.

$$\overline{H}(x_1) = \frac{1}{L_2 L_3} \cdot \iint H(\underline{x})\, dx_2 dx_3 \qquad (6.5a)$$

This function exhibited a few large scale fluctuations around the

theoretical linear mean $\overline{H} = - J_1 \cdot x_1$, with a wavelength typically on the order of the full domain length: see Figure 6.3 for illustration.

A zero-mean head perturbation h was then obtained by detrending the numerical head field with the nonlinear mean $\overline{H}(x_1)$:

$$h(\underline{x}) = H(\underline{x}) - \overline{H}(x_1) \qquad (6.5b)$$

This quantity was assumed to be statistically homogeneous in all three space directions in the interior of the domain. Therefore, the head variance (σ_h^2) and covariance function (R_{hh}) were computed by using the standard spatial averaging procedure as described previously for the case of the log-conductivity field (replace f by h in equations 6.4c and 6.4d). The domain of integration was usually taken slightly smaller than the computational flow domain in order to avoid including data located near the boundaries.

The procedure used to analyze the statistical properties of the flux vector $Q_i(\underline{x})$ was similar, however with one essential difference. By construction, the cross-flow average:

$$\overline{Q}_i(x_1) = \frac{1}{L_2 L_3} \cdot \iint Q_i(\underline{x}) \cdot dx_2 dx_3 \qquad (6.7a)$$

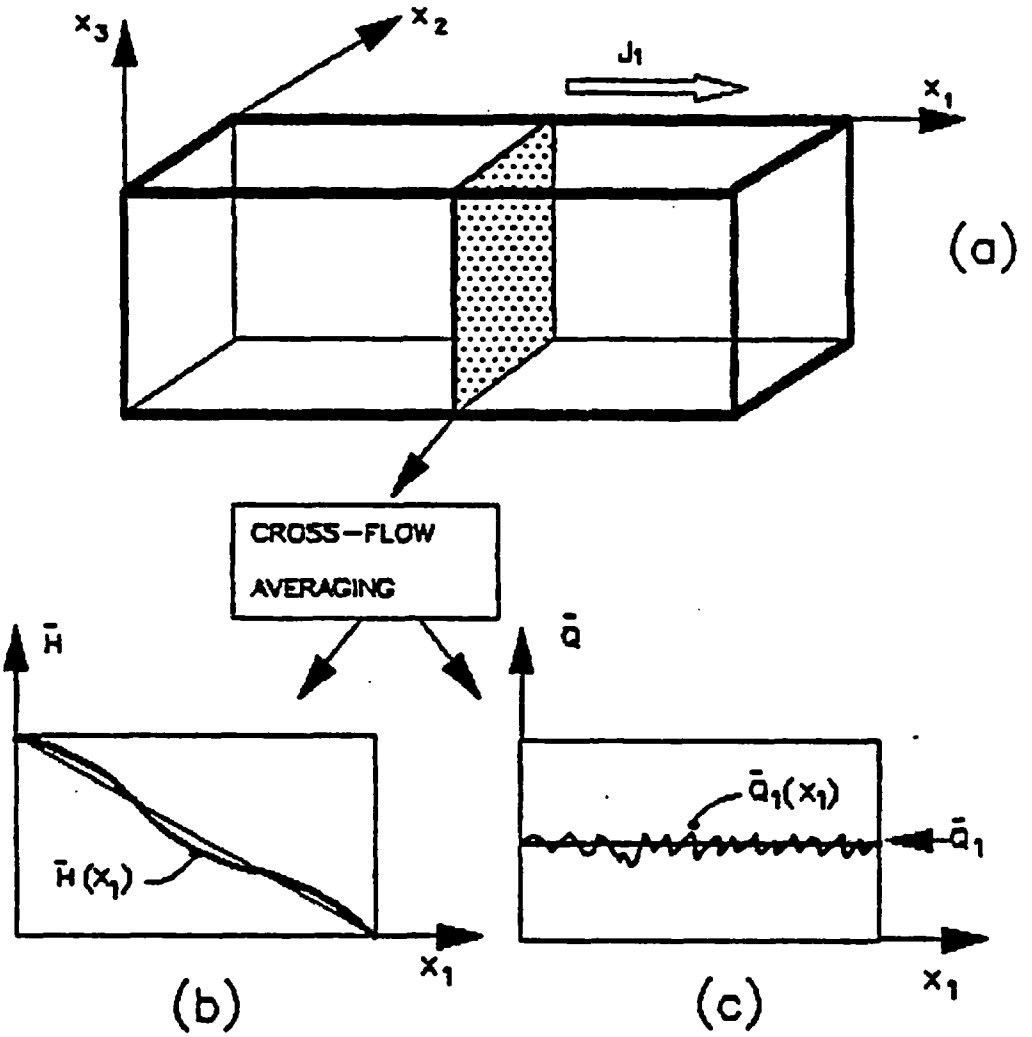

Figure 6.3 Illustration of the spatial averaging procedures used to detrend the hydraulic head field and the flux vector field: (a) Cross-flow averaging. (b) Nonlinear trend $\overline{H}(x_1)$, and (c) Approximately constant mean $\overline{Q}_1$

is in principle independent of the longitudinal coordinate x_1, and the transverse mean flux components $\bar{Q}_2, \bar{Q}_3$ should vanish since all lateral boundaries are impervious. In actual practice, the "one-dimensional" conservative nature of the mean flow was not exactly satisfied by the numerical flux field due to the discrete nature of the solution (numerical errors) leading to slightly inaccurate mass balance. We have found that these discrepancies were sufficiently small to be neglected, particularly for the highest resolution problem A of Table 6.1. Thus $\bar{Q}_1$ was approximately constant along x_1, which justified using a three-dimensional average to evaluate the constant mean flux as follows:

$$\bar{Q}_1 = \frac{1}{L_1 L_2 L_3} \cdot \iiint Q_1(x_1, x_2, x_3)\, dx_1 dx_2 dx_3$$

and similarly for $\bar{Q}_2$ and $\bar{Q}_3$. The ratios $\bar{Q}_i/\bar{Q}_1 (i=2,3)$ were used to evaluate the relative mass balance error of the numerical solution (ideally $\bar{Q}_2 = \bar{Q}_3 = 0$).

In practice, the flux-integral above was converted into a discrete sum, and the fluxes were evaluated by a finite difference approximation of Darcy equation at mid-nodal locations (staggered grid $(i_1+1/2, i_2, i_3)$) as explained in Chapter 5, equations (5.4) and (5.7). In certain cases (problem B), the

fluxes were evaluated as local cell-averages of neighboring mid-nodal fluxes, in order to obtain a tractable representation of the random velocity field for use in a particle-tracking simulator of solute transport (ongoing research by Gelhar and co-workers at MIT). Finally, the zero-mean flux perturbation:

$$q_i(\underline{x}) = Q_i(\underline{x}) - \overline{Q}_i \qquad (6.7b)$$

was assumed to be statistically homogeneous in three-dimensional space. Consequently, the variances $\sigma^2_{q_i}$ and covariance functions $R_{q_i q_i}(\underline{\xi})$ were evaluated, for each flux component (i=1,2,3), by the standard three-dimensional spatial averaging procedure described in equations (6.4c) an (6.4d), with f replaced by q_i. A similar procedure was also applied to the head gradient field $G_i = \partial H/\partial x_i$ (replace Q_i by G_i in equations 6.7).

Last, but not least, the *effective conductivity* in the longitudinal direction was simply evaluated by:

$$\hat{K}_{11} = \frac{\overline{Q}_1}{\overline{J}_1} \qquad (6.8)$$

where $\overline{J}_1$ is the prescribed mean hydraulic gradient (6.2), and $\overline{Q}_1$ the computed mean flux defined by (6.7a). In the special case of statistically isotropic log-conductivity field, equation (6.8) gives in fact the value of the effective conductivity along any

direction (problems A and B of Table 6.1). On the other hand, in the case of statistically anisotropic log-conductivity (with principal axis x_1 aligned with the mean flow) the transverse components $\hat{K}_{ii}$ ($i = 2,3$) remain unknown. An additional flow simulation with the mean gradient oriented perpendicularly to the x_1 axis would be needed to determine the effective conductivity perpendicular to stratification.

[d] Finite Size Effects on Estimated statistics

At this point, it may be instructive to examine the possible inaccuracies that may arise from the sampling of a single finite-domain realization of the flow field. We have already pointed out in particular that the hydraulic head field is inherently *non-stationary in the mean* (ideally linear) and has a *larger correlation range than the input conductivity field*. Therefore we expect that the computed mean and second order moments of the hydraulic head could be affected by finite-size sampling errors. We propose a simple evaluation of the "equivalent number of independent samples" (sample size) for evaluating sampling errors. Let $Y(\underline{x})$ be a random field with constant mean, λ_y its correlation scale, and L the size of the domain of averaging used to estimate its moments. Intuitively, it seems reasonable to define the equivalent sample size as the size of the averaging domain expressed in correlation scale

units, that is:

$$N_Y = \left(\frac{L}{\lambda_Y}\right)^m \tag{6.9}$$

where m is the dimensionality of the averaging domain (m = 1,2,3 for 1D, 2D, 3D averaging). According to standard sampling theory, (Appendix 2A), the sampling errors on the mean and on the standard deviation are of the form:

$$\mathrm{Var}(\bar{Y}) \simeq \frac{\sigma^2}{N_Y}$$

$$\mathrm{Var}(\sigma_Y) \simeq \frac{\sigma_Y^2}{2N_Y}$$

to leading order in N_Y. This gives a *rough* estimate for the relative sampling errors (ϵ) in terms of the sample size (N_Y) as follows:

$$\epsilon(\bar{Y}) = \sqrt{\frac{\mathrm{Var}(\bar{Y})}{\sigma_Y^2}} \approx \frac{1}{\sqrt{N_Y}}$$

$$\epsilon(\sigma_Y) = \sqrt{\frac{\mathrm{Var}(\sigma_Y)}{\sigma_Y^2}} \approx \frac{1}{\sqrt{2N_Y}} \tag{6.10}$$

Let us now illustrate the implications of (6.9) and (6.10) for the 1 million node single-realization problem A of Table 6.1 ($\Delta x_i/\lambda_i = 1/3$ and $L_i/\lambda_i \simeq 33.3$). According to

equation (6.9), the sample size of the log-conductivity field is about 37,000 samples in 3D space. From equation (6.10), this implies that the sampling error on the mean ($\ell n\, K_G$) and the standard deviation (σ_f) should be on the order of 1% or less. On the other hand, for the hydraulic head field, the spectral theory predicts that the head correlation scales in the longitudinal (i=1) and transverse (i=2,3) directions are:

$$i = 1: \lambda_H^{(1)} \simeq 3.0\lambda$$
$$i = 2,3: \lambda_H^{(i)} \simeq 7.5\lambda$$

Therefore, the three-dimensional size of the hydraulic head field is only about 220 independent samples. Moreover, in a 2D cross-section such as the one shown in Figure (6.3), the sample size drops to just about 20 independent head samples!

We may now apply equation (6.10) to evaluate, the sampling errors on the cross-sectional mean $\overline{H}(x_1)$ and on the standard deviation σ_H. At each given location x_1, the mean trend $\overline{H}(x_1)$ was evaluated by a 2D average as defined in equation (6.5a). Therefore, the sampling size is only 20 and the relative error on the mean will be quite large:

$$\epsilon(\overline{H}(x_1)) \simeq \frac{1}{\sqrt{20}} \simeq 20\%$$

For the head standard deviation, the averaging domain is three-dimensional. Applying equation (6.10) with sample size 220 gives:

$$\epsilon(\sigma_H) \simeq \frac{1}{\sqrt{440}} \simeq 5\%.$$

The relatively large sampling error on the mean $\bar{H}(x_1)$ reflects the fact that, in any given cross-section x_1, the number of independent samples of the head field is quite low. To reduce the error $\epsilon(\bar{H})$ to 5% would require increasing the lateral side of the domain by a factor of 4 in each transverse direction. This would lead to a grid size of 16 million nodes if the resolution $\Delta x/\lambda = 1/3$ is kept fixed! Unfortunately, the truncation error analysis of Chapter 5 (Section 5.2) showed that a grid resolution on the order of 1/3 or less was required to obtain a reasonable numerical accuracy on the computed flux vector field, which has a much smaller correlation range than the head (typically on the order of λ). The inherent disparity in the fluctuation scales of the flux and head fields is therefore the main cause of trouble in the single-realization approach, as will be seen.

In summary, we have found that the soundness of the single-realization approach depends on the competing requirements of large domain size (in order to obtain a large number of samples of the hydraulic head in space), and fine grid resolution (in order to capture the short range fluctuations of the

conductivity and flux vector). The situation will be even more severe in the case of statistically anisotropic log-conductivities, as will be seen later (section 6.4). Our particular choices of domain size and grid resolution (Table 6.1) usually tended to sacrifice sample size for resolution. The sampling errors due to modest domain size relative to the long range correlation of the hydraulic head, were alleviated in part by using the "ad hoc" detrending procedure of the head field as explained in equations (6.5) above.

In the sequel, we will rely on the methodology just described for analyzing the single-realization flow simulations listed in Table 6.1 above. The table also indicates the section where each particular flow simulation is being analyzed. Section 6.2 treats the medium-size isotropic problem B (130,000 nodes) and emphasizes some of the most obvious physical features of the flow field. The preliminary statistical analysis there does not include correlation functions. Section 6.3 develops a more comprehensive statistical analysis of the flow field for the isotropic problem A (1 million nodes), including a systematic comparison to spectral solutions in terms of single-point and two-point moments. Finally, Section 6.4 focuses on preliminary results obtained with the anisotropic problems E and F (220,000 nodes). The key results of these analyzes are summarized and discussed in the last section 6.5.

6.2 Preliminary Analysis of 3D Isotropic Flow Simulations (130,000 Nodes)

In this section, we analyze in some detail the numerical flow fields obtained for the isotropic problem (B) of Table 6.1 for two different values of the log-conductivity standard deviation ($\sigma_f = 1.0$ and $\sigma_f \simeq 2.3$). The statistical analysis will be limited here to single-point moments, due to the relatively modest size of the grid. On the other hand, we have chosen in this example to emphasize physical interpretation rather than statistical analysis, by using visual representations of the hydraulic head and flux vector fields. Some of the results discussed in this section were reported in a recent paper by Ababou et al. (1987).

[a] Flow field visualization:

The method used here to visualize the three-dimensional flow fields relies heavily on "two-dimensional plots" showing contour lines in selected slices, and occasionally on "one-dimensional plots" of the solution along selected transects. In all cases, the slices and transects were selected at locations coinciding with the geometric center of the flow domain. For the

"isotropic" simulations at hand, the domain was a cube. Figure 6.4 shows the location and orientation of three different slices of interest. It is worth noting that the flow patterns in the horizontal slice parallel to flow (top) and in the vertical slice parallel to flow (centerpiece) should be statistically indistinguishable in the "isotropic" case. The flow pattern in the cross-flow slice (bottom) should look quite different, since the mean hydraulic gradient should be approximately zero in that plane.

In addition, we have included visual representations of the input conductivity fields in the form of 2D contour lines and, occasionally, 3D contour surfaces. We recognize that a three-dimensional representation of the flow fields could be also of interest, possibly in the form of contour surfaces of the hydraulic head and/or stream-surfaces of the flux vector field. This however was not attempted here. Nevertheless, we will see that a number of interesting features emerge from a visual inspection of low-dimensional plots of the random flow fields.

[b] Qualitative Analysis of the Flow Pattern

Let us now discuss the numerical solutions obtained for the isotropic problem "B" of Table 6.1. This flow problem was solved for two different values of the log-conductivity standard

deviation (σ_f = 1.0 and σ_f = 2.3025) on a cubic grid of size N ≃ 130,000 nodes. Recall that the boundary conditions were fixed heads on two opposite faces, and zero fluxes on all other boundaries (Figure 6.1). We have seen that this is equivalent to imposing a large-scale hydraulic gradient aligned with the mean flow direction. The value chosen for the hydraulic gradient (J_1 = 0.004) is typical for natural groundwater flow systems. The random conductivity field was obtained from a single replica of the 3D isotropic Markov field, generated by the Turning Band Method. The grid resolution $\Delta x_i/\lambda_i$ was taken equal to one half, and the cubic domain size was 25 correlation scales in each direction. About one hundred line processes were used in the Turning Band generator, with a random distribution of lines in space according to a uniform spherical distribution (see Chapter 2 and Tompson et al., 1987). The resulting ℓn K field is Gaussian, with an isotropic exponential covariance function in 3D space, as explained in the previous section. Note that the same replica was used for the two sub-problems σ_f = 1.0 and σ_f = 2.3025, by rescaling the ℓn K field in the obvious way.

Figure 6.5 shows the low and high conductivity regions (respectively black and white patches) in a two-dimensional slice for the case $\sigma_f \simeq 2.3$. The contouring routine we used for this and all other contour plots in this work was the Gconmap program

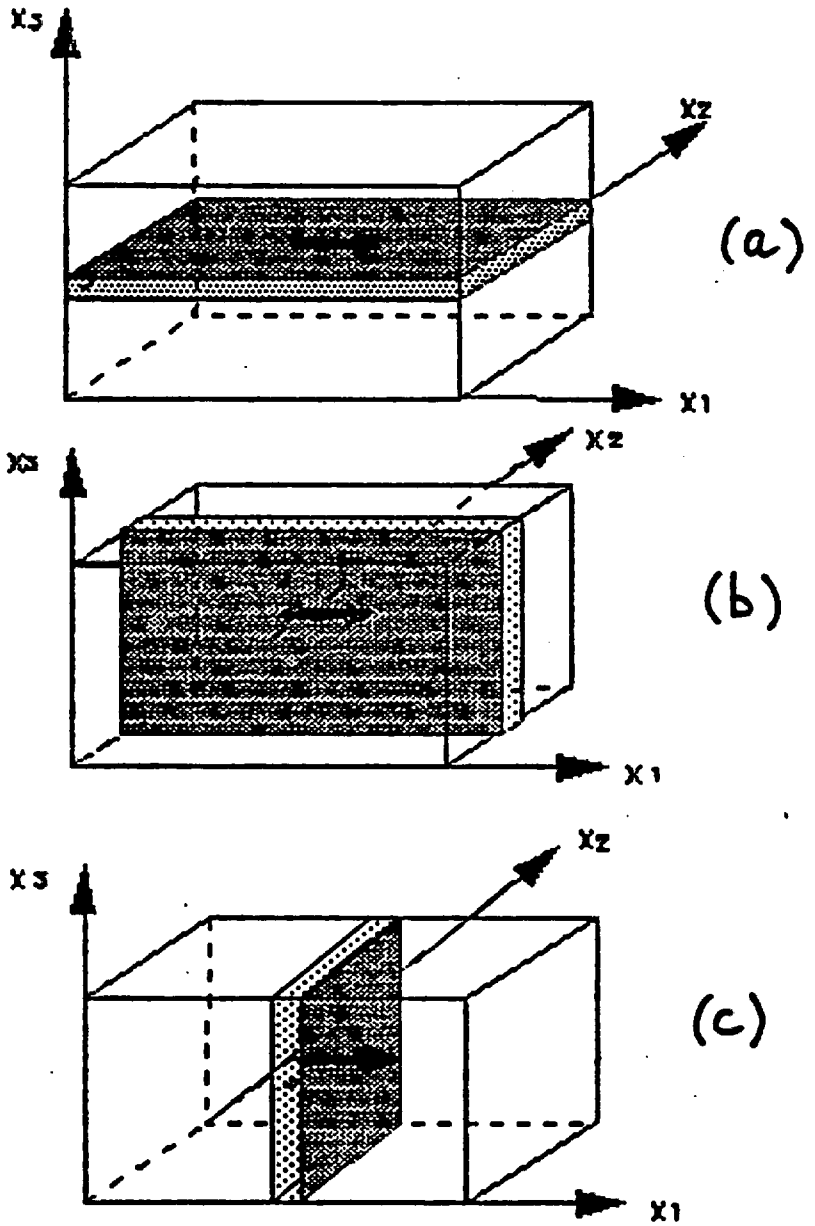

Figure 6.4 Sketch of the two-dimensional slices used for contour plots of the three-dimensional flow fields. The mean flow direction is x_1. From top to bottom: (a) Horizontal slice parallel to flow, (b) Vertical slice parallel to flow, and (c) Vertical slice orthogonal to flow

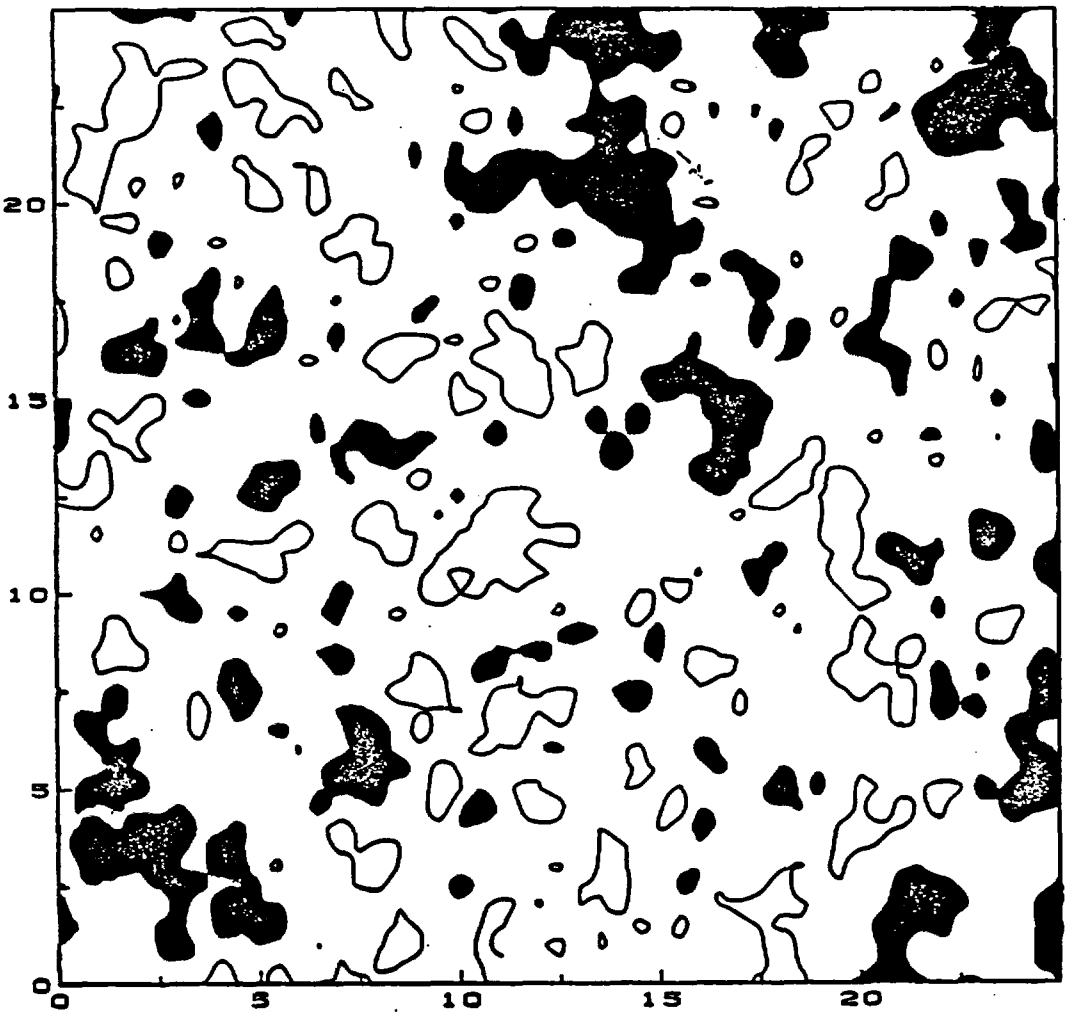

Figure 6.5 Two-dimensional excursion regions of the 3D random conductivity field in a slice (problem B with σ_f = 2.3025). The black and white patches indicate regions where $K/K_G \leq 0.1$ and $K/K_G \geq 10$, respectively.

(Dennis McLaughlin). The contours correspond to regions where the conductivity is one order of magnitude larger or one order of magnitude smaller than the geometric mean ($K_G = 1$). For $\sigma_f \simeq 2.3$, about 30% of the whole space is occupied by such regions, equally distributed among low and high values (15% each). Note that some of the patches appear to be significantly larger than the correlation length ($\lambda = 1$). As expected, they seem isotropically oriented in space.

Figure 6.6 shows an attempt at representing the corresponding high conductivity contour surfaces in three-dimensional space. Here, we have represented only those excursion regions where the conductivity is one order of magnitude *larger* than the geometric mean. The smallest excursion regions had to be filtered out in order to obtain a clearer representation. This was done by applying a linear filter based on a weighted local average of nearest neighbors. Even with this artificial device, the picture remains somewhat misleading: the excursion regions seem to crowd the page, although they really occupy only 15% of the three-dimensional cube. In order to give a feeling of the technical difficulty, we also show in Figure 6.7 a similar plot for the excursion regions corresponding approximately to $K/K_G > 3$. It may be hard to believe that these regions only occupy about 30% of the cubic domain. The "hidden

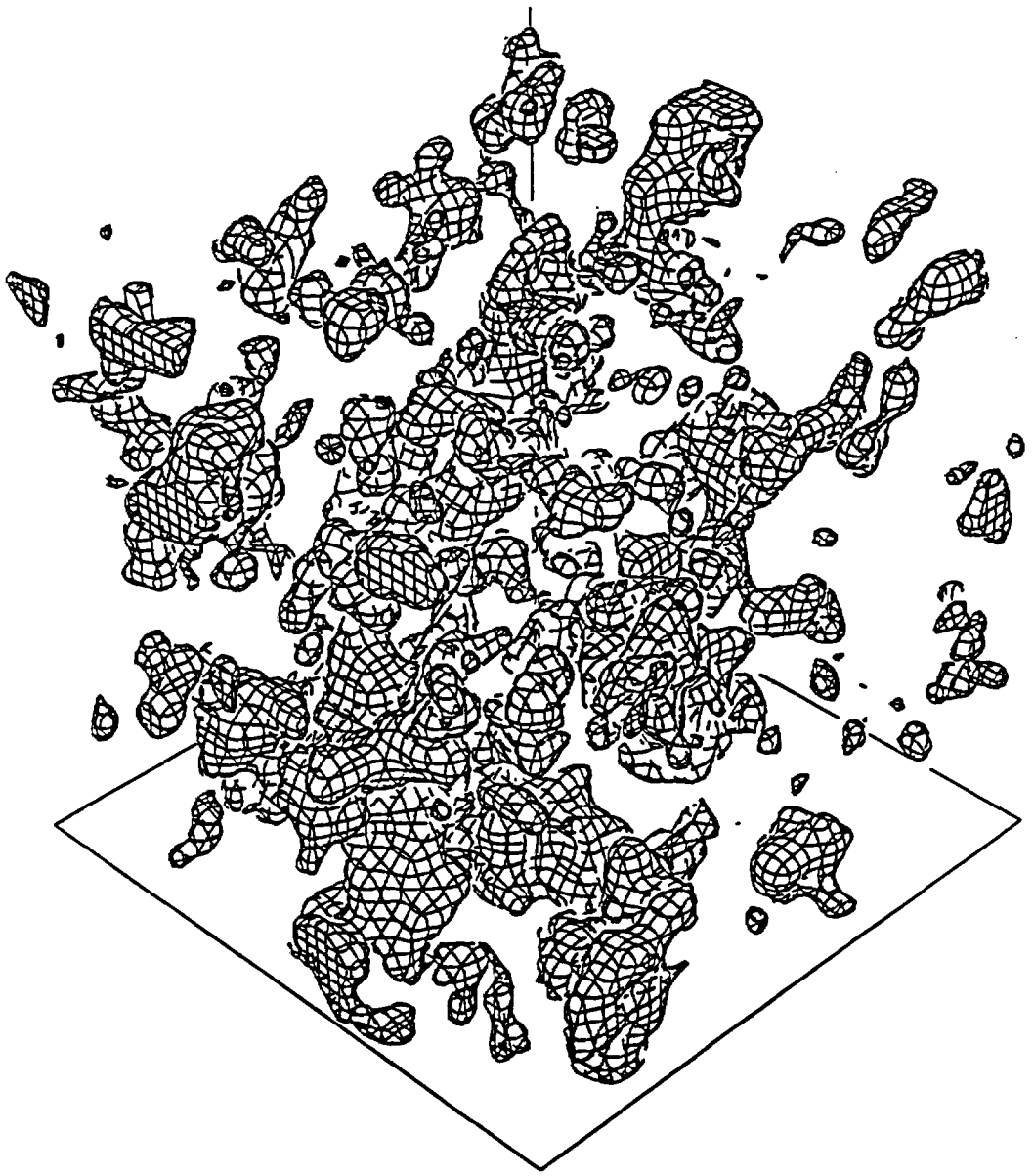

Figure 6.6 Three-dimensional excursion regions of the 3D random conductivity field in a cubic domain with 130,000 grid points (problem B with $\sigma_f = 2.3025$). The regions correspond to high values of the conductivity such that $K/K_G \geq 10$.

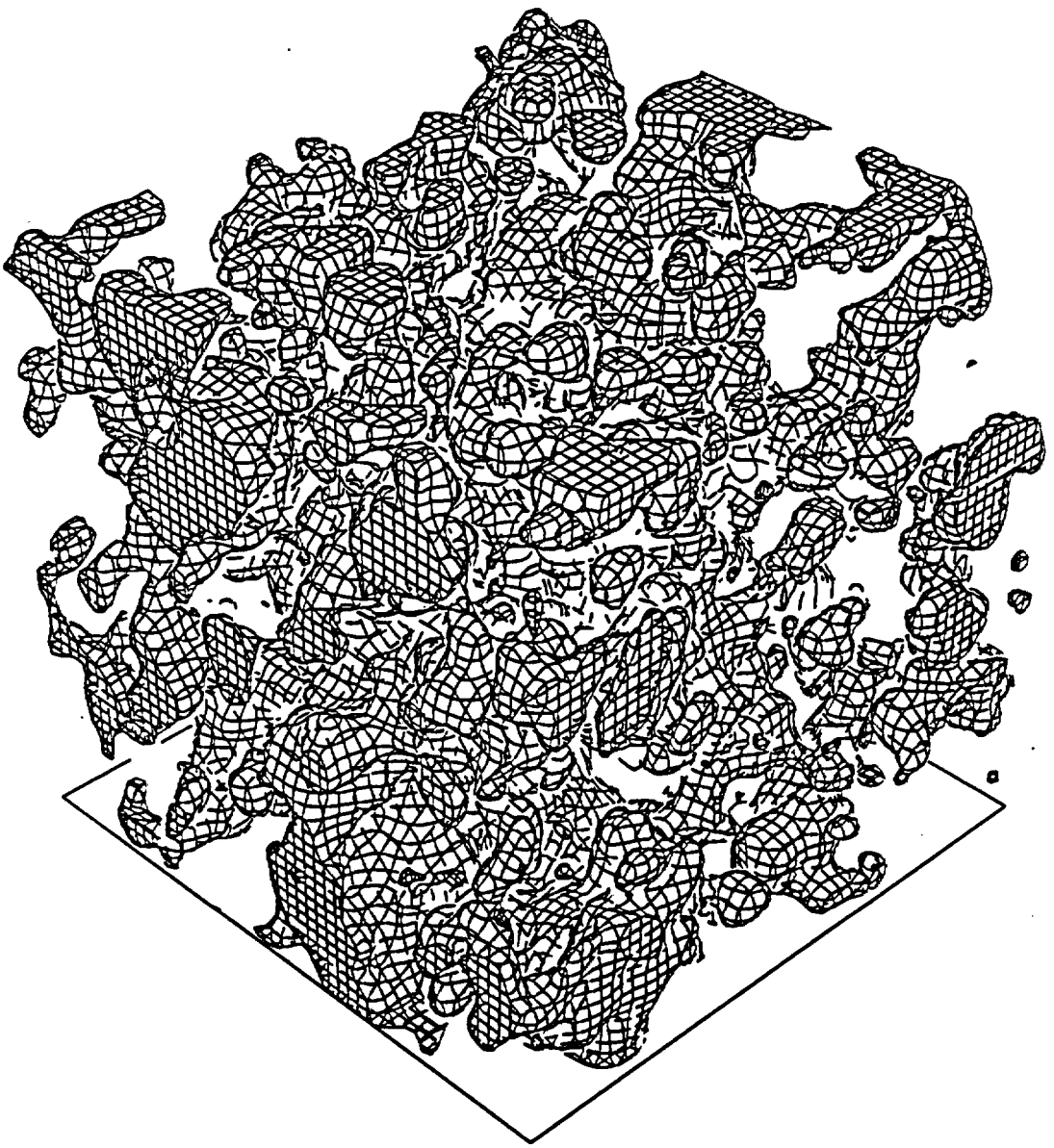

Figure 6.7 Same as Figure (6.6) except that $K/K_G \geq \sqrt{10}$.

lines algorithm" of the package we used (Graf Kit), did not seem able to handle properly such a contorted, random-like function of space. More advanced 3D contouring softwares should be used in these difficult cases.

Figure 6.8 displays the contour lines of the computed hydraulic head in a horizontal slice parallel to the mean flow, for $\sigma_f \simeq 2.3$. Low conductivity contours are also shown in the background. The white areas, devoid of background conductivity contours, correspond to regions where the conductivity is greater than about 30% the geometric mean value (pathways for flow). It is worth noting that the head gradient steepens near local minima of the conductivity fields, and becomes flatter in the white areas corresponding to larger conductivities. This interesting behaviour could perhaps be deduced from the one-dimensional Darcy equation:

$$q = - K(x) \frac{dH}{dx} \text{ (constant)}$$

However, the generalization to three-dimensional flow is far from obvious. The observed one-dimensional behavior could be explained by the fact that the flow field in this example is *globally* one-dimensional, since all lateral boundaries are impervious. Incidentally, note that the head contour lines are

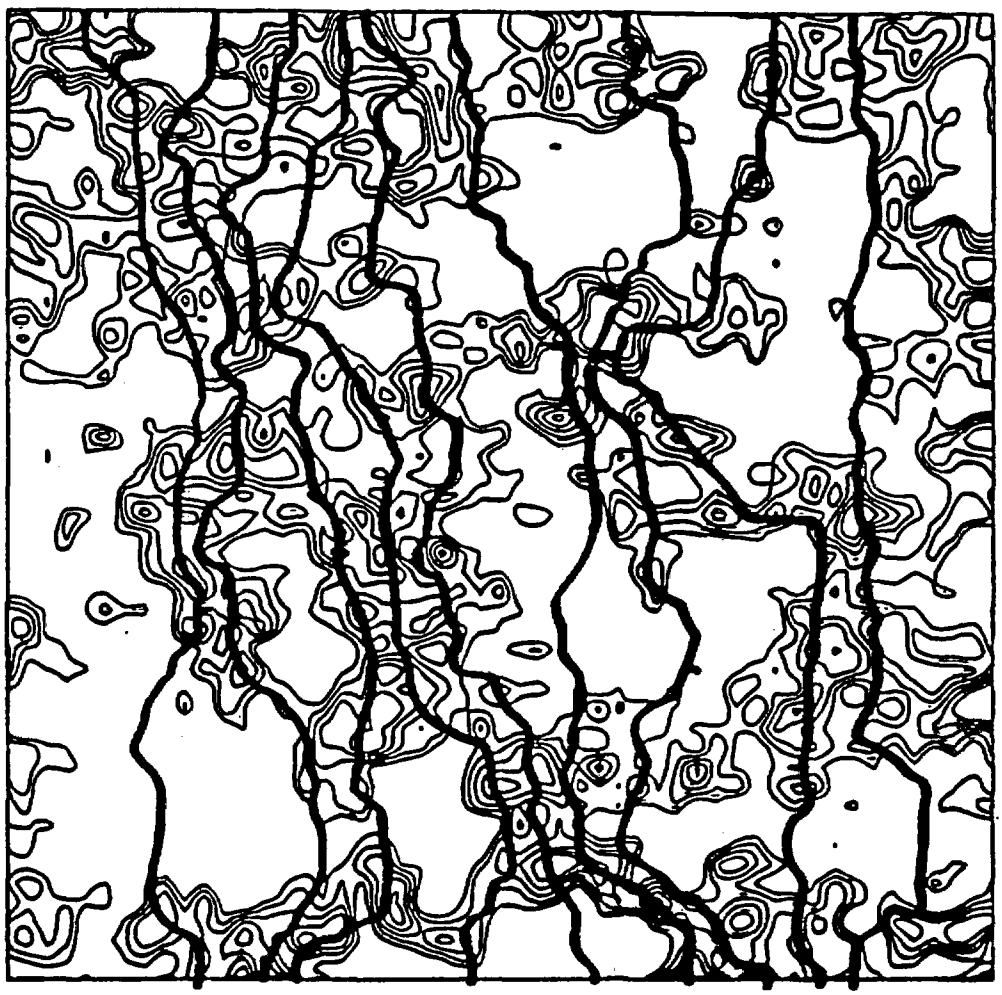

Figure 6.8 Hydraulic head contours in a horizontal slice parallel to the mean flow for problem B with σ_f = 2.3025. There are 10 contour lines of equally spaced head values including the right and left boundaries. Low conductivity contours are shown in the background ($\log_{10}(K/K_G)$ = 0,-0.5, -1, -5,-2)

orthogonal to the lateral boundaries (as they should). The influence of such artificial boundaries on the fluctuations of the head in the interior does not seem overly important: see for instance how the left-most head contour line of Figure (6.8) joins the two lateral boundaries.

Figure 6.9 compares the hydraulic head contours for $\sigma_f = 1.0$ and $\sigma_f \simeq 2.3$ in the same horizontal slice as Figure (6.8). The influence of the log-conductivity variability (σ_f) is quite dramatic: both the small scale and large scale fluctuations (wiggles and smooth undulations) of the head contour lines are significantly amplified when σ_f increases from 1.0 (top) to 2.3 (bottom). Note that the same replica of the log-conductivity field was used, so that the pattern of fluctuations of $\ell n\, K$ was the same for the top and bottom pictures of Figure (6.9). Another remarkable feature that emerges from these pictures is that the hydraulic head contours are relatively smooth compared to the noisy input conductivity. The typical fluctuations scale of the head contour lines in the cross-flow direction seems to be much larger than the λ-scale of conductivity. This feature is indeed predicted by the spectral theory.

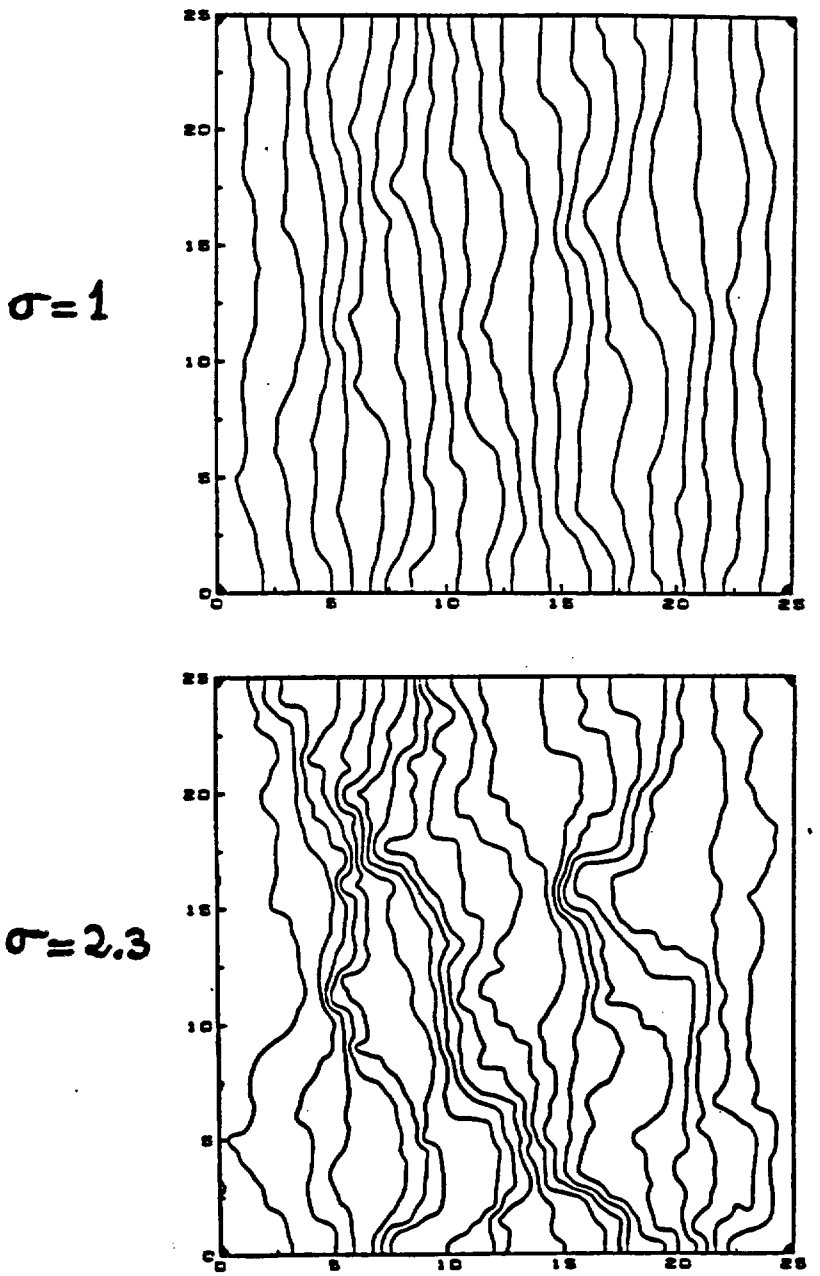

Figure 6.9 Comparison of hydraulic head contours in a horizontal slice parallel to flow for $\sigma_f = 1$(top) and $\sigma_f \simeq 2.3025$ (bottom) (Problem B). These are 21 contour lines of equally spaced head values, including the right and left boundaries.

More precisely, recall from Chapter 3 that the head correlation function predicted by the spectral theory has a larger correlation range than the input log-conductivity fields, about 7.5λ in the transverse direction and 3.0λ in the mean flow direction (see Figure 3.1). Our preliminary calculations of the head covariance function, based on the spatial averaging method outlined in the previous section (equations 6.4 and 6.6), showed approximately the same behaviour for the case of moderate variability $\sigma_f = 1$. However, the head covariance functions obtained for the case of higher variability did not agree with the spectral theory, probably due to the limited size of the domain and, perhaps, to the relatively coarse grid resolution (see problem B data in Table 6.1).

Nevertheless, it turns out that the computed head standard deviations matched to within 10% the values predicted by the spectral theory (equation 3.21) for both cases of moderate and high variability, $\sigma_f = 1.0$ and $\sigma_f \simeq 2.3$. Figure (6.10) shows the slowly fluctuating nonlinear trend around which the head variance was computed; a hypothetical linear mean head profile is superimposed for comparison (top picture). The bottom part of the figure displays a typical transect of the head process around the nonlinear trend. It is important to note that the computed head deviation would have been much larger than the

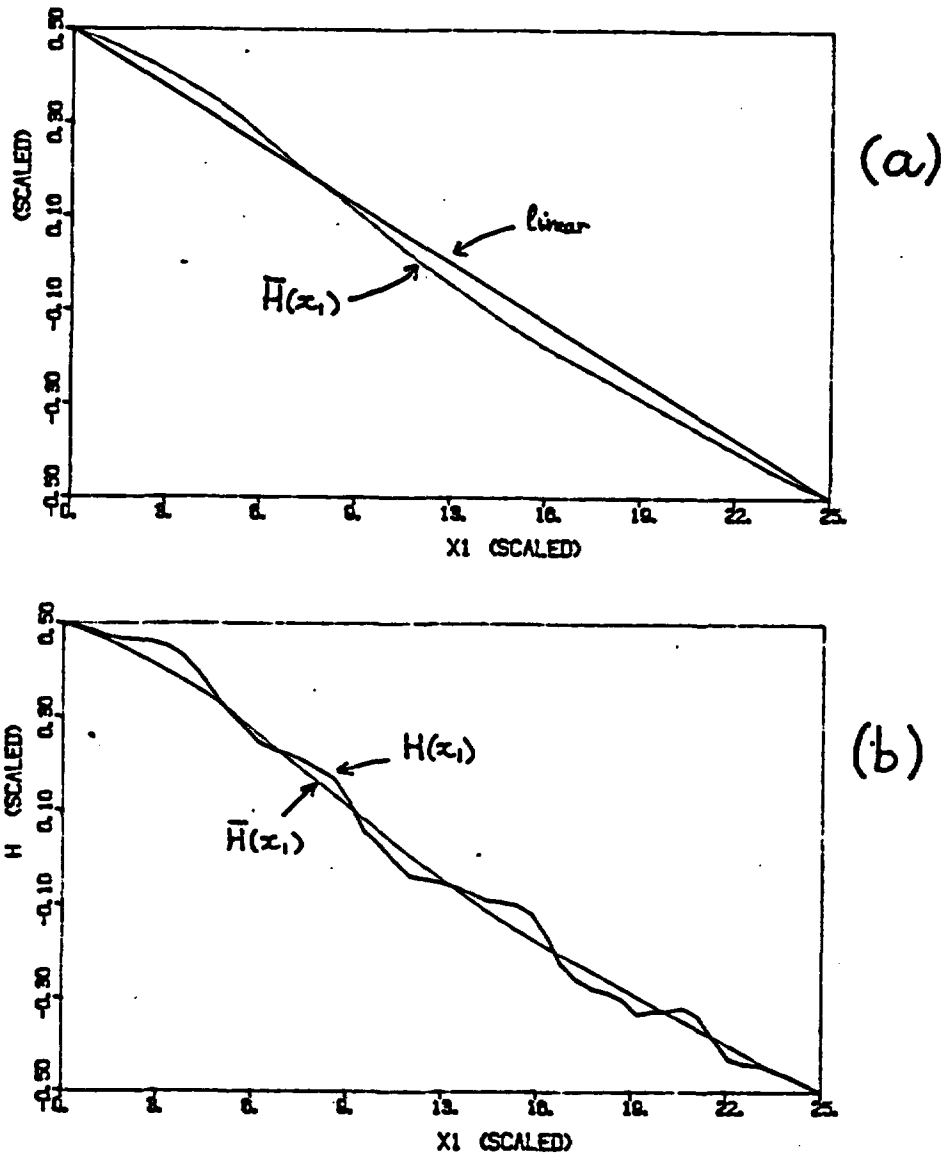

Figure 6.10 One-dimensional representation of the spatial fluctuations of the hydraulic head (Problem B - $\sigma_f \simeq 2.3$):

(a) Comparison of computed trend $\bar{H}(X_1)$ with hypothetical linear profile

(b) Fluctuations of the head field around the trend for a particular transect parallel the mean flow

predicted spectral value if the hypothetical linear mean had been used instead. In our view, the head variance obtained in this way would be meaningless, since the whole method is based on the premise that the second order moments of the flow field are spatially homogeneous.

It is rather encouraging that our detrending technique leads to a close agreement between the theoretical (spectral) and numerical standard deviations of the head field, even for the relatively modest size problem at hand. This was confirmed for a number of other cases, isotropic and anisotropic, as will be seen in later sections.

[c] Statistical Analysis of Single-point Moments

A more complete set of single-point moments of the numerical flow field is given in Table 6.2. The table lists the values of the head and flux vector standard deviations, as well as the effective conductivities, obtained by the spatial averaging techniques described in the previous section (equations 6.1-6.8). For comparison, the values predicted by the spectral theory are also listed in the same table (in parenthesis). The spectral formulas used to compute σ_H, K_{eff}, and σ_{q_i}, were given in equations (3.21), (3,23) and (3.26) of Chapter 3. Note that

TABLE 6.2

COMPARISON OF NUMERICAL AND SPECTRAL THEORY STATISTICS FOR THE "ISOTROPIC" FLOW PROBLEM B OF TABLE 6.1 (N ≃ 130000 NODES). THE SPECTRAL THEORY STATISTICS ARE SHOWN IN PARENTHESIS.

	$\sigma_f = 1.0$	$\sigma_f = 2.3025$
σ_f	.002510 (.002309)	.005901 (.005317)
σ_{q_1}	.003820 ((.003451))	.04630 ((.01628))
σ_{q_2}	.001299 ((.001220))	.01959 ((.00576))
σ_{q_3}	.001313 ((.001220))	.02148 ((.00576))
$\sigma_{q_3}/\sigma_{q_1}$	.344 (.354)	.464 (.354)
$\bar{Q}_1$	.00527 (.00472)	.01604 (.00968)
$\bar{Q}_2/\bar{Q}_1$	.054 (.000)	.161 (.000)
$\bar{Q}_3/\bar{Q}_1$	-.066 (.000)	.011 (.000)
K_{eff}	1.318 (1.181)	4.010 (2.420)

the flux standard deviations σ_{q_i} shown in double parenthesis were computed from a *modified* version of the spectral theory of Gelhar and Axness (1983), as explained in Section 4.3 of Chapter 4. The conclusions to be drawn from Table 6.2 are summarized below.

The most encouraging result from Table 6.2 is that all the statistics computed from the simulated flow field in the case of moderate variability ($\sigma_f = 1.0$) agree with the spectral theory with a 10% margin of error. On the other hand, in the case of large variability ($\sigma_f \simeq 2.3$), there is a serious discrepancy for most of the statistics related to the flux vector. The most robust statistics appear to be the head standard deviation (σ_H) and the ratio of transverse to longitudinal flux standard deviations ($\sigma_{q_T}/\sigma_{q_L}$):

$$\sigma_H \simeq \frac{1}{\sqrt{3}} \sigma_f \, J_1 \, \lambda$$

$$\frac{\sigma_{q_T}}{\sigma_{q_L}} \simeq \frac{1}{\sqrt{8}}$$

It is remarkable that the ratio $\sigma_{q_T}/\sigma_{q_L}$, which indicates the relative variability of the transverse-versus-longitudinal flux

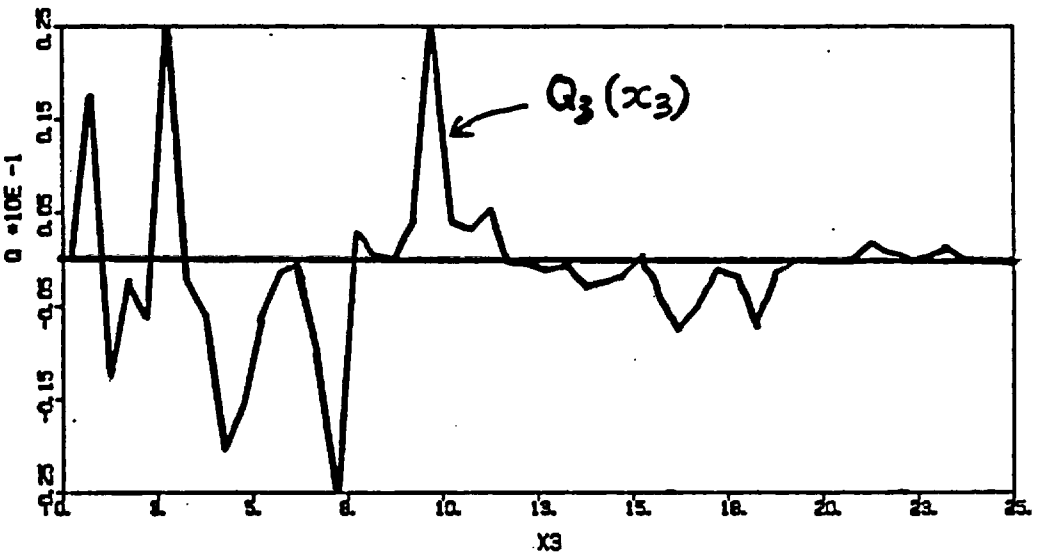

Figure 6.13 Transverse flux component Q_3 along a transect x_3 transverse to the mean flow (isotropic Problem B, σ_f = 2.3025)

components, does not depend on σ_f. This particular property of the flow field predicted by the spectral theory, is approximately verified by the numerical solutions.

We believe that the discrepancies between the theoretical and numerical values of the flux deviation and effective conductivity obtained for $\sigma_f \simeq 2.3$ are due to the combined effects of insufficient domain size (K_{eff}), insufficient grid resolution (σ_{q_i} and K_{eff}), and perhaps inaccurate first order spectral solution in cases of high variability (small σ_f assumption). The unsufficient grid resolution (1/2) could be at the origin of the mass balance error indicated by the non-zero ratio $\overline{Q}_2/\overline{Q}_1$ (11.6% for $\sigma_f \simeq 2.3$); this significant error could also be explained by the fact that the fluxes were computed in this case as local "cell averages" of mid-nodal values, which might not be the best strategy. At any rate, the questions raised above motivated our subsequent use of supercomputing capabilities to simulate stochastic flow problems on larger and finer grids (1 million nodes); this will be examined separately in a forthcoming section. In comparison, recall that the grid size for the flow problem at hand was "only" 130,000 nodes.

[d] Qualitative Analysis of Flux Vector Field

In spite of the insufficient grid resolution, we found that the flow problem at hand was sufficiently representative to justify a preliminary qualitative analysis of the simulated flux vector field. Figures (6.11) to (6.15) depict the spatial variability of various flux components in the case $\sigma_f \simeq 2.3$. The first three figures show the fluctuations of $Q_i(\underline{x})$ along selected transects, and the next two figures display the pattern of $Q_i(\underline{x})$ in selected slices. In Figure (6.11), the longitudinal flux component Q_1 is plotted along the mean flow direction x_1; the mean trend $\bar{Q}_1(x_1)$ is also displayed for comparison. Observe the sharp peaks of $Q_1(x_1)$ at local maxima, compared to the smooth local minima near zero. This behaviour indicates a positively skewed distribution, as would be the case for a positive log-normally distributed random function: see for instance the plot $K(\underline{x})$ given in Figure 2.3 of Chapter 2. In contrast, the transverse flux components Q_2 and Q_3 depicted in Figure (6.12) and Figure (6.13) appear to fluctuate symmetrically around their zero mean value, as expected, due to the absence of a mean driving force in the transverse directions.

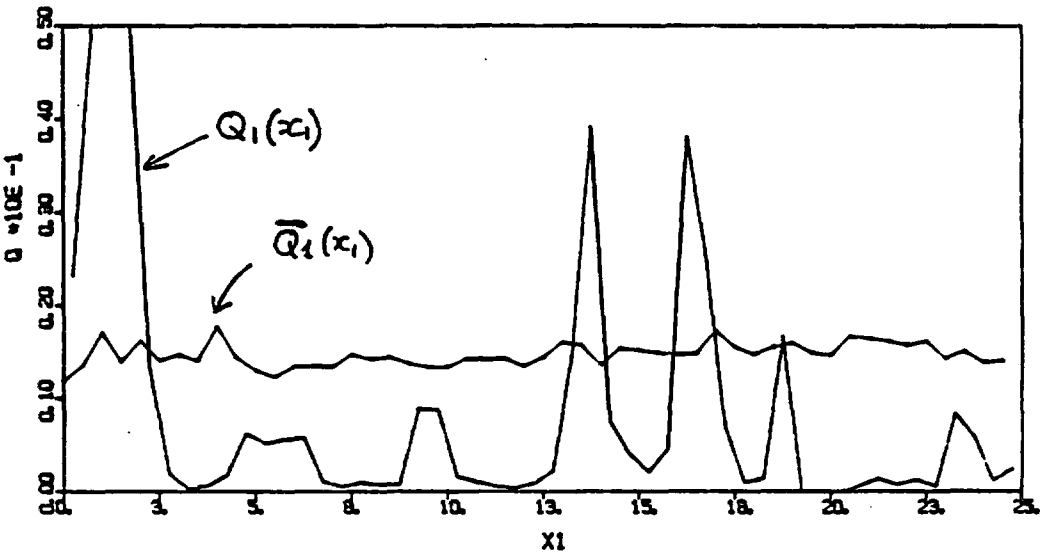

Figure 6.11 Longitudinal flux component Q_1 along a transect parallel to the mean flow direction x_1 (isoptropic Problem B, σ_f = 2.3025)

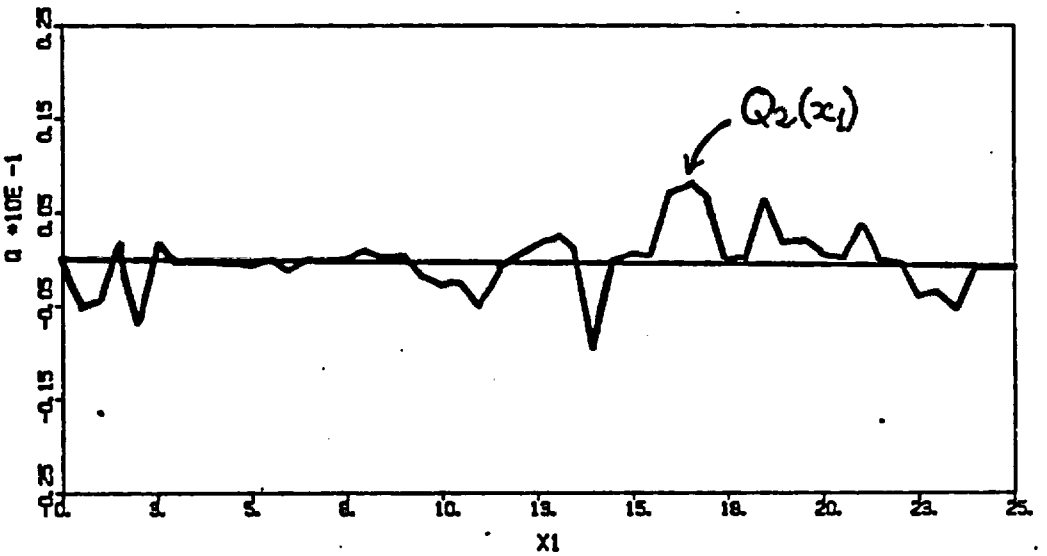

Figure 6.12 Transverse flux component Q_2 along a transect parallel to the mean flow direction x_1 (isotropic Problem B, $\sigma_f = 2.3025$)

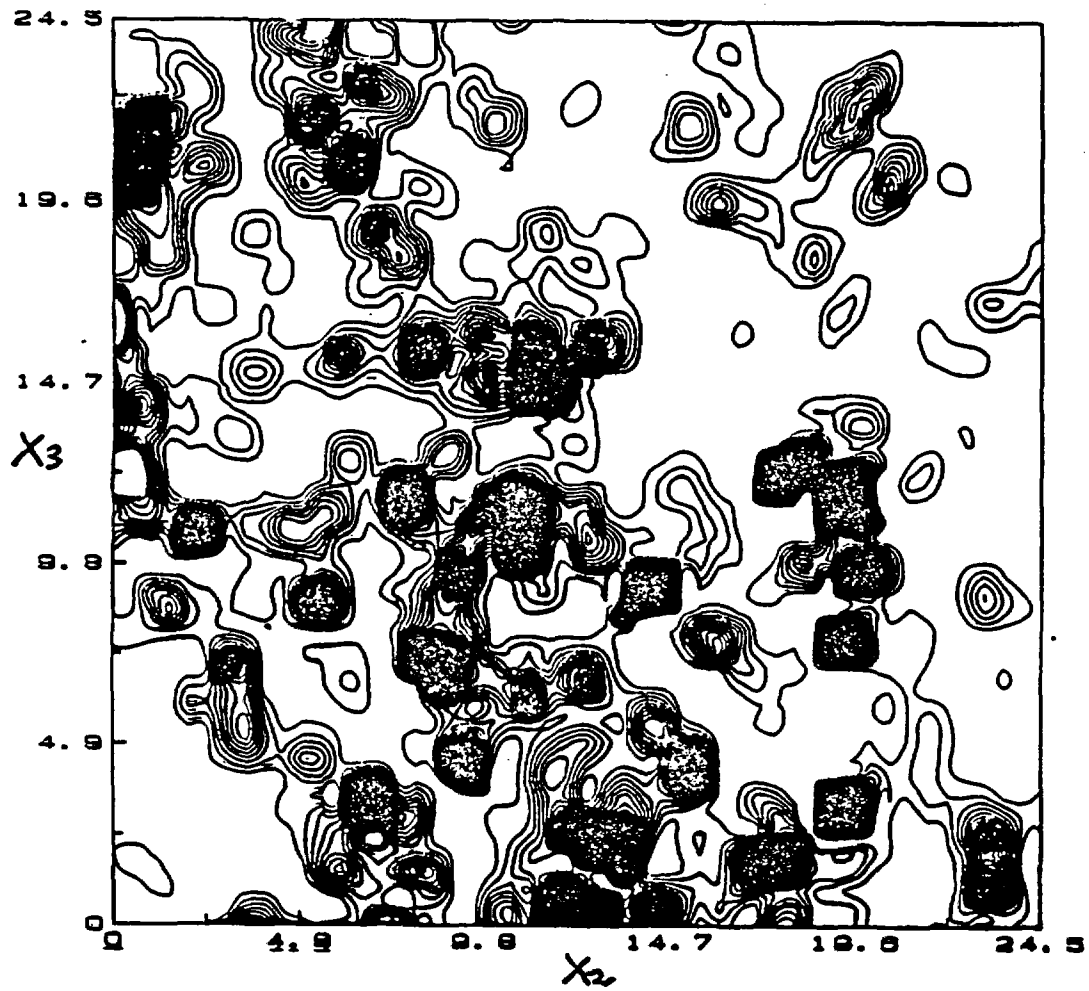

Figure 6.14 Contour lines of the longitudinal flux component Q_1 in a vertical slice transverse to the mean flow (isotropic Problem B, $\sigma_f = 2.3025$). The isovalues are equally spaced, from $Q_1 = 0$ up; the black patches correspond to high values of Q_1 well above the mean $\overline{Q}_1$

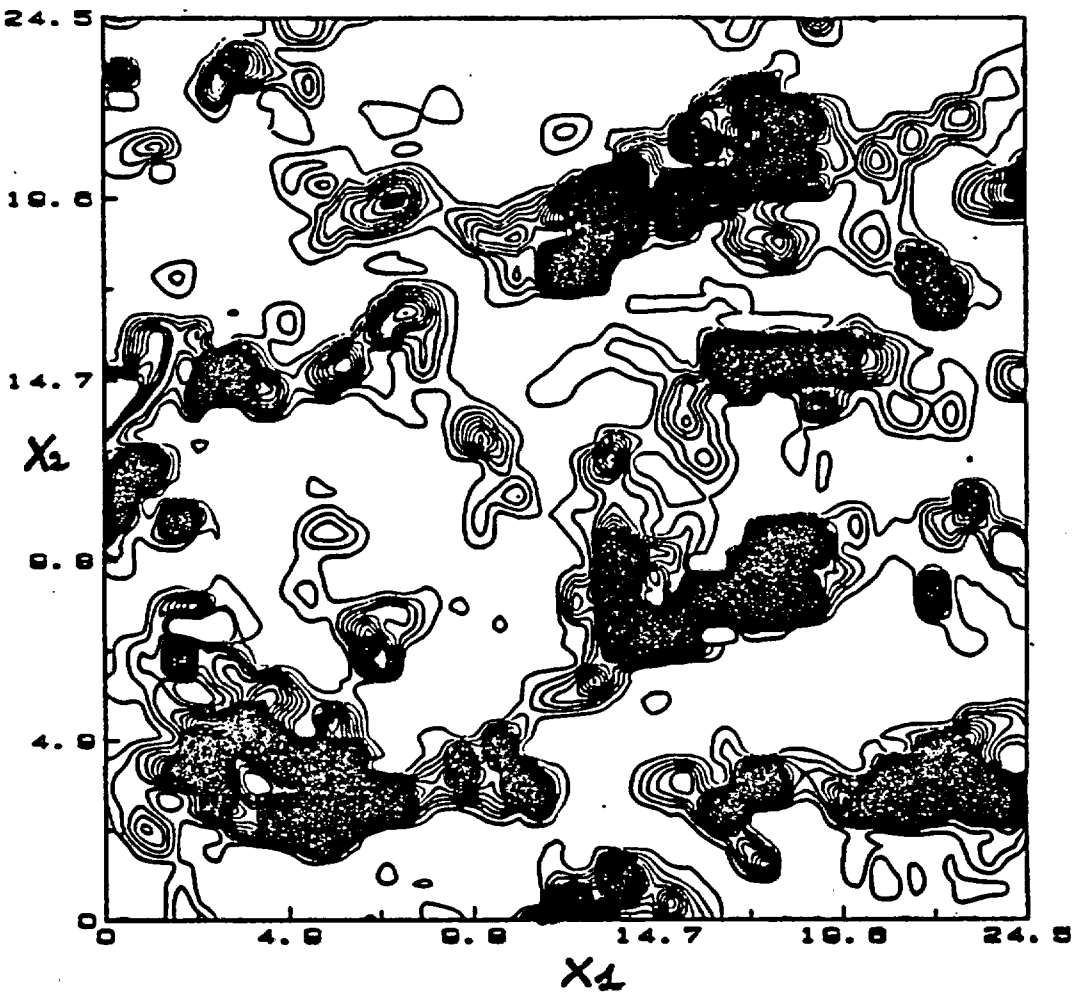

Figure 6.15 Same as Figure 6.14, except that the Q_1-contour lines are shown in a horizontal slice parallel to the mean flow (isotropic Problem B, $\sigma_f = 2.3025$). The isovalues are equally spaced, from $Q_1 = 0$ up; the black patches correspond to high values of Q_1 well above the mean $\overline{Q}_1$.

Finally, let us comment on two more figures showing equally spaced isovalue contours of the longitudinal flux component Q_1 in selected slices. Figure (6.14) shows $Q_1(\underline{x})$ in a vertical plane transverse to the mean flow, i.e., such that the mean flow is orthogonal to the sheet of paper, pointing towards it. The regions of high "velocity" are highlighted in black: one might think of a sieve, with the black patches corresponding to holes or preferential pathways for flow. Two notable features emerge from this picture. First, it appears once again that local maxima (black patches) are much narrower than local minima (white areas). Second, the excursion regions of Q_1 (e.g., the black patches) are more or less isotropically oriented in the cross-flow plane, as expected. However, note the quasi-rectangular shape of some of the smaller patches. This is probably due to insufficient grid resolution: the orthogonal geometry of the grid induces an artificial anisotropy of the flow field at the scale of the mesh.

It may be interesting to compare the near isotropic pattern of excursion regions of Figure (6.14) to those shown in the last Figure (6.15). In the latter case, the selected slice was in a horizontal plane parallel to flow (water moves from left to right in the plane of the sheet). The high excursion regions of Q_1 appear to be elongated in the longitudinal direction.

This indicates that the longitudinal flux is more strongly correlated in the mean flow direction than across the flow. This property is indeed in agreement with the findings of the spectral theory (Figure 3.2 of Chapter 3). A direct comparison of numerical and theoretical flux correlation functions for the larger simulation (1 million node problem "A") will confirm these qualitative observations.

[e] Summary of Findings

In summary, we have found that the relatively modest size flow simulation at hand (130,000 nodes) produced a flow pattern in accordance with the findings of the spectral theory for a number of features, such as the head variance and, for moderate variability, the flux variance and the effective conductivity. The spatial structures of the hydraulic head and the longitudinal flux component were *qualitatively* in agreement with the behavior predicted by the spectral theory. It is remarkable that meaningful information could be obtained from a single realization of the flow field small enough to be produced on a minicomputer (Microvax 2).

However, we have also found some significant discrepancies between the spectral theory and the numerical solutions at high variability, particularly concerning the flux standard deviations σ_{q_i}, and the effective conductivity K_{eff}. The observed discrepancies could be due to a combination of truncation errors (insufficient resolution), sampling errors (finite size effects), and possibly to the increasing inaccuracy of the spectral theory as σ_f increases. This latter possibility may be indicated by the fact that the longitudinal flux component appeared to have a positively skewed distribution. This behavior seems to make sense intuitively, as the Darcy equation shows that Q_1 can be expressed by Darcy's equations:

$$Q_1(\underline{x}) = K(\underline{x}) \cdot J_1 - K(\underline{x}) \cdot \frac{\partial h}{\partial x_1}$$

where the first term is a log-normally distributed random field. Now, the first order spectral theory obviously cannot take this kind of third order effect into account, since third order moments are ignored.

In order to try to resolve the questions of the accuracy of the spectral theory as σ_f increases, we proceed to

analyze in the next section a series of larger flow realizations on a 1 Million node grid.

6.3 Statistical Analysis of 3D Isotropic Flow Simulations (1 Million Nodes)

[a] Preliminary Considerations

The large single-realization flow problem to be analyzed here (problem A of Table 6.1) is similar to the previous one except for the finer grid resolution ($\Delta x_i/\lambda_i$ = 1/3 instead of 1/2) and larger domain size (L_i/λ_i = 33 instead of 25). It may be instructive to begin by comparing how the difference in size could affect the statistical representativity of the flow field. For this purpose, let us use the simplified analysis of sampling errors outlined in section 6.1 (*see equation 6.10 and the example below it*). Thus, the sampling error on the mean hydraulic head $\overline{H}(x_i)$ was evaluated as the inverse square-root of the number of head samples available in a cross-section transverse to the mean flow direction. This number is 20 for the problem (A) at hand,

compared to 10 for the previous problem (B). The relative sampling error on the mean $\overline{H}(x_1)$, according to equation (6.10), would then be about 20% for problem A, compared to about 30% for problem B. Thus, we expect that the fluctuations of the nonlinear trend $\overline{H}(x_1)$ will be less pronounced for the larger problem A. In addition, we also expect a better accuracy on the flux variance due to the finer grid resolution. This point will be discussed in more detail later.

We focus now on the three single-realization flow fields (σ_f = 1.0, 1.732, 2.3025) corresponding to the isotropic problem (A) of Table 6.1. On the numerical side, let us mention that the iterative solution of these 1 Million node problems was fully analyzed in Chapter 5 (Section 5.3, Table 5.4 and accompanying figures). Recall in particular that the three subproblems were solved in sequence on a Cray 2 machine, requiring a total of about four hours of CPU time. Finally, it may be worth noting that a single replica of the log-conductivity field was used for the three subproblems. This was done by rescaling $\ell n\, K(\underline{x})$ in the obvious way to accommodate different values of the log-conductivity standard deviation σ_f.

[b] Conductivity Field Generation and Analysis:

The conductivity field was generated, as before, by the three-dimensional Turning Band generator of Tompson, Ababou and Gelhar, 1987. For the case at hand, a three-dimensional isotropic Markov field $\ell n\ K(\underline{x})$ was generated over the 101 × 101 × 101 cubic finite difference grid. The particular data used in the Turning Band generator were as follows: 1000 lines distributed randomly in space ("turning band"), 300 harmonics per line for the generation of each line spectrum, and a few hundred points per line (up to 500) for the generation of the corresponding line processes. Thus, the spatial resolution on each line was about 1/5 relative to the mesh size. The resolution in Fourier space was $\Delta\tilde{k} = 1/3$, and the high wavenumber cut-off was $\tilde{k}_{max} = 100$ ($\tilde{k}$ is a normalized wavenumber equal to λk). According to the empirical rules developed by Tompson et al. 1987, these parameters are quite conservative and should lead to statistically meaningful results as far as the conductivity field is concerned.

It may also be important to note that the random number generator we used was slightly different from Tompson et al. 1987. We took advantage of the fact that the largest integer on the 64-bit words Cray 2 machine is very large ($N = 2^{63} \simeq 9\ 10^{18}$). In these conditions, our literature review indicated that one of

the most reliable random number generators available to date was the "Type 2" congruent method of Fishman and Moore (1986) as defined below. Let R be a random number uniformly distributed in $[0,1]$. Then a sequence of pseudo-random numbers R_k is obtained by:

$$\begin{cases} N_{k+1} = L \cdot N_k \ (\text{mod}.M) \\ \\ R_{k+1} = \text{Float}\ (N_{k+1})/\text{Float}(M) \end{cases} \tag{6.11a}$$

where the modulus (M) and the multiplier (L) are, respectively:

$$\begin{cases} M = 2^{31} - 1 = 2,147,483,647 \\ \\ L = 950,706,376 \end{cases} \tag{6.11b}$$

and the initial seed N_o can be any number less than M (e.g., $N_o = 1$). The advantage of this particular random number generator is that it is equidistributed and has a very large cycle length $M - 1$, i.e., about 2 billion numbers. The multiplier L given above was among the "best" in a series of tests developed by Fishman and Moore (1986).

To illustrate the soundness of the random field generator, we show in Table 6.3 a comparison between the

TABLE 6.3

COMPARISON OF THEORETICAL (ENSEMBLE) MOMENTS AND COMPUTED (SPATIAL) MOMENTS, FOR THE SINGLE REPLICA OF THE ISOTROPIC 3D MARKOV LOG-CONDUCTIVITY FIELD GENERATED BY THE TURNING BAND METHOD (1 MILLION NODE FLOW PROBLEM)

	INPUT Theoretical Values	OUTPUT Computed Values	RELATIVE ERROR
$\langle F \rangle$	0	0.1966	+2 %
σ_f	1.0	0.9983	-0.2%
$R_{ff}(\lambda,0,0)$	0.3679	0.3860	+5 %
$R_{ff}(0,\lambda,0)$	0.3679	0.3785	+ 3 %
$R_{ff}(0,0,\lambda)$	0.3679	0.3781	+ 3 %

Note: The relative error on the estimated mean was defined as $(\bar{f}-\langle f \rangle)/\sigma_f$. In this particular case, $\sigma_f=1$ and $f=\ell n(K/K_G)$ is a zero-mean Gaussian random field with isotropic correlation function $e^{-\xi/\lambda}$. At separation distance $\xi=\lambda$, the correlation is $e^{-1} \simeq 0.3679$.

prescribed ensemble moments of the log-conductivity field and the computed spatial moments obtained by the spatial averaging method described previously (equations 6.4). Note that the relative errors on the mean and standard deviation are very small; the error on the covariance function at separation distance λ is also quite small. This excellent agreement indicates that the turning band generator can produce statistically accurate realizations of random fields at reasonable costs: the 1 million node realization at hand required only 10 minutes of CPU time on the Cray 2 machine (without the use of Fast Fourier Transforms). Furthermore, this also illustrates in a concrete way the equivalence of ensemble and spatial moments for large realizations of homogeneous-ergodic fields. In other words, the particular log-conductivity realization at hand appears to be fairly representative of the whole ensemble of possible realizations.

(c) Visual representation of the head field

The three flow realizations obtained by numerical simulation for the cases $\sigma_f \simeq 1.0, 1.7, 2.3$ were statistically analyzed by using the same spatial averaging procedures described in the methodology section (6.1). This will not be repeated

here; the reader is referred to equations (6.4)-(6.8). In order to illustrate concretely the spatial structure of the head field, we show in Figure 6.16, (a),(b),(c) the contour lines of the hydraulic head in a horizontal slice parallel to the mean flow, for each of the three cases $\sigma_f \simeq 1.0$, 1.7, and 2.3. Note that each slice contains about ten thousand mesh points. The spatial structure of the head does not seem to differ much from the similar pictures obtained previously for a smaller flow problem (Section 6.2).

In addition, Figures 6.17 (a),(b),(c) show the fluctuations of the hydraulic head along a transect parallel to the mean flow. The nonlinear trend $\overline{H}(x_1)$ obtained by cross-flow averaging was superimposed for comparison. It should be noted that the nonlinearity of $\overline{H}(x_1)$ seems milder than it was for the smaller flow realizations analyzed previously: compare figure 6.17a to figure 6.10. This finding is in accordance with our previous evaluation of finite size sampling errors, at least qualitatively. The improvement seems to be even better than expected, due to the fact that boundary effects were not included directly in the aforementioned analysis of finite size effects.

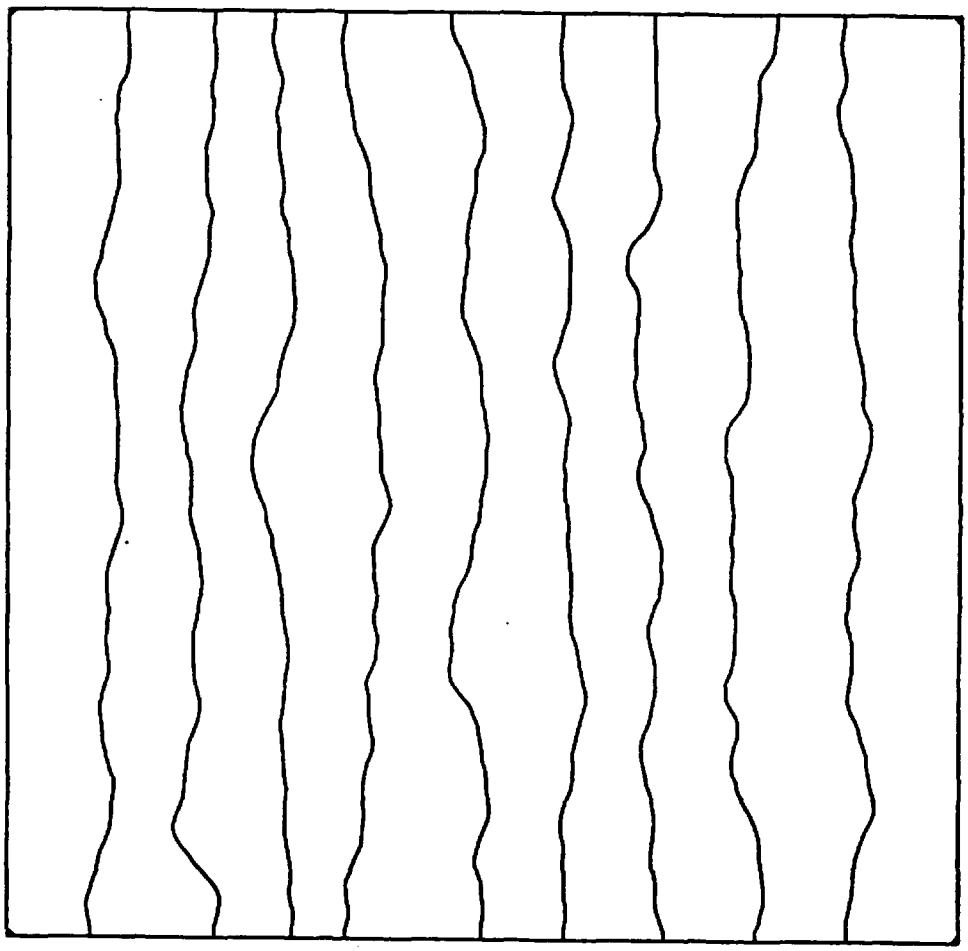

Figure 6.16 (a) Contour lines of the three-dimensional hydraulic head field in a horizontal slice parallel to the mean flow (pointing right). There are 11 iso-value contours including the left and right boundaries (equally spaced values). Flow problem A with 1 Million nodes: (a) case $\sigma_f = 1.0$.

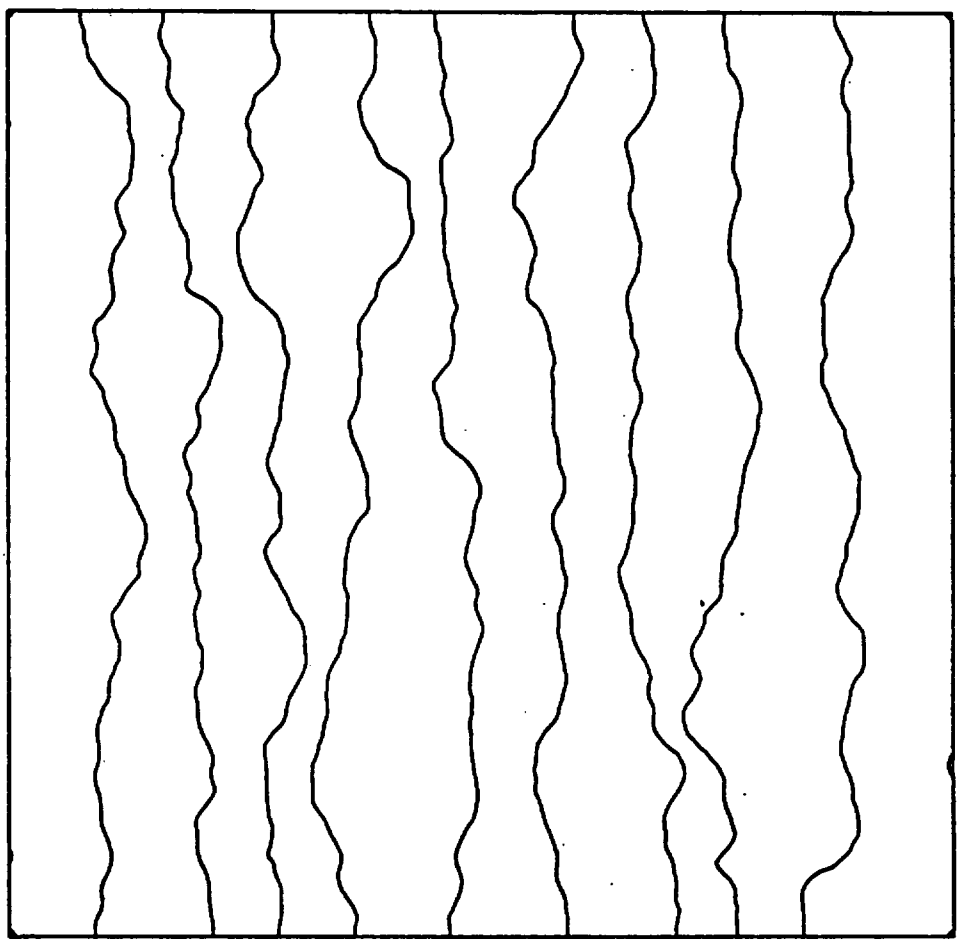

Figure 6.16 (b) Same as (a), with $\sigma_f = 1.732$.

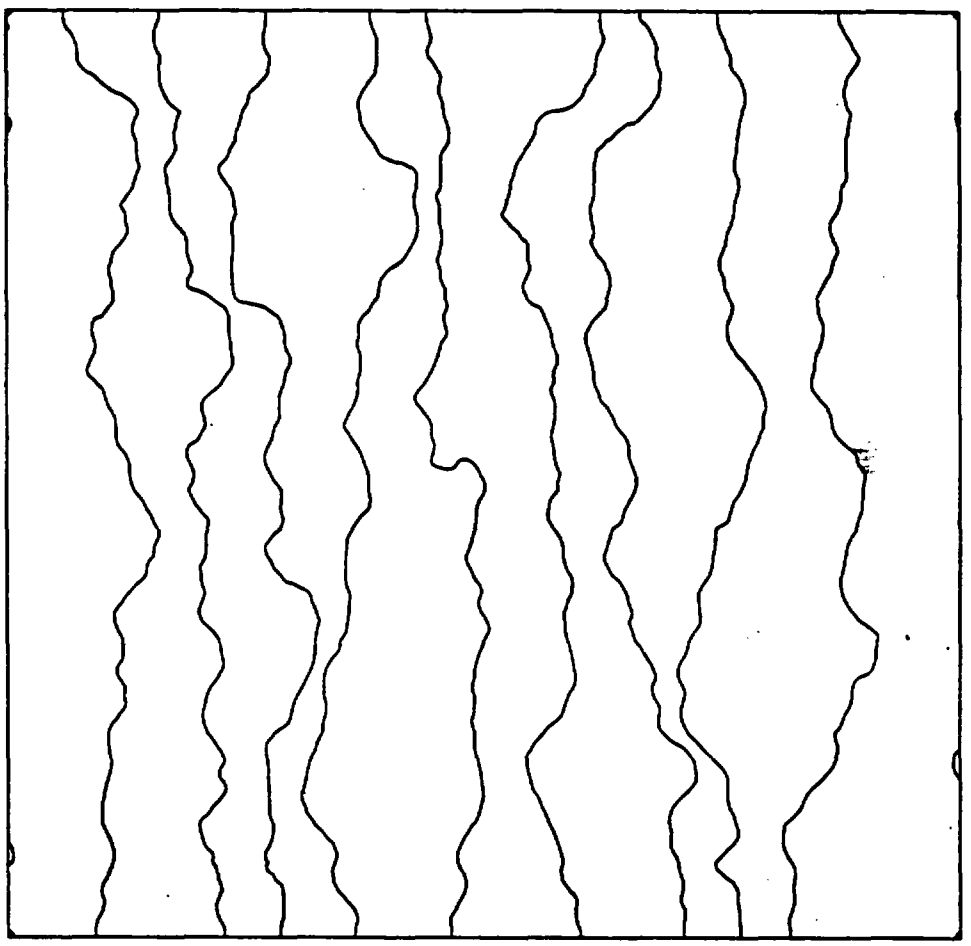

Figure 6.16 (c) Same as (a), with $\sigma_f = 2.305$.

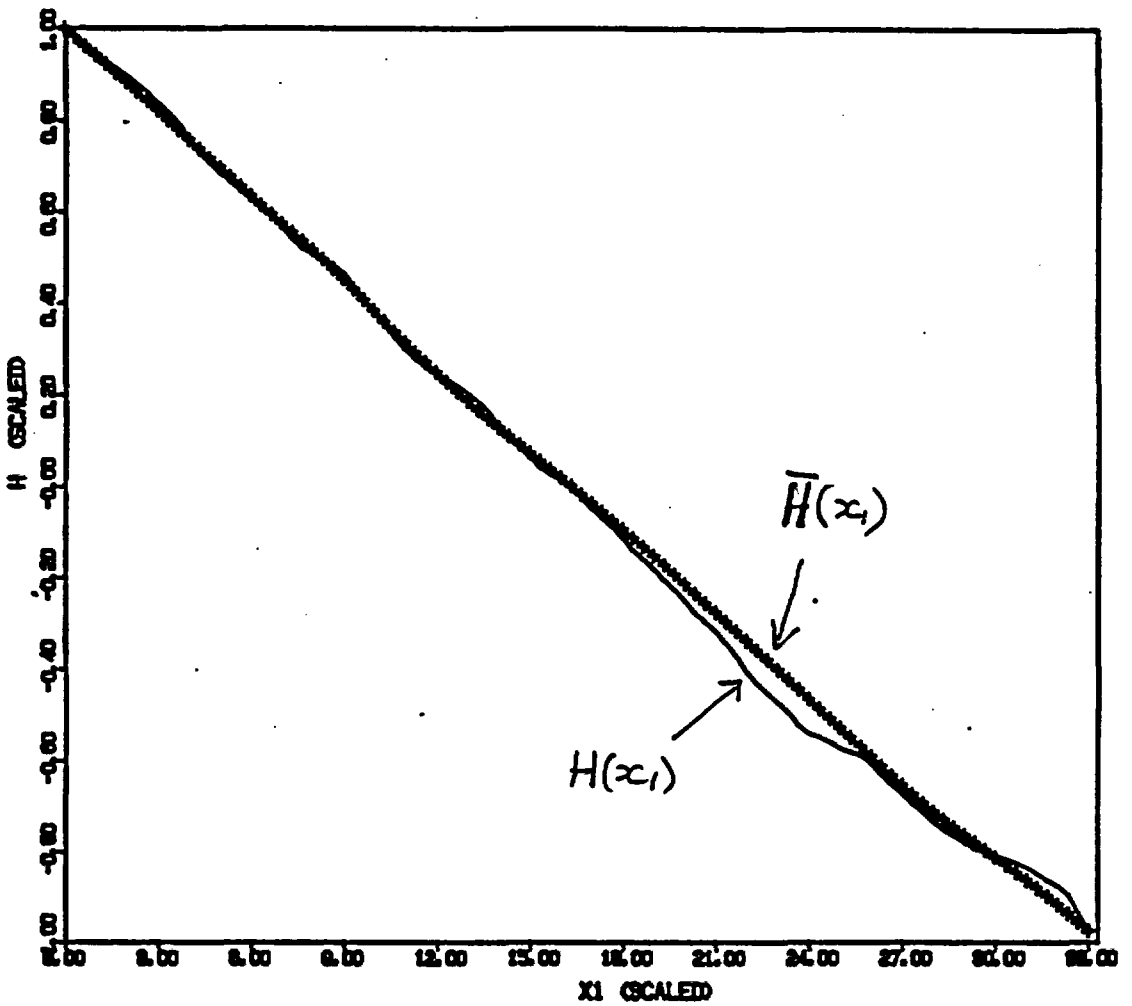

Figure 6.17 (a) One-dimensional representation of the head field (sample function $H(x_1)$, and nonlinear trend $\bar{H}(x_1)$) along a transect parallel to the mean flow direction. Flow problem A with 1 Million nodes: (a) Case $\sigma_f^2 = 1.0$.

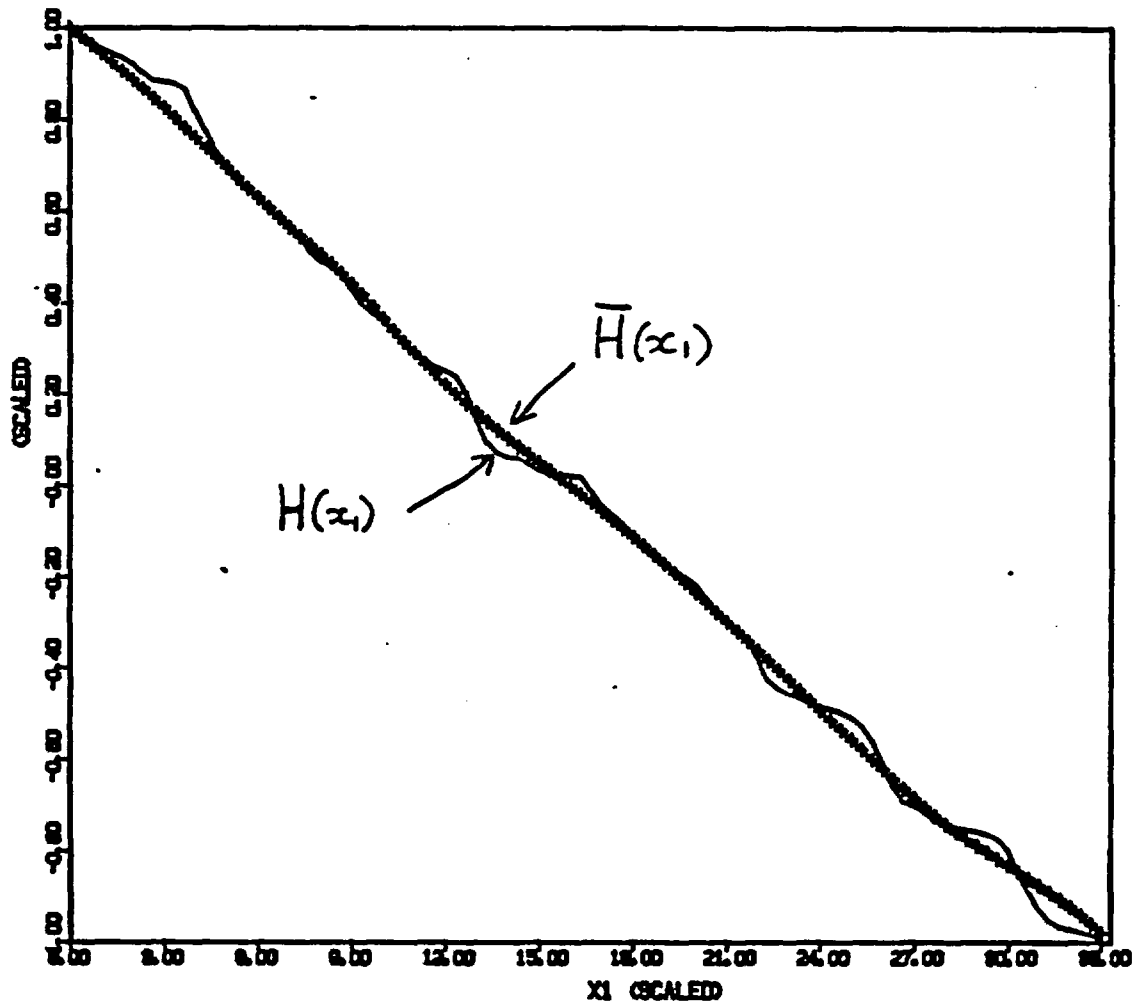

Figure 6.17 (b) Same as (a), with $\sigma_f = 1.732$

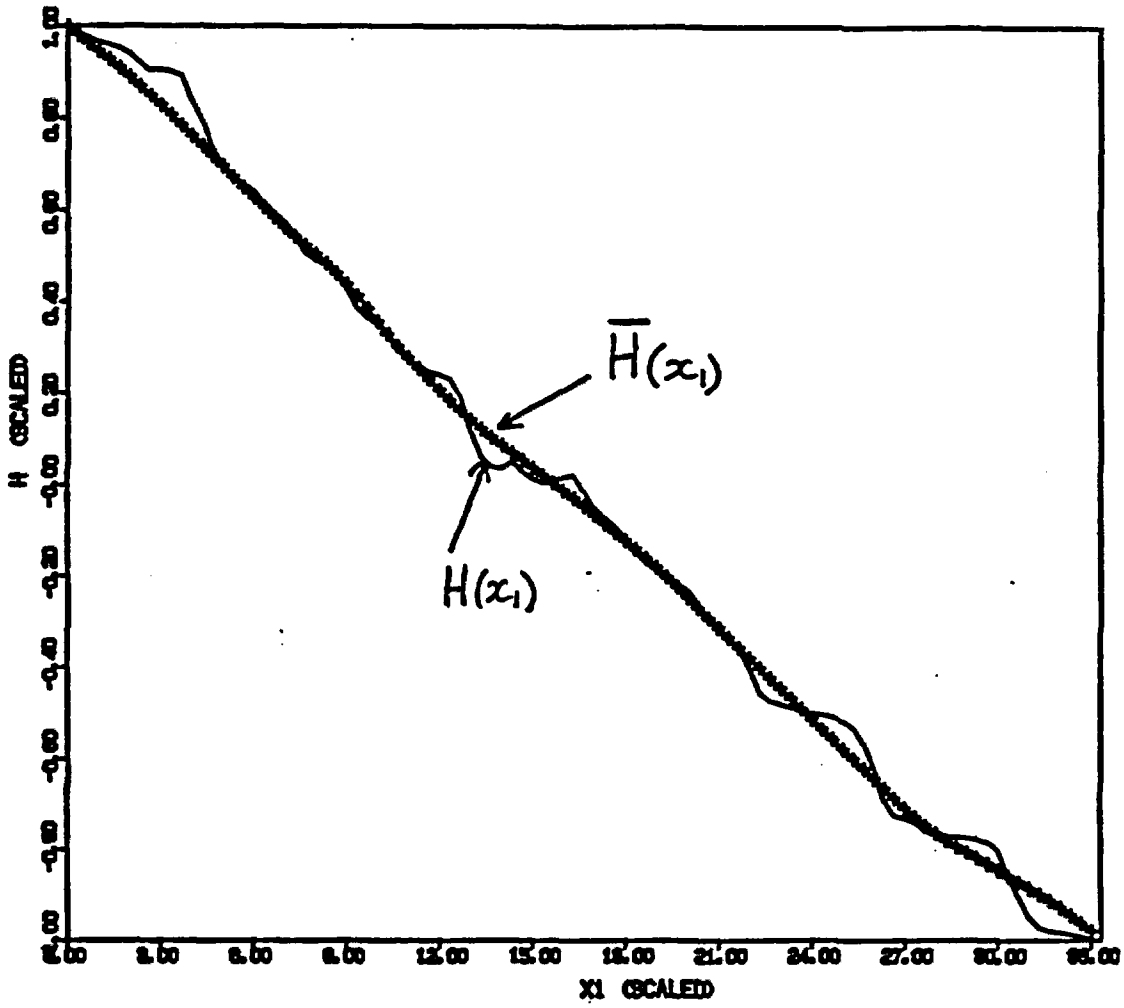

Figure 6.17 (c) Same as (a), with $\sigma_f = 2.3205$.

The flux vector field was not processed for graphic representations due to technical reasons. However, the reader is referred to the visual representations of the longitudinal flux component $Q_1(\underline{x})$ obtained for the smaller flow realization of Section 6.2 (Figures 6.11-6.15). At any rate, it will be more informative to analyze the behavior of the flow fields in statistical terms. This is now examined.

[d] Single Point Statistics of the Flow Field.

The results of statistical analysis of the flow fields ($H(\underline{x})$, $Q_i(\underline{x})$) obtained for different values of σ_f are presented in the form of tables (for single-point statistics) and figures (for correlation functions). In each case, we develop a systematic comparison with the results of the infinite-domain spectral theory. For convenience the analytical results of the spectral theory concerning the single-point moments of the flow field are summarized in Table 6.4 below.

The numerical values of the single-point moments of the flow fields obtained in the cases $\sigma_f \simeq 1.0$, 1.7, and 2.3, are summarized in a compact form in Table 6.5. The values predicted

TABLE 6.4
SUMMARY OF ANALYTICAL EXPRESSIONS FOR VARIOUS STATISTICS FROM THE FIRST ORDER (•) AND HIGHER ORDER ((•)) SPECTRAL SOLUTIONS. TO BE USED AS A REFERENCE FOR TABLES 6.5 AND 6.6 (CASE OF ISOTROPIC 3D MARKOV LOG CONDUCTIVITY)

Statistics	Expression	Equation Number	Other References
(σ_H)	$\frac{1}{\sqrt{3}}\sigma_F J_1\lambda$	Equation (3.21)	Bakr et. al 1978
$((\sigma_H))$	$\sqrt{\frac{1-.058\sigma_F^2}{3}}\cdot\sigma_F J_1\lambda$	Equation (4.2)	Gelhar (pers. com.) Dagan (1985)
(σ_{G_i})	$i=1$: $\frac{1}{\sqrt{5}}\sigma_F J_1$ $i=2,3$: $\frac{1}{\sqrt{15}}\sigma_F J_1$	Equation (3.22)	Appendix 3.B
(σ_{q_i})	$i=1$: $\sqrt{\frac{8}{15}}K_G\sigma_F J_1$ $i=2,3$: $\sqrt{\frac{1}{15}}K_G\sigma_F J_1$	Equation (3.24)	Appendix 3.B
$((\sigma_{q_i}))$	$i=1$: $\sqrt{\frac{8}{15}}\sigma_F\bar{Q}_1$ $i=2,3$: $\sqrt{\frac{1}{15}}\sigma_F\bar{Q}_1$	Equation (3.26)	Chapter 4 (section 4.3)
$(\bar{Q}_i)$	$i=1$: $K_{eff}J_1$ $i=2,3$: 0	Equation (3.14)	Gelhar-Axness 1983
(K_{eff})	$K_G\exp(\sigma_F^2/6)$	Eqs.(3.19),(3.23)	Gelhar 1984

TABLE 6.5
SUMMARY OF COMPUTED STATISTICS OBTAINED FOR THE 1 MILLION NODE FLOW SIMULATIONS (PROBLEM "A" WITH THREE VALUES OF LOG-CONDUCTIVITY STANDARD DEVIATION), AND COMPARISON TO SPECTRAL THEORY (IN PARENTHESIS). THE STATISTICAL QUANTITIES ARE DEFINED IN THE TEXT

Statistics	σ_f = 1.0	σ_f = 1.732	σ_f = 2.3025
σ_H	.002050 (.002309) ((.002241))	.003579 (.004000) ((.003635))	.004774 (.005317) ((.004425))
σ_{G_1}	.001558 (.001789)	.002711 (.003098)	.003625 (.004119)
σ_{G_2}	.000979 (.001033)	.001817 (.001789)	.002569 (.002378)
σ_{G_3}	.000975 (.001033)	.001793 (.001789)	.002518 (.002378)
σ_{q_1}	.003779 ((.003451))	.01103 ((.00834))	.02516 ((.01628))
σ_{q_2}	.001435 ((.001220))	.005075 ((.002950))	.01328 ((.00576))
σ_{q_3}	.001476 ((.001220))	.005285 ((.002950))	.01381 ((.00576))
$\sigma_{q_3}/\sigma_{q_1}$	.3906 ((.3536))	.4791 ((.3536))	.5489 ((.3536))
$\overline{Q}_1$	.004856 (.004725)	.006889 (.006595)	.01004 (.00968)
$\overline{Q}_2/\overline{Q}_1$	.004 (.000)	.009 .000	.013 (.000)
$\overline{Q}_3/\overline{Q}_1$	.013 ((.000))	.024 ((.000))	.033 ((.000))
K_{eff}/K_G	1.214 (1.181)	1.722 (1.645)	2.510 (2.420)

by the spectral theory are shown in parenthesis immediately below the numerical value. The values in single parenthesis (•) were obtained from the standard first order spectral theory of Bakr et. al. (1978) and Gelhar and Axness (1983). On the other hand, the values in double parenthesis represent some higher order or improved spectral solutions, as defined in Table 6.4. In particular, note that the flux standard deviations ($((\sigma_{q_i}))$) were calculated from the improved spectral solutions developed in this work (Chapter 4, Section 4.3). The statistical quantities listed in Table 6.5 are as follows: standard deviations of the head (σ_H), head gradient (σ_{G_i}); ratio of transverse/longitudinal flux deviations ($\sigma_{q_3}/\sigma_{q_1}$); mean longitudinal flux component ($\overline{Q}_1$); relative mass balance errors ($\overline{Q}_i/\overline{Q}_1$ for i=2,3); and effective conductivity (K_{eff}).

In order facilitate the comparison between numerical and spectral results, we also show in Table 6.6 the relative error on the spectral solutions for σ_H and σ_{q_i}, relative to the numerical solutions $\hat{\sigma}_H$ and $\hat{\sigma}_{q_i}$. Our choice here has been to use the numerical solutions rather than the spectral solutions as a reference. Thus, the relative errors listed in the table were defined as:

$$e(\sigma_Y) = \frac{\sigma_Y - \hat{\sigma}_Y}{\hat{\sigma}_Y}.$$

TABLE 6.6
COMPARISON OF FIRST ORDER (•) AND HIGHER ORDER ((•)) SPECTRAL SOLUTIONS WITH NUMERICAL RESULTS. THE NUMBERS IN PARENTHESIS GIVE THE RELATIVE ERROR ON σ_H AND σ_{q_1} WITH RESPECT TO THE VALUES OBTAINED BY NUMERICAL SIMULATION

	$\sigma_f = 1.0$	$\sigma_f = 1.732$	$\sigma_f = 2.3025$
$e(\sigma_H)$	(+ 13%)	(+12%)	(+11%)
	((+ 9%))	((+ 2%))	((- 7%))
$e(\sigma_{q_1})$	(- 23%)	(-54%)	(-73%)
	((- 9%))	((-24%))	((-35%))
$e(\sigma_{q_2})$	(-28%)	(-65%)	(-82%)
	((-15%))	((-42%))	((-57%))
$e(\sigma_{q_3})$	(-30%)	(-66%)	(-83%)
	((-17%))	((-44%))	((-58%))

Note: The relative error $e(\sigma_Y)$ is defined as the ratio $(\sigma_Y - \hat{\sigma}_Y)/\hat{\sigma}_Y$ where σ_Y corresponds to the spectral theory, and $\hat{\sigma}_Y$ is the value obtained from the numerical simulation. See also Table (6.4).

In addition, Table 6.6 allows for a direct comparison between the standard first order spectral solutions (single parenthesis) and higher order or modified spectral solutions ((double parenthesis)). The analytical form of each of these spectral solutions was given in Table 6.4 above.

Our observations based on Tables 6.4, 6.5 and 6.6, can now be summarized as follows:

(i) The most robust statistics are σ_H, σ_{G_i}, and K_{eff}. For these quantities, the values obtained with the spectral theory match the numerical results within 10% (5% for the effective conductivity), for the whole range of log-conductivity variability. The ratio of transverse to longitudinal flux standand deviations (e.g., $\sigma_{q_3}/\sigma_{q_1}$) is also relatively robust, although the spectral result is off the numerical value by (-35%) in the case of highest variability ($\sigma_f \simeq 2.3$). Note that these comparisons are based on the modified spectral solutions for the flux statistics.

(ii) At moderate variability ($\sigma_f = 1.0$), all the single-point statistics predicted by the spectral theory match the numerical results to within 15%, or 10% if the transverse flux deviations (σ_{q_2}, q_{q_3}) are excluded. Again, these comparisons are based on the modified spectral solutions for the flux statistics.

(iii) However, there are some significant discrepancies between the spectral theory and the numerical simulations concerning the values of the flux standard deviations at higher variability ($\sigma_f \geq 1.7$). In the case of highest variability ($\sigma_f \simeq 2.3$) the error on the spectral results σ_{q_1} is quite high relative to the numerical results, particularly concerning the transverse flux standard deviations (-50% with the modified spectral theory, and as much as -83% with the standard spectral theory).

(iv) The modified spectral theory proposed in this work for the flux spectrum (Chapter 4, Section 4.3) produces values of σ_{q_1} that are in closer agreement with the numerical simulations, than the standard spectral theory. The improvement is uniform over the whole

range of conductivity variability ($\sigma_f \simeq 1.0, 1.7, 2.3$), and is particularly significant for the longitudinal flux component (σ_{q_1}).

(v) Finally, the Gelhar-Dagan second order spectral solution for σ_H does not uniformly improve the standard spectral result over the whole range of conductivity variability. The agreement with the numerical results is not significantly better with the second order solution, except for a particular value of σ_f ($\sigma_f \simeq 1.7$). At any rate, the standard spectral solution σ_H was already quite close to the numerical values within the whole range $\sigma_f \simeq 1.0$–2.3.

These observations lead us to the conclusion that the (modified) spectral theory and the numerical single-realization simulations produced nearly identical results for most of the single-point moments of the flow field, within a wide range of log-conductivity variability (up to $\sigma_f \simeq 2.3$). However, it should also be recognized that the predictions concerning the degree of variability of the flux components (σ_{q_i}) were not in such a good agreement for medium to large log-conductivity

variability ($\sigma_f \simeq 1.7$ or larger). Nevertheless, the σ_{q_i}'s obtained from the modified spectral solutions developed in this work were significantly closer to the numerical results than those predicted by the standard spectral theory. It is also interesting to note that the second order spectral solution of Gelhar-Dagan for the standard deviation of the head did not significantly improve on the standard spectral solution relative to the numerical results. We conclude that the most important "high order effects" concern the degree of variability of the flux vector. This may have important implications for solute transport in a stochastic velocity field, and needs to be discussed further.

The observed discrepancy on the degree of variability (standard deviation) of the flux vector raises a question about the accuracy of the spectral theory and/or the numerical single-realization solution. The problem can be narrowed down further by observing that, for moderate variability $\sigma_f = 1.0$, the discrepancy between the two methods is on the same order as the estimated accuracy of the numerical solution (truncation error) when the *modified* spectral theory is used. This can be seen by comparing directly Table 6.6 to Table 5.2 of Chapter 5 (Section 5.2) for $\sigma_f = 1.0$ and $\Delta x/\lambda = 1/3$, as will be explained below.

The result of this comparison is shown in Table 6.7. It is important to note that the *standard* spectral theory is off the numerical solution by an amount too large to be explained solely by numerical truncation errors. On the other hand, the *modified* spectral theory is close enough to the numerical solution that the discrepancy could be due solely to numerical truncation errors (for $\sigma_f = 1.0$). Note that the relative truncation error approximates the relative error between the exact and numerical values of σ_{q_i}. Indeed, recall that the relative truncation error on the flux was defined as:

$$\frac{\sigma_{\delta q_i}}{\sigma_{q_i}}$$

where δq_i is the truncation error on the flux:

$$\delta q_i = \hat{q}_i - q_i .$$

$\hat{q}_i$ is the numerical solution while q_i is the exact (unknown) solution. Therefore, it is not difficult to see that:

TABLE 6.7

TRUNCATION ERROR AND DISCREPANCY BETWEEN THE SPECTRAL AND NUMERICAL SOLUTIONS, FOR THE FLUX STANDARD DEVIATIONS σ_{q_i}

(1 Million node problem A $\sigma_t = 1.00$ and $\Delta x/\lambda = 1/3$).

	(1) Relative truncation error (exact/ numerical)	(2) Relative error (modified spectral/num.)	(3) Relative error (standard spectral/num.)...
$e(\sigma_{q_1})$	- 17%	- 9%	- 23%
$e(\sigma_{q_2})$	- 14%	- 15%	- 28%
$e(\sigma_{q_3})$	- 14%	- 17%	- 30%

Note: (1) Relative truncation error on the flux in the root-mean-square norm, approximating the relative error between the exact and numerical σ_{q_i}.

(2) Relative error between the modified spectral result and the numerical σ_{q_i}.

(3) Relative error between the standard spectral result and the numerical σ_{q_i}.

$$\hat{\sigma}^2_{q_i} = \sigma^2_{q_i} + 2\,\langle q_i \cdot \delta q_i \rangle + \sigma^2_{\delta q_i}$$

Now, it seems reasonable to assume that the random error δ_{q_i} will be generally proportional to q_i. This yields:

$$\langle q_i \cdot \delta q_i \rangle \simeq \sigma_{q_i} \cdot \sigma_{\delta q_i}.$$

By using also the known fact that:

$$\sigma_{\delta q_i} \ll \sigma_{qi}$$

we obtain finally the approximate relation:

$$\frac{\sigma_{q_i} - \hat{\sigma}_{q_i}}{\hat{\sigma}_{q_i}} \simeq - \frac{\sigma_{\delta q_i}}{\sigma_{q_i}} \qquad (6.12)$$

where the left term is the relative error listed in column (1) of Table 6.7, and the right term is just the relative truncation error of Chapter 5 (Table 5.2) with the sign reversed.

Thus, the result of Table 6.7 indicates that the values of σ_{q_i} obtained by the modified spectral theory are statistically indistinguishable from the numerical values, in the

case of $\sigma_f = 1.0$. (This does not hold when the standard spectral theory is used instead.) On the other hand, recall that all the other single-point statistics predicted by the spectral theory were quite close to the numerical results for $\sigma_f = 1.0$ (and for larger variability as well). We conclude that, at least for mdoerate variability ($\sigma_f \simeq 1$), both the modified spectral theory and the numerical simulations must be quite close to the unknown exact solution of the infinite-domain stochastic flow problem, as far as single-point moments are concerned (standard deviations of head and flux, and effective conductivity).

This encouraging conclusion seems justified if we reject the possibility of a mere chance coincidence, given the fact that the two methods are based on different kinds of approximations, as shown below:

Spectral Theory	Single-realization Simulations:
- Infinite domain	- Finite domain
- Small parameter expansion (σ_f)	- Finite difference discretization
- First or second order approximations	- Approximate factorization and iterative solution
- Ensemble moments (Fourier integrals)	- Spatial moments (physcial space summation)

On the other hand, the discrepancy between the σ_q's predicted by the (modified) spectral theory and the numerical simulations become statistically significant as σ_f increases over

unity ($\sigma_f \simeq 1.7$ and 2.3). Indeed, Table 6.6 shows that the relative error between the two solutions increases with σ_f, while we know from Chapter 5 (Section 5.2) that the relative truncation error does not increase with σ_f as a first approximation (i.e., to first order in σ_f). If the results of the truncation error analysis are to be trusted, this implies that the *modified* spectral theory significantly underestimates the degree of variability of the flux vector as σ_f increases, say for $\sigma_f > 1\text{-}1.5$. It is also clear from Table 6.6 that the *standard* spectral theory leads to even more severe discrepancies, as noted previously.

Based on these remarks, we have obtained empirical expressions for the flux standard deviations (σ_{q_i}) that fit extremely well the numerical results for the three values of σ_f tested in this work ($\sigma_f \simeq 1.0,\ 1.7,\ 2.3$). These conjectural expressions are simple and take a form similar to the spectral solutions, as follows:

$$\sigma^*_{q_1} = \sqrt{\frac{8}{15}}\,\sigma_f\, J_1\, K_G\, e^{\sigma_f^2/4} \tag{6.13a}$$

$$\sigma^*_{q_2},\ \sigma^*_{q_3} = \sqrt{\frac{1}{15}}\,\sigma_f\, J_1\, K_G\, e^{\sigma_f^2/3}$$

Equivalently, by using the relation between the arithmetic and

geometric mean conductivities ($K_A = K_G \exp(\sigma_f^2/2)$), these relations can be expressed as:

$$\sigma^*_{q_1} = \sqrt{\frac{8}{15}}\,\sigma_f\,K_G\,J_1\left[\frac{K_A}{K_G}\right]^{1/2}$$

$$\sigma^*_{q_2},\sigma^*_{q_3} = \sqrt{\frac{1}{15}}\,\sigma_f\,K_G\,J_1\left[\frac{K_A}{K_G}\right]^{2/3} \qquad (6.13b)$$

Equations (6.13) agree with the numerical results listed in Table 6.5 within a margin of error of 3% (σ_{q_1}) and 6% ($\sigma_{q_2},\sigma_{q_3}$) for the whole range of conductivity variability up to $\sigma_f \simeq 2.3$. These equations may be viewed as an empirical correction to the spectral theory to compensate for "unmodeled" high order effects in the case of large σ_f. It seems clear, at least from all our previous observations that the *exact* values of σ_{q_i} must lie between the values predicted by the *modified* spectral theory (Table 6.4) and the empirical relations (6.13) - presumably very close to the latter.

To complete our analyzis of single-point moments of the flow field, let us recall form the previous section 6.2 that the longitudinal flux component was found to be positively skewed, based on a visual inspection of Q_1 along selected transects and slices (Figures 6.11, 6.14, and 6.15). This, in our view, is another manifestation of high order effects not taken into

account by the spectral theory as it stands now. Thus, it should not be surprising that similar high order effects can contribute to the variance of the flux vector. The proposed correction (6.13) indicates that the effect of the high order terms, ignored by the spectral theory, is exponential in σ_f^2 . With this correction, the σ_{q_i} and all other single-point statistics predicted by the spectral theory agreed well with the numerical results up to large conductivity variability ($0 \leq \sigma_f \leq 2.3$). It will be interesting in the future to evaluate quantitatively the entire probability distribution of the flux components from the numerical results. Another key feature of the flow field is its spatial structure, which will be investigated next in connection with the predictions of the spectral theory.

[e] Spatial structure (two point correlations):

In the framework of the spectral theory, the spatial structure of the flow field can be described by the three-dimensional two-point correlation functions of the flow variables $H(\underline{x})$ and $Q_i(\underline{x})$. Although we have seen that this information may not be sufficient ($Q_i(\underline{x})$ has a skewed distribution, requiring three-point correlation functions), it will nevertheless be instructive to determine the two-point correlation functions of the numerical flow field and compare with the results of the spectral theory.

In the present case, we have evaluated the unidirectional correlation functions:

$$R(\xi_1) = R(\xi_1, 0, 0)$$

$$R(\xi_2) = R(0, \xi_2, 0)$$

$$R(\xi_3) = R(0, 0, \xi_3)$$

for each of the flow variables:

-- hydraulic head H

-- flux vector components Q_1, Q_2, Q_3

-- (head gradient components G_1, G_2, G_3)

In actual practice, we computed first the covariance functions by using the spatial averaging procedure explained previously in equations (6.4, 6.5, 6.7) of Section (6.1). The correlation functions were then simply obtained by dividing the covariances by the variances (covariances at lag zero). Thus, we obtained the correlation functions $R_{HH}(\xi_j)$, $R_{Q_iQ_i}(\xi_j)$, and $R_{G_iG_i}(\xi_j)$ for $i = 1, 2, 3$ and $j = 1, 2, 3$. Note that we use here the notation $R(\xi_j)$ to denote unidirectional correlation functions (equal to unity at lag zero), although the notation $R(\underline{\xi})$ was used elsewhere to designate covariance functions.

Figures (6.18) and (6.19) show the correlation structure of the hydraulic head field and a comparison with the head correlation functions predicted by the spectral theory (see Chapter 3, Section 3.3, Figure 3.1). The unidirectional correlation functions from the numerical head field are shown in Figures 6.18(a), (b), (c) for the cases σ_f = 1.0, 1.7, 2.3, respectively. In all three cases, the head correlation structure appears to be nearly isotropic in the cross-flow plane, as it should, i.e.:

$$R_{HH}(0, \xi_2, 0) \simeq R_{HH}(0,0,\xi_3)$$

In addition, the head correlation range is larger in the cross-flow plane than in the longitudinal direction ξ_1 parallel to the mean flow. This feature is indeed predicted by the spectral theory.

However, the agreement with the spectral theory is only qualitative, as can be seen from the comparison of numerical and spectral head correlations show in Figure (6.19) for the case $\sigma_f \simeq 1.0$. It is clear from this figure that the numerical result underestimates the correlation range of the head field with respect to the spectral result, particularly in the cross-flow directions. This is presumably due to the limited size of the flow domain, as can be seen by examining the number of available

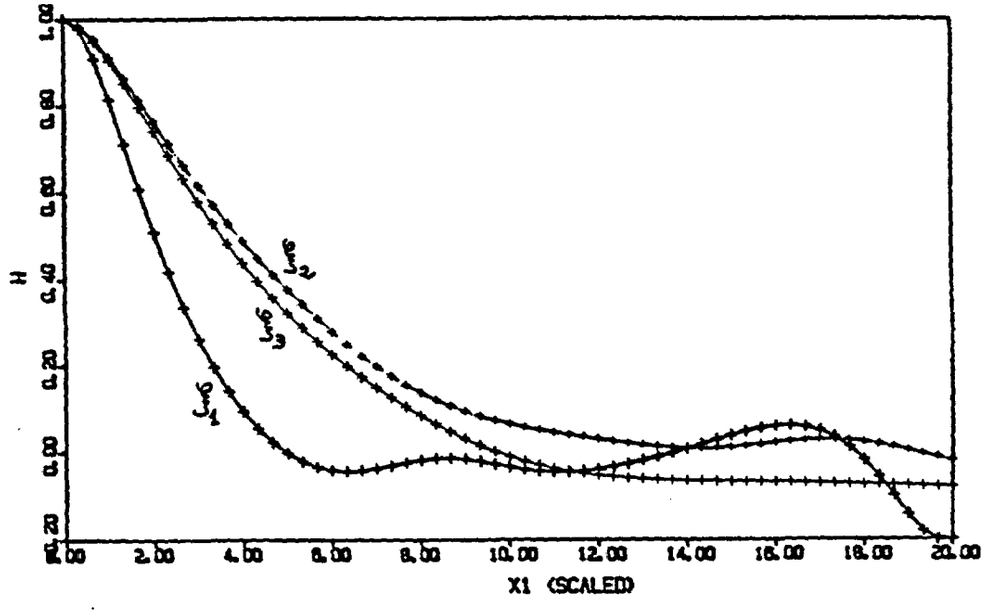

Figure 6.18 (a) Numerical head correlation functions along three directions, for the 1 Million node "isotropic" problem A (σ_f = 1.0).

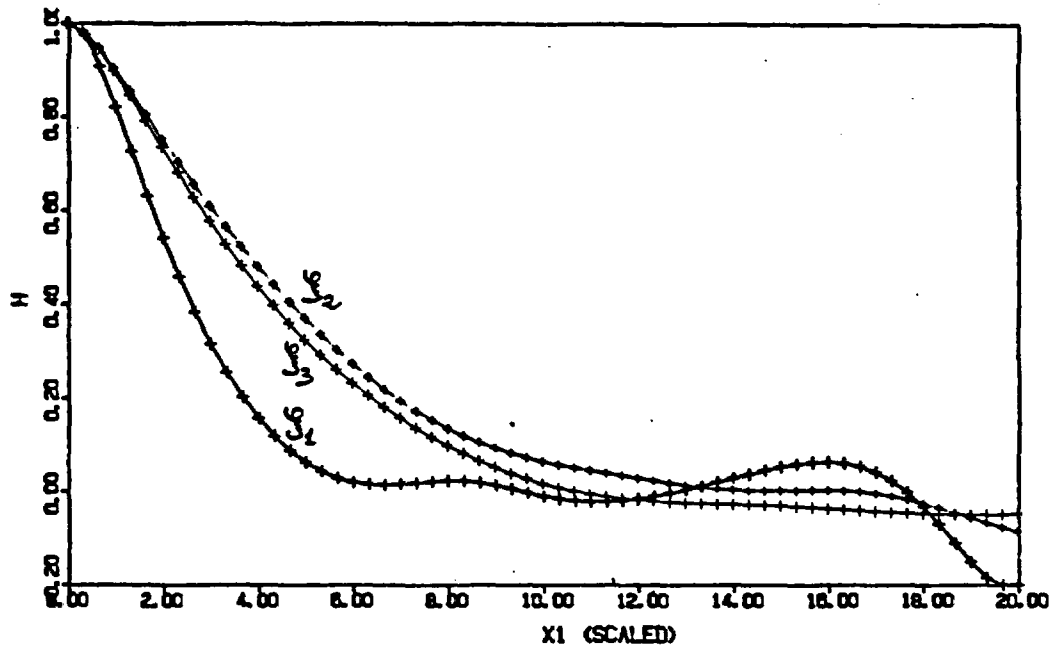

Figure 6.18 (b) Same as (a), with $\sigma_f = 1.732$.

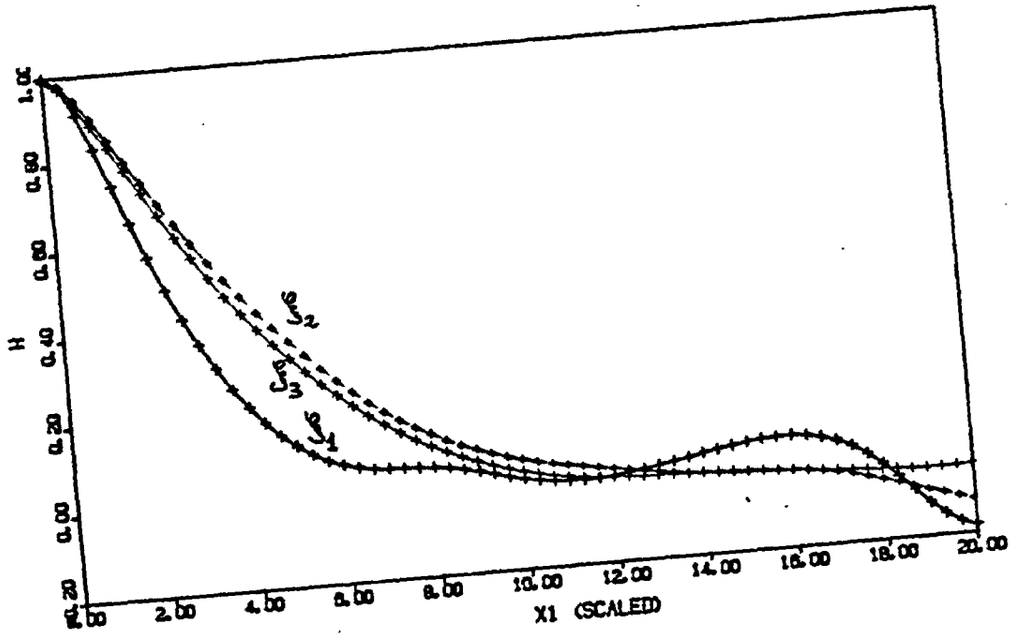

Figure 6.18 (c) Same as (a), with $\sigma_f = 2.3025$.

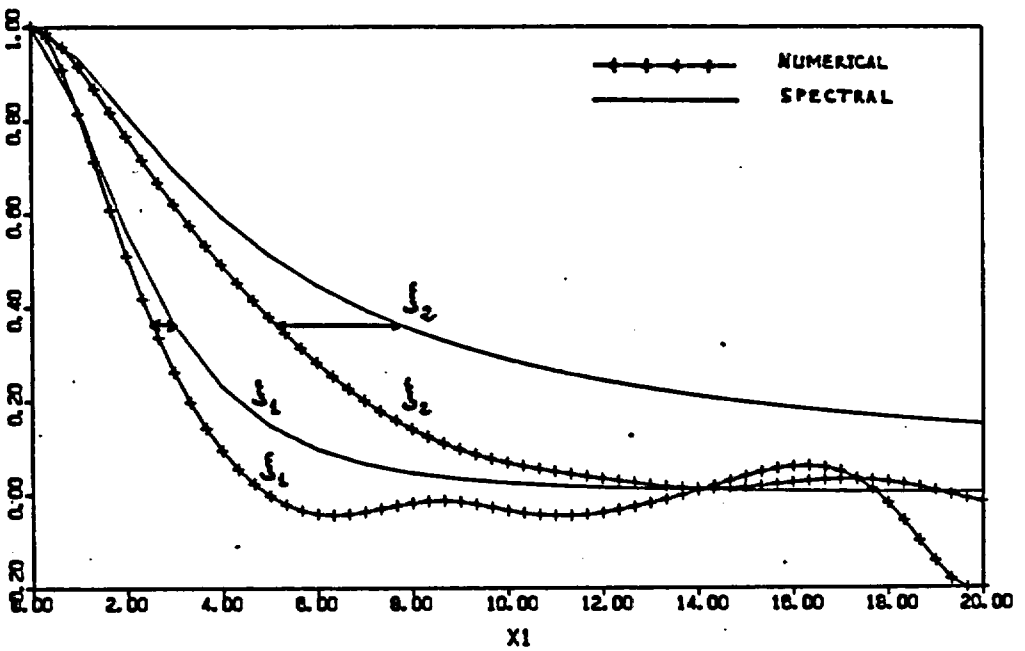

Figure 6.19 Comparison of numerical and theoretical (spectral) head correlation functions in the longitudinal and transverse directions ξ_1 and ξ_2 (1 Million node isotropic Problem A, with $\sigma_f = 1.0$).

"head samples" along the three axes. The transverse sample size is:

$$\frac{L}{7.5\lambda} \simeq \frac{33.3}{7.5} \simeq 4.5$$

while the longitudinal sample size is:

$$\frac{L}{30.\lambda} \simeq \frac{33.3}{3.0} \simeq 11.$$

Therefore, it is not surprising that the numerical head correlation functions obtained by finite-domain averaging differ somewhat from the results of the infinite-domain spectral theory, particularly in the transverse direction where the equivalent number of head samples is so small. See Appendix 2A for more rigorous statements on sampling uncertainty.

It may be also instructive to compare directly the head correlations in terms of correlation scales. Table 6.8 compares the e-correlation scales of the head field for the spectral and numerical solutions ($\sigma_f \simeq 1.0,\ 1.7,\ 2.3$). The e-correlation scale was defined as the distance at which the correlation drops to $e^{-1} \simeq 0.3679$. Note that this definition coincides with the integral correlation length in the case of the Markov log-conductivity field (but not for other random fields such as

TABLE 6.8

CORRELATION SCALES OF THE HYDRAULIC HEAD FIELD ALONG THREE DIRECTIONS: COMPARISON OF SPECTRAL SOLUTION WITH THE NUMERICAL RESULTS OF THE 1 MILLION NODE "ISOTROPIC" FLOW PROBLEM A.

Correlation Function	Spectral theory for σ_f	Numerical Results (σ_f=10)	(σ_f=1.7)	(σ_f=2.3)
$R_{HH}(\xi_1)$	3.0	2.5	2.7	3.0
$R_{HH}(\xi_2)$	7.5	5.1	5.0	4.9
$R_{HH}(\xi_3)$	7.5	4.6	4.6	4.6

Note: The numbers give the e-correlation scale λ_e, defined by $R(\lambda_e) = e^{-1} \simeq 0.3679$. Since the e-correlation scale λ of the log-conductivity was unity, the numbers can also be viewed as dimensionless ratios (λ_e/λ).

the hydraulic head). This table shows that, depending on σ_f, the longitudinal head correlation length obtained numerically is 0% - 15% smaller than the spectral theory predicts. For the transverse head correlation length, the numerical value is about 40% smaller than predicted by the spectral theory. Although this is a serious discrepancy, the spatial structure of the numerical head field is qualitatively similar to that predicted by the spectral theory. Incidentally, it may be surprising that the numerical head correlation lengths appear to increase with σ_f, thus getting closer to the spectral values as σ_f increases. The reason for this behavior is not all clear, and might result from complex interactions between different kinds of sampling errors in the numerical approach (finite domain effects, nonhomogeneous head field, empirical detrending).

At any rate, it seems very likely that the observed differences in the head correlation structure are due to the limited size of the domain with respect to the head correlation range, as explained above. Due to this limitation, we can only conclude here that the numerical results do not invalidate the predictions of the spectral theory concerning the infinite-domain correlation structure of the hydraulic head. In practice however, the spectral theory may not be applicable to flow systems of limited size. In the case of a confined aquifer for instance, our results suggest that the depth of the aquifer must

be several tens of conductivity correlation scales (say 50-100) in order to satisfy approximately the assumption of infinite domain. This kind of limitation will be discussed again with the anisotropic flow simulations presented in the next section.

Let us now focus on the correlation structure of the flux vector field, which has important implications for solute transport macrodispersion. Figures (6.20) through (6.28) show various components of the numerical flux correlation tensor along three directions. Each of these figures includes also a comparison with the results of the spectral theory. But first, it may be useful to provide some background on the method used to represent the flux correlation structure.

For a vector field like the flux, the correlation structure is defined by the tensor function $R_{ij}(\underline{\xi})$ of the log vector $\underline{\xi}$ in 3D space. The more restricted subset of correlation functions discussed below corresponds to the diagonal components of this tensor, with separation vectors parallel to any of the three principal axes (x_1, x_2, x_3): unidirectional functions $R_{ii}(\xi_j)$. The physical meaning of these correlation functions can be better apprehended by examining Figure (6.20). For instance, the function $R_{11}(\xi_1)$ is the longitudinal flux correlation in the longitudinal direction, while the function $R_{22}(\xi_3)$ is the transverse flux correlation in the other transverse direction.

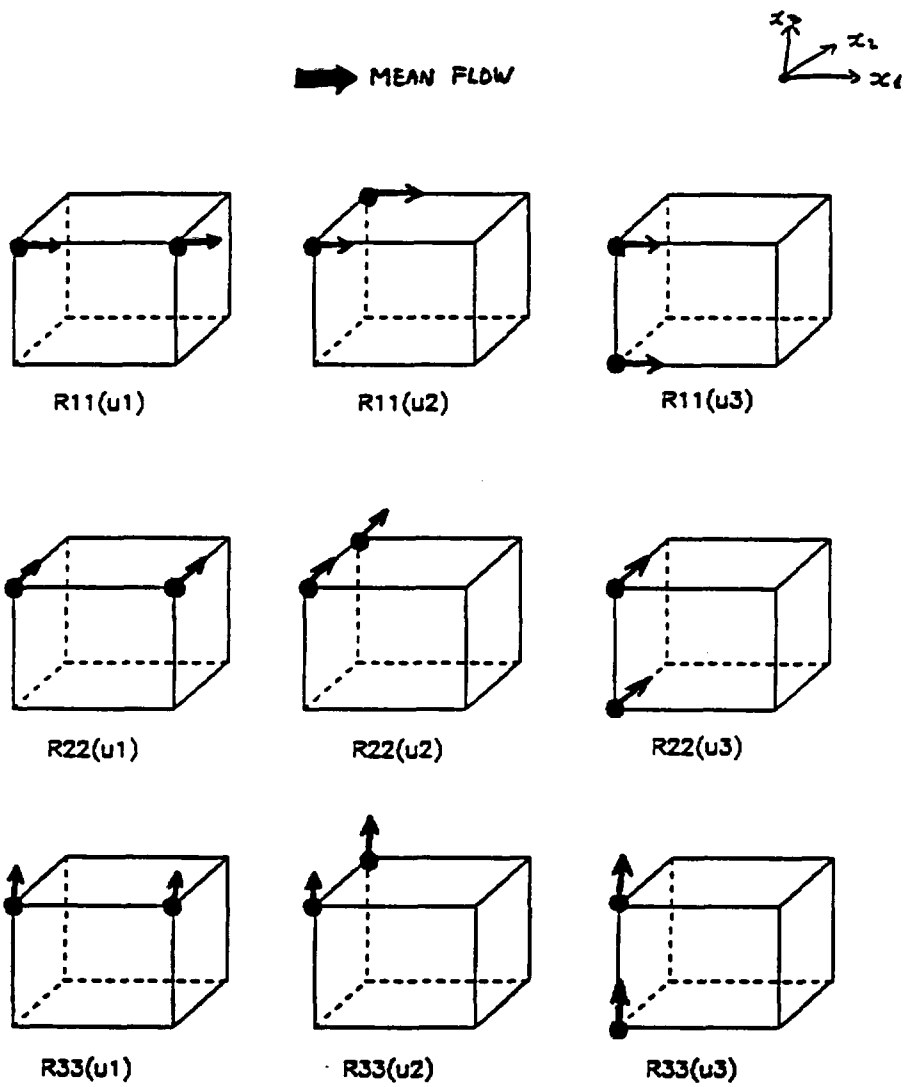

Figure 6.20 Subset of vector-vector correlation functions, restricted to the diagonal components of the correlation tensor and to separation vectors parallel to the principal axes.

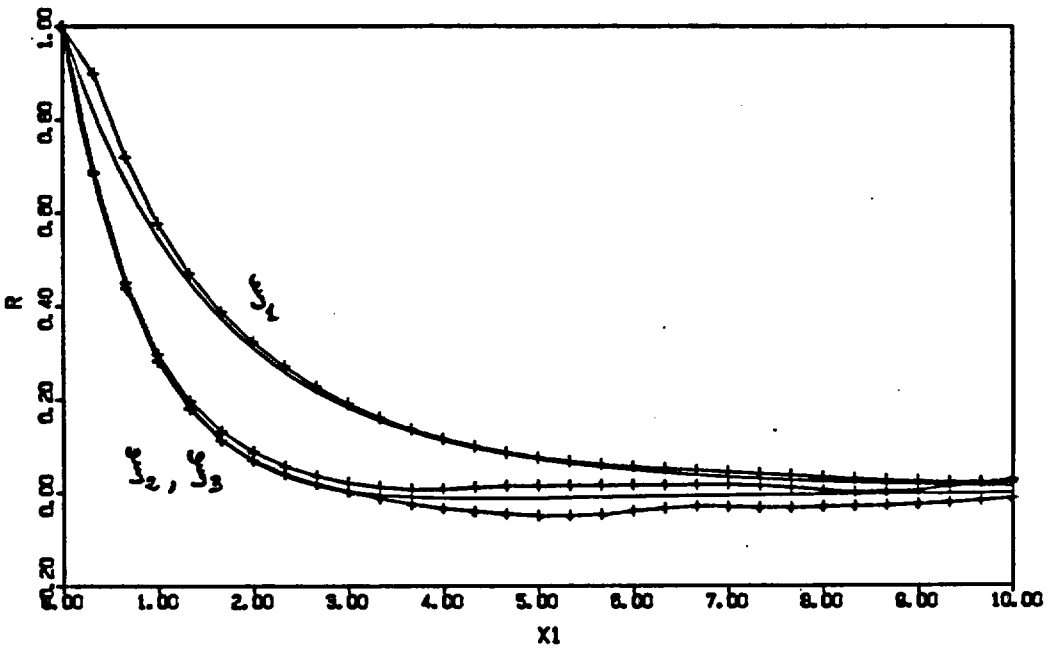

Figure 6.21: Flux correlation functions $R_{Q_1Q_1}(F_j)$ for $\sigma_f = 1.0$ (solid lines: spectral theory; crosses: numerical simulation).

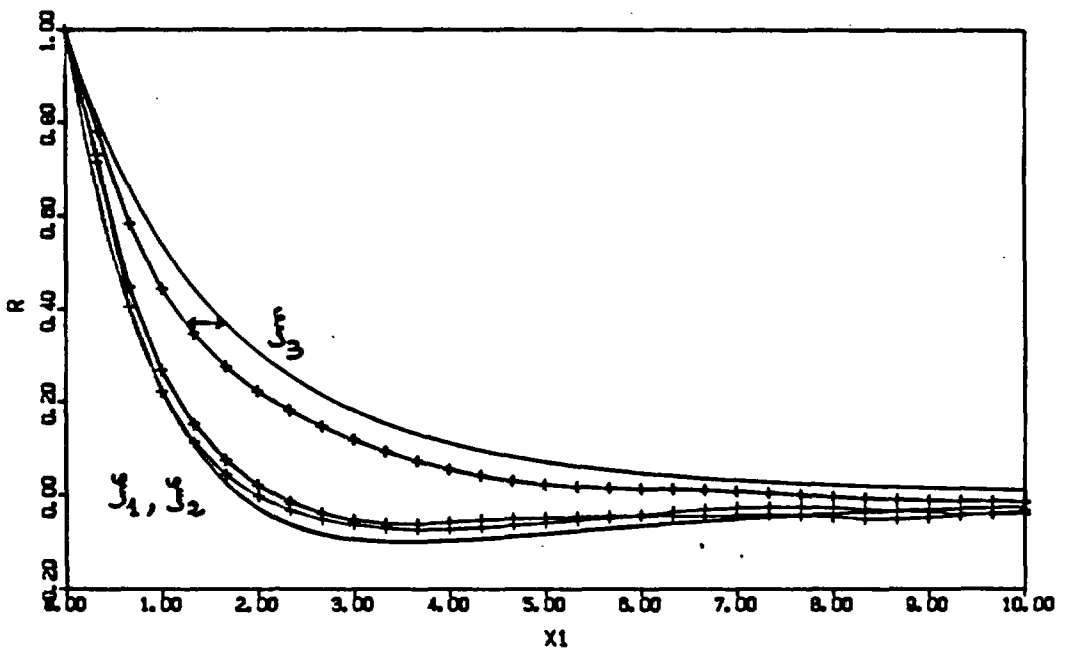

Figure 6.22 Flux correlation functions $R_{Q_2Q_2}(\xi_j)$ for $\sigma_f = 1.0$ (solid lines: spectral theory; crosses; numerical simulation).

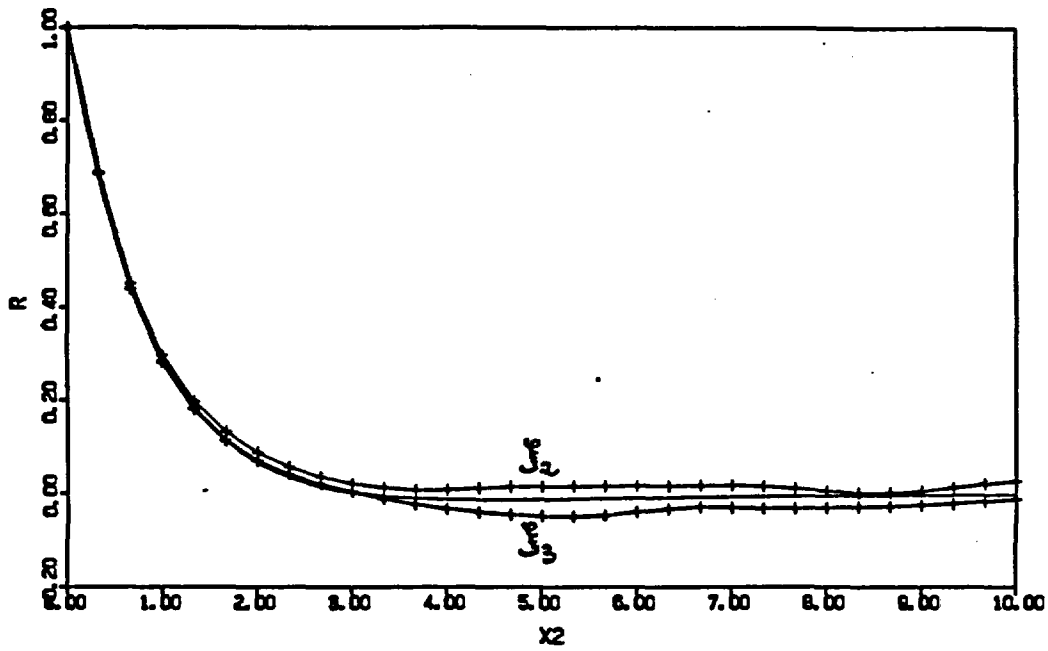

Figure 6.23 Verification of statistical symmetries on the numerical flux correlation functions ($\sigma_f = 1.0$): $R_{Q_1Q_1}(\xi_2) \simeq R_{Q_1Q_1}(\xi_3)$.

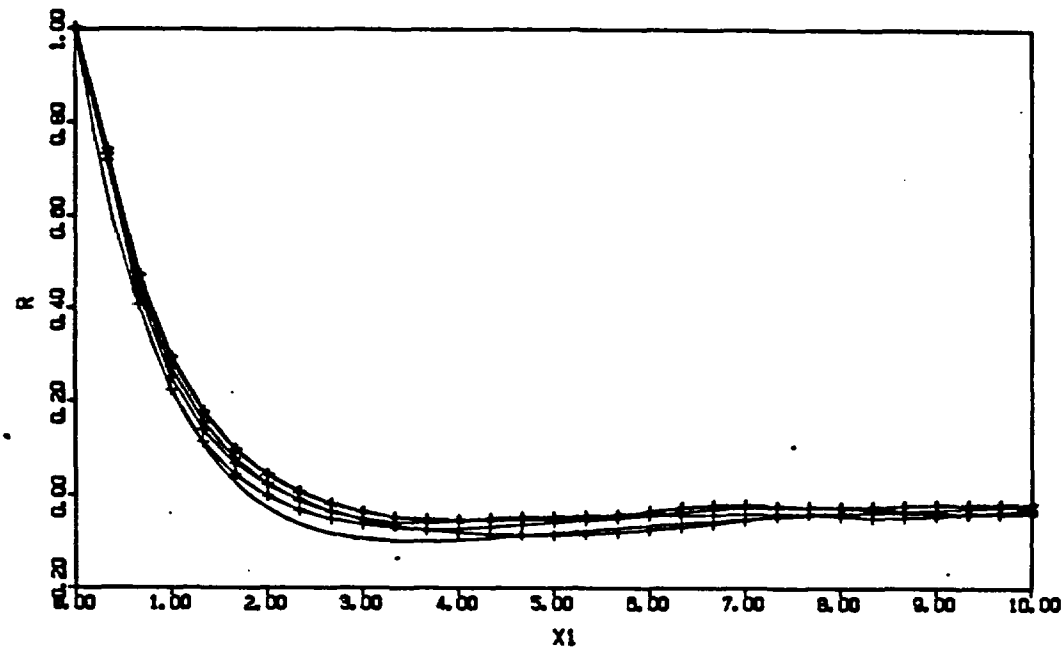

Figure 6.24 Verification of statistical symmetries of the numerical flux correlation functions (σ_f = 1.0): $R_{Q_2Q_2}(\xi_1)$. $R_{Q_2Q_2}(\xi_2)$. $R_{Q_3Q_3}(\xi_1)$. $R_{Q_3Q_3}(\xi_3)$ are nearly identical.

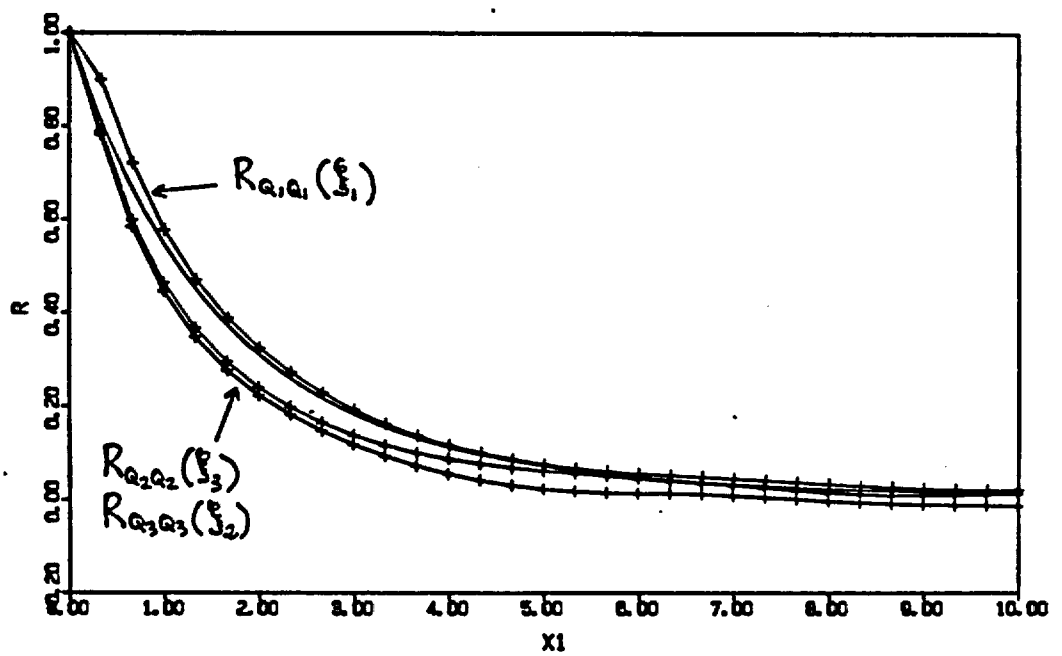

Figure 6.25 Verification of statistical symmetries on the numerical flux correlation functions ($\sigma_f = 1.0$): $R_{Q_2Q_2}(\xi_3) \simeq R_{Q_3Q_3}(\xi_2) \simeq R_{Q_1Q_1}(\xi_1)$.

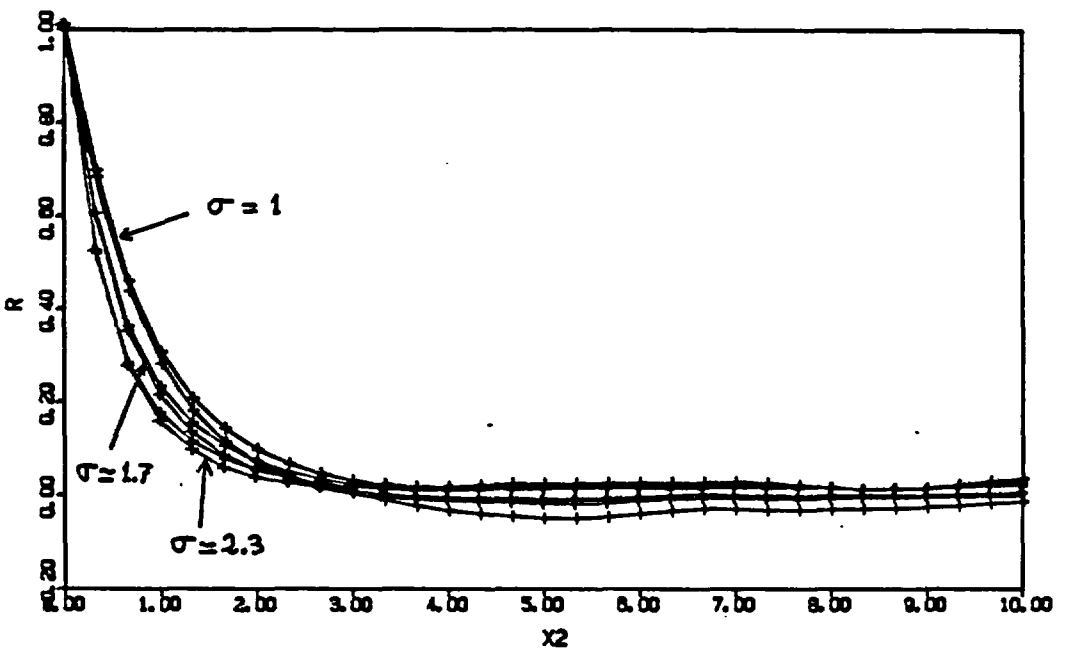

Figure 6.26 Numerical flux correlation functions $R_{Q_1Q_2}(\xi_2)$, and $R_{Q_1Q_1}(\xi_3)$ for $\sigma_f \simeq 1.0$, 1.7 and 2.3.

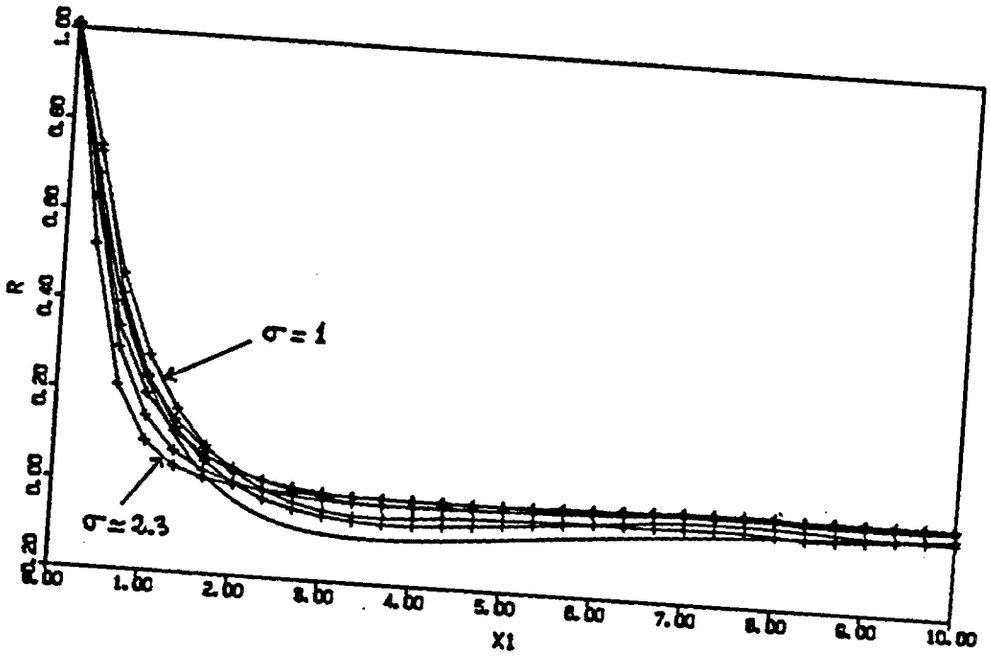

Figure 6.27 Numerical flux correlation functions $R_{Q_2Q_2}(\xi_1)$, and $R_{Q_2Q_2}(\xi_2)$ for $\sigma_f \simeq 1.0$, 1.7, and 2.3.

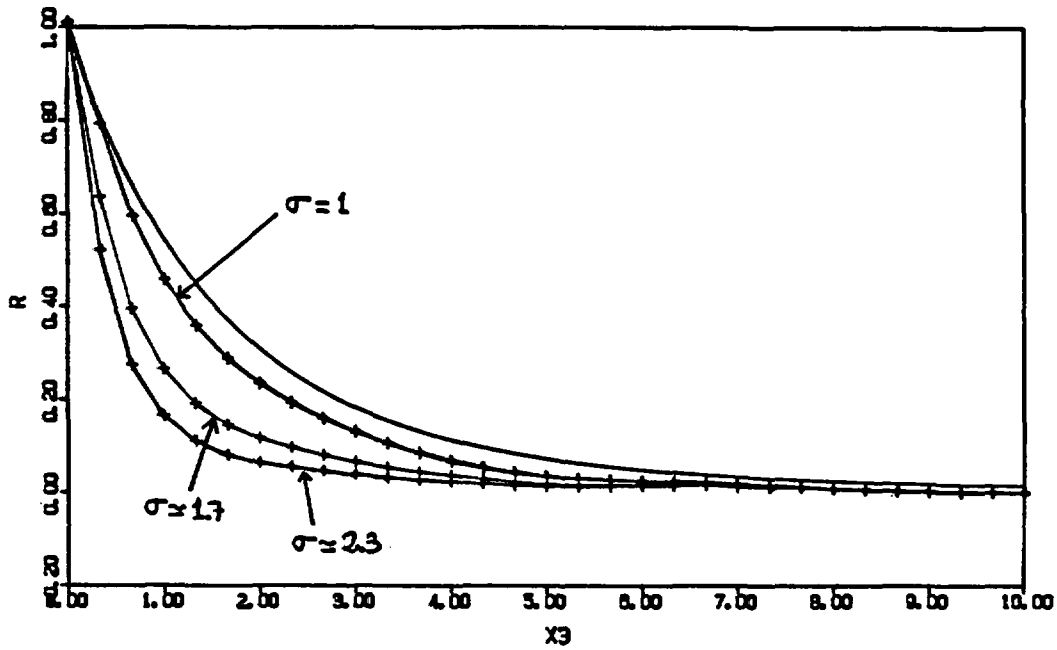

Figure 6.28 Numerical flux correlation function $R_{Q_2Q_2}(\xi_3)$, for $\sigma_f \simeq 1.0$, 1.7, and 2.3. The solid line corresponds to the result of the spectral theory, independent of σ_f.

These functions satisfy a number of symmetry relations which were discussed in Chapter 4 (Section 4.2).

With this in mind, let us now focus on the results obtained for the flux vector correlation functions. For moderate variability $\sigma_f = 1.0$, Figures 6.21 and 6.22 show a surprisingly good agreement between the flux correlation function obtained numerically and those predicted by the spectral theory (Chapter 3, Section 3.3, Figures 3.2 and 3.3). There is in particular an excellent agreement for the correlation functions of the longitudinal flux component in any direction ($R_{Q_1Q_1}(\xi_j)$ in Figure 6.21). The agreement is also excellent for the correlation functions $R_{Q_2Q_2}(\xi_1)$ and $R_{Q_2Q_2}(\xi_2)$ shown in Figure (6.22). Finally, note that the numerical solution slightly underestimates the correlation $R_{Q_2Q_2}(\xi_3)$ with respect to the spectral theory, although the agreement is still fairly good.

Furthermore, it is also important to note that the correlation structure of the numerical flux vector field appears to satisfy the symmetry relations implied by the statistical isotropy of the input log-conductivity field (Chapter 4, Section 4.2). This can be verified by assembling on the same plot the numerical correlation functions that should be identical in theory. The results of these comparisons are shown in Figures (6.23, (6.24), and (6.25) for the case $\sigma_f = 1.0$. The theoretical

symmetry identities (listed below) are indeed satisfied quite accurately by the numerical results:

Figure (6.23): $R_{Q_1Q_1}(\xi_2) = R_{Q_1Q_1}(\xi_3)$

Figure (6.24): $R_{Q_2Q_2}(\xi_1) = R_{Q_2Q_2}(\xi_2)$
$= R_{Q_3Q_3}(\xi_1)$
$= R_{Q_3Q_3}(\xi_3)$

Figure (6.25): $R_{Q_2Q_2}(\xi_3) = R_{Q_3Q_3}(\xi_2)$

Overall, these encouraging results lead us to conclude that the correlation structure of the flux vector field predicted by the spectral theory must be fairly close to the exact result in the case $\sigma_f = 1.0$. This conclusion is warranted if one rejects the possibility of a mere chance coincidence between the spectral solutions and the numerical single-realization simulations. The reliability of the numerical flux correlations does not seem questionable, in view of the fact that they satisfied fundamental symmetry relations with excellent accuracy. Thus, our simulation results confirm the validity of the Gelhar-Axness spectral theory (Gelhar and Axness, 1983) concerning the correlation structure, or shape of the flux spectrum, at least for moderate variability ($\sigma_f \lesssim 1$). Note that the same remark applies to the *modified* spectral solutions developed in this work, since the proposed modification (Chapter

4, Section 4.3) did not affect the *shape* of the flux spectrum, but only the flux variances.

Let us now focus on the effect of increasing log-conductivity variability on the correlation structure of the flux vector field. First of all, note that the flux correlations obtained from the spectral theory are independent of σ_f. Now, this appears to be approximately satisfied by the *numerical* flux correlation functions $R_{Q_iQ_i}(\xi_j)$, except for one particular correlation function $R_{Q_2Q_1}(\xi_3)$, as shown in Figures (6.26), (6.27), and (6.28). In each figure, the numerical correlation functions obtained for the three cases $\sigma_f \simeq 1.0, 1.7, 2.3$ were superimposed. It seems clear that the only significant departure from the spectral theory concerns the "correlation of the transverse flux component in the other transverse direction", $R_{Q_2Q_2}(\xi_3)$, as depicted in Figure (6.28). Nevertheless, the other flux correlation functions appeared to be relatively stable with respect to σ_f, in accordance with the spectral theory.

Again, these results suggest that the spectral theory of Gelhar and Axness (1983) is remarkably robust as far as the flux correlation structure or *shape* of the flux spectrum is concerned. The agreement between the numerical and "spectral" flux correlation functions was reasonably good within the whole range of log-conductivity variability up to $\sigma_f \simeq 2.3$. This can

be seen more directly by inspection of Table 6.9, where the correlation scales of various flux correlation functions are compared to those predicted by the spectral theory. However, this kind of comparison does not fully reflect the good agreement observed from the plots. In our view, the only major point of concern here is the behavior of the flux correlation $R_{Q_2Q_2}(\xi_3)$, and its identical "twin" $R_{Q_3Q_3}(\xi_3)$. The reason for the discrepancy on this particular correlation is not clear to us at this point, although the theoretical results of Chapter 4 might provide a clue for future investigation.

Finally, it might also be of interest to mention, without going into details, that the correlation functions of the head gradient (G_1) were also in good agreement with the spectral theory. At large variability, there was a closer agreement between the numerical and spectral correlations of the head gradient than between the numerical and spectral correlations of the flux. Since we also found that the standard deviations of the head gradient predicted by the theory were quite close to the numerical results for all values of σ_f, we conclude that the head gradient field is not affected much by high order effects. This finding might be useful for further refinement of the spectral theory.

TABLE 6.9

CORRELATION SCALES OF THE FLUX VECTOR COMPONENTS ALONG THREE DIRECTIONS ($R_{Q_iQ_i}(\xi_j)$): COMPARISON OF SPECTRAL SOLUTION WITH THE NUMERICAL RESULTS OF THE 1 MILLION NODE "ISOTROPIC" FLOW PROBLEM A

Correlation Function	Spectral theory for all σ_f	Numerical Results (σ_f=1.0)	(σ_f=1.7)	(σ_f=2.3)
$R_{Q_1Q_1}(\xi_1)$	1.70	1.75	1.41	1.16
$R_{Q_2Q_2}(\xi_3)$	1.70	1.26	0.71	0.53
$R_{Q_3Q_3}(\xi_2)$	1.70	1.33	0.77	0.55
$R_{Q_1Q_1}(\xi_2)$	0.80	0.83	0.65	0.54
$R_{Q_1Q_1}(\xi_3)$	0.80	0.85	0.64	0.52
$R_{Q_2Q_2}(\xi_1)$	0.72	0.72	0.58	0.49
$R_{Q_2Q_2}(\xi_2)$	0.72	0.81	0.71	0.63
$R_{Q_3Q_3}(\xi_1)$	0.72	0.78	0.60	0.51
$R_{Q_3Q_3}(\xi_3)$	0.72	0.85	0.76	0.66

Note: The numbers give the e-correlation scale λ_e defined by $R(\lambda_e) = e^{-1} \simeq 0.3679$. The correlation scale of the log-conductivity field was equal to unity.

[f] Summary of results:

The single-realization results obtained in this section confirmed many aspects of the spectral theory previously developed by Bakr et al. (1978) and Gelhar and Axness (1983). Our arguments to accept (or reject) the single-realization simulation results were based on a number of criteria: evaluation of sampling errors for the head field, truncation errors for the flux field, symmetry relations for the flux correlation functions, and, last but not least, agreement with spectral theory.

Some of our conclusions in particular seem beyond doubt in view of the close agreement with the spectral theory for a wide range of conductivity variability. Thus, it seems that the standard spectral theory gives essentially exact solutions for the standard deviations of the head (σ_H) and head gradient (σ_{G_i}), as well as the effective conductivity (K_{eff}), up to large variability $\sigma_f \simeq 2.3$. Furthermore, the results also indicate that the flux correlation structure predicted by the spectral theory is very accurate at $\sigma_f = 1.0$, and remains still fairly reliable up to large conductivity variability ($\sigma_f \simeq 2.3$) except perhaps for one particular flux correlation function.

On the other hand, our analysis suggested that the

standard spectral theory significantly underestimates the degree of variability of the flux vector (σ_{q_i}) even in the case of moderate variability (σ_f = 1.0 and larger). When the *modified* spectral theory developed in Chapter 4 (Section 4.3) was used instead, the theoretical values of σ_{q_i} became closer to the numerical ones. However the discrepancy was still larger than the allowable margin of error (numerical truncation error on the flux) in the case of large variability $\sigma_f \geq 1.7$. New analytical expressions (6.13) were proposed for the σ_{q_i} in order to compensate for unmodeled high order effects. It may be more than a coincidence that these expressions, which involve combinations of arithmetic and geometric mean conductivities, fit the numerical results with very good accuracy for σ_f = 1.0, 1.7 and 2.3 as well. We therefore conclude that it may be important to consider higher order spectral solutions of the flux vector (such as those proposed in this work) for applications to groundwater flow and transport in highly heterogeneous aquifers (say $\sigma_f \simeq$ 1-1.5 or larger).

In addition, we have found that the spatial structure of the head field could be significantly different from that predicted by the spectral theory in the case of finite size flow domains, although the magnitude and anisotropy of the head correlations were qualitatively in accordance with the spectral theory. For the isotropic flow problem at hand, our analysis of

finite size effects suggests that the "infinite domain" assumption of the spectral theory will hold in cases where the longitudinal size is on the order of 25-50λ, and the transverse size 50-100λ. This might be important for applications involving confined aquifers with finite thickness.

Apart from the above reservations concerning the flux standard deviations and the head correlations, it seems that all other large scale flow properties predicted by the spectral theory are reasonably accurate within a wide range of log-conductivity standard deviations, say up to $\sigma_f \simeq 2$ or so.

6.4 Summary Analysis of 3D Anisotropic Flow Simulations (220,000 Nodes)

This section is devoted to the analysis of single-realization flow simulations in the case of a statistically anisotropic log-conductivity field (3D Markov ellipsoidal) with principal axis parallel to the mean hydraulic gradient. The "anisotropic" flow problems E and F of Table 6.1 were designed to mimick the case of horizontal groundwater flow in a horizontally "stratified" aquifer, with anisotropy ratio $\epsilon = 1/4$ (ratio of vertical to horizontal correlation scales of log-conductivity). Observe that the variability of the log-conductivity field is the same for both problems ($\sigma_f = 1.0$)

but the geometry of the discrete grid differs.

For Problem E, the grid resolution was taken to be one-half with respect to the conductivity correlation scales in each direction ($\Delta x_i/\lambda_i=1/2$). On the other hand, for problem F, the grid resolution in the vertical was much coaser ($\Delta x_3/\lambda_3=4$) but, as a result, the vertical size of the domain was much larger. The total number of nodes was the same for both problems (220,000 nodes). These problems were designed to test the applicability of the single-realization approach in the case of statistically anisotropic media, and notably to evaluate the numerical requirements implied by anisotropy. These *preliminary results* are presented here because of their relevance for practical applications, in view of the fact that most natural formations exhibit some kind of stratification (see Figure 2.3. of Chapter 2 for a comparison of the anisotropic Markov conductivity with field measurements). However, there will be no attempt here at obtaining an exhaustive statistical description of the flow field, as was done in the case of isotropic conductivities. The reasons for the limited scope of this study may become clearer in the sequel.

In what follows, it will be convenient to designate the anisotropic problem (E) as the "*shallow stratified aquifer*" flow problem, and the anisotropic problem (F) as the "*deep stratified*

aquifer" flow problem. Indeed, it can be seen from Table 6.1 that the aquifer thickness is just 7.5 units in the first case, compared to 60 units in the second case, in units of the *horizontal* correlation scale λ of the log-conductivity field. By the same token, recall that Problem E (shallow aquifer) has a much finer grid resolution than problem F (deep aquifer), particularly in the vertical direction. Despite these differences, recall that the size of the grid was the same for each case, comprising 61 nodes in each direction (220,000 nodes).

With this distinction in mind, we now proceed to develop a succinct analysis of the simulated flow fields, limited to the study of spatial variability of the hydraulic head. The spatial variation of the head is depicted graphically in Figures (6.29), (6.30), (6.31) along selected slices (respectively: horizontal parallel to flow, vertical parallel to flow, and vertical transverse to flow). Each of these figures shows the numerical head fields obtained for:

(a) — the "shallow stratified aquifer" problem (E)

(b) — the "deep stratified aquifer" problem (F)

Figures 6.31(a), (b) in particular seem to indicate that the pattern of hydraulic heads in the cross-flow plane perpendicular to stratification is more anisotropic for the "shallow stratified

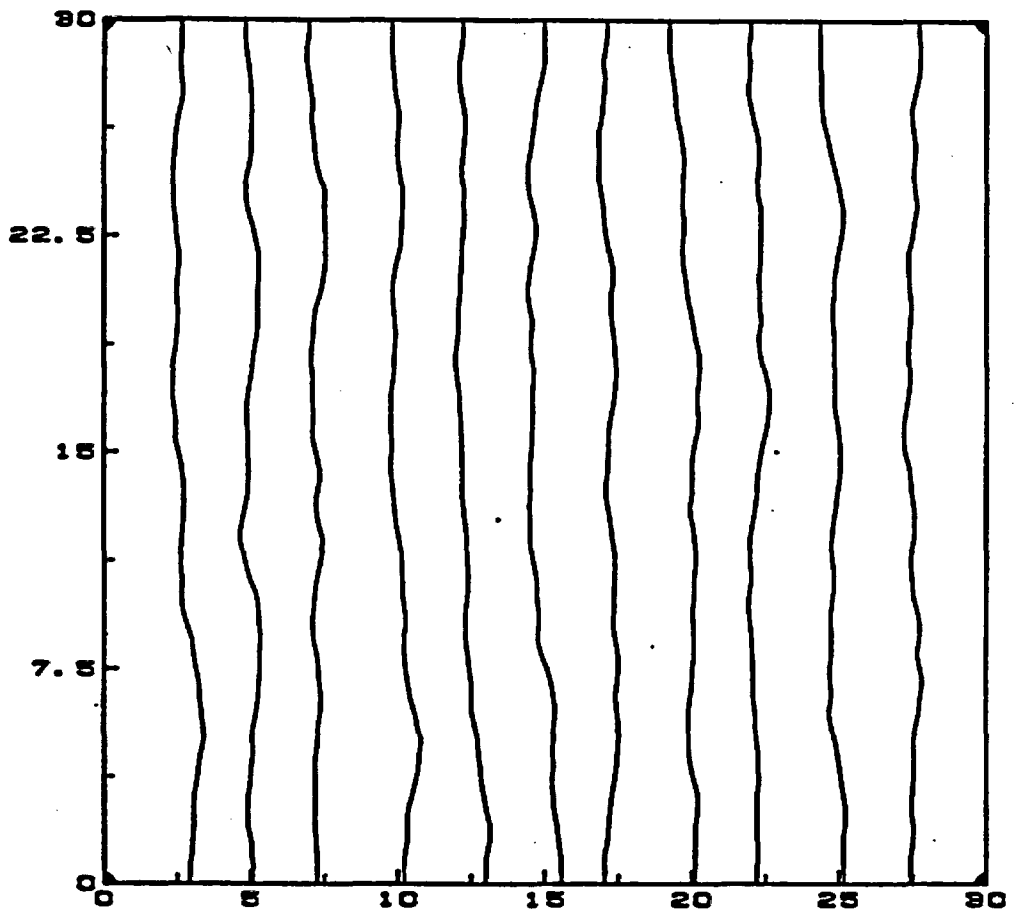

Figure 6.29 (a) Hydraulic head contours in a horizontal slice parallel to the mean flow, for a "shallow stratified aquifer" (Problem E)

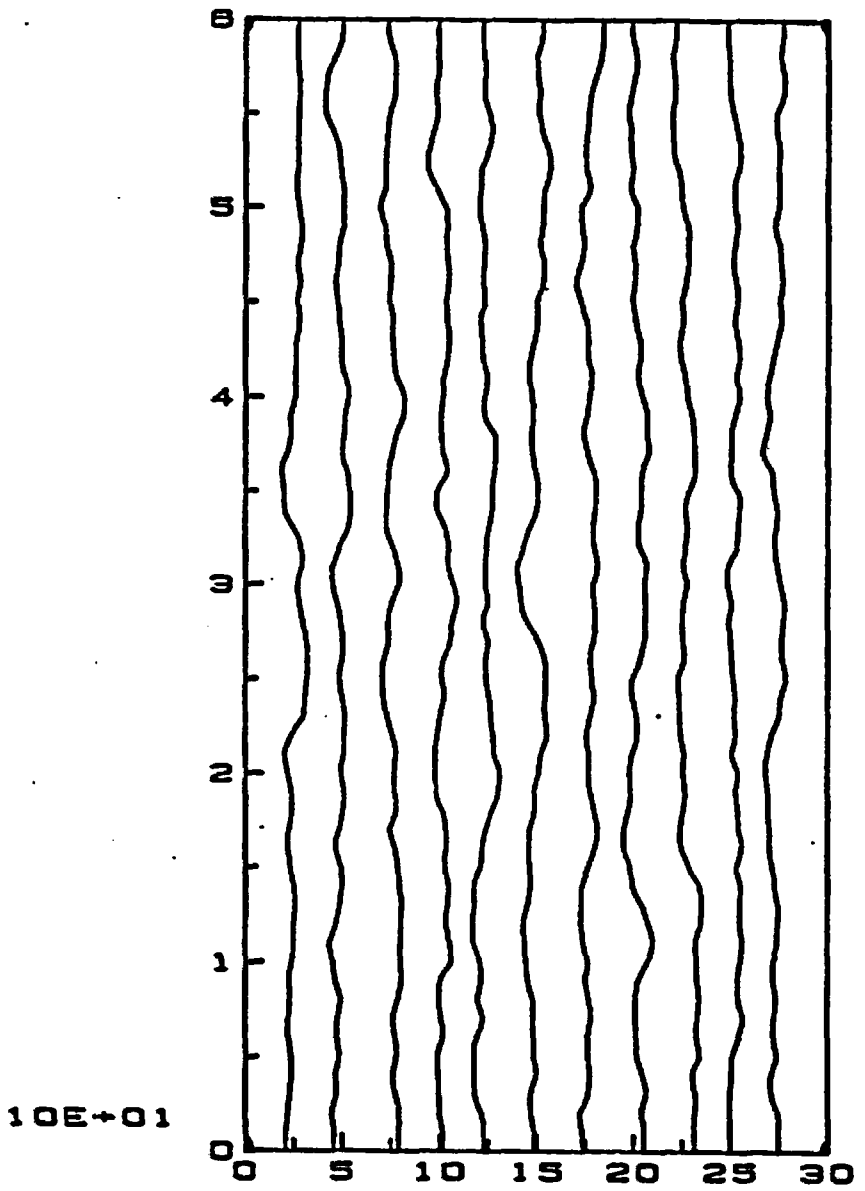

Figure 6.29 (b) Same as (a), for a "deep stratified aquifer" (Problem F)

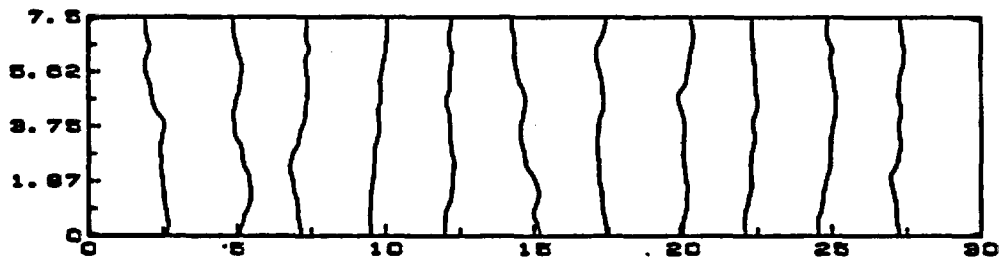

Figure 6.30 (a) Hydraulic head contours in a vertical slice parallel to the mean flow, for a "shallow stratified aquifer" (Problem E)

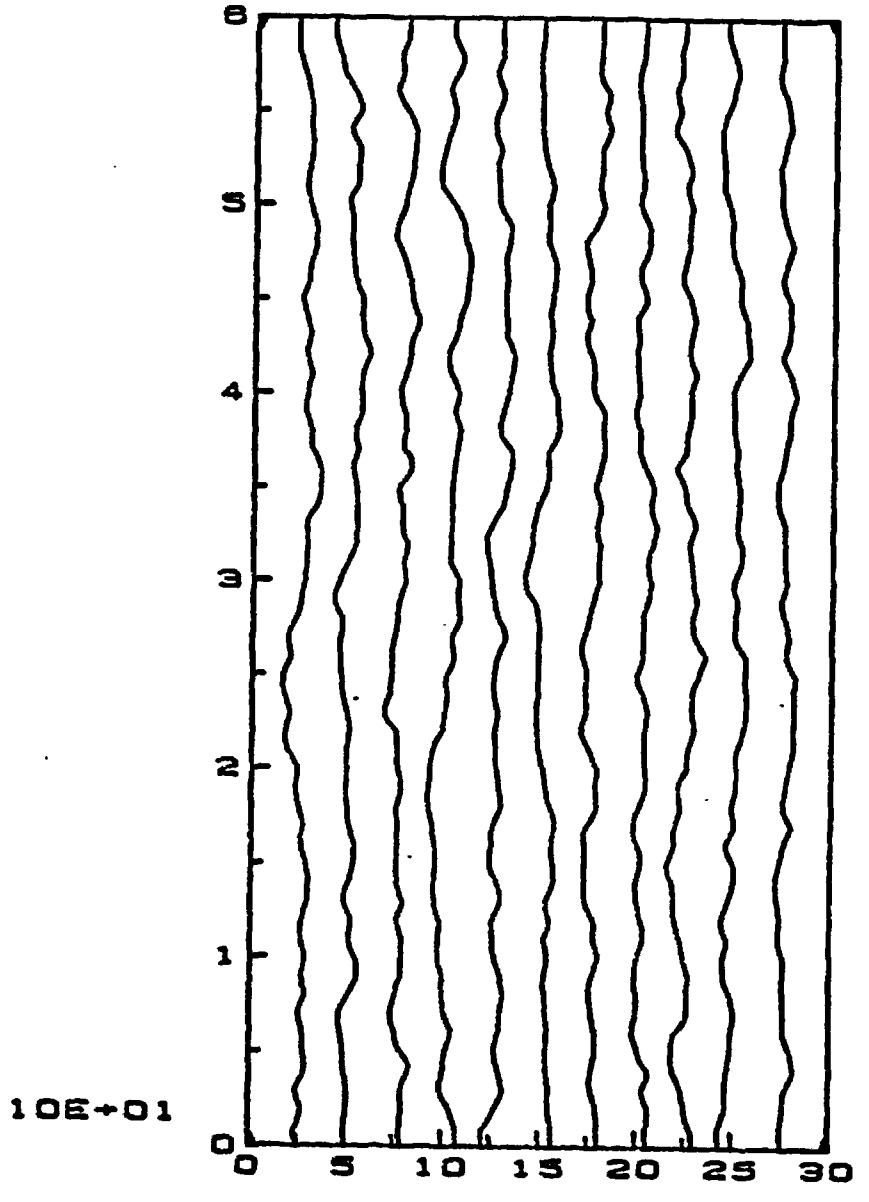

Figure 6.30 (b) Same as (a), for a "deep stratified aquifer" (Problem F).

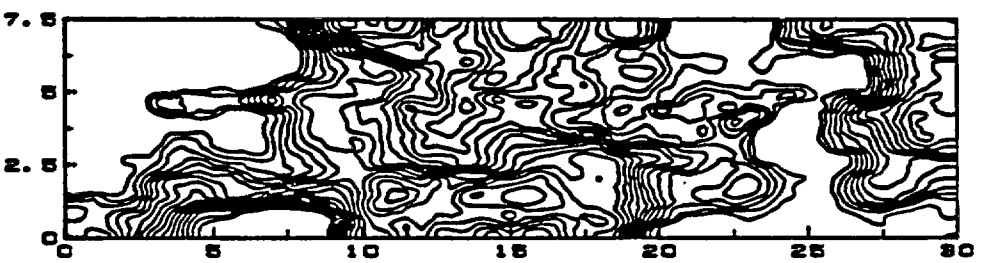

Figure 6.31 (a) Hydraulic head contours in a vertical slice transverse to the mean flow, for a "shallow stratified aquifer" (Problem E)

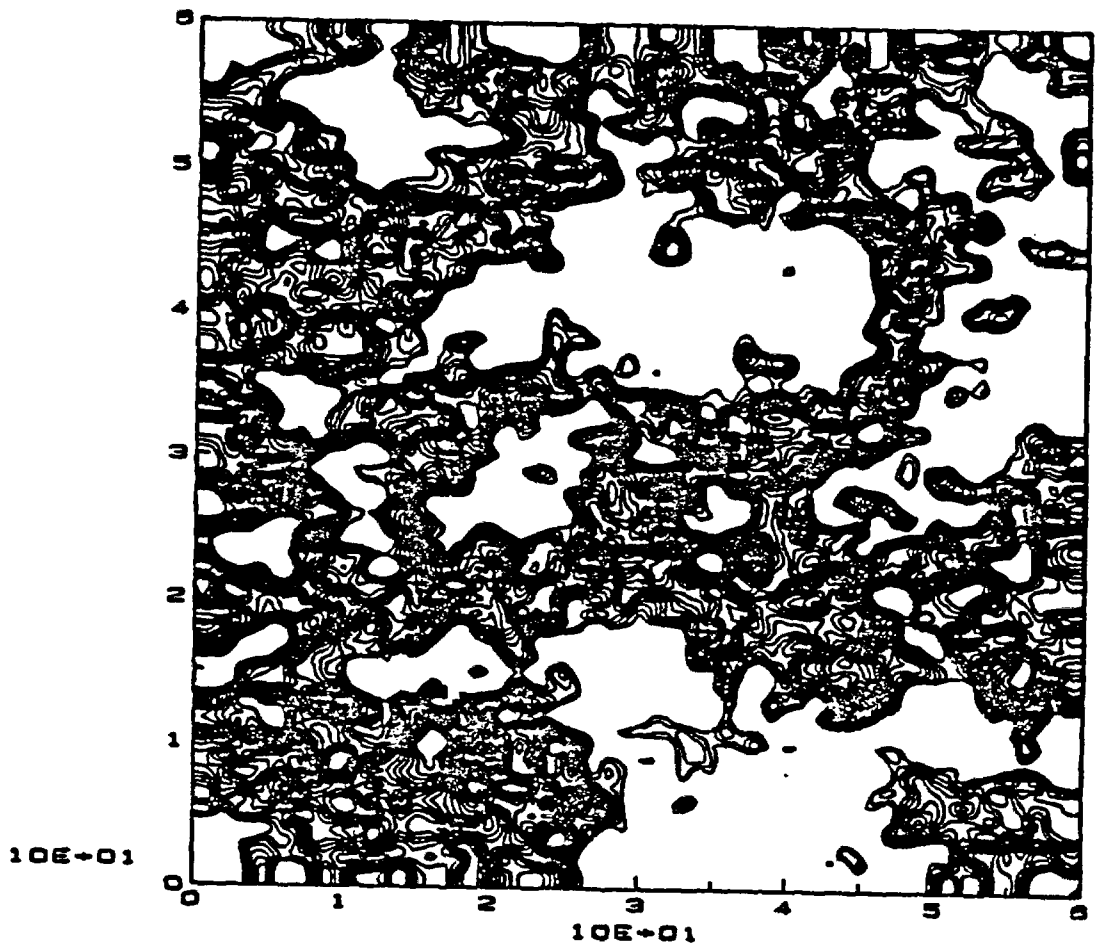

Figure 6.31 (b) Same as (a), for a "deep stratified aquifer" (Problem F).

aquifer" (a), than for the "deep stratified aquifer" (b). It may be preposterous to draw any definite conclusions from such limited observations, however we will see shortly that the above conclusion is confirmed by statistical analysis.

The standard deviation and correlation functions of the head were computed in each case by using the same longitudinal detrending technique as in the previous sections (see section 6.1 on methodology). Figure (6.32) shows in each case (a) and (b) a typical sample function of the head $H(x_1)$ along the mean flow direction, superimposed on the cross-flow average $\overline{H}(x_1)$ as defined in equation (6.5). These pictures suggest that the head variability around the nonlinear trend is smaller for the shallow aquifer (a) than for the deep aquifer (b).

Indeed, Table 6.10 (top) shows that the head standard deviation for (a) is significantly smaller than for (b). The infinite-domain spectral theory (equation 3.28 of Section 3.4, Chapter 3) gives the same value of σ_H in both cases. Furthermore, it appears that the value predicted by the spectral theory lies in between the numerical solutions of (a) and (b). This might be explained by the fact that, in (a), the flow domain was too small to allow for fully three-dimensional fluctuations of the hydraulic head whereas in (b), the grid resolution was coarse enough to generate significant numerical noise that may

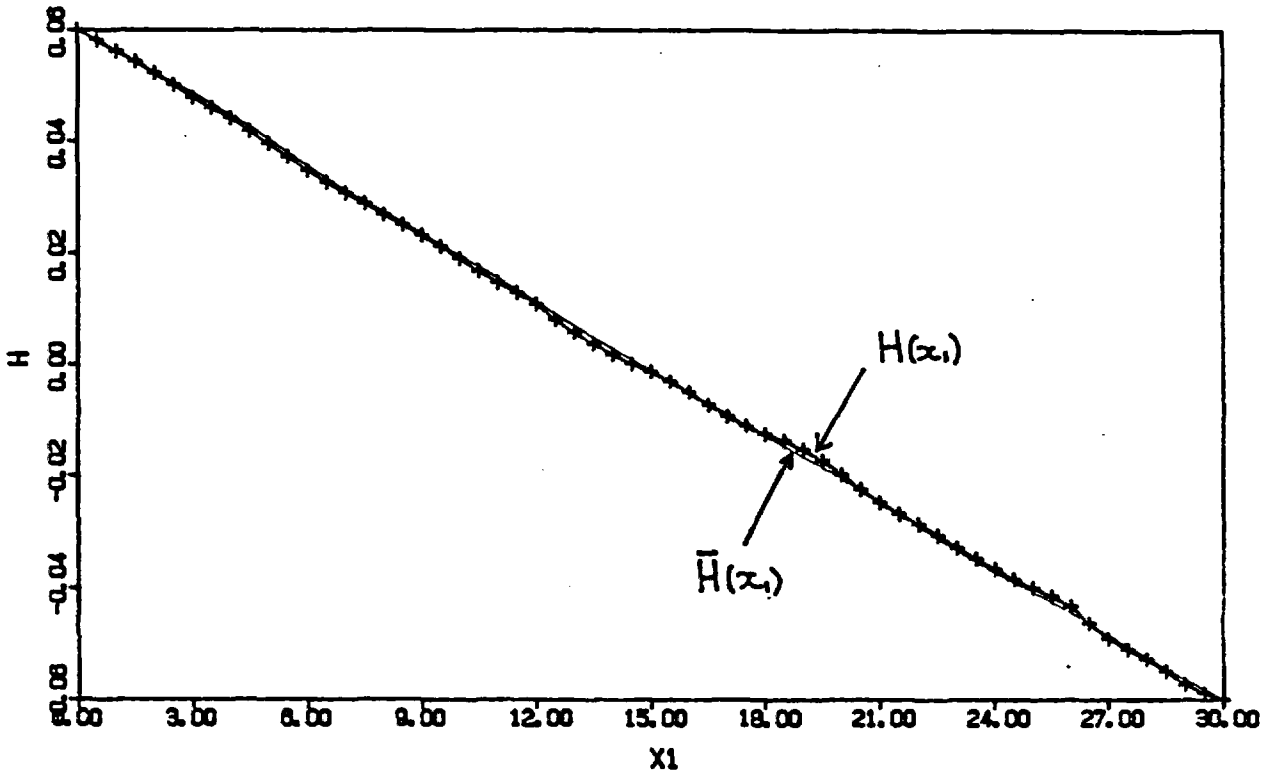

Figure 6.32 (a) Sample function of the head field $H(x_1)$ along a selected transect parallel to the mean flow, and cross flow average $\bar{H}(x_1)$: case of the "shallow aquifer" Problem E.

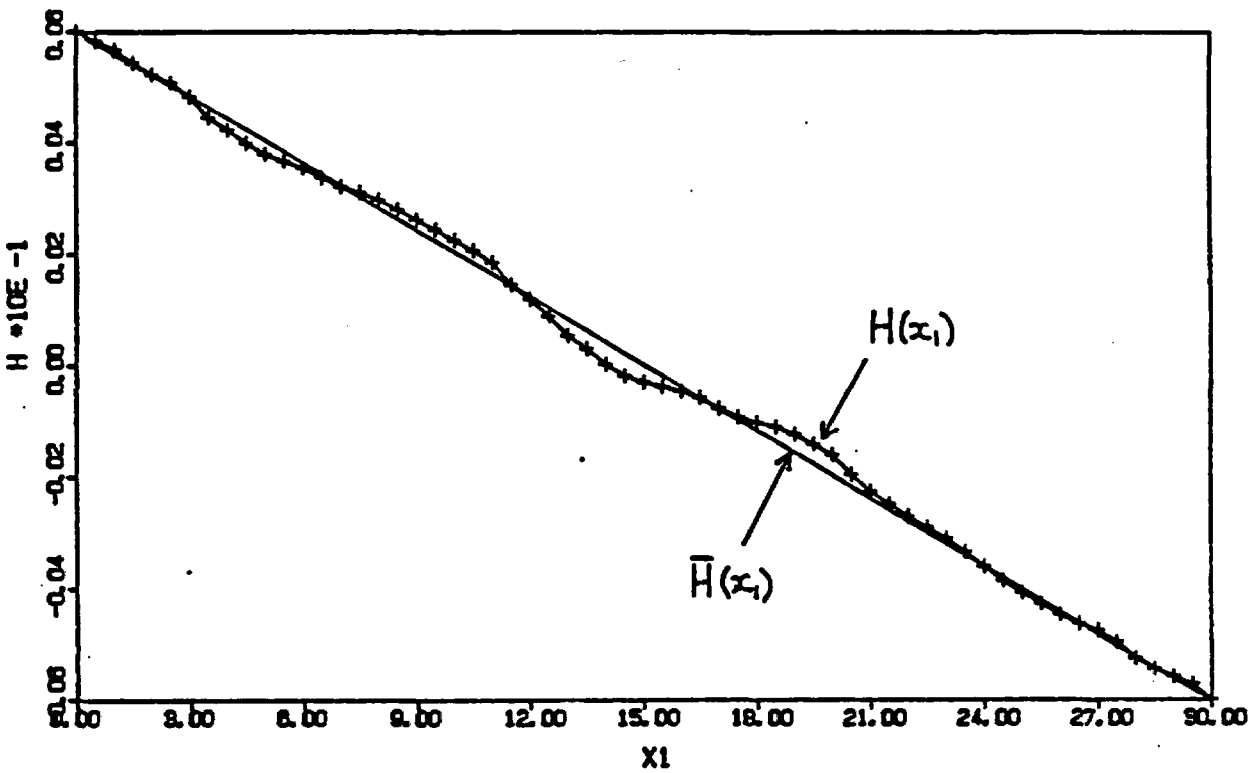

Figure 6.32 (b) Same as (a) for the "deep aquifer" Problem F.

TABLE 6.10
COMPARISON OF PRELIMINARY "ANISOTROPIC FLOW SIMULATIONS"
WITH THE RESULTS OF THE SPECTRAL THEORY:
HEAD STANDARD DEVIATION AND CORRELATION SCALES
(220,000 NODE FLOW PROBLEMS E AND F. $\sigma_f = 1.0$ and $\varepsilon = 1/4$).

Normalized Head Standard Deviation	Spectral Theory	(a): Shallow Aquifer (Problem E)	(b): Deep Aquifer (Problem F)
σ_H/J_1	0.3100	0.2654	0.3678
$\frac{\hat{\sigma}_H-\sigma_H}{\sigma_H}$	---	-14%	+18%

Correlation Scales	Longitudinal (i=1)	Transverse Horizontal (i = 2)	Transverse Vertical (i = 3)
$\lambda_{\ell n\ K}$	1.00	1.00	0.25
λ_H (spectral)	3.0	7.5	7.0
(a): λ_H (Problem E)	2.2	3.7	2.6
(b): λ_H (Problem F)	2.2	5.7	3.7

have contributed to the standard deviation of the head. Thus, σ_H was underestimated in the first case and overestimated in the second case, with respect to the spectral result. Note that σ_H was normalized by the mean head gradient, which was not the same in the two simulations.

Let us now focus on the statistical correlation structure of the simulated hydraulic head fields. It may be instructive to examine first the correlation structure of the single realization log-conductivity fields generated in each case. Figures 6.33 (a) and (b) show the computed log-conductivity correlation functions along the three principal directions, respectively for the "shallow aquifer problem" (a) and the "deep aquifer problem" (b). It is interesting to note that, in the latter case, the ℓn K-correlations along the vertical axis are not very well captured due to the coarse grid resolution $\Delta x_3/\lambda_3=4$. Nevertheless, in both cases (a) and (b), the computed correlations agree with the theoretical anisotropic Markov correlation function. In addition, the computed standard deviation of ℓn K were in each case very close to the theoretical value $\sigma_f=1.0$, with a 2% margin of error.

The unidirectional head correlation functions were computed from the detrended head fields according to the procedure outlined in Section 6.1 (same procedure used for

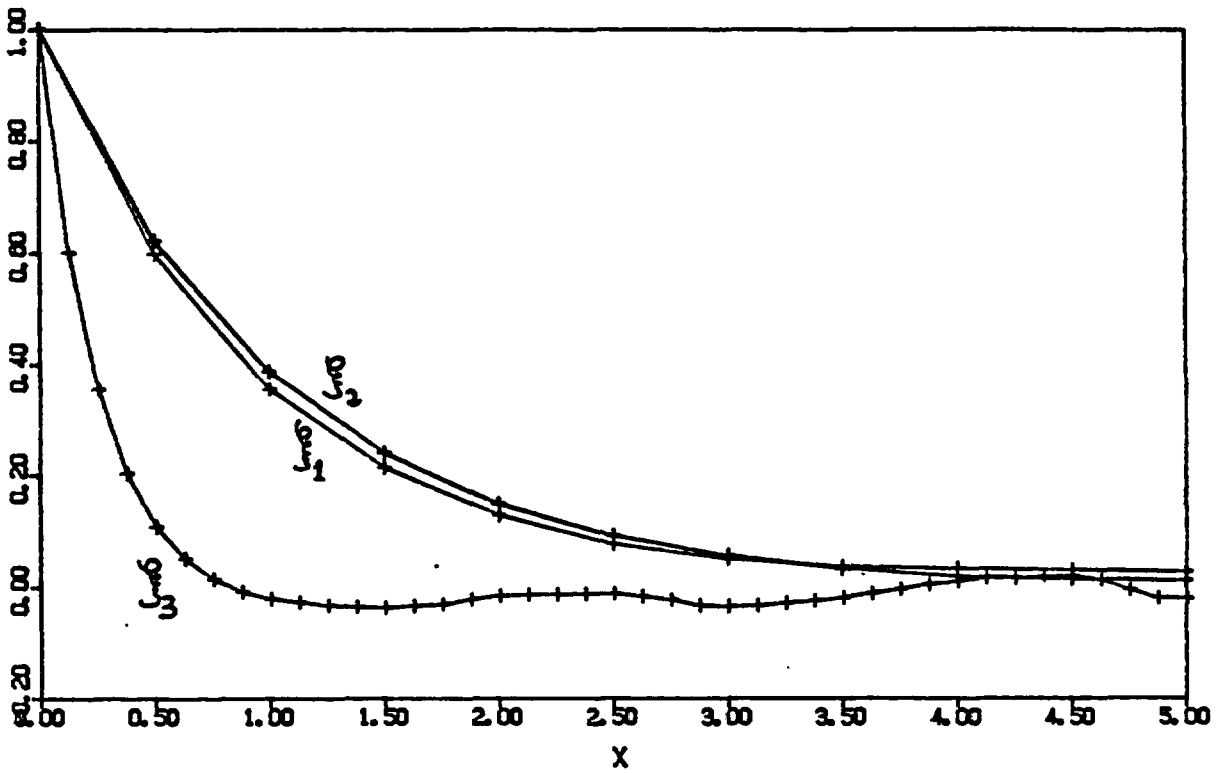

Figure 6.33 (a) Computed log-conductivity correlation functions for the single-realization anisotropic Problem E (shallow aquifer, fine grid)

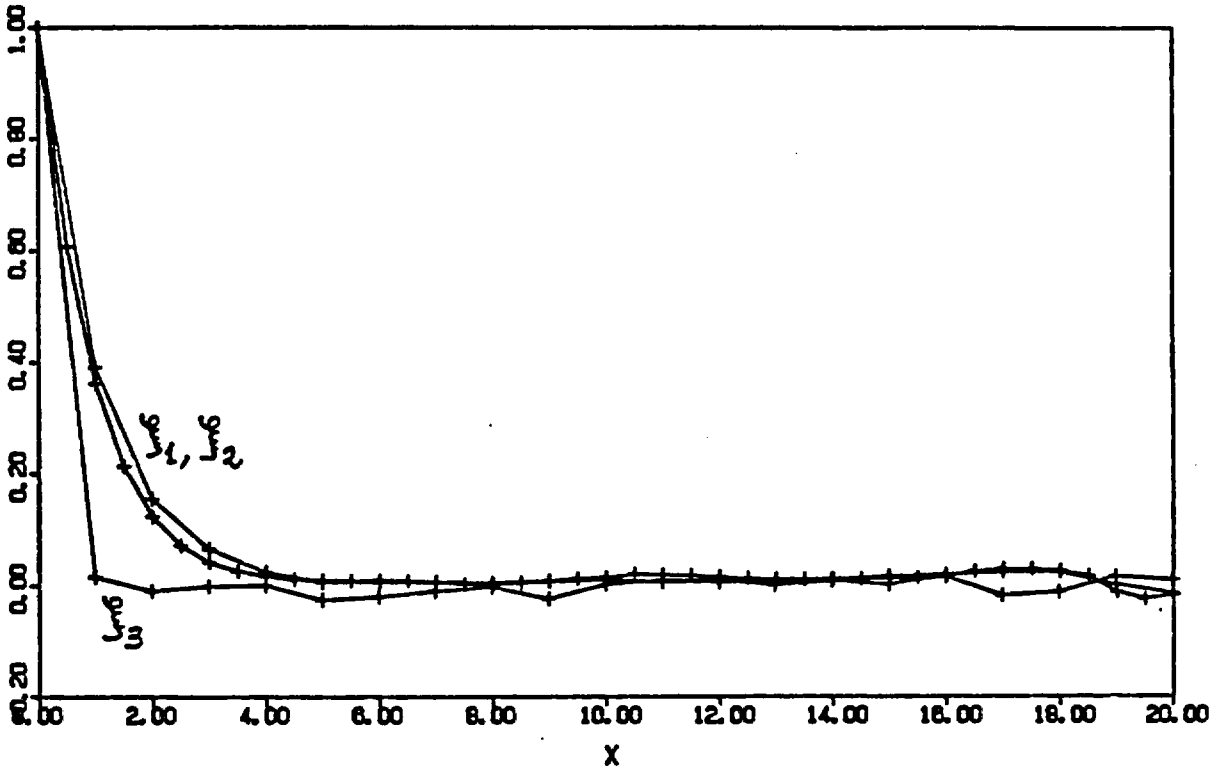

Figure 6.33 (b) Computed log-conductivity correlation functions for the single-realization anisotropic Problem F (deep aquifer coarse grid)

analyzing the isotropic flow problems in previous sections). The numerical head correlation functions corresponding to the "shallow" and "deep" aquifer problems (a) and (b) are shown in Figures 6.34(a) and (b). For comparison, the correlation functions obtained from the spectral theory (Chapter 3, section 3.4) are also displayed in Figure 6.34(c).

As expected, it appears that the head correlation structure obtained for the "shallow stratified aquifer" (a) disagrees more strongly with the infinite-domain spectral theory than the correlations obtained for the "deep stratified aquifer" (b). This can be also seen by comparing directly the head correlation scales $\lambda_H^{(i)}$, as shown in Table 6.10 (bottom).

Thus the simulation results at hand confirm our previous conclusions about the applicability of the spectral theory in the case of stratified aquifers (Chapter 3, section 3.5). It seems clear that the spatial structure of the head field in the case of the shallow stratified aquifer could not be adequately modeled by the infinite-domain spectral theory, since the aquifer thickness (7.5 λ) was on the same order as the vertical correlation range of the head field (about 7.0 λ according to the spectral theory, or 2.0 λ according to the finite domain simulation). In these conditions, the hydraulic head field obtained for the shallow case (a) may not be

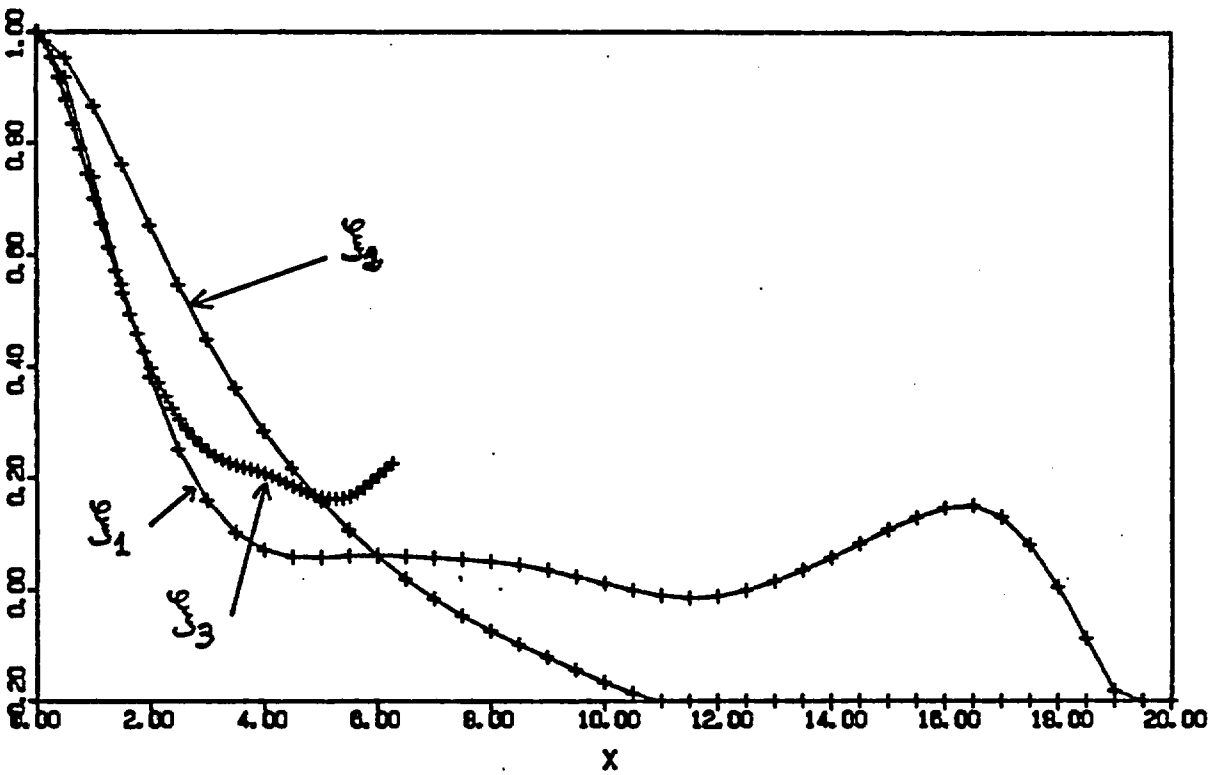

Figure 6.34 (a) Computed head correlation functions for the single-realization anisotropic flow Problem E (shallow aquifer, fine grid)

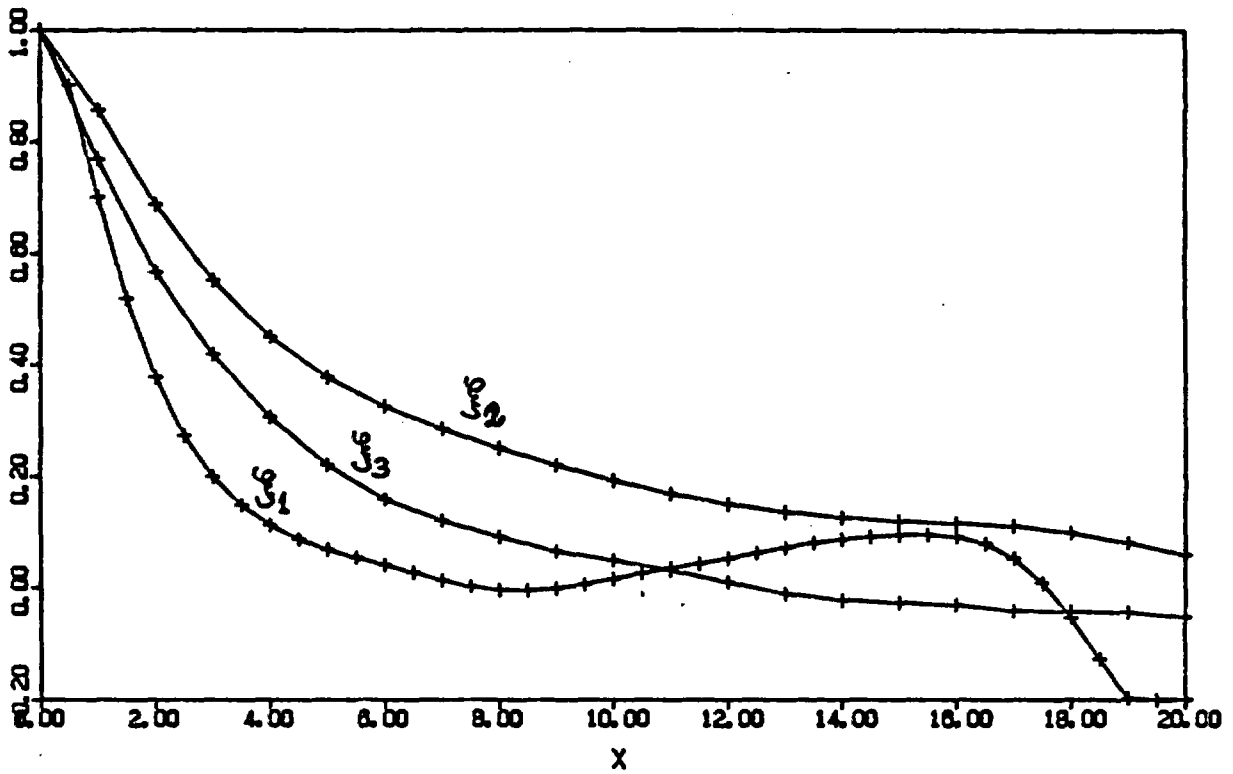

Figure 6.34 (b) Computed head correlation functions for the single-realization anisotropic flow problem F(deep aquifer, coarse grid).

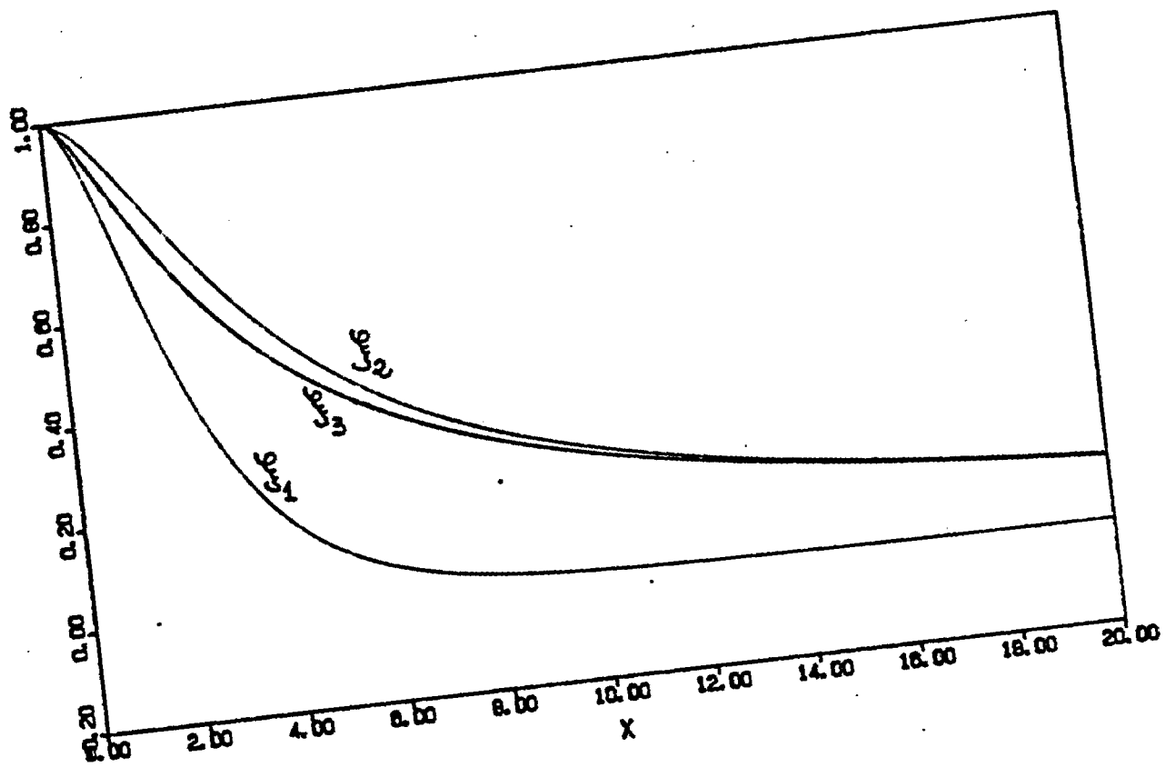

Figure 6.34 (c) Theoretical head correlation functions as predicted by the spectral theory for anisotropy ratio $\epsilon = 1/4$ ($\lambda_i = 1, 1, .025$).

representative of the ensemble of possible flow realizations, and the stochastic single-realization approach becomes meaningless.

On the other hand, the head correlations obtained for the "deep stratified aquifer" case (b) agree more closely with the infinite-domain spectral theory. This leads us to believe that the predictions of the spectral theory (near-isotropy of the head in the vertical and horizontal directions transverse to the mean flow) could be confirmed more conclusively with a larger flow domain and improved geometry/resolution of the grid.

To obtain also an accurate statistical representation of the *flux vector field*, however, the grid resolution may have to be fine in proportion to the smallest correlation scale of the input conductivity field ($\lambda_3=\lambda/4$). Indeed, our previous discussion of stratified flow systems (Chapter 3, sections 3.4 and 3.5) suggested that the correlation scales of the transverse flux components could be only a fraction of the geometric mean of horizontal and vertical conductivity scales ($\lambda_G = \sqrt{\lambda \cdot \lambda_3}$). The reader is referred in particular to Figures (3.5) to (3.7) and equation (3.22). The latter equation can be used to evaluate the fluctations scales A_{ii} corresponding to the flux correlations $R_{Q_iQ_i}(\xi_i)$. For the case at hand, this yields:

$$\Lambda_{11} \simeq \lambda = \lambda_1$$

$$\Lambda_{22} \simeq 0.15 = 0.15\lambda_2$$

$$\Lambda_{33} \simeq 0.30\lambda = 1.20\lambda_3$$

In comparison, remember that the finest mesh size in the simulations at hand was $\Delta x_i = 0.5\lambda_i$ ("shallow aquifer" problem E of Table 6.1). Thus, it appears that the grid resolution was probably much too coarse in the horizontal cross-flow direction (x_2) to be able to capture the fluctuations of the transverse flux $Q_2(\underline{x})$. Moreover, the grid resolution used for the "deep aquifer" problem was even coarser.

For "anisotropic" media, we conclude that the grid size may have to be exceedingly large in order to obtain a statistically representative flow realization (*hydraulic head H*) while capturing the finest fluctuations of the flow field (*transverse flux component* Q_2). The severe requirements of the single realization approach for stratified flow systems could possibly lead to prohibitive grid sizes in regard to current numerical/computing capabilities (i.e., well above 1-10 million nodes). This question could be examined further in the future by analyzing the numerical flux vector fields for the currently available "modest size" flow realizations (220,000 nodes), or perhaps from new simulations with improved grid resolution and geometry.

6.5 Summary and Discussion:

The stochastic flow simulations analyzed in this chapter were aimed at evaluating the range of validity of the spectral theory in the case of groundwater flow in finite (but large) realizations of random porous formations. The assumptions of the spectral theory, infinite domain and homogeneity-ergodicity of the flow field, were not required in the direct simulation approach. Thus, the simulated flow fields were statistically analyzed by using spatial averaging and detrending techniques very much like those frequently used to analyze field data. Furthermore, the small parameter expansions in the log-conductivity standard deviation (σ_f) required in the spectral theory, were not needed in the direct numerical simulation approach. Admittedly, the latter approach introduces new kinds of errors, such as truncation errors, solution errors due to approximate factorization of the matrix system and incomplete convergence of iterations, and round-off errors. However, these were presumably kept under control by using various tools from numerical analysis and by numerical experimentation (Chapter 5). In contrast, the accuracy of the spectral solutions was essentially unknown before the present research was initiated, except for a few special cases where exact solutions were available (effective conductivities for one-dimensional, and two-dimensional isotropic, random media).

The most significant results in this chapter were those obtained from large flow simulations with *statistically isotropic* log-conductivities (3D Markov field with exponential covariance) in section 6.3. The numerical flow fields obtained on a large three-dimensional grid (1 million nodes) were compared to the spectral solutions, via statistical analysis, for a wide range of conductivity variability ($1 \leq \sigma_f \leq 2.3$). There was a surprisingly good agreement for the effective conductivity (K_{eff}) and the degree of variability of the hydraulic head (standard deviation σ_H around the empirical trend) for all values of σ_f. On the other hand, the degree of variability of the flux vector field Q_i was significantly underestimated by the spectral theory for large variability ($\sigma_f > 1$-1.7). In addition, our visual observations fo the flux field (section 6.2) strongly suggested that the probability distribution of the longitudinal flux Q_i was significantly skewed positively. Both these effects are presumably due to high order interactions not taken into account by the first order spectral theory.

Nevertheless, the flux standard deviations σ_{q_i} predicted by the modified (higher order) spectral solutions of Chapter 4 (section 4.3) were more closely in agreement with the numerical results, than the standard spectral theory of Gelhar and Axness (1983). A further empirical modification of the spectral theory to account for high-order effects at large values

of σ_f finally produced a near-perfect fit with the numerical results. The empirical analytical expressions for σ_{q_i} were given in equations (6.13), to be compared to the standard and modified spectral solutions listed in Table 6.4.

On the other hand, the flux correlation functions (related to the *shape* of the flux spectrum) obtained from the Gelhar-Axness spectral theory agreed remarkably well with the numerical flux correlations in the case of moderate variability ($\sigma_f = 1.0$). Even for higher variability, there was still a fair qualitative agreement between the spectral and numerical flux correlation structures, except for one particular component of the flux correlation tensor, $R_{Q_2Q_3}(\xi_3)$. These results are particularly important for applications to stochastic solute transport. For instance, Gelhar (1987) shows that the macrodispersivity of a solute convected in a random velocity field $Q_i(\underline{x})$ is proportional to the integrated velocity covariance (see for instance equations 4.64-4.65 of Chapter 4). Overall, our results strongly suggest that the flux covariance predicted by the spectral theory will be accurate for a wide range of conductivity variability, provided the use of high-order corrections for the flux variance as explained above. The Gelhar-Axness theory of macrodispersion may have to be modified accordingly, especially for cases of large variability.

The hydraulic head correlation functions obtained numerically did not agree so well with the spectral results, even for moderate conductivity variability. In view of the very good agreement observed for the flux correlation functions, we conclude that the discrepancies concerning the spatial structure of the head field were mainly due to the large fluctuation scales of the head relative to the size of the flow domain. Thus, we conjectured from a simplified analysis of sampling errors that the infinite-domain spectral theory ideally requires a domain size on the order of 25-50 correlation scales in the mean flow direction, and as much as 50-100 correlation scales in the transverse directions, in order to be applicable to practical field situations (*isotropic case*). In fact, the spatial structure of the head field obtained on a domain of size $(33\lambda)^3$ still agreed reasonably well with the spectral theory, at least qualitatively. Thus, in the *isotropic case*, the numerical head field appeared to be statistically anisotropic as predicted by the theory, although the numerical correlation ranges were systematically smaller.

For the *anisotropic case* on the other hand, the restrictions on the range of applicability of the spectral solutions seemed to be more severe (see Section 6.4). First of all, it appeared that even for fairly large size flow problems (the "deep aquifer" case), there was still a significant

finite-size effect, resulting in smaller head correlations and more pronounced head anisotropy than predicted by the spectral theory (see Figures 6.34). Furthermore, we conjectured that a severe restriction on the mesh size may have to be satisfied in order to obtain a meaningful numerical solution for the flux vector field. The strict resolution requirement is due to the very small fluctuation scales of the transverse flux in the case of a stratified aquifer (small vertical/horizontal anisotropy ratio). Overall, the requirements of large domain size and very fine grid resolution may lead to discrete systems too large to be handled with current machine capabilities and/or with the class of numerical methods considered in this work. At any rate, the numerical simulations of Section 6.4 concerning the cases of "deep" and "shallow" stratified aquifers, seem to confirm our previous concerns about the possible inapplicability of the three-dimensional anisotropic spectral solutions in the case of confined aquifers of moderate thickness (Chapter 3, section 3.5).

Note finally that these possible limitations of the spectral theory concern only the *correlation structure* of the hydraulic head, not its global variability. Thus, we have found that, for all domain sizes and in all cases of anisotropy and variability, the head standard deviation σ_H calculated by empirical detrending of the numerical solution, matched to within 10-15% the spectral result. The fact that this worked also for

the case of the "shallow" stratified aquifer indicates that the spectral solution for σ_H can be quite robust, i.e., unaffected by finite size effects and/or domain scale inhomogeneities, provided that appropriate detrending techniques be used to smooth out the observed inhomogeneities. More generally, our results strongly suggest that the spectral theory provides an essentially correct description of the correlation structure of the flow in sufficiently large flow domains (deep aquifers), provided that the effects of domain scale or large scale inhomogeneities be smoothed out by detrending the observed hydraulic head field. In actual practice, such inhomogeneities could be caused by the presence of natural boundaries (or artificial boundaries in a numerical model), and/or distributed sources, and/or inherent inhomogeneities of the porous formation at the scale of the domain or larger. This should be taken into account in particular in the solution of the inverse problem based on field measurements of conductivity (or transmissivity) and of hydraulic head.

In summary, our direct simulations of single-realization stochastic flow problems in finite domains have helped defining the range of applicability of the infinite-domain spectral perturbation solutions (Gelhar and Axness, 1983, and this work, Chapters 3 and 4). Some of the limitations of the spectral theory may have implications for the

solution of inverse flow problems (correlation structure of the head field), and for the theory of stochastic solute transport (macrodispersion of a solute convected in a random velocity field). Our results show that the restrictions of the spectral theory, large domain and small variability, may be loosened greatly by using appropriate detrending techniques to evaluate the spatial structure of the head perturbations, and by using higher order approximations for the flux variance as proposed in this work. More research will be needed to evaluate the applicability of the Gelhar-Axness theory for stratified aquifers, particularly in the case of a *dip angle* between the mean flow and the principal axis of statistical anisotropy, which was not explored in this work (see indications in Section 6.1).

CHAPTER 7: THREE-DIMENSIONAL SINGLE-REALIZATION SIMULATIONS OF UNSATURATED INFILTRATION IN RANDOM SOILS

7.1 Scope and Objectives

This chapter is devoted to the numerical simulation and interpretation of large scale realizations of stochastic unsaturated flow in random soils. The principle of the single-realization approach was explained in Chapter 2, and the related numerical issues were discussed in Chapter 5. The statistical aspects of the method were illustrated quite concretely in Chapter 6 for the case of steady state groundwater flow under a given regional hydraulic gradient.

However, here, a new difficulty arises due to the severe nonlinearity and inhomogeneity of the infiltration problem. For example, the preliminary infiltration experiments presented in Chapter 5 (section 5.4.3) clearly demonstrated the strongly inhomogeneous nature of the pressure field during the early stages of infiltration from a local strip source (evolving wetting front). When strong nonlinearity dominates the flow process, the assumptions of the linearized spectral theory of Mantoglou and Gelhar (1987) may be too constraining to warrant a precise quantitative comparison between the ensemble moments

obtained by the theory, and the spatial moments obtained from the numerical solutions. Therefore, unlike the case of groundwater flow, we do not have here the support of a robust analytical theory to guide our numerical experiments. For instance, little is known about the behavior of the wetting front in the presence of random heterogeneities. The reader is referred to Mantoglou (1984) and the above-quoted work, for a detailed account of the assumptions of homogeneity and the various linearization and "small parameter" approximations involved in their spectral solutions of transient unsaturated flow.

In addition, there is another difficulty inherent to the single-realization approach when dealing with localized and inhomogeneous transient flow processes, as occurs during infiltration from a local source. In such cases, the actual size of the flow domain (evolving wet zone) is regulated by the physics and depends on the time scale of interest. Thus, a single realization solution may not be statistically representative of the ensemble of possible realizations unless the time scale is large and/or the size of the source is large.

Our choice of strip-source infiltration problems was motivated in part by this kind of limitation. In the strip-source case, the source and the flow domain can be taken arbitrarily large in the longitudinal direction parallel to the

strip, at least within the limits imposed by computing capabilities. By symmetry arguments, we expect the flow field to be statistically homogeneous in the longitudinal direction, as illustrated in Figure 7.1. By sampling the solution along the longitudinal axis, one may obtain a representative picture of the effects of spatial variability from a single realization of the strip-source flow.

Accordingly, the next two sections will be devoted to the study of transient strip-source infiltration in random soils. In section 7.2, we investigate specifically the influence of the variability of the unsaturated conductivity curve on the flow pattern for a statistically isotropic soil. In section 7.3, we analyze one very large realization of strip-source infiltration in a statistically anisotropic soil, designed to mimick an on-going experiment at the Las Cruces experimental farm of the University of New Mexico. In either case, however, direct statistical analysis of the pressure field will not be attempted, due to the limitations mentioned above.

In addition, Section 7.4 is devoted to a class of infiltration problems where the solution is expected to be statistically homogeneous in all three space directions. Thus, we have chosen to study the case of steady state infiltration from a uniform plane source of constant intensity (uniform

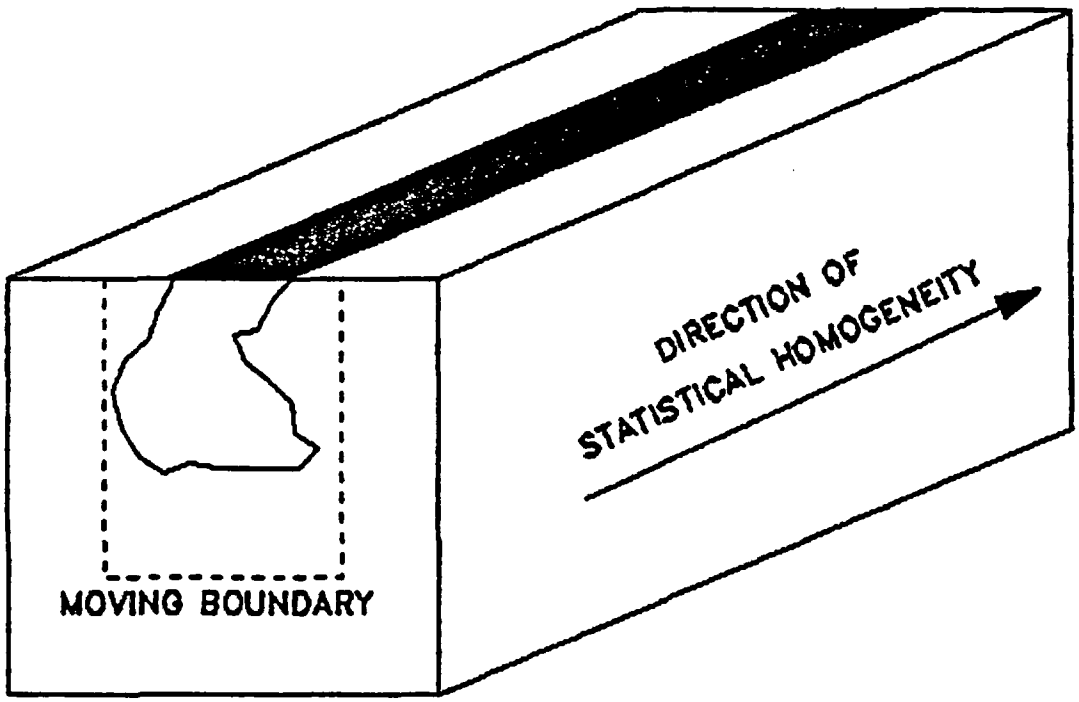

Figure 7.1 Illustration of a strip-source infiltration problem having one spatial direction of statistical homogeneity (longitudinal direction).

"rainfall"). Some preliminary statistical analysis will be briefly presented, for comparison with the results of the steady state linearized spectral theory of Yeh et al. (1985), later extended by Mantoglou and Gelhar (1987).

The strip-source and the steady uniform infiltration problems of Sections 7.3 and 7.4 were solved for the same large realization of a statistically anisotropic random soil, over a grid of size 300,000 nodes. To run these two problems required a CPU time on the order of 10 hours on a Cray 2 machine, including trial and errors for adjusting the time steps. Note that the steady state infiltration problem of section 7.4 was in fact solved by way of transient simulation up to a relatively large time of infiltration (3 months), and required about 3 CPU hours on the Cray 2 machine. In contrast, the preliminary strip-source infiltration problems presented in section 7.2 were solved on relatively "modest" grid sizes (25,000 nodes) using the Microvax 2 minicomputer. It should be noted that the purposes of the three sets of simulations (sections 7.2, 7.3, 7.4) were somewhat different. The contents of each section are summarized below for convenience.

Section 7.2 (25,000 nodes/transient):

Preliminary simulations of transient strip-source

infiltration on statistically isotropic soils for relatively small time and length scales (3 days of infiltration, 1.4 x 4 x 4 meters domain). Test of different assumptions concerning the variability of the ℓn K(h) curve, and qualitative interpretation of simulation results.

Section 7.3 (300,000 nodes/transient):

Single-realization simulation of transient strip-source infiltration and drainage on a statistically anisotropic soil for relatively large time and length scales (20 days of infiltration and drainage, 5 x 15 x 15 meters domain). The geometry, boundary conditions, hydraulic properties, and spatial variability data were selected to mimick the on-going "trench" experiment at Las Cruces. Qualitative interpretation of simulation results.

Section 7.4 (300,000 nodes/steady):

Single-realization simulation of steady state infiltration from a plane source of constant intensity (uniform rainfall). Same geometry, grid size, and soil data as in the previous strip-source "experiment". Qualitative interpretation and preliminary statistical analysis of pressure head variability and effective conductivity. Comparison with linearized spectral solutions.

A few additional comments may be useful to complete this summary. In all cases, the unsaturated conductivity curve was assumed to vary randomly in space (one different curve for each node of the grid), while the water retention curve was assumed to be the same at all locations (deterministic). The unsaturated conductivity-pressure relation was assumed to be exponential, and the water retention curve was represented by the Van Genuchten function, as explained in Chapter 5 (section 5.1.3). The precise data and the assumed stochastic properties of the conductivity curve will be given in more detail in the sequel: see in particular the next section (7.2) concerning the method used to generate random conductivity parameters. On the whole, the single realization solutions presented in this chapter constitute, as far as we know, the largest high-resolution representations of heterogeneous three-dimensional unsaturated flow systems available to date.

7.2 Strip Source Infiltration in Statistically Isotropic Soils (25,000 nodes):

7.2.1 Model problems and input data

The nonlinear conductivity and water retention curves adopted in the sequel are, respectively, the exponential and the Van Genuchten functions (see Chapter 5):

$$K(h,\underline{x}) = \begin{cases} K_s(\underline{x}) \exp(\alpha(\underline{x})h) & \text{if } h \leq 0 \\ K_s(\underline{x}) & \text{if } h \geq 0 \end{cases} \tag{7.1}$$

$$\theta(h) = \theta_s + \frac{\theta_s - \theta_r}{(1+ (-\beta h)^n)^{1-1/n}} \tag{7.2}$$

Both parameters $K_s(\underline{x})$ and $\alpha(\underline{x})$ of the unsaturated conductivity curve (7.1) are assumed to be random functions of three-dimensional space. On the other hand, we assume that the water retention curve (7.2) is deterministic, i.e., the same at all spatial locations. This simplifying assumption was motivated by the findings of Mantoglou (1984) and Mantoglou and Gelhar (1987), whose linearized spectral results suggest that the variability of $\theta(h,\underline{x})$ plays a minor role compared to the variability of $K(h,\underline{x})$. Their results also indicate that the statistical properties of the flow will be quite sensitive to the mean *and* variance of $\alpha(\underline{x})$.

The parameter α corresponds to the slope of the log-conductivity curve, obtained by differentiating $\ell n\, K(h,\underline{x})$ with $\underline{x}$ fixed. Various physical interpretations of α were discussed in Chapter 5 (section 5.4.2), e.g. inverse height of the capillary fringe, pore size distribution index, or convection/diffusion ratio. Field data concerning the variability of the conductivity curve were discussed in

Chapter 2 (section 2.3.2, table 2.2). It should be pointed out that the degree of correlation between $K_s(\underline{x})$ and $\alpha(\underline{x})$ remains unknown. On the other hand, the linearized spectral solutions of Mantoglou and Gelhar (1987) seem to be fairly sensitive to the assumed correlation between these two random field parameters (correlated/uncorrelated) and very sensitive to the degree of variability of the α-parameter in particular.

In the present section, we propose to investigate directly the effect of variability of the α-parameter and of the correlation between α and K_s, by way of numerical simulations of strip-source infiltration for relatively modest time and length scales. The relevant input data used in these simulations are summarized in Table 7.1 below. Three types of variability were assumed for the random conductivity curve of equation (7.1):

Case (1): $K_s(\underline{x})$ random, α constant.

Case (2): $(K_s(\underline{x}), \alpha(\underline{x}))$ random and perfectly correlated.

Case (3): $(K_s(\underline{x}), \alpha(\underline{x}))$ random and perfectly uncorrelated.

In each case, the parameters ℓnK and/or $\ell n\alpha$ were assumed to be statistically isotropic Markov random fields in three-dimensional space, with a constant-mean Gaussian distribution. Thus, defining K_G and α_G the geometric means of $K_s(\underline{x})$ and $\alpha(\underline{x})$, we used the turning band method (Chapter 2 and

TABLE 7.1
SUMMARY OF INPUT DATA FOR THE SINGLE-REALIZATION
SIMULATIONS OF STRIP-SOURCE INFILTRATION IN STATISTICALLY ISOTROPIC SOILS
(25,000 NODES)

Type of Data	Description	Value
Domain Geometry, Boundary Conditions, and Initial Conditions	Vertical domain size	$L_1 = 1.40$ m
	Transverse horizontal domain size	$L_2 = 4.00$ m
	Transverse longitudinal domain size	$L_3 = 4.00$ m
	Strip source width	$W_s = 1.10$ m
	Flux at the surface of the strip	$q_o \equiv 2$ cm/day
	Condition at the bottom boundary	$q_1 = - K(h)$
	Initial pressure head	$h_{in} = - 150$ cm
Space-Time Discretization	Time step	Variable
	Mesh size Δx_i $(i=1,2,3)$	$\Delta x_i = 0.10$ m
	Unidirectional number of nodes n_i	$n_i = (5, 41, 41)$
	Total number of nodes of 3D grid	$N = 25215$
Exponential Conductivity Curve (Random)	Geometric mean saturated conductivity	$K_G = 541$ cm/d
	Standard deviation of $\ell n\ K_s$	$\sigma_f = 0.7$
	Geometric mean of the ℓn K-slope	$\alpha_G = 0.09\ cm^{-1}$
	Standard deviation of $\ell n\ \alpha$	$\sigma_a = 0.3$
	Isotropic correlation scales λ_i	$\lambda_i = 0.20$ m
Van-Genuchten Water retention Curve (Deterministic)	Saturated moisture content	$\theta_s = 0.38$
	Residual moisture content	$\theta_r = 0.07$
	Scaling parameter	$\beta = 0.05\ cm^{-1}$
	Shape factor (real number)	$n = 2.00$

Chapter 6) to generate the zero-mean Gaussian random fields:

$$f(\underline{x}) = \ell n(K_s(\underline{x})/K_G)$$

$$a(\underline{x}) = \ell n(\alpha(\underline{x})/\alpha_G) \qquad (7.3)$$

with isotropic exponential covariance function. The corresponding spectral density can be found in Table 3.1 of Chapter 3 (special case of ellipsoidal Markov-spectrum, with equal correlation lengths in all three directions).

Note that we assumed the log-normality of the α-parameter. This differs from the assumption of normality implicit in the theoretical work of Mantoglou and Gelhar (1987). In our opinion, the log-normal behavior of α makes sense in view of the fact that this parameter, like K_s, is necessarily positive for all usual types of rigid porous media. This is also supported by the experimental observations discussed in the data survey section of Chapter 2. In particular, Russo (1983) found that $\alpha(\underline{x})$ followed a log-normal distribution with skewness coefficient equal to 1.36 (similarly, $K_s(\underline{x})$ was log-normal with skewness 2.49). Now, equations (2.19-2.21) can be used to relate the mean and variance of a log-normal variable (Y) to the geometric mean (Y_G) and the variance of ℓnY. These equations also show that the skewness of a log-normal variable is always

positive and increases rapidly with its coefficient of variation. On the other hand, in the case of mild variability ($\sigma_{\ell nY} << 1$) the skewness of Y becomes negligible, the standard deviation of ℓnY becomes approximately equal to the coefficient of variation ($\sigma_Y/\bar{Y}$), and the geometric mean (Y_G) becomes close to the mean ($\bar{Y}$). These simple observations may help compare our simulation data to other data or theories published in the literature.

A few single-realizations of the log-normal random fields $K_s(\underline{x})$ and $\alpha(\underline{x})$ were produced in order to simulate the three cases outlined above. In case (1), only K_s was random. The turning band method was used to generate one realization of a Gaussian random field, say $u_1(\underline{x})$, and the desired K_s-field was obtained by rescaling $u_1(\underline{x})$ and applying an exponential transform in the obvious way. In case (2), where ℓnK_s and $\ell n\alpha$ were perfectly correlated random fields, the same realization $u_1(\underline{x})$ was used to obtain both $K_s(\underline{x})$ and $\alpha(\underline{x})$ after rescaling and exponentiating. Finally, in case (3), two independent realizations $u_1(\underline{x})$ and $u_2(\underline{x})$ were used to obtain $K_s(\underline{x})$ and $\alpha(\underline{x})$ independently from each other. The procedures just described are summarized below for convenience, along with a possible generalization to handle the case of imperfect correlation, as may be needed in the future when more data become available.

Case (1):

$$K_s(\underline{x}) = K_G \cdot \exp(\sigma_f \cdot u_1(\underline{x})) \tag{7.4}$$
$$\alpha(\underline{x}) = \alpha_G$$

Case (2):

$$K_s(\underline{x}) = K_G \cdot \exp(\sigma_f \cdot u_1(\underline{x})) \tag{7.5}$$
$$\alpha(\underline{x}) = \alpha_G \cdot \exp(\sigma_a \cdot u_1(\underline{x}))$$

Case (3):

$$K_s(\underline{x}) = K_G \cdot \exp(\sigma_f \cdot u_1(x)) \tag{7.6}$$
$$\alpha(\underline{x}) = \alpha_G \cdot \exp(\sigma_a \cdot u_2(\underline{x}))$$

General case (imperfect correlation):

$$K_s(\underline{x}) = K_G \exp(\sigma_f \cdot u_1(\underline{x})) \tag{7.7}$$
$$\alpha(\underline{x}) = \alpha_G \exp\{\sigma_a(\rho\, u_1(\underline{x}) + \sqrt{1-\rho^2}\, u_2(\underline{x}))\}$$

In the latter case, ρ designates the correlation coefficient between f(x) and a(x) $(-1 \leq \rho \leq 1)$. More precisely, the covariance tensor of the jointly Gaussian random fields $(a(\underline{x}), f(\underline{x}))$ is of the form:

$$\begin{bmatrix} R_{aa}(\underline{\xi}) & R_{af}(\underline{\xi}) \\ R_{fa}(\underline{\xi}) & R_{ff}(\underline{\xi}) \end{bmatrix} = \begin{bmatrix} \sigma_a^2/\sigma_f^2 & \rho\sigma_a/\sigma_f \\ \rho\sigma_a/\sigma_f & 1 \end{bmatrix} . R_{ff}(\underline{\xi})$$

Accordingly, case (1) obtains by taking $\sigma_a = 0$, case (2) by taking $\rho = 1$, and case (3) by taking $\rho = 0$. The two special cases $\rho = 1$ and $\rho = 0$ were motivated by the observation that (α, K_s) should be positively correlated $(0 \leq \rho \leq 1)$ since *both* α and K_s generally increase with soil coarseness, and decrease with clay content.

Figure 7.2 illustrates the two extreme assumptions of perfect correlation and perfect independence ($\rho = 1$ and $\rho = 0$) corresponding to cases (2) and (3). The $\ell n\ K(h)$ functions were plotted schematically for different spatial locations. The log-conductivity curves shown in the top part of Figure 7.2 have perfectly correlated slope and intercept ($\ell n\ \alpha$ and $\ell n\ K_s$). Their envelope has the shape of a hyperbole. On the bottom part of the figure, the case of perfect independence between $\ell n\ \alpha$ and $\ell n\ K_s$ is represented in the same fashion. There is no well-defined envelope in this case. Figure (2.2) of Chapter 2 suggests that a reasonable description of natural conductivity variability stands somewhere between these two cases. Admittedly, more work is needed to refine these simplified representations of unsaturated soil variability (see discussion of field data in Chapter 2).

Let us now comment briefly on our choice of some of the other data of Table 7.1, in relation with numerical and statistical issues. First of all, observe that the statistical

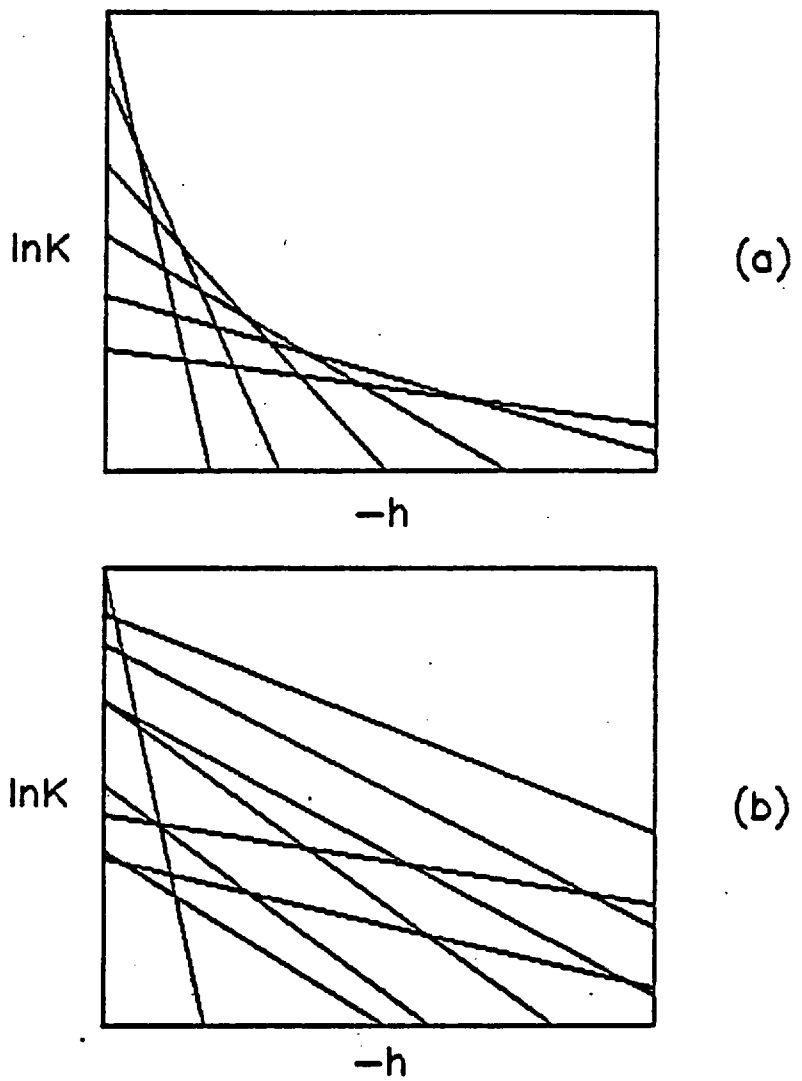

Figure 7.2 Schematic representation of unsaturated log-conductivity variability in two cases. On top, the parameters $\ell n\ K_s$ and $\ell n\ \alpha$ are perfectly correlated (Case 2 in the text). On bottom, they are perfectly uncorrelated (Case 3 in the text).

resolution of the grid is moderate:

$$\frac{\Delta x_i}{\lambda_i} = \frac{1}{2},$$

and isotropic in space (same in all directions). Second, note that the Peclet number constraint:

$$Pe = \alpha \Delta x_i \lesssim 2$$

which arose as a "nonlinear stability condition" in Chapter 5 (section 5.4.2, equation 5.128) seems to be satisfied if α is replaced by its geometric mean value α_G. Thus, we obtain for the α_G of Table 7.1:

$$\overline{Pe} = \alpha_G \cdot \Delta x_i = 0.9 \lesssim 2.$$

The procedure used to control the size of the variable time step was described in Chapter 5 (section 5.4.3). In no case was the time step allowed to grow at a rate faster than $\Delta t_{n+1}/\Delta t_n = 1.25$. The initial time step size was $\Delta t_{in} = 0.003$ day (4mm 20 sec). Infiltration lasted for about 3 days, after which the simulation was halted. The results shown in this section were obtained with a fixed domain size, but similar results were also obtained by using the variable domain size algorithm (see Figures 5.11-5.13 of Chapter 5). Finally, it

is worth noting that the size of the domain is relatively small: the "sample size" L_i/λ_i is 7 in the vertical, and 20 in both horizontal directions. The infiltration experiment was stopped at $t = 3$ days because the flow domain was too small to approximate a "semi-infinite" medium for larger times. The selected output times were $t = 0.5$, 1.0, 2.0 and 3.0 days. The resulting three-dimensional pressure head fields are being analyzed below.

7.2.2 Simulation results

We now discuss the simulation results (pressure head fields) obtained for the three cases of unsaturated conductivity variability described above (equations 7.4, 7.5, 7.6 and Figure 7.2). The geometry and boundary conditions were illustrated in Figure 7.1, and the complete set of input data was given in Table 7.1. Recall in particular that the initial pressure h_{in} was -150 cm.

Figures 7.3, 7.4 and 7.5 give three-dimensional views of a single pressure contour surface obtained after two days of infiltration. These figures show essentially the shape of the wet zone ($h \geq -90$ cm) in perspective view. Figure 7.3 corresponds to K_s random and α constant (case 1), Figure 7.4 to $\ell n\, K_s$ and $\ell n\, \alpha$ random but perfectly correlated (case 2),

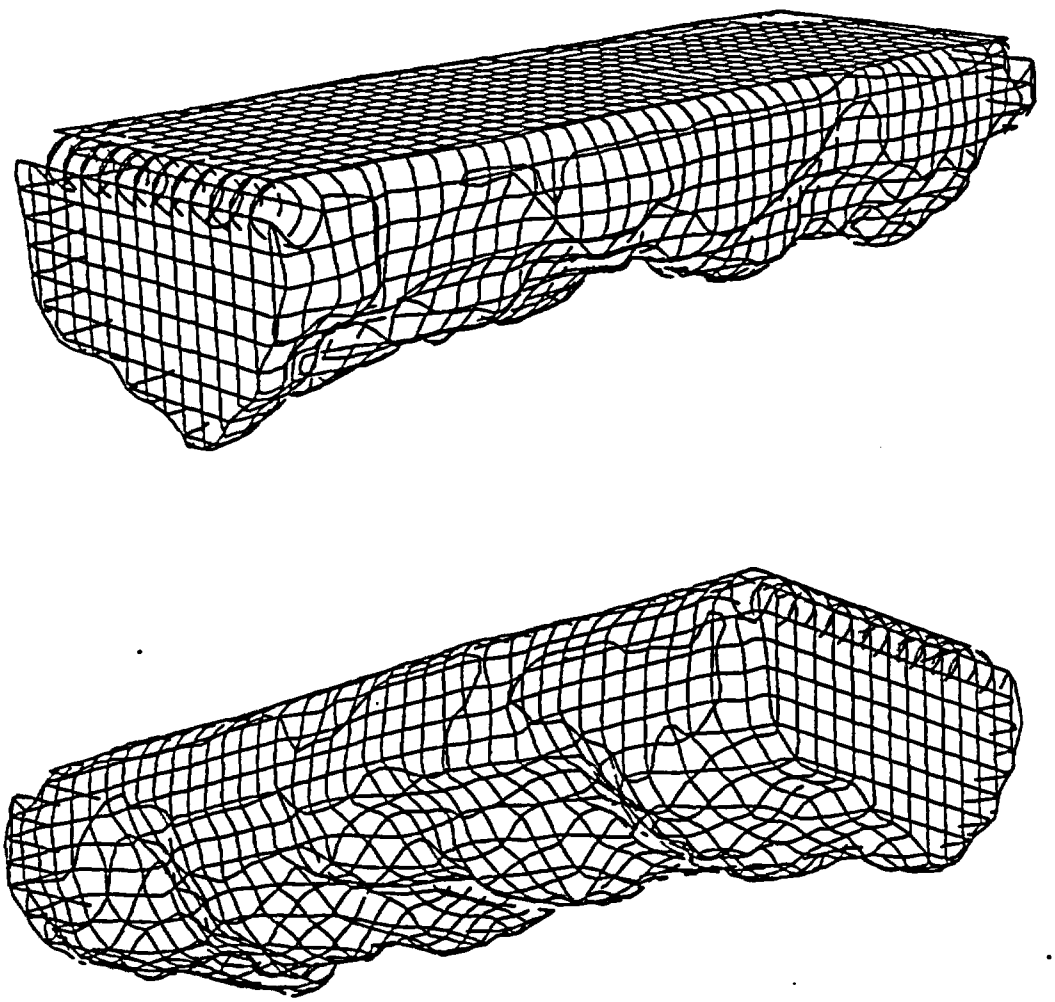

Figure 7.3: Two perspective views of the pressure contour surface h = - 90 cm at t = 2 days for strip-source infiltration in a statistically isotropic soil with initial pressure h_{in} = - 150 cm (Case 1: K_s random, α constant)

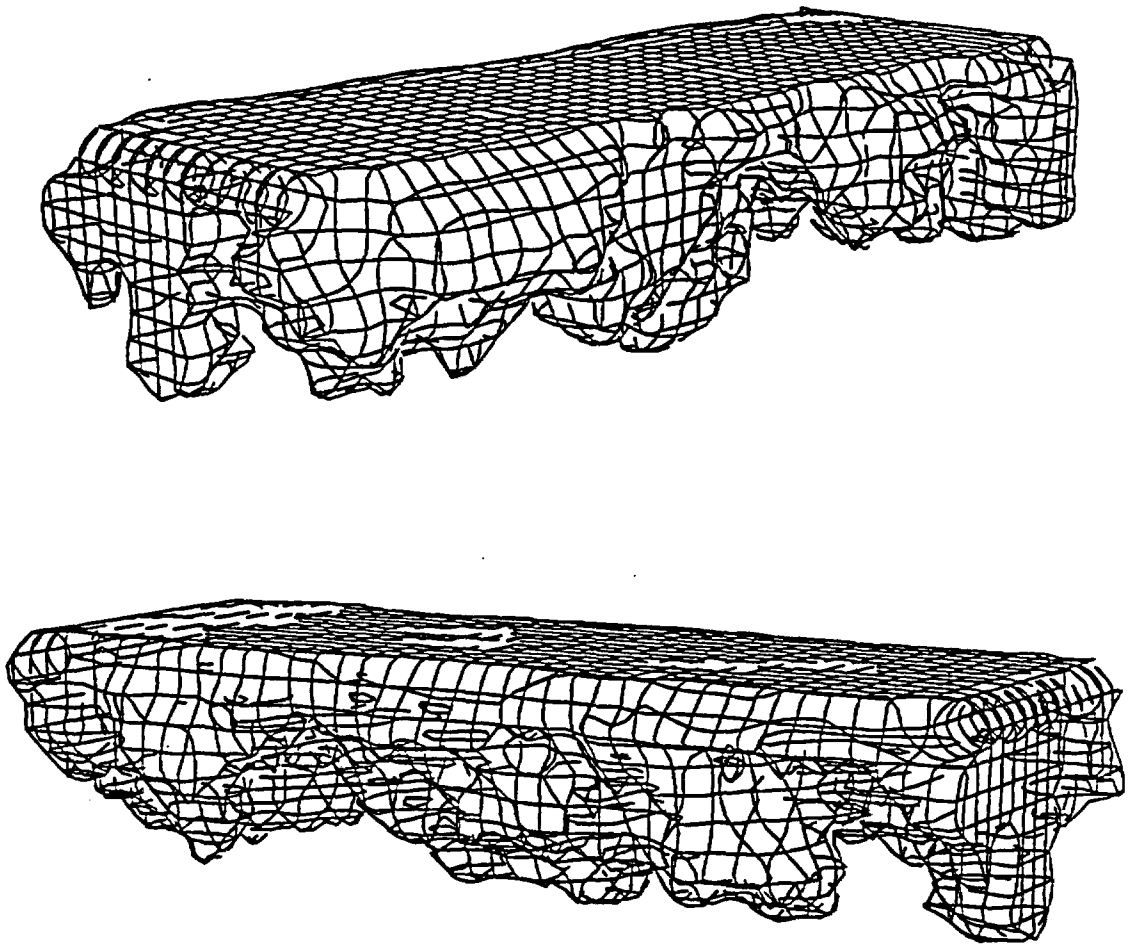

Figure 7.4 Two perspective views of the pressure contour surface $h = -90$ cm at $t = 2$ days for strip-source infiltration in a statistically isotropic soil with initial pressure $h_{in} = -150$ cm (Case 2: K_s and α random, perfectly correlated).

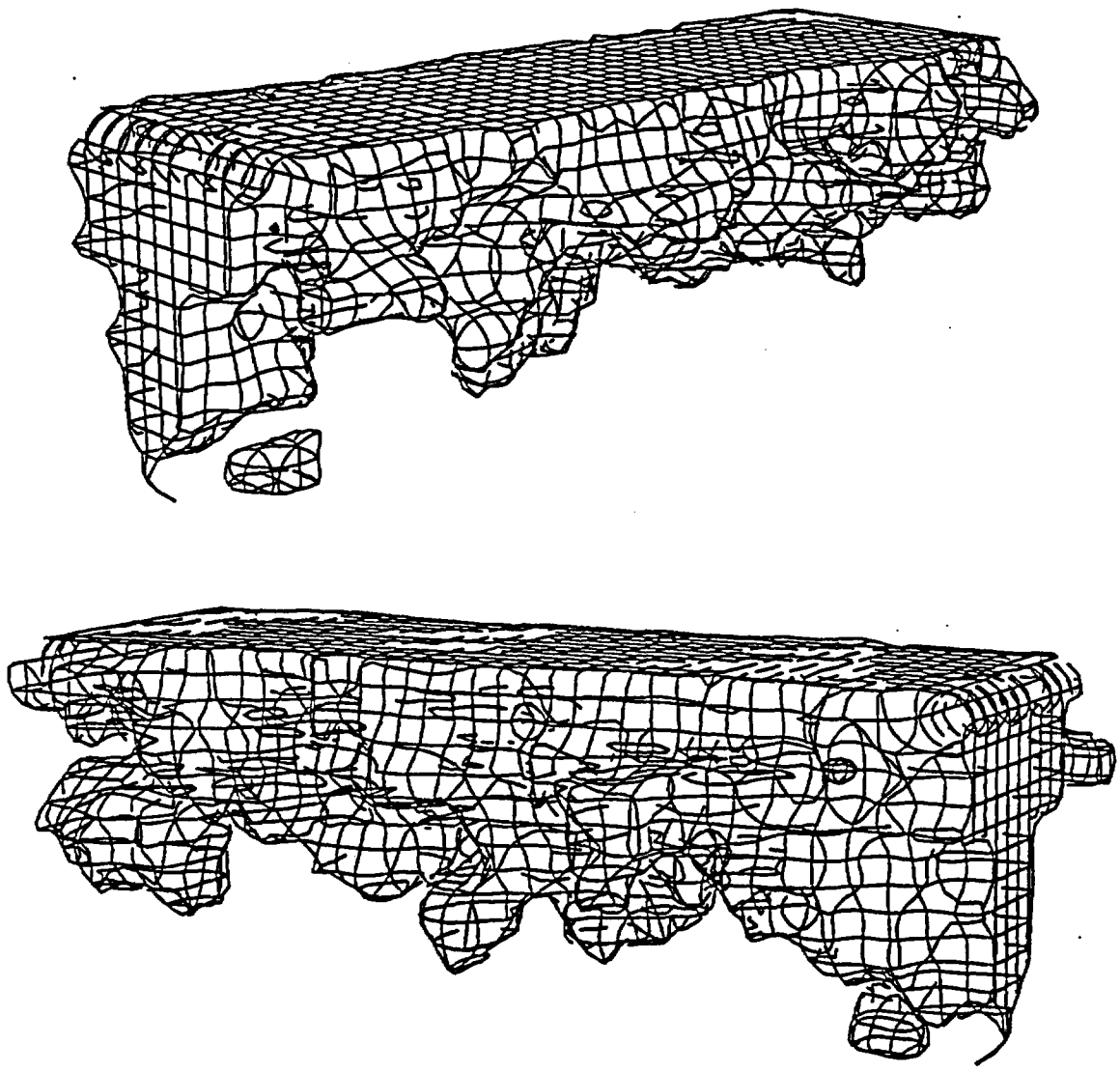

Figure 7.5 Two perspective views of the pressure contour surface h = - 90 cm at t = 2 days for strip-source infiltration in a statistically isotropic soil with initial pressure h_{in} = - 150 cm (Case 3: K_s and α random, perfectly independently).

and Figure 7.5 to $\ell n\ K_s$ and $\ell n\ \alpha$ random and perfectly uncorrelated (case 3).

Comparing figures 7.3 and 7.4 (cases 1 and 2) clearly shows that the variability of the log-conductivity slope (α) plays a more important role than the variability of the saturated conductivity (K_s). Despite the relatively small variability of α in Figure 7.4 ($\sigma_{\ell n\ \alpha} = 0.3$) the shape of the wet zone is much more contorted than in Figure 7.3 where only K_s is variable ($\sigma_{\ell n\ K_s} = 0.7$). Furthermore, comparing figures 7.4 and 7.5 (cases 2 and 3) indicates that the spatial variability of the wet zone is increased further when α is allowed to vary independently from $K_s(\underline{x})$. In the latter case (Figure 7.5) the wet zone at $t = 2$ days appears to be extremely contorted, and even disconnected. This indicates that soil heterogeneity can induce the creation of local wet regions entirely surrounded by dryer regions, at least in the transient flow regime.

Some of these observations are also illustrated by Figure 7.6, which depicts the pattern of pressure head contours in a vertical plane transverse to the strip-source for the three cases discussed above. Note the separation of the wet plume in two distinct plumes on the bottom part of Figure 7.6 (case 3, $K_s(x)$ and $\alpha(x)$ independent). The two "halves" of the wet plume could perhaps reconnect at a later time. Incidentally, our

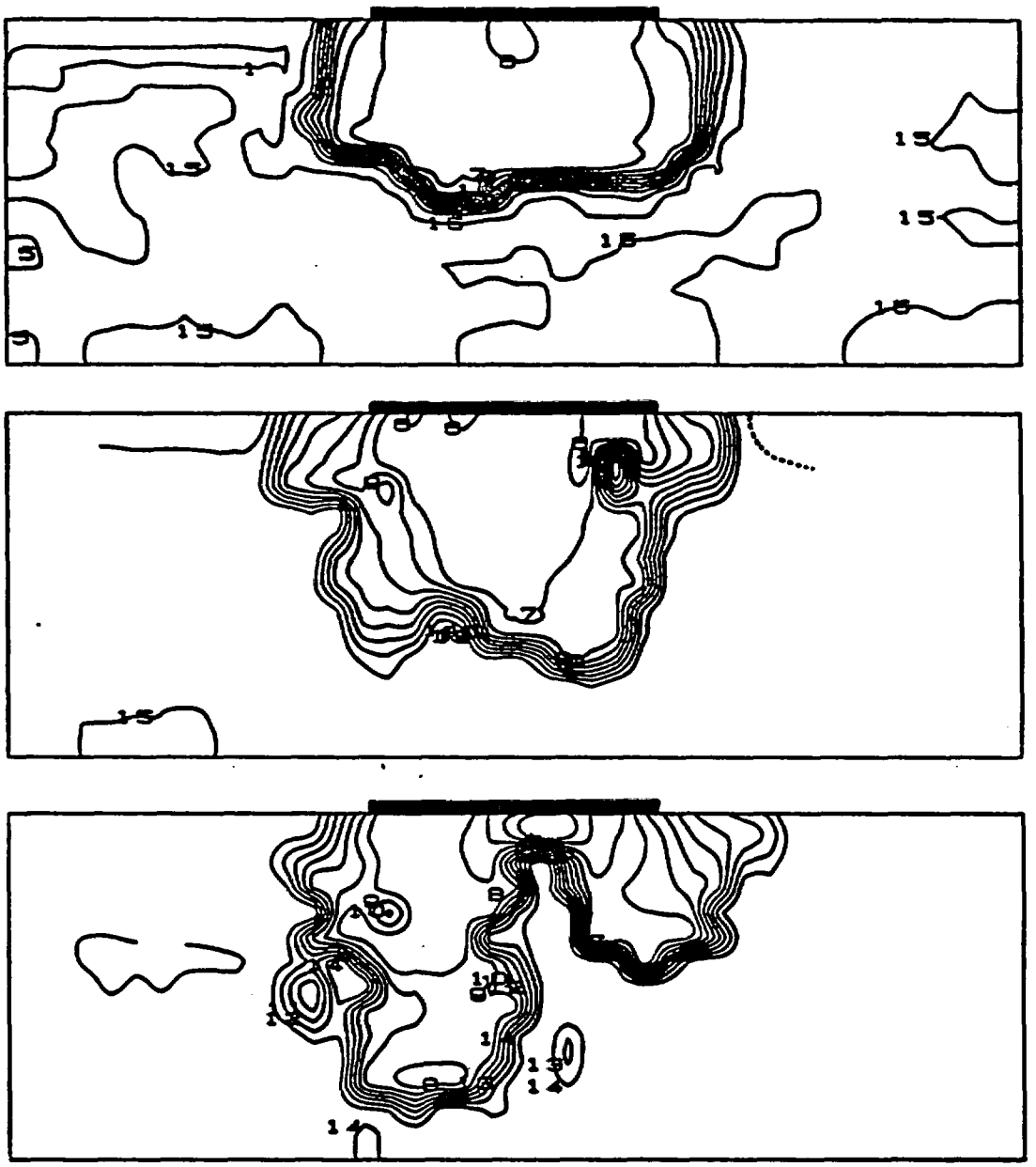

Figure 7.6 Pressure head contour lines in a vertical plane transverse to the strip source for cases (1), (2), (3) as in Figures (7.3), (7.4), (7.5). The pressure contours are labelled every 10 cm, e.g., contour #6 corresponds to - 60 cm, and contour #9 to - 90 cm.

choice of the value h = -90 cm to represent the 3D pressure surfaces in the previous plots, was motivated by the fact that this value corresponds fairly well to the wetting fronts appearing in the 2D contour maps of Figure 7.6. The wetting fronts are sharply defined in all three cases, as could be expected for early times of infiltration in a relatively dry soil.

Overall, these pictures clearly show that the pressure field becomes increasingly variable and "chaotic" as the log-conductivity slope $\alpha(\underline{x})$ becomes more variable and independent of $K_s(\underline{x})$. When α is constant, the variability of $K_s(x)$ produces only mild variability of the unsaturated pressure field. When $\alpha(\underline{x})$ is variable, the unsaturated plume develops mushroom-shaped regions oriented downwards, especially in the longitudinal direction (as can be seen from Figures 7.4 and 7.5), but also in the transverse direction (Figure 7.6 bottom). The size of these "mushrooms" seems to be on the order of 0.6-1.0 m, or about 3-5 correlation scales (λ = 0.2 m).

These observations lead us to think that the typical scale of fluctuation of the pressure field could be on the order of 1 meter, or 5 correlation scales. However, the pressure fluctuations are too large, and the domain too small, to permit a meaningful statistical analysis in the case of random $\alpha(\underline{x})$.

Furthermore, it is not clear how the length and width of the strip influence the flow pattern at early times. It seems possible that the width of the strip imposes a definite length scale to the fluctuating pressure field, both in the longitudinal and transverse directions (in the present case, the strip width is 1.1 m, or 5.5 correlation scales). At any rate, the influence of the strip source width could be considerably reduced for large times of infiltration and large wet zones, as far as the fluctuation scales are concerned.

To verify these conjectures would require simulations on larger domains, and for larger times of infiltration. The transverse size of the domain should be taken larger in order to avoid interactions between the wet zone and the lateral (no-flow) boundaries as the unsaturated plume evolves. In addition, the length of the strip should be taken much larger than the typical fluctuation scale of the pressure field in order to obtain meaningful spatial moments by longitudinal averaging (i.e., by averaging in the direction of statistical homogeneity as illustrated in Figure 7.1). It seems reasonable to require that the strip length be at least 10^2-10^3 pressure correlation scales. For a grid resolution $\Delta x/\lambda$ equal to one-half, and assuming a pressure fluctuation scale on the order of 5λ, this would lead to 10^3-10^4 mesh points *in the longitudinal direction*. In comparison, there were only 41 nodes along the strip length in

the case at hand, and a total of 25,000 nodes in 3D space. To obtain statistically meaningful large-time solutions (in the sense defined above) would therefore require a three-dimensional grid size of *at least* 1-10 million nodes for the isotropic case at hand, and probably even more for the anisotropic case.

In this discussion, we assumed implicitly that a mesh size equal to one-half the correlation scale of input hydraulic properties provided adequate resolution. It may be instructive to examine the grid resolution problem more closely here. Inspection of the pressure contours shown in Figure 7.6, suggests that the 10 cm mesh was perhaps too coarse to resolve the smallest scales of fluctuations of the pressure field (see the rectangular and straight-line shapes of the pressure contour fluctuations at the small scale). This is even more apparent in the pressure contour plot of Figure 7.7, which represents the pressure field in the vertical plane coinciding with the longitudinal axis of the strip source (case 1: $\ell n\, K_s$ and $\ell n\, \alpha$ perfectly correlated). This indicates that grid resolution may have to be refined further, especially in view of analyzing the flux vector field and the related convection-dispersion pattern of a contaminant carried in the flow.

On the other hand, the chosen grid resolution of one half was perhaps fine enough to obtain a reasonably accurate

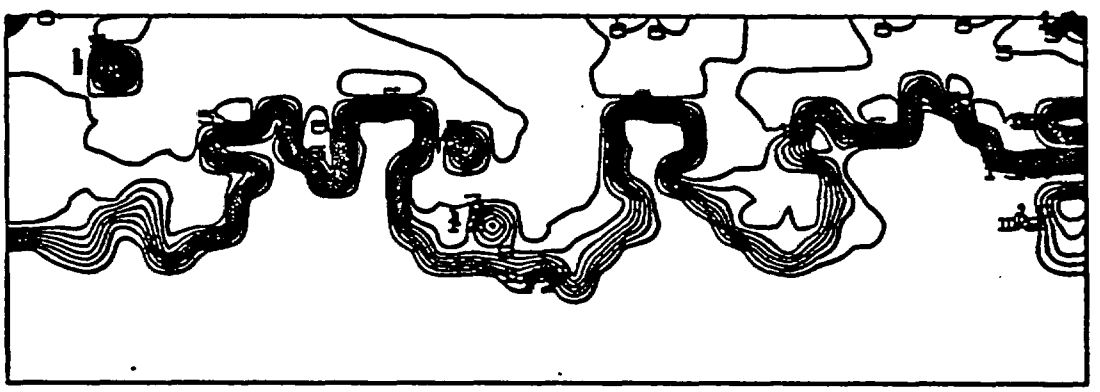

Figure 7.7 Pressure head contour lines in a vertical plane parallel to the strip source for case (2) as in Figure (7.4). The pressure contours are labelled every 10 cm, e.g., contour #6 corresponds to -60 cm, and contour #9 to -90 cm.

picture of pressure variability. The numerical experiments of Chapter 5 with uniformly layered soils showed that the mesh size could be taken equal to layer thickness without distorting the overall pattern of the pressure fields (see Figures 5.23, 5.24 and 5.25 of Chapter 5, section 5.4.3). There is also the remaining constraint of a low Peclet number, or small vertical mesh size, that must be satisfied in order to avoid instabilities. There were no particular instability problems in the case at hand.

7.3 Strip Source Infiltration in a Statistically Anisotropic Soil (300,000 nodes)

7.3.1 Model problem and input data

[a] - Overview of data

In this section, we present the results of a single-realization simulation of strip source infiltration in a more realistic case than before. The soil data, geometry, and boundary conditions were chosen to mimick an on-going "trench experiment" at the New Mexico State University College Ranch of Las Cruces, New Mexico (Wierenga, Gelhar et. al. 1986, and Wierenga, Porro et. al. 1986). The major differences with the simulations of the previous section are the following:

-- the strip source does not span the whole length of the computational domain
-- the soil is *statistically anisotropic*, with a larger correlation scale in the horizontal than in the vertical.
-- the space-time scales of simulation are relatively large (5 m x 15 m x 15 m and 20 days)
-- both the infiltration phase and the *natural drainage after the end of infiltration* are being simulated (10 days of infiltration followed by 10 more days of drainage).

Figure 7.8 shows a schematic representation of the computational flow domain in perspective view. Its size is 5 m in the vertical, and 15 m in both horizontal directions. However, note that the strip source only extends over a length of 9.8 m in the longitudinal direction (4 m in width). The vertical plane in the forefront represents the face of the trench in the experimental set-up of Wierenga et al. (1986). This was approximated as a "no-flow" boundary in our simulation, despite evidence that some evaporation actually occured in the field experiment. The other vertical faces of the domain were assumed also to be "no-flow" boundaries; they did not seem to interfere with the infiltration and drainage processes at the time scale of the simulation. The bottom boundary, however, was not deep

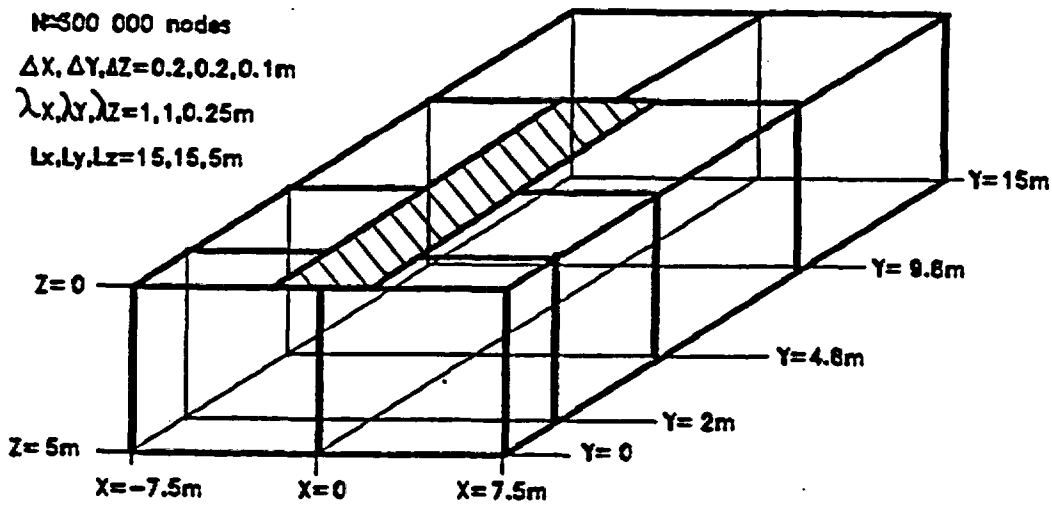

Figure 7.8 Schematic representation of the flow domain geometry for the 300,000 node simulation of strip-source infiltration in a statistically anisotropic soil ("trench experiment"). The numerical solution was sampled along certain slices (Y = 2, 4.8, 9.8m and X = 0).

enough to avoid interactions with the evolving wet zone during the last part of the drainage phase (more on this later). The flux at the surface of the strip was 2 cm/day during infiltration, and zero during the redistribution phase. A zero flux was imposed over the remaining part of the soil surface at all times.

Table 7.2 summarizes the input data used for the *simulated* "trench experiment" just described, including geometry, initial and boundary conditions, space-time discretization, and hydraulic properties of the hypothetically random soil. Some of these data were chosen in accordance with available field observations or were imposed by the experimental set-up (the infiltration experiment at the Las Cruces site was in fact designed in part for purposes of comparison with mathematical models like ours). However, some of the other data of Table 7.2 were only indirectly related to field observations, or were imposed by numerical constraints. The rationale behind the selected inputs shown in Table 7.2 is explained in more detail below for each category of data.

[b] Space-time discretization and computational issues

The three-dimensional mesh size was chosen as a compromise between the numerical constraints (Peclet number

TABLE 7.2
SUMMARY OF INPUT DATA FOR THE SINGLE-REALIZATION SIMULATION OF STRIP-SOURCE INFILTRATION IN A STATISTICALLY ANISOTROPIC SOIL ("TRENCH EXPERIMENT")

Type of Data	Description	Value
Domain Geometry, Boundary Conditions, and Initial Conditions	Vertical domain size	$L_1 = 5.0$ m
	Transverse horizontal domain size	$L_2 = 15.0$ m
	Transverse longitudinal domain size	$L_3 = 15.0$ m
	Strip source width	$W_s = 4.0$ m
	Strip source length	$L_s = 9.9$ m
	Flux at the surface of the strip	$q_o = 2$ cm/day
	Condition at the bottom boundary	$q_1 = -K(h)$
	Initial pressure head	$h_{in} = -150$ cm
Space-Time Discretization	Time step	Variable
	Mesh size Δx_i (i=1,2,3)	$\Delta x_i = 0.10, 0.20, 0.20$ m
	Unidirectional number of nodes n_i	$n_i = 52, 76, 76$
	Total number of nodes of 3D grid	$N = 300352$
Exponential Conductivity Curve (Random)	Geometric mean saturated conductivity	$K_G = 100$ cm/d
	Standard deviation of $\ell n\, K_s$	$\sigma_f = 0.6083$
	Geometric mean of the ℓn K-slope	$\alpha_G = 0.0494\ cm^{-1}$
	Standard deviation of $\ell n\, \alpha$	$\sigma_\alpha = 0.2202$
	Anisotropic correlation scales λ_i	$\lambda_i = 0.25, 1.0, 1.0$ m
Van-Genuchten Retention Curve (Deterministic)	Saturated moisture content	$\theta_s = 0.368$
	Residual moisture content	$\theta_r = 0.102$
	Scaling parameter	$\beta = 0.0334\ cm^{-1}$
	Shape factor (real number)	$n = 1.982$

constraint $\alpha\Delta x_i \ll 2$ in the vertical, and statistical resolution requirement $\Delta x_i/\lambda_i \ll 1$ in all three directions) and computational feasibility (total number of nodes on the order of 10^5-10^6 at most). In addition, we rejected any solution that would have resulted in a large discrepancy between Δx_1, Δx_2, Δx_3 by a factor of more than 2. Our choice Δx_i = (10 cm,20 cm,20 cm) seems to satisfy approximately all these requirements. Note that the statistical resolution of the grid in the vertical direction (2/5) is coarser than in the horizontal directions (1/5). There are 52 nodes in the vertical, and 76 nodes in each horizontal direction, resulting in a total of about 300,000 nodes in three dimensions.

On the other hand, the time-step was variable, typically on the order of 5 minutes initially, up to several hours towards the end of the drainage phase (t = 20 days). As a consequence, the computational work was mostly consumed by the early stages of the infiltration phase. For example, the simulation of the first quarter of the infiltration stage, from t = 0 to 2.5 days, consumed 1.5 hour of CPU time on a Cray 2 machine (NASA Ames Research Center). For the whole infiltration phase, t = 0 to 10 days, the computational work was about 4 CPU hours. Only one additional hour was consumed in the simulation of 10 days of natural drainage after the end of infiltration (t = 10 to t = 20 days). Therefore, the total computational

work was about 5 hours of Cray 2 CPU time for the whole 20 day simulation.

[c] Soil properties and spatial variability

As before, we assumed that the water retention curve $\theta(h)$ was deterministic, i.e. independent of spatial location. The $\theta(h)$ curve was assumed to follow the Van Genuchten relation (equation 7.2 in the previous section). The "mean" parameters of $\theta(h)$ were obtained by fitting the Van Genuchten function to a set of measured values $\theta_i(h_i)$ obtained from samples taken within the upper soil layer (0-75 cm). Figure 7.9 shows the data points and the fitted "mean" $\theta(h)$ curve, from Wierenga, Porro et al. (1986) and D. Polmann (personal communication).

The unsaturated conductivity was assumed to be an exponential function of pressure, as in equation 7.1 in the previous section, with random saturated conductivity $K_s(\underline{x})$ and random slope $\alpha(\underline{x})$ of the $\ell n\ K(h)$ curve. Furthermore, $\alpha(\underline{x})$ and $K_s(\underline{x})$ were assumed to be statistically independent (i.e. uncorrelated). This corresponds to "case 3" of the previous section (see bottom part of Figure 7.2), which produced a greater variability of the flow pattern than the case of perfect correlation. The standard deviations of $\ell n\ K_s$ was evaluated from field measurements and, indirectly, by relating the spatial

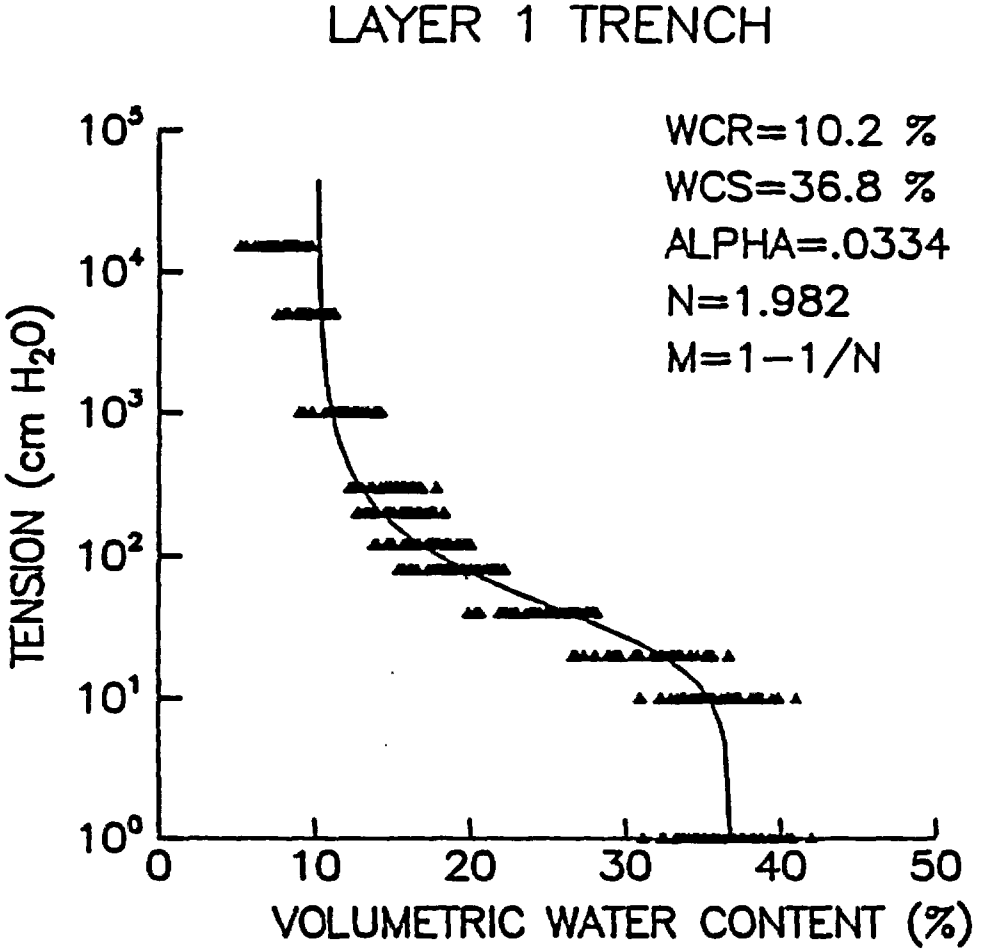

Figure 7.9 Water retention curve (tension versus volumetric moisture content) for the soil of the strip-source simulation ("trench experiment", Wierenga, et. al., 1986).

variability of K(h) to that of θ(h) through a conceptual model (Mualem-Van Genuchten). The latter procedure was also used to evaluate the standard deviation of $\ell n\alpha$, since *direct* measurements of $\ell n\alpha$ were not available. In addition, the geometric means K_G and α_G were evaluated indirectly by fitting a tangent straight-line to the Mualem-Van Genuchten log-conductivity function at K = 2 cm/day (value of the infiltration flux at the strip source) as shown in Figure 7.10. Note that the unsaturated conductivity values predicted by the two models are roughly in agreement (same order of magnitude) within the range of pressures $-150 \text{ cm} \leq h \leq -50 \text{ cm}$.

The $\ell n\ \alpha$ and $\ell n\ K_s$ random fields were assumed to be independent Markov fields with anisotropic correlation lengths $\lambda_1 = 0.25$ m, $\lambda_2 = \lambda_3 = 1$ m. These values were chosen based in part on variograms of $\ell n\ K_s$ measured in the field (Wierenga et al., personal communication). However, note that the same anisotropic correlation scales were used for $\ell n\alpha$, for which no data were available. Although there is a great part of subjectivity in this choice, it seems reasonable to assume the same anisotropy ratio ($\lambda_1/\lambda_3 = 1/4$) for both parameters of the conductivity curve. The turning band method was used to generate two independent realizations of the 3D anisotropic Markov random fields $\ell n\ K_s$ and $\ell n\ \alpha$ over the 300,000 node grid. In actual practice, two isotropic fields were generated, and the

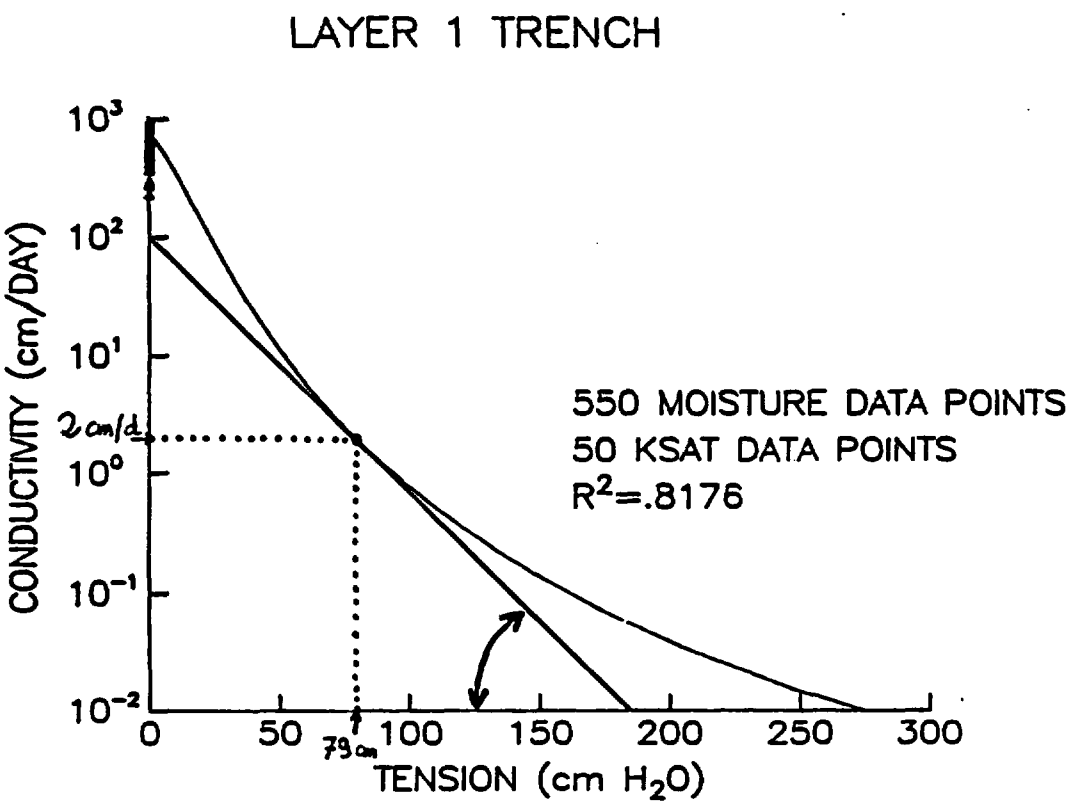

Figure 7.10 Mean unsaturated conductivity curve K(h) for the soil of the strip-source "trench experiment": the straight line corresponds to the exponential model actually used in the numerical simulation; the other curve is the Mualem-Van Genuchten model indirectly fitted to field data by Wierenga et. al., 1986.

desired anisotropy was obtained by rescaling the three coordinate axes (see Chapter 2, equation 2.18).

[d] Initial conditions:

Selecting an adequate initial condition in agreement with field observations proved to be a major difficulty, due to the restricted range of applicability of the exponential conductivity model used in the flow simulator. Field observations based on direct measurements of in-situ moisture contents suggested that the soil was initially very dry, near its residual moisture content (negative pressures on the order of 10^4 cm). However, preliminary numerical experiments with an initial pressure $h_{in} = -$ 300 cm, corresponding to $K_{in} = 3 \cdot 10^{-5}$ cm/day in the mean, showed that there was a severe restriction on the time step size in order to avoid divergence of the nonlinear system solver (nonlinear SIP, based on Picard iterations for linearization). The initial pressure was finally revised to a higher value $h_{in} = -$ 150 cm, corresponding to $K_{in} = 0.06$ cm/day in the mean.

For further reference, we give below a list of numerical values of some "mean" hydraulic properties corresponding to the *initial state* of the soil:

-- Pressure: $h_{in} = -150$ cm

-- Relative conductivity: $K_{in}/K_G = 0.6\ 10^{-3}$

-- Conductivity/flux ratio: $K_{in}/q_o = 0.03$

-- Moisture content: $\theta_{in} = 0.155$

-- Degree of saturation: $S_{in} = \frac{\theta_{in} - \theta_r}{\theta_s - \theta_r} = 0.20.$

Note that the soil is relatively dry, since only 20% of the porosity is initially filled with water. In addition, the following parameters may help evaluate, in different ways, the downward velocity of the wet zone:

-- Maximum pressure at the source: $h_{max} = -79.2$ cm

-- Maximum moisture content at the source: $\theta_{max} = 0.198$

-- Downward velocity (mass balance):

$$V = \frac{q_o - K_{in}}{\theta_{max} - \theta_{in}} = 20.2 \text{ cm/day}$$

-- Downward velocity (wetting front):

$$v = \left(\frac{dK}{d\theta}\right)_{in} = 8.8 \text{ cm/day}$$

The so-called maximum pressure h_{max} was evaluated by solving the equation:

$$K(h_{max}) = q_o$$

and the velocity v was evaluated by using the following

identities:

$$v = \left(\frac{dK}{d\theta}\right)_{in} = \alpha \left(K \frac{dh}{d\theta}\right)_{in} = \frac{\alpha K_{in}}{C_{in}}$$

In the case at hand, $\alpha = 0.0494\ cm^{-1}$, $K_{in} = 0.06$ cm/day, and $C_{in} = 0.00034\ cm^{-1}$. The result for v, given above, follows immediately. These relations are only intended to provide "order of magnitude" estimates of the downward velocity of the wet zone for mean values of the hydraulic parameters of the soil.

[e] Boundary conditions:

As stated earlier, all lateral boundaries were assumed impervious (including the face of the trench). The boundary conditions at the soil surface were a fixed flux ($q = q_o$ on the strip source, and $q = 0$ elsewhere). During infiltration the source flux was $q_o = 2$ cm/day. The condition at the bottom boundary was variable. During the early stages of infiltration, the moving boundary algorithm was used (see Chapter 5, section 5.4.3, Figure 5.11). However, this procedure proved to be inefficient, as the artificial bottom boundary moved rapidly downwards to reach the maximum prescribed depth (5m). After that time, a zero pressure gradient was imposed at the fixed bottom boundary:

$$\frac{\partial h}{\partial z} = 0 \rightarrow q = - K(h)$$

Since the initial conductivity was quite small (K_{in} = 0.06 cm/day, compared to q_o = 2 cm/day) the downward flux through the bottom boundary was essentially negligible as long as the wet zone had not reached that boundary (infiltration phase and part of the drainage phase). The influence of the zero-pressure gradient boundary during the passage of the downward moving wet zone will be discussed later, based on visual inspection of the simulated pressure field.

7.3.2 Simulation Results

[a] Infiltration Phase:

The simulated infiltration phase lasted for 10 days, at a specific discharge rate of q_o = 2 cm/day over the strip source. Given the width and length of the strip (4 m x 9.9 m) the total quantity of water applied to the soil was about 7.9 m^3 (2100 gallons). A simple calculation shows that, if this amount of water was distributed uniformly beneath the strip-source (*without lateral spread*) over a 4 meter deep layer, the increase in volumetric soil moisture in that region would be 0.05, which approximately brings the moisture content to its potential maximum (θ_{max}) as evaluated in the previous sub-section. The

corresponding degree of saturation in that region of soil would be 40%, compared to 20% initially, still a moderate amount. These preliminary considerations may give an idea of the meaning of the term "wet zone" in this case of relatively slow-rate infiltration. Indeed, the so-called "wet zone" will presumably be only moderately wet, i.e., quite drier than the saturation point on average. This should be kept in mind when the terms "wet zone" and "wetting front" are being employed in the sequel.

The simulated three-dimensional pressure head fields (300,000 nodal values) were saved at times 1.0, 2.5, 5.0, 7.5, 10, 15, and 20 days. A post-processor code was used to sample the three-dimensional pressure fields along certain slices (2D) and transects (1D). The location of some of the selected slices was outlined in Figure 7.8 above. Three vertical slices transverse to the strip source, and one vertical slice coinciding with the longitudinal axis of the strip, were selected in order to display the transverse and longitudinal pressure field patterns at different times of infiltration and drainage. In addition, certain transects were selected along these slices in order to display in a single graph the time evolution of unidirectional pressure profiles. Occasionally, we will also show the pressure pattern in a horizontal slice or along a horizontal transect located at a given depth. For clarity of

exposition, let us define below our terminology concerning the sampled slices and transects (see Figure 7.8):

-- X, Y, Z coordinates:

X = lateral coordinate (horizontal, transverse to strip)

Y = longitudinal coordinate (horizontal, parallel to strip)

Z = vertical coordinate (depth below soil surface)

-- "Transverse" slices:

Vertical slices transverse to the strip source:

Y = 2 m (near trench face)

Y = 4.8 m (mid-point along the strip)

Y = 9.8 m (free edge of the strip)

-- Vertical transect:

Vertical transect located in the transverse slice Y = 4.8 m, and passing approximately through the geometric center of the strip (X = 0, Y = 4.8 m)

-- "Longitudinal" slice:

Vertical slice parallel to the strip and coinciding with its longitudinal axis of symmetry (X=0)

-- "Longitudinal" transect:

Horizontal transect lying in the horizontal slice X = 0, at some specified depth Z.

-- "Transverse" transect:

Horizontal transect lying in the transverse slice Y = 4.8 m, at some specified depth Z.

-- Horizontal slice:

Horizontal slice located at some specified depth Z (Z = 0.5 m: "shallow"; Z = 2.0 m: "deep").

A fairly representative picture of the three-dimensional pressure field can be obtained by looking at the pressure contours in three different "transverse slices" on the same page. This is shown in Figures 7.11, 7.12, 7.13, and 7.14 at times t = 5 days, t = 10 days, t = 10 + 5 days, and t = 10 + 10 days, respectively. A general observation that can be made is that the lateral *edges* of the wetted zone have a propension to spread laterally (see the contour line h = -125 cm during infiltration, or h = -70 cm during drainage). In contrast, there are some isolated (disconnected?) wet regions of high pressure which seem to be quite stable throughout the process of infiltration and drainage. A localized region of high pressure can be observed just beneath the center of the source

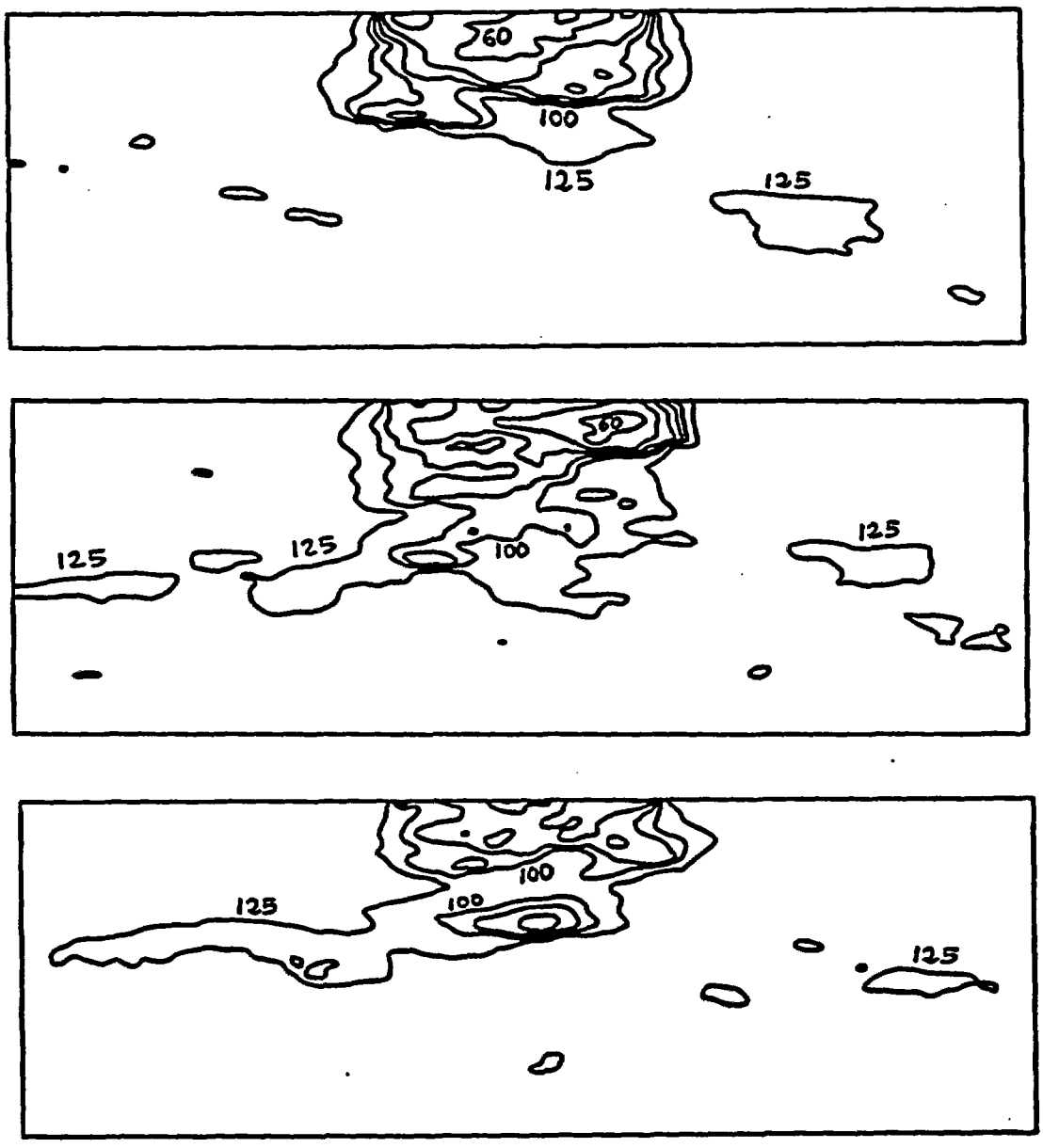

Figure 7.11 Contour lines of pressure head in three vertical-transverse slices during the simulated strip-source experiment after 5 days of infiltration (t=5 days). From top to bottom: Slices Y = 2m, Y = 4.8m, Y = 9.8m.

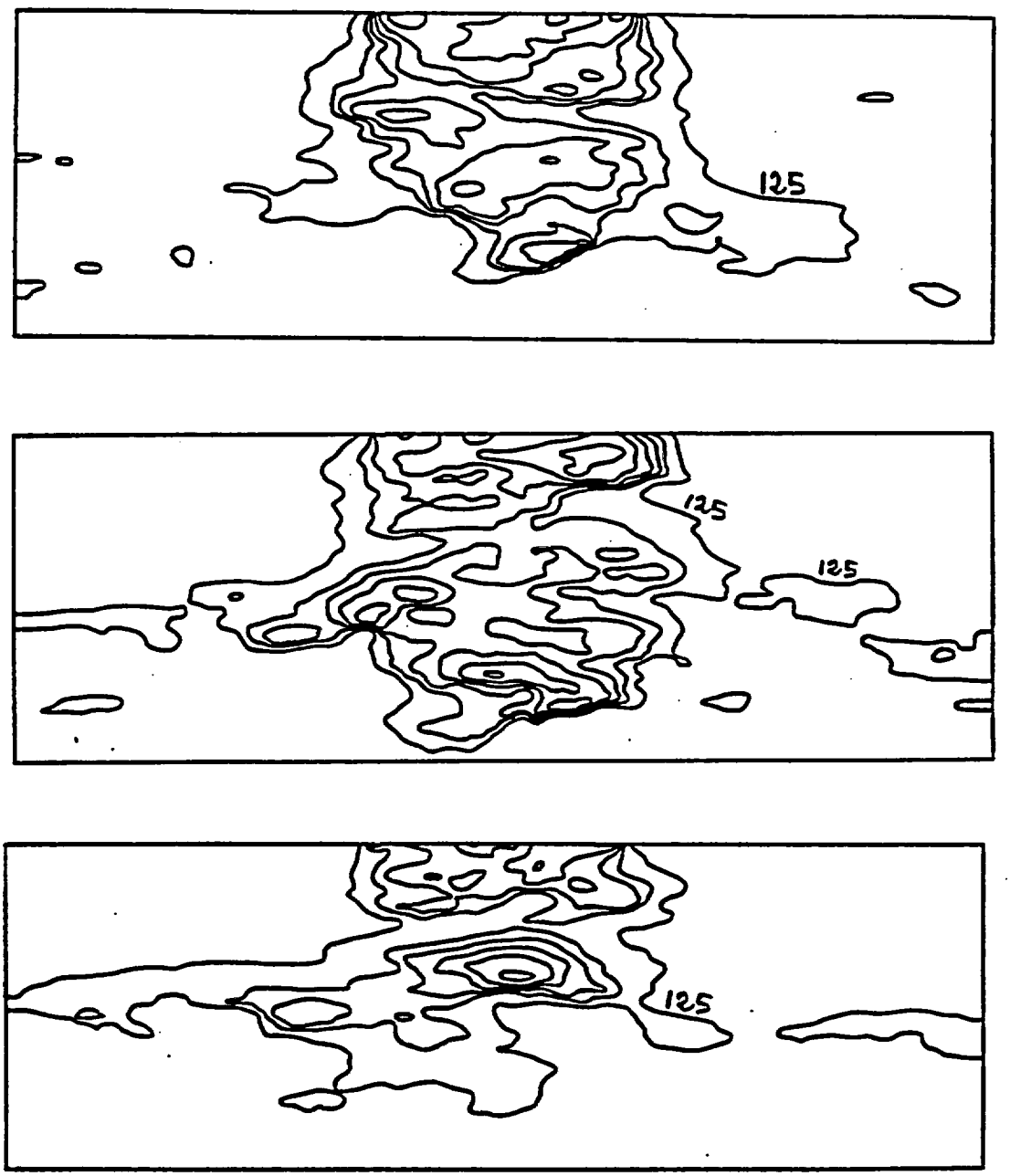

Figure 7.12 Contour lines of pressure head in three vertical-transverse slices during the simulated strip-source experiment after 10 days of infiltration (t = 10 days). From top to bottom: slices Y = 2m, Y = 4.8m, Y = 9.8m.

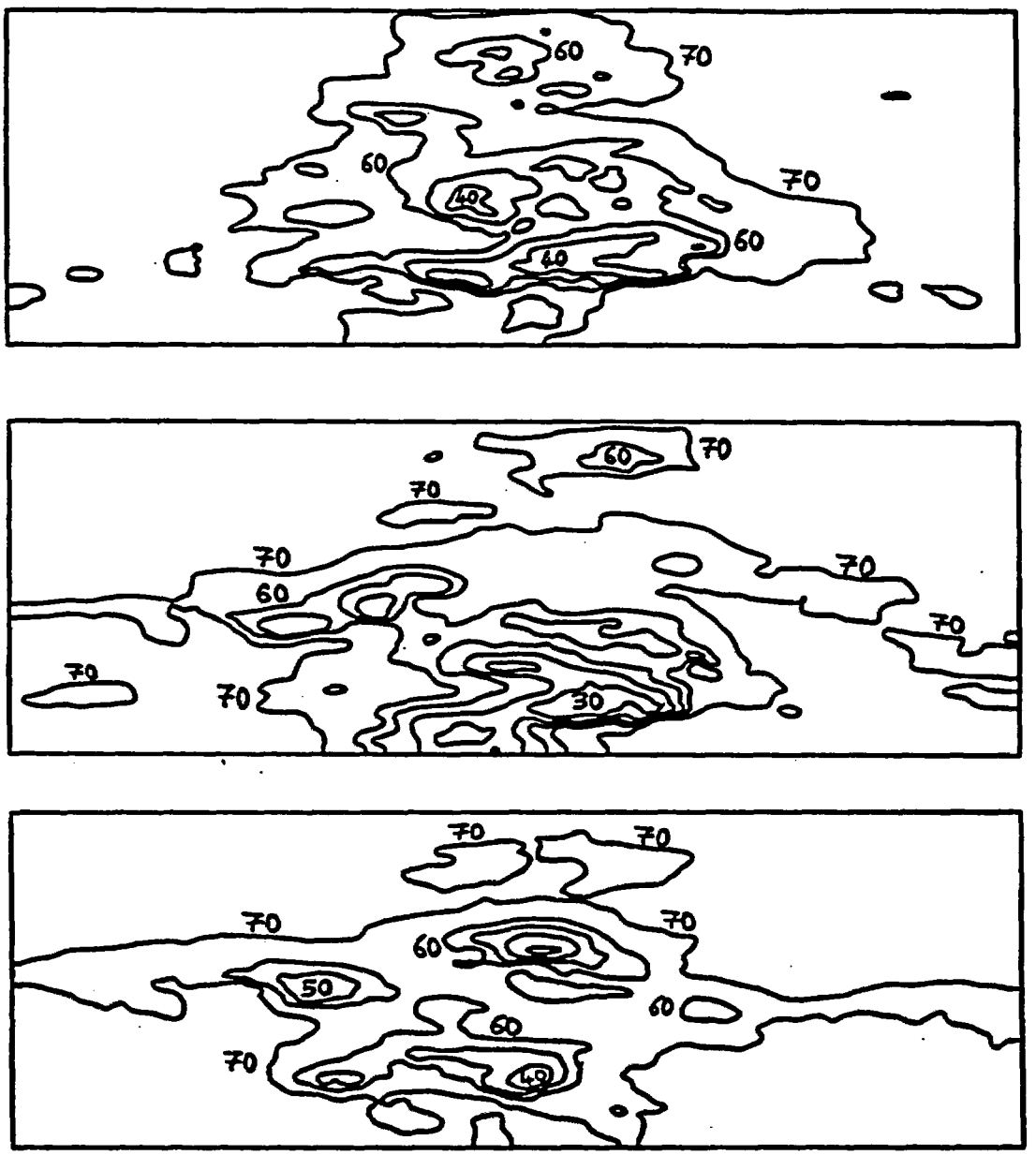

Figure 7.13 Contour lines of pressure head in three vertical-transverse slices during the simulated strip-source experiment after 10 days of infiltration and 5 days of drainage (t = 15 days). From top to bottom: slices Y = 2m, Y = 4.8m, Y = 9.8m.

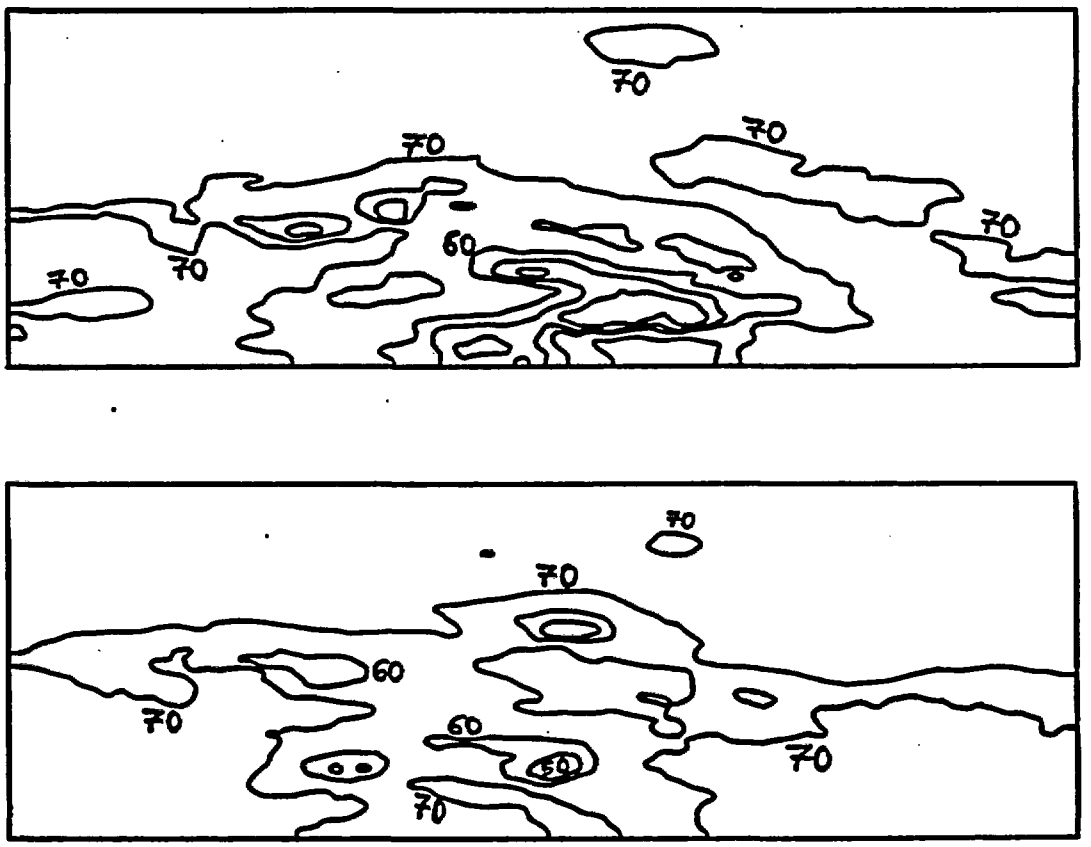

Figure 7.14 Contour lines of pressure head in three vertical-transverse slices during the simulated strip-source experiment after 10 days of infiltration and 10 days of drainage (t = 20 days). From top to bottom, slices Y = 4.8 m and Y = 9.8m.

(approximately 2 m deep) in the bottom parts of figures 7.11 through 7.14. Overall, these pictures leave the impression that the stratified structure of the soil (i.e., the statistical anisotropy of the conductivity curve) produces a differentiated anisotropy of the wetted zone, with a more pronounced lateral spreading of soil moisture in marginally wet regions than in the core of the wetted zone.

The evolution of the wetted zone can be followed by looking at a single "transverse slice" at successive times, as depicted in Figure 7.15. The pressure contours are shown at times t = 5 days, t = 10 days, and t = 10 + 5 days (from top to bottom) for the "transverse slice" located near the free edge of the strip source (Y = 9.8 m). During infiltration, the flow pattern beneath the strip source seems to be quasi-one dimensional down to a depth of approximately one meter, below which lateral spreading takes place. The same feature can also be observed at other locations along the strip (see previous figures 7.11-7.14). During the drainage phase, the wet region just beneath the strip source moves downward, and diffuses away laterally as well.

It may be also instructive to examine the evolution of the wetted zone in a longitudinal slice. This is shown in Figure 16 at three different times during infiltration and

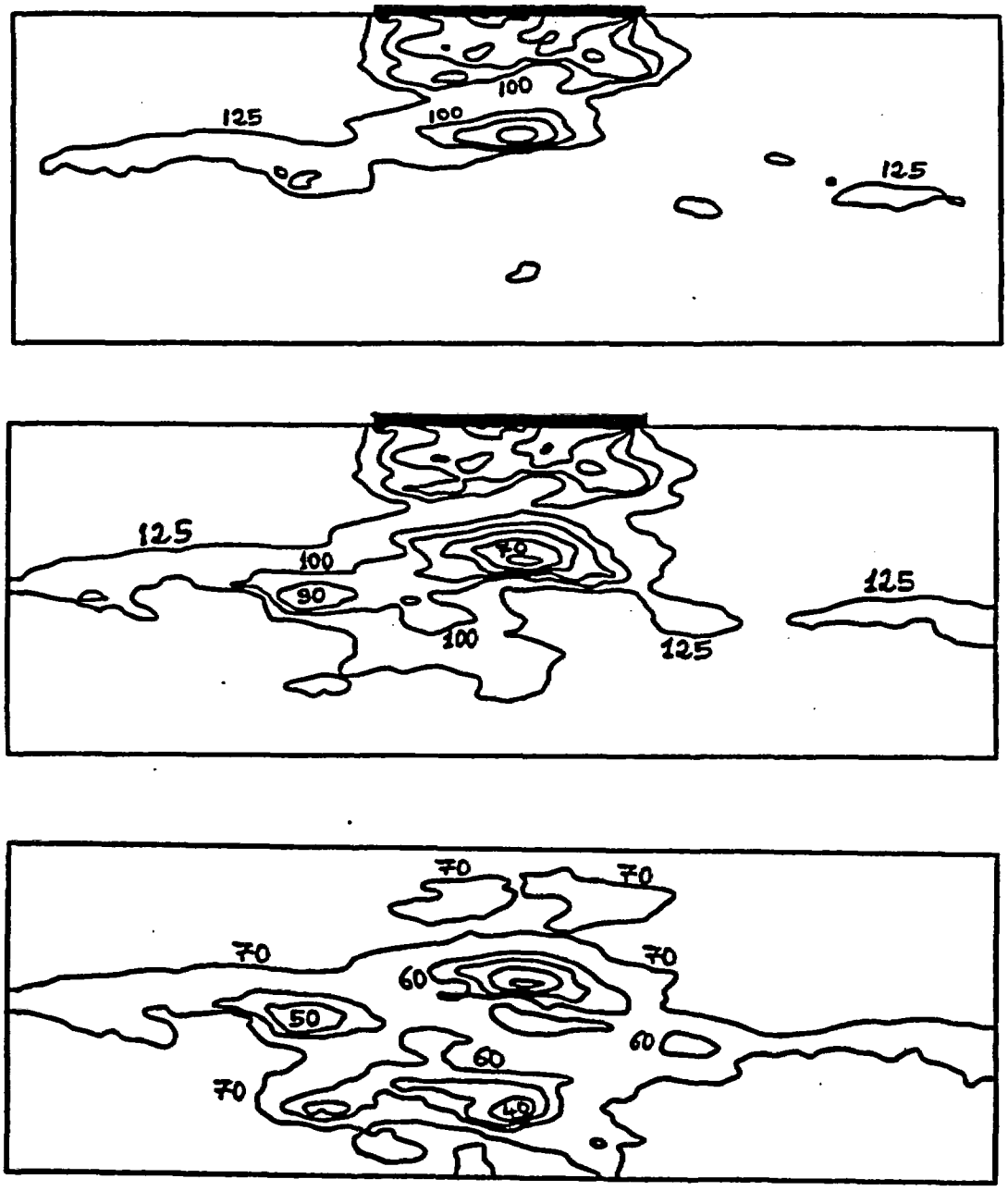

Figure 7.15 Contour lines of pressure head in the vertical-transverse slice located near the free edge of the strip (Y = 9.8 m) at three different times. From top to bottom: t = 5 days, t = 10 days, and t = 15 days (10 days infiltration + 5 days drainage).

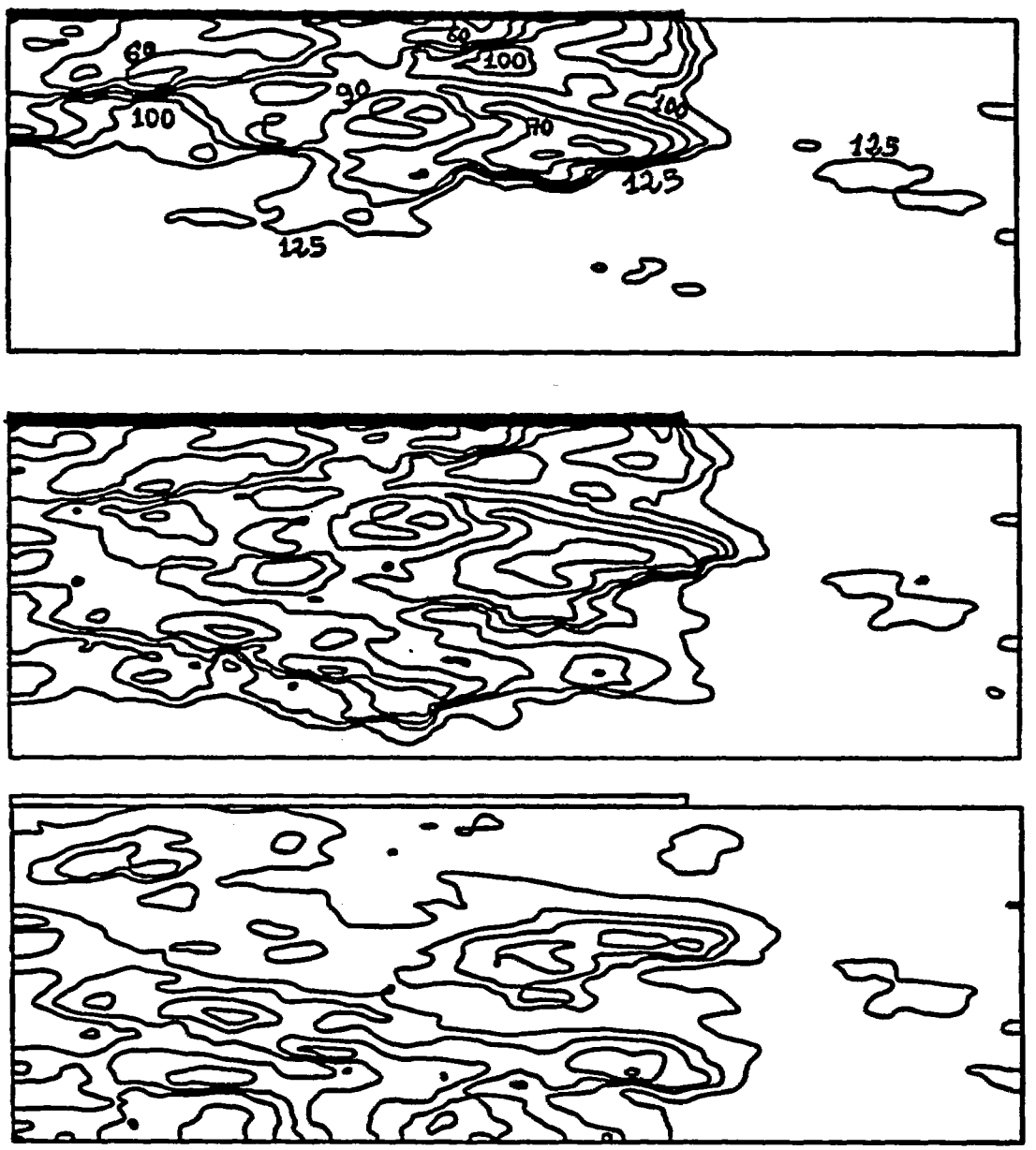

Figure 7.16 Contour lines of pressure head in the vertical-longitudinal slice (X= 0) at three different times. From top to bottom: t = 5 days, t = 10 days, and t = 15 days (10 days infiltration and 5 days drainage).

drainage, for the vertical-longitudinal slice coinciding with the axis of symmetry of the strip . This figure illustrates the complex three-dimensional nature of the flow system. In a homogeneous soil, the flow pattern along the strip (from left to right on Figure 7.16) would be quasi uniform, except for a possible edge effect on the free end of the strip (right part of the graphs). This edge effect, i.e., diffusion of moisture away from the free edge of the strip, seems to be minimal during infiltration, but more pronounced during natural drainage. In any case, the influence of vertical/horizontal anisotropy appears once again to be quite important, as can be seen from the elongated shape of pressure contour lines below the strip. Note that the length of the strip is only ten times larger than the horizontal correlation scale λ of $\ell n\, K_s$ and $\ell n\, \alpha$, i.e. much too short for a statistical analysis of the (presumably homogeneous) longitudinal fluctuations of pressure.

To complete our visual representation of the three-dimensional pressure pattern, we show in Figure 7.17 (a) and (b) the pressure contour lines in two horizontal slices, located respectively at depth Z = 0.5 m and Z = 2.0 m, during the drainage phase (time t = 15 days). These figures should be compared to the vertical-longitudinal pressure map of Figure 7.16 at the same time t = 15 days. The horizontal pressure map obtained at shallow depth Z = 0.5 m (Figure 7.17a)

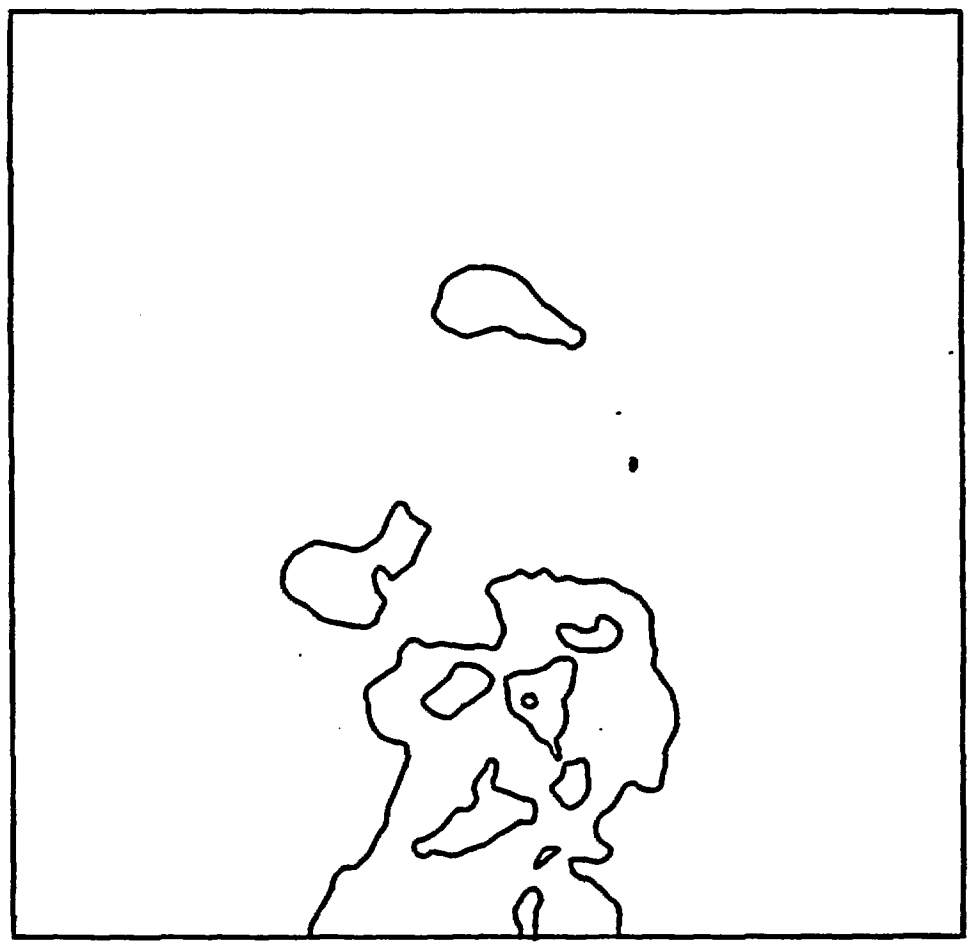

Figure 7.17 (a) Contour lines of pressure head in a horizontal slice at shallow depth Z = 0.5 m. Time t = 15 days (10 days of infiltration and 5 days drainage).

Figure 7.17 (b) Same as (a), for a horizontal slice at a larger depth Z = 2.0m.

is not surprising in view of the previous figure. For the larger depth Z = 2.0 m (Figure 7.17 b), the horizontal pressure map reveals previously unnoticed features: non-symmetric spreading of the relatively "dry" part of the moisture plume in the transverse direction, compared to the nearly axi-symmetric pattern of "wet" pressure contours. It is not clear whether these features are due to a three-dimensional edge effect, or merely to the particular soil heterogeneity below the free edge of the strip at that depth.

Finally, it is also instructive to examine the evolution of pressure profiles along selected transects in the vertical, transverse, and longitudinal directions. This is shown in the following figures: vertical pressure profiles during the infiltration phase (Figure 7.18) and the drainage phase (Figure 7.19); horizontal-transverse pressure profiles during the drainage phase at depth 0.5 m and 2.0 m (Figure 7.20 (a) and (b)); and horizontal-longitudinal pressure profiles during the drainage phase at depths 0.5 m and 2.0 m (Figure 7.21 (a) and (b)).

The vertical pressure profiles of Figure 7.18 depict the downward movement of the local "wetting front" at that particular location. A simple calculation shows that the downward velocity of the front decreased with time, from

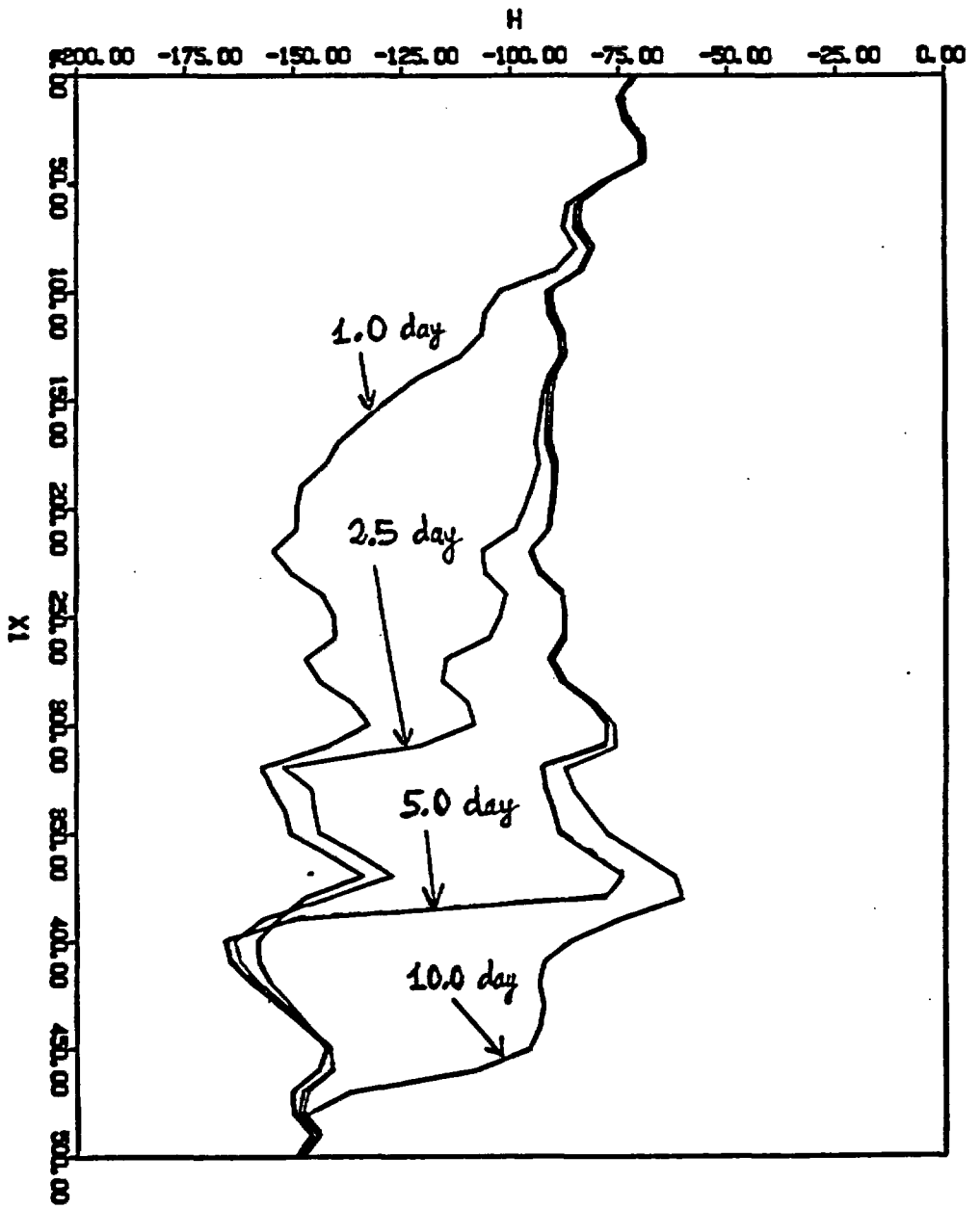

Figure 7.18 Pressure head profiles in the vertical direction during infiltration (times t = 1.0, 2.5, 5.0 and 10 days). The vertical transect is located near the geometric center of the strip (X=0,Y=4.8m).

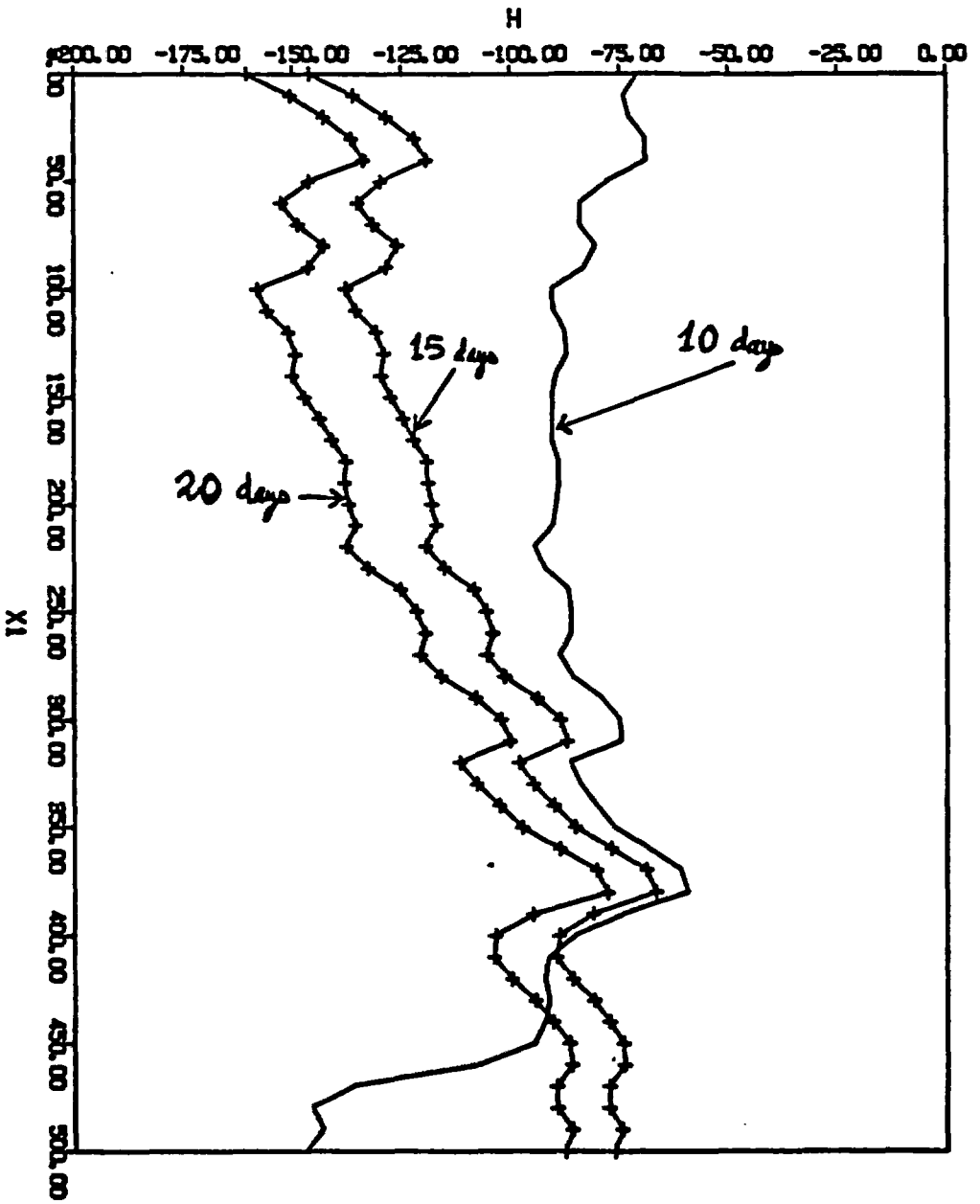

Figure 7.19 Pressure head profiles in the vertical direction during drainage (times t = 10, 15 and 20 days). The vertical transect is located near the geometric center of the strip (X = 0, Y = 4.8m).

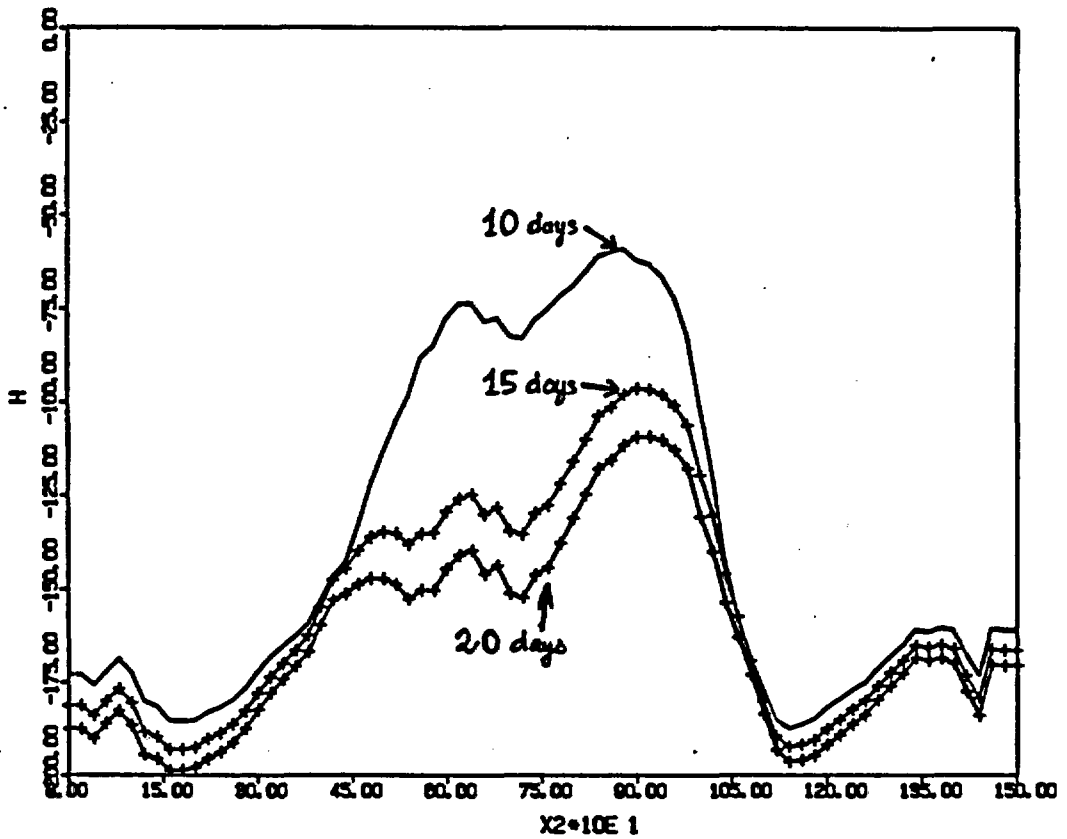

Figure 7.20 (a) Pressure head profiles in the horizontal-transverse direction during drainage (times t = 10, 15 and 20 days). The transect is located at depth Z = 0.5 m beneath the strip source.

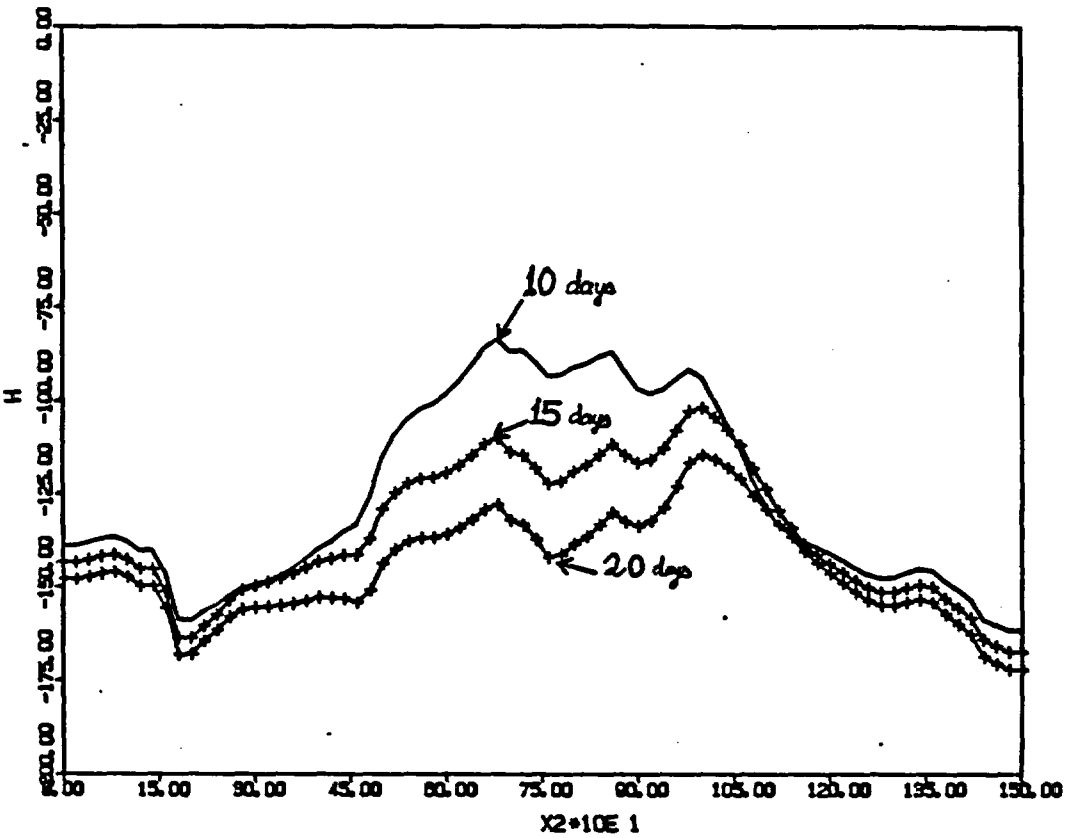

Figure 7.20 (b) Same as (a), for a larger depth Z = 2.0m.

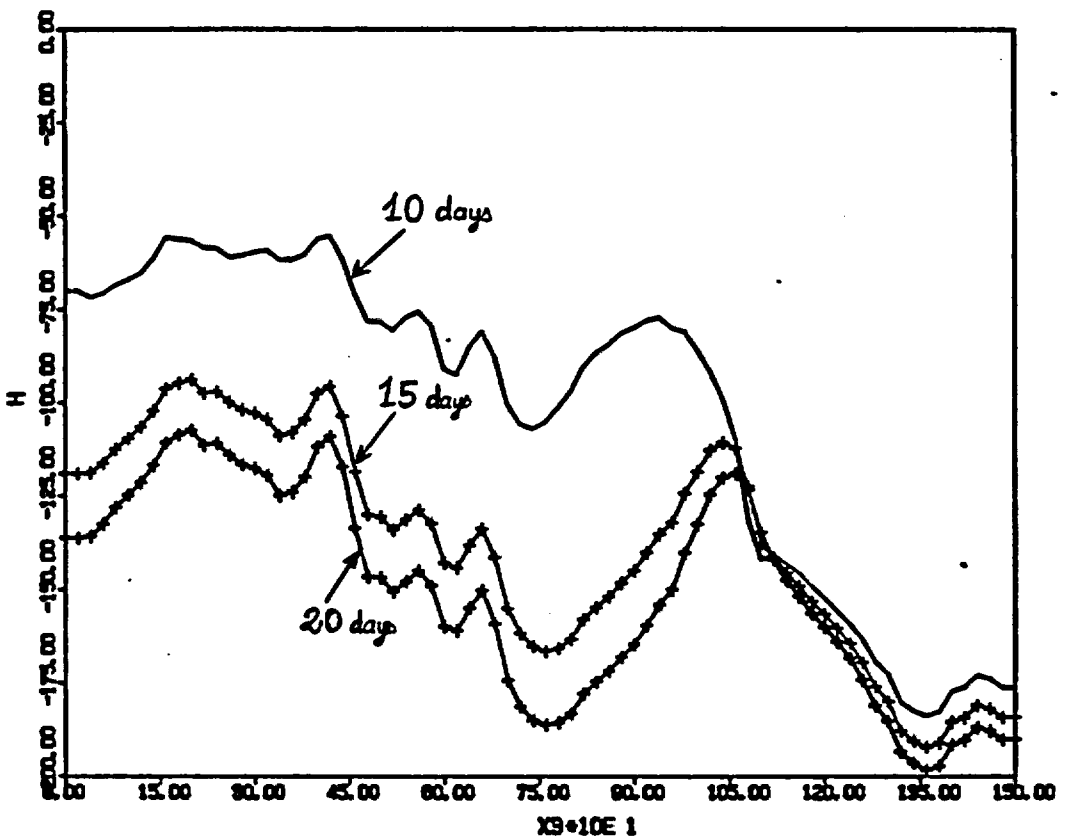

Figure 7.21 (a) Pressure head profiles in the horizontal-longitudinal direction during drainage (times t = 10, 15 and 20 days). The transect is located at depth Z = 0.5m.

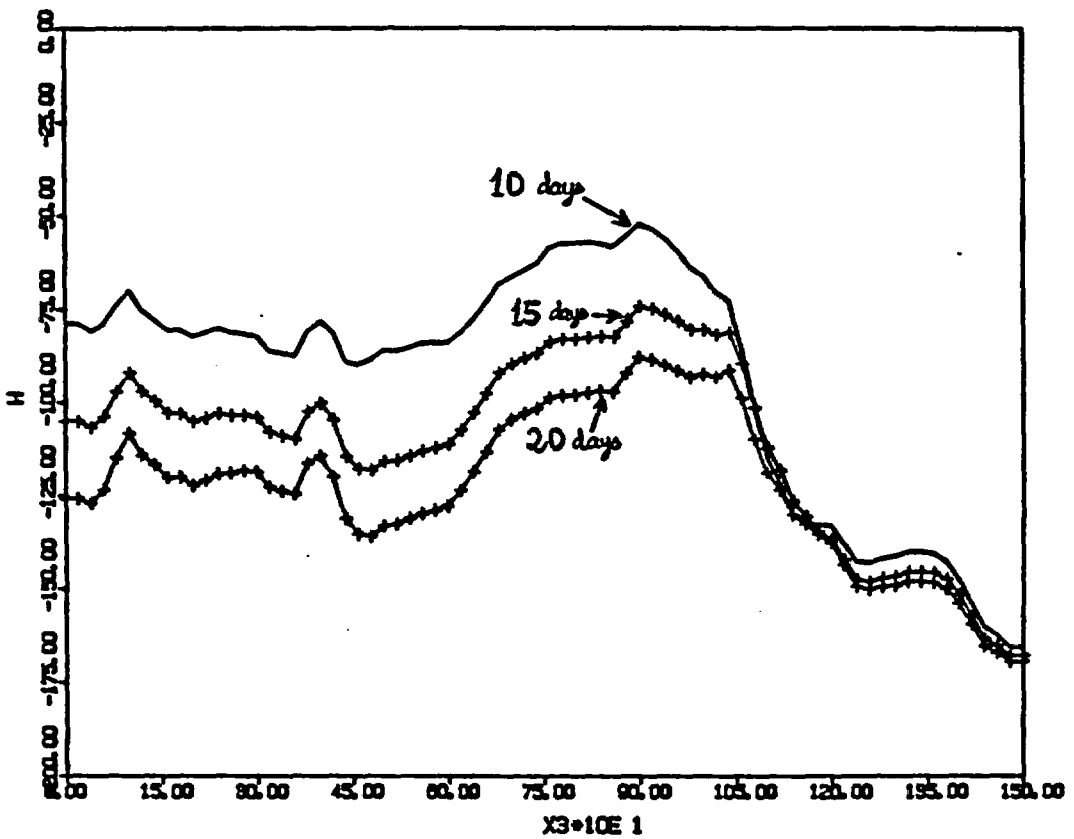

Figure 7.21 (b) Same as (a), for a larger depth Z = 2.0m.

1.5 m/day during the first day, to 1.1 m/day during the next 1.5 days, then 0.3 m/d during the next 2.5 days, and finally 0.2 m/day during the last 5 days of infiltration. The latter value coincides with our previous estimate (V) based on mass balance:

$$V = \frac{q_o - K_{in}}{\theta_{max} - \theta_{in}} \simeq 0.2 \text{ m/day},$$

but is still higher than the asymptotic velocity (v) of the wetting front, previously evaluated as:

$$v = \left(\frac{dK}{d\theta}\right)_{in} \simeq 0.1 \text{ m/day}.$$

At any rate, it seems that the pressure profiles of Figure 7.18 tend to a quasi-steady downward translation as time evolves (compare t = 2.5, 5.0, and 10.0 days). This, however, could be particular to the soil region traversed by the vertical transect located at the center of the strip. The seemingly one-dimensional behavior of the transient wetting front along that transect could be perhaps explained by the large width of the strip source, on the same order as the total depth of the flow domain (4 m compared to 5 m).

The remaining figures (7.19, 7.20, 7.21), shown just above, depicted the evolution of pressure profiles during the

drainage phase. Figure (7.19) shows that the soil was constantly drying above depth 3.5–4.0 m, and wetting below 4.0 m depth. The "gravity-driven" flow condition imposed at the bottom boundary ($q = -K(h)$ at depth $Z = 5.0$ m) allowed water to cross that boundary downward as natural drainage took place. Figure (7.20) clearly shows the persistent effect of the strip-source infiltration phase during drainage: the soil remains wetter beneath the strip source during the whole drainage period, particularly at shallow depth $Z = 0.5$ m (Figure 7.20 (a)). At larger depth $Z = 2.0$ m, the contrast of pressures beneath and away from the strip is milder due to lateral spreading (Figure 7.20 (b)). However, this kind of effect is not observed in the longitudinal direction parallel to the strip (Figure 7.21): the longitudinal wetting front near the free edge of the strip does not seem to smooth out with depth and/or with time. The dimensions of the strip are such that there is little lateral diffusion at the edge of the strip (apparently no more than 1 m). See however Figure (7.17 b) for a two-dimensional picture of edge effects.

Some other observations on the statistical nature of pressure variability can be made, in view of the one-dimensional pressure profiles just discussed. The vertical profiles of Figure (7.18) display quasi-homogeneous pressure fluctuations over several meters (below the wetting front for $t = 1$ day, and

above the wetting front for t = 10 days). It can be seen by visual inspection that the amplitude of pressure fluctuations is larger on average for dryer soil:

$$\Delta h \simeq 25 \text{ cm} \qquad \text{for} \quad \bar{h} \simeq -150 \text{ cm}$$

$$\Delta h \simeq 5\text{-}10 \text{ cm} \qquad \text{for} \quad \bar{h} \simeq -80 \text{ cm}.$$

This observation agrees qualitatively with the findings of the linearized spectral theory of Mantoglou and Gelhar (1987).

Incidentally, it is also interesting to note that the mean pressure $\bar{h} \simeq -80$ cm (t = 10 days) coincides with our previous estimate of the maximum asymptotic pressure h_{max}. This implies that the "mean" conductivity of the wetted soil beneath the center of the strip becomes about equal to the infiltration flux at the surface of the strip, after a sufficiently large time of infiltration. Note that the mean conductivity is defined here at the deterministic K(h) curve corresponding to geometric mean parameters K_G and α_G. Now, the fact that the mean vertical pressure gradient is zero (Figure 7.18 at t = 10 days) suggests that the "mean" conductivity coincides with the large-scale effective conductivity in the vertical, i.e.:

$$\hat{K}_{11}(\bar{h}) \simeq K_G \cdot \exp(\alpha_G \cdot \bar{h}).$$

Finally, it should also be noted that the pressure fluctuations in the vertical appear to have a relatively small length scale (on the order of $\lambda_1 = 0.25$ m) whenever a relatively constant mean pressure can be identified (Figure 7.18). In contrast, the pressure fluctuations in the horizontal directions appear to have a more complex structure, with a superposition of small and large scales of fluctuations: see in particular Figure (7.20 a) and Figure (7.21 a). The largest scale of fluctuations of pressure (apparently several meters) may reflect the large horizontal correlation scale of the anisotropic soil (1 m). However, these large scale fluctuations could also be due to a phenomenon of "scale selection" in relation to the size of the strip source itself (4 m x 9.8 m).

The ensemble of observations presented just above will be summarized in the last section of this chapter (section 7.5: summary and discussion). Before this, we present below the results of another large infiltration simulation on the same random soil, but for a very different type of flow conditions.

7.4 Steady "Rainfall" Infiltration in a Statistically Anisotropic Soil (300,000 nodes)

7.4.1 Model problem and input data:

In this section, we present the results of a large single-realization of steady state infiltration from a uniform planar source with constant flux. The geometry of the flow domain as well as the random soil properties are the same as in the previous section. In particular, we use here the same realization of a statistically anisotropic random conductivity curve on the 300,000 node grid, as previously. See subsection 7.3.1, Figure 7.8, and Table 7.2 concerning input data (except for boundary conditions).

The steady state solution was obtained by running the flow simulator in the transient regime until a steady state was reached beyond "reasonable doubt". The boundary condition over soil surface was a uniform constant flux $q_o = 0.060517$ cm/day, approximately equivalent to a mean "rainfall" rate of 213 mm per year (arid climate). The condition at the bottom boundary (Z = 5m) was a zero pressure gradient, i.e., by Darcy equation:

$$q = -K(h, \underline{x}).$$

The initial condition was a uniform pressure:

$$h_{in} = -150 \text{ cm.}$$

Note that q_o and h_{in} were chosen in such a way that the final solution should be close to the "initial guess" (h_{in}) on average:

$$q_o = K_G \exp(\alpha_G h_{in}) = \bar{K}(h_{in}).$$

All lateral boundaries were assumed impervious (zero flux).

The transient simulation was conducted in several pieces, with intermediate solutions saved at times:

$$t = 4.92,\ 14.44,\ 44.03,\ 64.33,\ 74.31, \text{ and } 114.00 \text{ days}$$

The flow had clearly reached a nearly steady state regime by the time $t \simeq 114$ days (approximately 4 months of infiltration). This was attested by the insignificant changes of pressure observed along a selected transect, beyond the first 2 weeks of infiltration. An example is shown in Figure 7.22 for a vertical transect located at the geometric center of the domain. The pressure profiles at times $t \simeq 44$, 64, 74 and 114 days were almost indistinguishable (only the last of these is represented in the figure). Moreover, the mass balance routine (Chapter 5, section 5.4.3) was used to monitor the global convergence of the

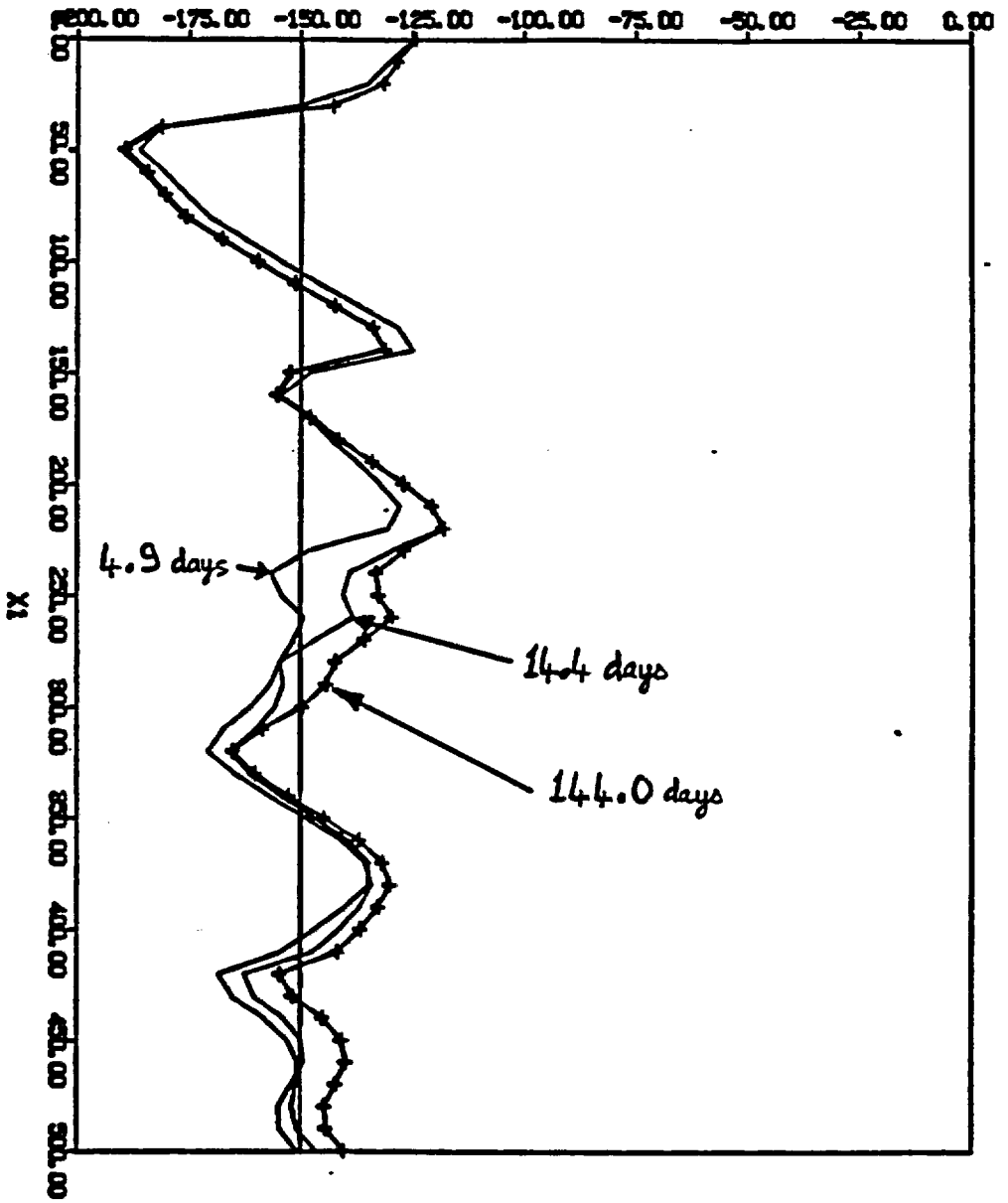

Figure 7.22 Vertical pressure head profiles obtained at different times during the transient simulation towards a steady state solution of the "rainfall infiltration" problem. Times t = 4.9 day, 14.4 day and 114 day: the crosses indicate the quasi-steady solution at t = 114 days. The vertical transect is near the center of the domain.

solution towards a steady state. The relative mass balance error:

$$E = \frac{Q_{in} - Q_{out}}{Q_{in}}$$

was only about +2% at time t = 114 days. Thus, it seems beyond doubt that a steady state flow regime was actually reached, at least in a mean sense.

7.4.2 Simulation Results and Statistical Analysis:

The steady-state three-dimensional pressure field was sampled along selected slices and transects, all traversing the geometric center of the flow domain. Figure 7.23 depicts the pressure head contour lines in a vertical slice and located midway between lateral boundaries, and Figure 7.24 shows the pressure contours in a horizontal slice located at mid-distance between the top and bottom boundaries. In both cases, the pressure contour values are equally spaced and range from -110 cm to -190 cm (recall that h_{in} = -150 cm). The contour values were not shown on these figures; some comments will help clarify their meaning.

The most striking feature in the vertical slice of Figure 7.23 is the presence of narrow-elongated "fronts" (nearly

Figure 7.23 Pressure head contour lines in a vertical slice for the steady state "rainfall" infiltration in a statistically anisotropic soil (300,000 nodes). The slice approximately crosses the geometric center of the domain (Y' = 7.4m).

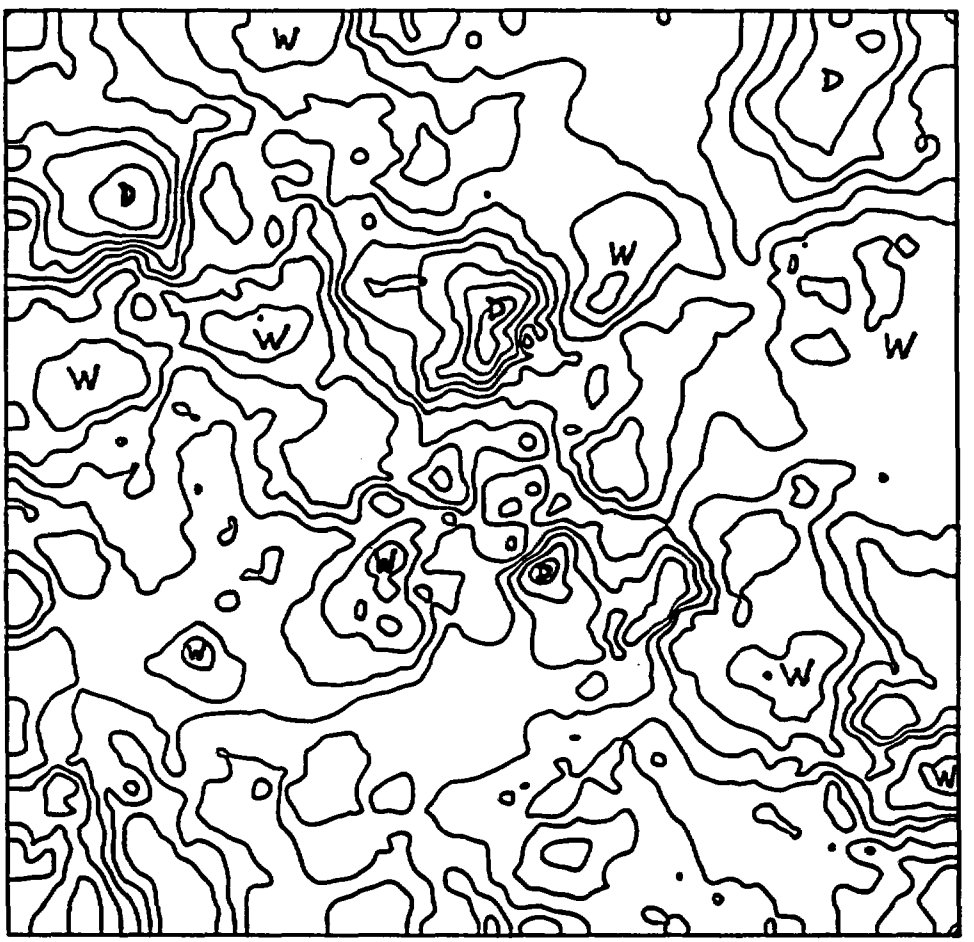

Figure 7.24 Pressure head contour lines in a horizontal slice for the steady state "rainfall" infiltration in a statistically anisotropic soil (300,000 nodes). The slice is approximately located at the mid-point between soil surface and bottom boundary (z = 2.5m).

black on the picture) separating two regions of local maxima of pressure, above and below. Inspection of contour values reveals that in most cases, the regions just above the horizontal fronts have a local maximum of pressure (relatively wet), and those below have a local minimum of pressure (relatively dry). See for instance the two zones marked "W" and "D" ("wet" and "dry") in Figure 7.23. The important role of statistical anisotropy of the soil parameters is quite evident. In its downward movement driven by gravity, water tends to accumulate above elongated lenses of low unsaturated conductivity, and spreads laterally from there by a kind of "diffusion" process.

On the other hand, the horizontal slice of Figure 7.24 displays a fairly isotropic pattern of pressure heads, as could be expected due to the horizontal isotropy of the soil and the horizontal uniformity of boundary conditions. The labels "W" and "D" were used here again to designate regions of maximum pressure (wet) and minimum pressure (dry). It seems that most of the relatively "wet" regions are larger and have smoother pressure gradients than the locally "dry" zones. This may indicate an assymmetry in the probability distribution of pressure, with negative skewness. Equivalently, the tension $\psi = - h$ could perhaps be represented by a log-normal random function having positive skewness. Another possible interpretation of the observed assymmetry (?) of the pressure field around the value

h_{in} = -150 cm could be that the actual mean $\bar{h}$ was in fact higher (wetter) than the initial state.

In order to obtain a more synthetic characterization of the steady pressure field, we have attempted a summary statistical analysis of $h(\underline{x})$ based on the assumption of statistical homogeneity of first and second moments in all three spatial directions. This was also complemented by a second statistical analysis of $h(\underline{x})$, assuming that the perturbation:

$$h'(\underline{x}) = h(\underline{x}) - \bar{h}(x_1)$$

is homogeneous in 3D space. The spatially variable mean $\bar{h}(x_1)$ intervening in this expression was obtained empirically by averaging the pressure in the horizontal plane at each different depth x_1. The results obtained by the two methods were fairly close, as shown in Table 7.3. However, the empirical mean $\bar{h}(x_1)$ was quite variable with depth.

Interpreting the statistical results of Table 7.3 to their face value, it appears that the pressure head standard deviation was about 20 cm around the constant mean $\bar{h} \simeq h_{in}$ = -150 cm. Furthermore, it turns out that $h(\underline{x})$ was negatively skewed (or $\psi = -h$ positively skewed) as conjectured earlier based on pressure contour maps. Finally, it appears that

TABLE 7.3
SINGE-POINT MOMENTS AND CORRELATION FUNCTION
OF THE PRESSURE HEAD FIELD FOR THE
SINGLE-REALIZATION "RAINFALL INFILTRATION"
SIMULATION ON A STATISTICALLY ANISOTROPIC SOIL
(300,000 NODE GRID)

Pressure Moments	$h'(\underline{x}) = h(\underline{x}) - \overline{h}$ $\overline{h}$ = 3D average	$h'(\underline{x}) = h(\underline{x}) - \overline{h}(x_1)$ $\overline{h}(x_1)$ = 2D average
Mean $\overline{h}$	- 147.5 cm	---
Stand. Dev. σ_h	19.1 cm	17.9 cm
Skewness γ_h	- 0.27	- 0.22
Kurtosis κ_h	+ 0.30	+ 0.22
$\rho(1.6\lambda_1)$	+ 0.352	+ 0.311
$\rho(1.6\lambda_2)$	+ 0.386	+ 0.298
$\rho(1.6\lambda_3)$	+ 0.381	+ 0.287

Note: $\rho(1.6\lambda_i)$ indicates the value of the pressure correlation function at lag $\xi_i = 1.6\lambda_i$ along the x_i axis ($\lambda_1 = 0.25$ m vertically, and $\lambda_2 = \lambda_3 = 1$ m horizontally).

the correlation scales of pressure in the vertical and horizontal directions are proportional to the soil parameter correlation scales. Thus, if λ_i^h designates the e-correlation scale of pressure (such that the correlation drops to $e^{-1} \simeq 0.37$), then we have from Table 7.3:

$$\lambda_i^h/\lambda_i \simeq 1.6$$

$$\rightarrow \begin{cases} \lambda_i^h \simeq 0.4\text{m vertically} \\ \lambda_i^h \simeq 1.6\text{m horizontally} \end{cases}$$

These results seem to be confirmed in part by the behavior of the fluctuating pressure head along selected transects. Figure 7.25 displays the vertical pressure profile along the transect located at the center of the domain, and Figure 7.26 shows two perpendicular transects in the horizontal plane. The degree of variability of pressure along these transects seems to agree with the computed standard deviation (amplitude of oscillations about ± 20 cm around the local mean). However, the spatial pattern of pressure along these transects does not seem to quite agree with the computed correlation scales, 0.4 m in the vertical and 1.6 m in the horizontal. There are apparently some very long range fluctuations of pressure along the selected transects. More work is needed before definite conclusions can be drawn regarding the anisotropic correlation structure of the steady pressure field.

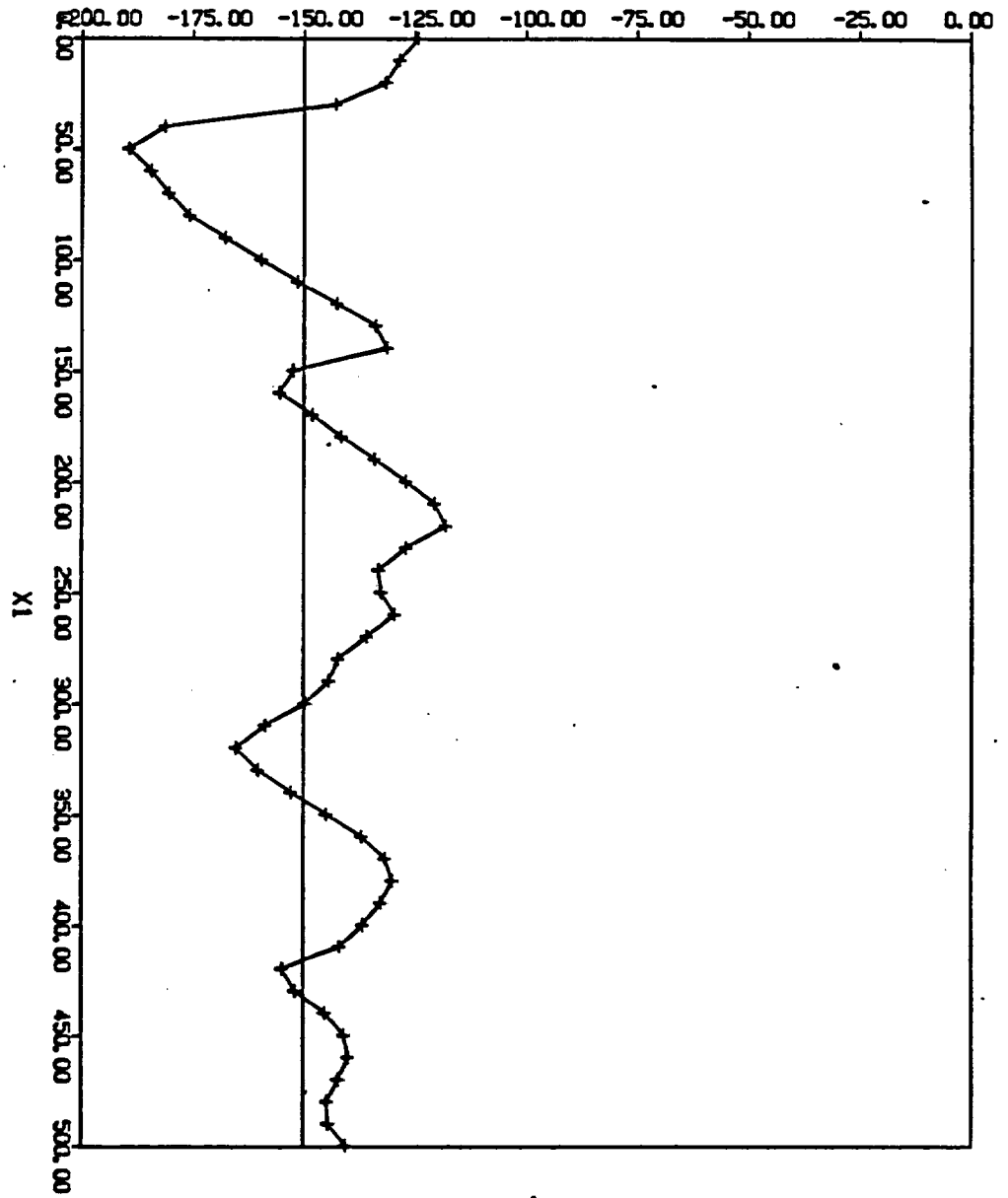

Figure 7.25 Pressure head profile in the vertical direction for the steady state "rainfall" infiltration simulation. The transect is located near the geometric center of the domain (X = 0, Y = 7.4m).

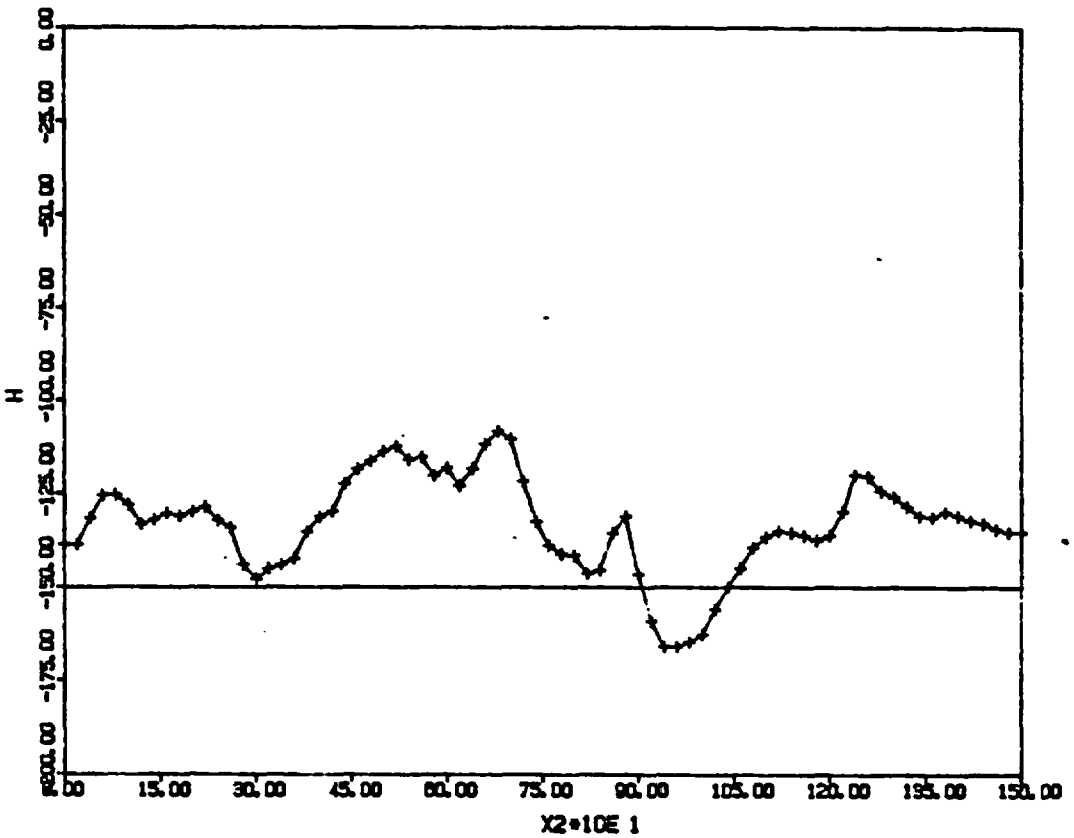

Figure 7.26 (a) Pressure head profile in the horizontal direction for the steady state "rainfall" infiltration simulation. The transect crosses the center of the domain and is oriented in the "transverse" direction (Y = 7.4m, Z = 2.5m).

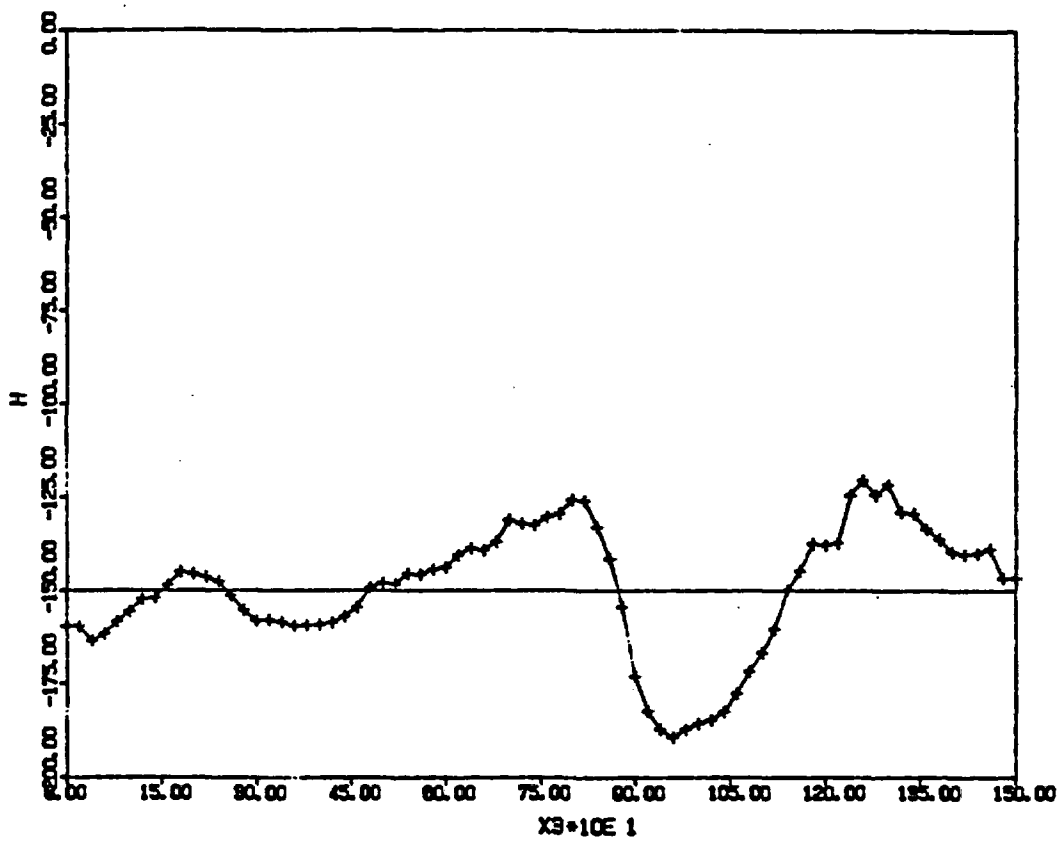

Figure 7.26 (b) Same as (a), for another horizontal transect crossing the center of the domain and oriented in the "longitudinal" direction (X=0, Z=2.5m).

On the other hand, a preliminary estimate of the effective unsaturated conductivity in the vertical direction was obtained by assuming a zero mean pressure gradient vertically. Using a "large scale Darcy equation", this gives the simple equation:

$$\hat{K}_{11}(\bar{h}) = - \bar{q}_1 .$$

The mean downward flux $\bar{q}_1$ was evaluated by using the boundary flux calculations generated by the mass balance subroutine of the flow simulator ($\bar{q}_1$ = -0.059974 cm/day). This eventually leads to an effective unsaturated conductivity of the form:

$$\hat{K}_{11}(\bar{h}) = 0.88\ \bar{K}(\bar{h})$$

where the so-called "mean" unsaturated conductivity $\bar{K}$ is the deterministic function:

$$\bar{K}(\bar{h}) = K_G \cdot \exp(\alpha_G \bar{h})$$

Now, Mantoglou and Gelhar (1987c) obtained the steady state effective conductivity as a solution of linearized spectral equations. In the case of independent (K_s,α) parameters and extreme anisotropy ($\epsilon = \lambda_1/\lambda \rightarrow 0$) they obtained a relation for $\hat{K}_{11}(\bar{h})$ in the form of an expression that depends on soil

variability, multiplied by the deterministic conductivity $\overline{K}(\overline{h})$ defined above. Using their equation (34.b) with $J_1 = L_1 = 1$, corresponding to a zero mean pressure gradient, we obtain the theoretical relation:

$$\hat{K}_{11}(\overline{h}) = \exp\left[-\frac{1}{2}\cdot\frac{\sigma_f^2+\sigma_\alpha^2\cdot(\overline{h}^2-2\lambda_1\overline{h})}{1+\overline{\alpha}\lambda_1}\right]\cdot\overline{K}(\overline{h})$$

For the case at hand, the single-point moments of $f = \ell n\, K_s$ and $a = \ell n\, \alpha$ were given in Table 7.2 of the previous section (shown below for convenience):

$$\sigma_f = \sigma_{\ell n\, K_s} = 0.6083; \quad K_G = 100 \text{ cm/d}$$

$$\sigma_a = \sigma_{\ell n\, \alpha} = 0.2202; \quad \alpha_G = 0.0494 \text{ cm}^{-1}$$

By using also some previously established identities (equations 2.19–2.21 of Chapter 2) we obtain:

$$\sigma_\alpha = 0.01128 \text{ cm}^{-1}$$

$$\overline{\alpha} = 0.0506 \text{ cm}^{-1}$$

With $\lambda_1 = 25$ cm, and $\overline{h} = -147.5$ cm (after Table 7.3 just above), this gives the theoretical result:

$$\hat{K}_{11}(\bar{h}) = 0.62\ \bar{K}(\bar{h})$$

Now, according to the previous numerical result, the coefficient 0.62 becomes 0.88. This can be regarded as a mild discrepancy between the theoretical and numerical effective conductivities, given the many assumptions that were made. In fact, we expected a theoretical value smaller than the numerical one, since we assumed $\epsilon \to 0$ for the spectral solution (asymptotic case of perfectly stratified soils), whereas the numerical simulation was carried out for a finite anisotropy ratio $\epsilon = 1/4$ (imperfectly stratified soil). The vertical conductivity must indeed be smallest in a perfectly stratified soil.

Similarly, the pressure head standard deviation ($\sigma_h \simeq 20$ cm in Table 7.3) can be compared to the steady state spectral solution obtained by Mantoglou and Gelhar [1987b, equation (28)]:

$$\sigma_h = \frac{1}{\bar{\alpha}} \cdot \left[\frac{\bar{\alpha}\lambda_1}{1+\bar{\alpha}\lambda_1}\right]^{1/2} \cdot (\sigma_f^2 + \sigma_\alpha^2 \cdot \bar{h}^2)^{1/2}$$

With the data at hand, this gives the theoretical value:

$$\sigma_h = 26.2 \text{ cm}.$$

Again, this compares very well with the numerical result

$\sigma_h \simeq 20$ cm; the slightly higher value of σ_h predicted by the theory could be due again to its asymptotic character (limit of perfectly stratified soil $\epsilon \to 0$, compared to $\epsilon = 1/4$ in the numerical simulation).

We conclude that the numerical single-realization solution of steady state rainfall infiltration was large enough to be statistically meaningful as far as the single-point moments of the pressure field are concerned. Indeed, we presume that the relatively good agreement between the spectral theory and the single-realization statistics could not be purely coincidental (mean pressure gradient *and* mean flux, intervening in the effective conductivity, and standard deviation of pressure). However, there remains a gray zone concerning the correlation structure of the pressure field. The flow domain may have been two small, despite the large size of the grid (300,000 nodes), to accurately represent the spatial structure of pressure in free space. More work is needed here in order to evaluate the statistical representativity of the observed spatial structure of the pressure field ($\lambda_I^h \simeq 1.6\ \lambda_I$?). Our results also showed that the probability distribution of tension head ($\psi = -h$) was positively skewed; it seems likely that the skewness would increase with increasing variability and/or increasing mean tension head. This complication reflects the complexity of stochastic unsaturated flow systems due to highly nonlinear

coefficients.

7.5 Summary and Discussion:

It may be useful to summarize the main results of the different single-realization simulations of unsaturated flow systems presented in this Chapter. The modest size simulations of strip-source infiltration in statistically isotropic soils (section 7.2) were intended to explore the sensitivity of the solution to different hypotheses of conductivity variability. It was clear, from the three hypothesis tested, that the spatial variability of the wetted zone was extremely sensitive to the degree of variability of the slope α of the log-conductivity curve $\ell n\ K(h)$. In addition, the degree of correlation between $\ell n\ K_s$ and $\ell n\ \alpha$ also had an important effect. For early times of infiltration ($t \simeq 2$ days) it was found that the 3D wetted zone was sharply defined (steep wetting front), and was extremely heterogeneous and contorted in the case of statistically independent parameters K_s and α (with $\sigma_{\ell nK_s} = 0.7$, and $\sigma_{\ell n\alpha} = 0.3$).

These findings suggest that future research on large scale flow and solute transport in the vadose zone should focus on the development of practical methods and/or conceptual models for determining the spatial variability of the nonlinear

conductivity curve. For instance, it could be useful to search for possible correlations between the slope of $\ell n\ K(h)$ and other hydraulic soil parameters (saturated conductivity, pore size distribution, etc.) or by using certain similarity assumptions (relation between $\theta(h)$ and $K(h)$).

In the case of *isotropic* soils, reviewed just above, the heterogeneity of the wet zone was manifested by the appearance of mushroom-shaped bulbs that evolved more or less independently, at least until reconnection occured. The spatial pattern of the wet zone for a statistically *anisotropic*, imperfectly layered soil was visually quite different, as shown in section 7.3. Indeed, the large single-realization solution obtained for 20 days of strip source infiltration and drainage (300,000 node simulation) exhibited pronounced lateral spreading of the edges of the wet zone. After a few days of infiltration, there appeared also several isolated wet regions of ellipsoidal shape. The vertical/horizontal aspect ratio of the marginally wet periphery of the unsaturated plume was much smaller than the aspect ratio of high moisture regions. This seemed to confirm the findings of Mantoglou and Gelhar (1987) concerning the pressure-dependent anisotropy of the effective conductivity for stochastic unsaturated flow systems.

Some other features of the heterogeneous flow system of section 7.3 seemed to be more specific to the particular boundary conditions and the geometry of the strip source, which were chosen to mimick an on-going field experiment. For instance, it appeared that the flow pattern beneath the center of the strip-source was fairly "one-dimensional" during the infiltration phase. The pattern of lateral diffusion around the free edge of the strip was also discussed. See subsection 7.3.2 for a detailed presentation of the 3D pressure field sampled at various locations of the 300,000 node grid during the 20 day simulation.

For applications to vadose zone contamination (say, resulting from the leak of a buried radioactive waste) it may be important to examine the possible effects of *anisotropy* over much larger time and length scales than those considered in our numerical simulations. The results obtained in section 7.3 suggest that the downward movement of the core of the unsaturated plume may continue to slow down indefinitely during the redistribution phase, while the marginally wet edges of the plume diffuse laterally and the mean moisture content of the plume decreases. This simplified "picture" may also indicate the possible behaviour of a contaminant carried in the unsaturated moisture plume. However, to simulate this type of phenomenon over three-dimensional length scales on the order of 100 m and time scales on the order of months or years may be too

prohibitive with the numerical single-realization approach adopted in this work, unless some new simplifying assumptions are adopted.

In addition, there is also the need for investigating the sensitivity of the wetting/drainage pattern with respect to initial conditions. In particular, the interpretation of our transient simulation results was somewhat obscured by the fact that a uniform pressure was prescribed initially. This simplifying assumption should be revised, as it ignores the past history of the heterogeneous flow system under natural conditions. Nevertheless, despite the limitations just discussed, the 20 day simulation of section 7.3 provided, for the first time, a detailed picture of a relatively large transient unsaturated flow system (5m × 15m × 15m) with highly variable nonlinear soil properties (random curve $K(h_1,\underline{x})$) and an unusually high grid resolution in 3D space ($52 \times 76 \times 76 \simeq$ 300,000 nodes). The results of this direct simulation could serve as a proving ground for future conceptual models.

In section 7.4, we showed more concretely how the single realization approach could be used to test current theories of spatially variable unsaturated flow. The statistically anisotropic soil of the previous section (7.3) was used to simulate a *steady state* infiltration under a *uniform*

constant flux at soil surface (uniform "rainfall"). The inherent statistical homogeneity of this type of infiltration problem justified our attempt at a direct statistical comparison with available spectral solutions (Mantoglou and Gelhar, 1987). The standard deviation of the pressure head and the effective unsaturated conductivity of the vertical infiltration system agreed with the spectral solutions within a margin of error of 20%.

This agreement is quite encouraging, but needs to be confirmed for a wider range of conditions, i.e., for other flow rates or mean pressure head values. Our results also suggested that the probability distribution of tension head ($\psi = -h$) was positively skewed. If the hypothesis of a log-normal distribution of the tension head was retained, the skewness would increase rapidly with the coefficient of variation of tension head (equation 2.19 of Chapter 2), which itself is known to increase with mean tension (spectral theory of Mantoglou and Gelhar, 1987). Therefore, it is possible that, for very dry soils, a second order moment description of tension head variability will not be sufficient to completely characterize the actual distribution of tensions. A log transform could be used, but third order moments may eventually be required.

Finally, it should be emphasized that the correlation scales of the pressure head random field were found to be proportional to the λ_i scales of the random soil parameters ($\lambda_i^h \simeq 1.6\ \lambda_i$). However, this result may not be representative of truly "infinite domain" pressure fluctuations, given the limited size of the flow domain with respect to the computed pressure correlation scales (about $10\ \lambda_i^h$ in each direction). Note that the total CPU time required to solve this steady state problem on a Cray 2 machine was not overly prohibitive. In spite of the large 300,000 node grid, only 3 CPU hours were required to converge to a steady solution (in 85 time steps or 114 days of infiltration). It seems feasible to simulate such statistically homogeneous unsaturated flow systems over larger grids, on the order of 1 million nodes or more.

In conclusion, the application of the numerical single-realization approach to stochastic unsaturated flow problems provided a means of direct visualization of plausible heterogeneous pressure fields in three-dimensional space, with a degree of detail unattainable by current field measurement techniques. A few numerical experiments unveiled the complex nature of unsaturated flow systems. One of the most striking features of the transient strip-source infiltration problem was its great sensitivity to the degree of variability of the conductivity curve (particularly its slope α) and to statistical

anisotropy. The complex interactions between the homogeneous random field fluctuations of hydraulic properties and the evolving nonlinear wetting front (and drying front) seem to defy current stochastic analyses. However, the good agreement obtained between the linearized spectral theory and the numerical solution of *steady state* "rainfall" infiltration suggests that a simplified conceptual model like the spectral theory can provide reliable predictions of unsaturated flow variability in certain cases. The encouraging results obtained in the steady state case may possibly be extrapolated (confirmed) for transient flow systems after sufficiently large times and/or in the absence of sharp wetting fronts.

CHAPTER 8: CONCLUSIONS

A number of approaches were developed in this work for the characterization of three-dimensional flow fields in randomly heterogeneous porous media. For the most part, this problem was tackled under the assumption that naturally heterogeneous subsurface formations can be realistically modeled in the form of statistically homogeneous random functions of space. Our focus on a fully three-dimensional representation of subsurface flow phenomena was motivated by experimental as well as theoretical evidence on the artificial character of lower dimensional representations. Most of our results confirm indeed that, in the general case, fluid pathways are inherently three-dimensional in heterogeneous porous media. On the other hand, experimental evidence supporting the assumptions of randomness and statistical homogeneity of the hydraulic properties of natural porous formations was discussed in the data survey section of Chapter 2.

These assumptions were at the basis of most of the conceptual approaches pursued in this work. For instance, statistically homogeneous (and ergodic) random hydraulic properties were postulated in most of the analytical contributions of chapters 3 and 4, except in the spectral conditioning approach. In a certain sense, the postulate of a homogeneous/ergodic porous medium was also used for the numerical

simulations of single-realization flow fields in chapters 6 and 7. With this in mind, we now proceed to summarize and discuss the interrelated results obtained in different parts of this work, as well as some practical consequences in the area of subsurface hydrology. The discussion will be followed by a "summary of contributions", and a brief epilogue presenting a more general assessment of the outlook for stochastic approaches to subsurface flow and contaminant transport.

[a] Discussion of results:

One of the main motivations of this work was to assess the range of validity of the spectral solutions of stochastic subsurface flow developed by Gelhar and others during the past decade (Bakr et al. 1978; Gelhar and Axness 1983; Mantoglou and Gelhar 1987; Gelhar 1986). The spectral theory of stochastic flow (and mass transport) relies on the postulate of statistical homogeneity of the random flow field (hydraulic or pressure head perturbation, and water flux or velocity vector). In addition, this approach implicitly assumes the existence of ergodic solutions, since it purports to characterize unique "effective" transport properties for infinite-domain realizations of the flow field. Finally, the spectral solution method also requires small parameter expansions and various linearization approximations, in order to arrive at tractable closed-form solutions of the

governing stochastic partial differential equations. Let us point out that similar approximate expansions were also required in other analytical and numerical stochastic approaches published in the literature (see review in Chapter 2).

The existing "spectral theory" developed by the above-mentioned authors was expounded in detail in Chapter 3 for the case of stochastic groundwater flow. . The approximate nature of the spectral solutions was made clearer by using σ-expansions, where σ is the standard deviation of the random log-conductivity field. The modern formalism of Fourier space representations of statistically homogeneous random fields was heavily used, and served as a background for subsequent developments. Some particular restrictions on the properties of the log-conductivity spectrum were discussed, in view of previous results obtained in the literature. In particular, we concluded that, in order to obtain a statistically homogeneous hydraulic head solution around its linear mean, the random conductivity field must be taken more nearly "periodic" as the degree of freedom of flow decreases, from fully three-dimensional and isotropic formations to the extreme case of one-dimensional flow, with all the conceivable intermediate cases corresponding to various configurations of stratified flow systems.

Furthermore, some new closed form results were inferred

by applying the spectral solution method to a variety of specific cases, in particular for horizontally stratified aquifers. Our findings regarding the correlation structure of the flow field led us to restrict the range of validity of the infinite-domain spectral solutions (aquifer thickness must be much larger than the horizontal fluctuation scales of the conductivity field). For stratified aquifers, the hydraulic head field was found to be nearly isotropic in vertical planes, and only moderately anisotropic in horizontal planes. An approximate analysis also suggested that the flux or velocity vector was much more strongly anisotropic in 3D space than the head field. These previously unknown results were confirmed in part by subsequent numerical experiments.

However, we recognize that more work will be needed in order to fully characterize the correlation structure of the velocity field in the case of stastically anisotropic aquifers. This may have important consequences regarding the validity of two-dimensional representations of groundwater flow and transport phenomena commonly used in engineering practice. In addition, we expect that stringent grid resolution constraints will be required for the numerical simulation of strongly anisotropic flow systems due to the disparity of fluctuation scales involved. Moreover, note that the analytical results just discussed were obtained within the framework of the spectral theory, based on

"small parameter" approximations, and on the assumption of statistical homogeneity of the input conductivity *and* the output flow field.

In contrast, we have developed in Chapter 4 new stochastic solutions of the groundwater flow equation without some of the limiting assumptions of the spectral theory (see discussion in section 4.1). Thus, the "small parameter" approximation was dropped altogether in section 4.2, devoted to the development of *non-perturbative* spectral solutions. In addition, we obtained in section 4.3 an "improved" spectral solution for the groundwater velocity spectrum, by linearizing the equations for the velocity components rather than that for head. Finally, the assumptions of infinite domain and statistical homogeneity of the flow field were abandoned in section 4.4, where a new "spectral conditioning" approach was developed to treat the case of finite size flow and transport phenomena. It may be worthwhile to recapitulate here on some of the main results obtained by these alternative spectral approaches.

The non-perturbative spectral relations obtained in section 4.2 were derived from fundamental statistical symmetries and other "exact" properties of the flow field in the case of statistically isotropic and homogeneous random conductivity. In

the 3D case, mass conservation and statistical axial symmetry were used to infer relations on the covariance or spectral structure of the flow field. A special conjugacy relation was found in the 2D case, leading to a statistical identity relating the head gradient and velocity fields. It was found that the previous first order spectral solutions (e.g. Gelhar and Axness, 1983) were consistent with these statistical identities in any number of dimensions (for isotropic media). However, a close inspection of the first order spectral solutions also revealed that the degree of variability of groundwater velocity was probably underestimated in the 3D case. A new, presumably "improved" spectral approximation, was developed in Section 4.3 for arbitrary conductivity spectrum. The new spectral solution, although not exact, turned out to agree better with subsequent numerical results, and was also consistent with the previous non-perturbative spectral relations for 3D isotropic media. Some of the implications of these results will be discussed shortly.

In the general case of statistically anisotropic aquifers, exact statistical identities of the type mentioned just above were not obtained, due to the lack of symmetry of the flow pattern. In any case, recall our previous finding that the infinite-domain spectral theory may not be directly applicable to shallow aquifers unless their thickness is much greater than the horizontal fluctuation scales of natural heterogeneities. Some

of the numerical experiments, to be discussed later in this chapter, suggested indeed that the aquifer thickness must be on the order of several tens of horizontal fluctuation scales for the spectral theory to be applicable. When this is the case, the spectral results of Gelhar and Axness (1983) can be used to infer the effective conductivity of the groundwater flow system at the large scale. These authors showed in particular that, as a first order approximation in σ, the effective conductivity is a second rank symmetric tensor whose degree of anisotropy depends (in a seemingly complex position) on the variance and statistical anisotropy of the underlying random conductivity field. Their result takes the form of complicated Fourier integrals, although some simplifications occur in assymptotic cases of perfect stratification (infinitely small or infinitely large anisotropy ratio) and in the isotropic case (anisotropy ratio equal to unity).

In contrast, we proposed in this work a simple analytical expression for the effective conductivity in the general anisotropic case, based on an empirical generalization of a previous conjecture by Matheron (1967). This author observed that, for isotropic formations, the effective conductivity seems to depend in a simple fashion on spatial dimension. Our generalization by way of induction, led to an expression relating the effective conductivity component K_{ii} to the log-conductivity

variance σ^2, the correlation scale λ_1, and the geometric and arithmetic averages of the three correlation scales (λ_1,λ_2,λ_3), as shown in equations (4.48-4.49) of Chapter 4, section 4.2.6. For illustration, let us use an example taken from a field contamination study discussed in Gelhar (1986). The three correlation scales, in the same order as above, were 60 m and 15 m (horizontal) and 1 m (vertical), and the log-conductivity variance was 4.2. By using the Gelhar-Axness formula, Gelhar (1986) was able to evaluate the anisotropy ratios of the effective conductivity (horizontal/vertical: K_{11}/K_{33}; horizontal/horizontal: K_{11}/K_{22}). His values were 47 and 1.3, respectively. By using instead the simple relation proposed in his work, the conductivity anisotropy ratios are found to be 45 and 1.2, very close to the values predicted by the Gelhar-Axness first order spectral theory. The proposed relation also coincides with the effective conductivity result of Bakr et al. (1978) in the 3D isotropic case. In addition, this relation coincides with all results known to be exact, such as the arithmetic and harmonic means for flow parallel and orthogonal to perfect stratification, and the geometric mean for two-dimensional isotropic media).

Some of the new analytical results established in this work may have direct implications for the study of solute transport in randomly heterogeneous groundwater flow systems. If

molecular diffusivity is neglected, the pathways of nonreactive solutes convected in the flow are the same as those of tagged fluid particles. Therefore, the variability and spatial structure of the groundwater velocity field determine entirely the overall transport properties of the flow, like "macrodispersivity". Furthermore, assuming for convenience that the porosity of the aquifer is approximately constant, the groundwater velocity is simply proportional to the Darcy flux. The two vector fields, velocity and flux, are therefore equivalent if one ignores the constant of proportionality. With this in mind, let us examine more specifically some of the consequences of our analytical results in the area of groundwater solute transport.

Approximate spectral solutions of stochastic groundwater solute transport were developed by Gelhar and Axness (1983) and others. Subsequently, Gelhar (1987) pointed out that the asymptotic or "large time" longitudinal macrodispersivity (A_{11}) was proportional to the correlation scale of the longitudinal velocity component in the longitudinal direction. The factor of proportionality was the longitudinal velocity variance divided by the square of the mean velocity. By plugging in this relation the Gelhar-Axness spectral solutions of stochastic groundwater flow, one obtains a simple closed form expression for A_{11} in the 3D isotropic case. Surprisingly, it

turns out that the resulting macrodispersivity has a maximum at some moderate value of the log-conductivity variance ($\sigma^2 = 3$) and tends to zero as σ goes to infinity. Now, this seemingly unphysical behavior disappears when the "improved" velocity spectrum proposed in this work (section 4.3) is used instead of the Gelhar-Axness spectrum. For 3D isotropic formations in particular, the large time macrodispersivity obtained with the higher order solution takes the simple form $A_{11} = \sigma^2\lambda$, where λ is the integral correlation scale of the isotropic log-conductivity field.

It is particularly instructive to note that the product of $\sigma^2\lambda$ is invariant under local averaging of the underlying conductivity field. Thus, Vanmarcke (1983) observed that the product "variance-correlation scale" quantifies the intrinsic amount of uncertainty carried by a homogeneous random field, independently of the scale of measurement. Our result concerning macrodispersivity suggests a parallel interpretation. The large time longitudinal macrodispersivity of a solute, convected over infinite distances in a statistically homogeneous groundwater velocity field, quantifies in effect the intrinsic variability of the porous formation independently of the scale at which this variability is "measured".

However, it should be emphasized that these results on

contaminant macrodispersion rely on quite stringent hypotheses: the large time and infinite domain assumptions, the postulate of a statistically homogeneous porous formation, and the first order perturbation approximations of the solute transport equation. Intuitively, the "large time" assumption means that the contaminant plume must have encountered a large number of conductivity fluctuations or formation heterogeneities. Assuming that the formation is statistically homogeneous, this becomes equivalent to requiring that the size of the plume or the mean travel distance (L) be much larger than the formation's correlation length (λ). In actual practice however, there may not exist a uniquely defined correlation length valid for a sufficiently large range of plume sizes or travel distances. It is this particular problem that was addressed in section 4.4 of Chapter 4 (Finite size effects: band-pass self-similar spectra, spectral conditioning and uncertainty).

The "spectral conditioning" approach was developed in order to characterize finite-size and evolving phenomena in stochastic flow and transport problems. This approach avoids the elusive concepts of correlation scales, infinite domains, and statistical homogeneity, while still retaining some of the analytical simplicity of the spectral solution method. By applying first the standard spectral solution method in conjunction with a band-pass self-similar model of

random field heterogeneity, based on data published in the literature, we evaluated explicitly the dependence of statistical properties on domain size (1- and 3-dimensional head variance, effective conductivity, and macrodispersivity). This motivated further development of the spectral conditioning approach for a consistent characterization of the effects of domain size on the mean, variance, and effective conductivity of the flow field. In particular, the *uncertainty* on these parameters was shown to be directly related to domain size, i.e. to the typical length scale of the phenomenon of interest. Although closed form solutions were limited to the case of one-dimensional flow, it seems that a similar spectral conditioning approach could be developed in order to quantify the effective transport coefficients *and* the uncertainty of evolving contaminant plumes in three-dimensional groundwater flow systems. Some of our preliminary results suggest that, for statistically isotropic 3D formations, both the macrodispersivity and the effective conductivity will grow with plume size, while the uncertainty on these coefficients will decrease (at least up to a certain cut-off scale many times larger than the largest size of geological heterogeneities). With some further refinements, it seems that this approach could provide an analytically tractable model of the process of evolving macrodispersion with only minimal assumptions on the random nature of the underlying porous formation.

Much of the remaining part of this work was devoted to the development and application of a *numerical approach* to saturated as well as unsaturated stochastic flow, under the postulate of statistically homogeneous random field properties of the porous medium. The proposed approach required solving numerically the governing flow equation for a single realization of random field properties in a large but finite domain, with approximate boundary conditions. Observe that no assumption whatsoever was made on the nature of the flow at the solution stage. The motivation behind this numerical "single-realization" approach was two-fold. First of all, our expectation was that the single-realization flow fields obtained numerically could be statistically analyzed by using standard detrending and spatial averaging methods under some weak assumptions of statistical homogeneity (section 6.1 of Chapter 6). In this way, the numerical simulations could be compared directly to available spectral results (second order moments of the flow field, and effective conductivity) like the Gelhar-Axness *groundwater flow* spectral solutions and the *unsaturated flow* spectral solutions of Mantoglou and Gelhar (1987). Moreover, because the single-realization method does not entail any a priori assumptions concerning the random nature of the simulated flow field, it lends itself naturally to an empirical evaluation of the validity of the homogeneity/ergodicity assumptions of the spectral theory. As will be seen, these assumptions may not be

justified in certain cases, but the single-realization approach can still be used as a means of obtaining, by way of direct numerical solution, a plausible realization of the detailed flow pattern in a typical heterogeneous or random porous formation.

To be successful, the proposed numerical approach must obviously take into account the specific numerical issues associated with the discrete solution of highly variable, random-like flow equations on large three-dimensional grids with fine mesh resolution. The saturated/unsaturated flow simulator developed and tested in Chapter 5 was designed specifically for that purpose ("Bigflo" code). An efficient finite difference system solver (the "strongly implicit procedure" or SIP method) was used to solve the saturated (linear) as well as unsaturated (nonlinear) flow equations, for large realizations of random hydraulic coefficients on three-dimensional grids as large as one million nodes. The largest simulations of Chapter 6 (saturated flow) and Chapter 7 (unsaturated flow) required the use of the Cray 2 supercomputer, with typical CPU times of a few hours per simulation. However, a number of meaningful "medium size" simulations were also obtained on a Microvax 2 minicomputer.

Typically, a "medium size" numerical problem in this work could involve a grid size of tens of thousands of nodes for unsaturated flow, and up to two hundred thousand nodes for steady

saturated flow. The largest numerical problems involved grid sizes of several hundred thousand nodes for unsaturated flow, and one million nodes for saturated flow. To obtain meaningful numerical solutions for such large random flow problems required a certain amount of numerical analysis and experimentation, the results of which are now being discussed. However, the reader is referred to Chapter 5 for details. See in particular *Appendix 5D* for an abstract of the "Bigflo" simulator used to generate all the numerical solutions analyzed in this work.

One important new result of numerical analysis concerned the question of consistency and accuracy of finite difference approximations of *stochastic* partial differential equations. This theoretical problem was tackled by developing a spectral method of truncation error analysis, leading to closed form expressions for the root-mean-square finite difference error in the case of stochastic groundwater flow with a statistically isotropic three-dimensional random conductivity field. More precisely, the Fourier-space spectrum of the stochastic error (difference between the discrete solution and the exact solution of the continuous equation) was explicitly evaluated - at least to the leading order of a double expansion in terms of the mesh size (Δx) and log-conductivity standard derivation (σ). The *relative* root-mean-square error was defined as the ratio of standard deviations of the error to that of the variable itself

(the variables of interest were the hydraulic head and the flux vector). It was found that the relative error was in general proportional to a fractional power (p) of the mesh resolution ratio ($\Delta x/\lambda$), where λ is some fluctuation scale or correlation scale of the conductivity field. The exponent p defines the order of accuracy of the finite difference scheme in a mean-square sense.

For the hydraulic head, the order of accuracy was 2 for a "smooth" log-conductivity field but dropped to 3/2 for a "noisy" log-conductivity field (respectively Hole-Gaussian and Markov three-dimensional spectra). For the flux or groundwater velocity vector, the order of accuracy was 1 in the "smooth" case, and only 1/2 in the "noisy" case. These previously unknown results show that the seven point centered finite difference scheme yields a consistent approximation of the exact hydraulic head *and* flux vector for a wide range of random log-conductivity fields, including the case of the "noisy" three-dimensional Markov field (non-differentiable in the mean-square sense). The specific results obtained for the isotropic Markov field indicated that a good accuracy on the hydraulic head, and a reasonable accuracy on the flux vector, could be obtained with a statistical grid resolution ($\Delta x/\lambda$) on the order of 1/3. Note however that these results may hold only for moderate conductivity variability (presumably for σ not much greater than

unity). These indications were used in Chapter 6 to design the numerical simulations of stochastic groundwater flow, and to evaluate confidence intervals on the numerical solutions for comparison with the results of the spectral theory.

In addition, we also developed in Chapter 5 a particularly cautions approach for estimating the error due to the approximate iterative solution of the finite difference system (SIP solver, based on approximate factorization of the coefficient matrix and Picard iterations). Thus, we used standard results of linear algebra to show that the Euclidian norm of the residual error may significantly underestimate the *true* root-mean-square solution error, particularly in cases of slow convergence. An approximate upper bound on the true error was evaluated in terms of the residual error and mean convergence rate of the iterative solver. Numerical experiments for steady state stochastic groundwater flow (similar to a "random heat equation") were conducted for values of σ up to 2.3 and grid sizes on the order of 100,000 to 1 million nodes, using a Cray 2 machine for the largest problems. Briefly, these experiments indicated that the convergence rate of the SIP solver was roughly proportional to the unidirectional size of the grid, a number presumably related to the square-root of the condition number of the random conductivity matrix. For the degree of variability and the problem sizes investigated, it was concluded that the

matrix system could be solved with 1% relative accuracy on the hydraulic head with a few hundred to a thousand underrelaxed iterations.

Overall, these results of truncation error analysis and iterative solver convergence lead us to believe that the stochastic groundwater flow simulations presented in Chapter 6 were generally quite accurate, particularly concerning the largest simulations with statistically isotropic conductivity (1 million nodes, with grid resolution 1/3). Likewise, the "turning band method" used to generate discrete realizations of random conductivities seemed adequate, since the spatial statistics of large conductivity realizations appeared to be very close to the prescribed ensemble statistics. These indications appear quite useful in view of the fact that there is no known *exact* solution to the stochastic groundwater flow equation.

Some aspects of the numerical/statistical methodology adopted in this work could be quite useful in other contexts. For example, our numerical approach and results on stochastic groundwater flow could be extended to other physical problems involving random conduction phenomena (thermal and electrical conduction in composite materials, and random resistance networks). In addition, our spectral analysis of stochastic truncation errors could perhaps be extended to other

discretization methods (weighted residuals and pseudo-spectral) and to other stochastic equations (convection-diffusion in random media). This may be particularly important for assessing the feasibility of direct numerical simulations of solute transport in random porous media.

Other numerical contributions of this work concerned the numerical solution of randomly heterogeneous unsaturated flow systems, involving highly nonlinear and spatially variable hydraulic coefficients. In the transient case, a fully implicit time discretization scheme was used. The method used to solve the resulting nonlinear finite difference system was basically the same as for linear flow problems, however with an additional outer Picard iteration loop to sequentially linearize the system (nonlinear SIP solver). A heuristic stability analysis of the nonlinear finite difference equations suggested that a severe constraint on the time step ($\Delta t/\Delta x^2$) may be required, unless a grid Pechet number condition be satisfied at each node of the grid ($\alpha \Delta x_i \leq 2$, where α is the slope of the unsaturated log-conductivity function of pressure, and Δx_i the vertical mesh size). However, any truly *rigorous* statements on numerical requirements were precluded by the complexity of the spatially variable unsaturated flow equation.

In view of these difficulties, the problem solving

capabilities of the transient unsaturated flow simulator were tested in an empirical fashion by way of numerical experimentation (comparisons with analytical solutions, mass balance checks, and other tests). In the process, some instructive observations were made on the physics of two-dimensional strip source infiltration in uniformly stratified soils with horizontal or vertical layers (cf. last section of Chapter 5). More importantly, some truly large simulations of three-dimensional infiltration in "random soils" were analyzed at length, in Chapter 7.

From a numerical viewpoint, the most difficult random infiltration problem was the case of transient strip source infiltration in a statistically stratified soil, with a different unsaturated conductivity curve defined at each mesh point of the 300,000 node grid in three-dimensional space. It may be of interest here to recall some of the details of this numerical experiment (see Chapter 7). About 5 CPU hours of Cray 2 time were consumed in the simulation of 10 days of infiltration and 10 subsequent days of drainage in a moderately dry soil, with initially small but increasing time step size. The exact size of the time step at initial time and at a few intermediate times, was set empirically by trial and error, although an automatic adjustment was also made by the code during simulation. Overall, our experience with this numerical experiments indicates that a

very severe constraint on the time step could be required for convergence of the nonlinear iterations in the case of dry soils. In the case at hand, the initial degree of saturation was only moderately low, about 20%.

Thus, it may be questioned whether a fully implicit finite difference method such as used in this work is truly adapted to the simulation of extremely sharp infiltration fronts in "air dry" soils, particularly in the presence of random heterogeneities. On the other hand, the extreme nonlinearity of the exponential conductivity-pressure relation assumed in this work may also be called into question. In any case, it should be kept in mind that, in spite of these difficulties, the flow code was efficient enough to simulate some rather large and highly heterogeneous unsaturated flow systems, with grid sizes on the order of tens of thousands of nodes (Microvax 2) to several hundred thousand nodes (Cray 2)... in reasonable amounts of CPU time. Some of the most important results of stochastic flow simulations will now be discussed, both for saturated and unsaturated flow.

The large high-resolution simulations of stochastic groundwater flow and unsaturated flow in random media were thoroughly analyzed and discussed in Chapter 6 and Chapter 7, respectively. Each of these chapters included a "summary and

discussion" section, of which some essential points are recalled here. Starting with the case of groundwater flow in statistically isotropic aquifers, it should be emphasized that a remarkably good agreement was found between the single-realization simulations and the spectral solutions, particularly concerning the effective conductivity and the head variance. For the latter quantities, the agreement between simulations and theory was quite good up to large conductivity variability ($\sigma = 2.3$, where σ is the standard deviation of ℓn K). However, the single-realization head variance was computed about a slightly nonlinear trend of hydraulic head in the mean flow direction, in contrast with the linear mean head assumed by the first order spectral theory. There was some evidence that the discrepancy in the mean head was due to the "modest size" of the flow domain relative to the large correlation range of the hydraulic head. As a consequence, the computed head correlations were systematically smaller than the theoretical ones, although there was a broad agreement concerning the three-dimensional structure of the head field. On the other hand, a similar but more pronounced discrepancy was observed in two cases involving statistically anisotropic conductivities ("shallow" and "deep" stratified aquifers). In the case of a shallow stratified aquifer, the spatial structure of the simulated head field did not agree with the infinite domain spectral result. This confirms our previous discussion

concerning potential restrictions on the range of applicability of the spectral theory.

With these results in mind, it might be useful at this point to discuss some implications for practical issues like the solution of inverse flow problems, or other questions where the spatial structure of the hydraulic head field (measured or predicted) may intervene. Broadly speaking, our numerical results indicate that the spectral theory is essentially correct for the head variance, and to a lesser degree the head correlation structure, *provided* that the effects of large scale inhomogeneities be removed by empirical detrending of measured hydraulic heads. In actual practice, statistical inhomogeneity can be equated to the nonlinearity of the observed mean head field. We expect that the head covariance function predicted by the spectral theory be relatively accurate when this nonlinearity is mild. In the case of shallow aquifers however, the predicted head covariance function may not be realistic if aquifer thickness is on the order of ten horizontal correlation scales or less. These indications may be particularly useful for the solution of inverse flow problems, where prior knowledge of the cross-correlation between heads and log-conductivities will be required.

The case of statistically anisotropic log-conductivity

fields is important for applications, as most natural geological formations appear to be stratified. In the case of horizontal stratification, the theoretical (spectral) results obtained in Chapter 3 suggested that the groundwater velocity vector was strongly anisotropic in proportion with the degree of anisotropy of the porous formation. However, recall that the hydraulic head appears to be only mildly anisotropic, independent of the formation's anisotropy (from theoretical and simulation results). Thus, it can be inferred that the hydraulic head carries little information about the covariance structure of groundwater velocities, which ultimately determines the fate of contaminants (dispersion). Now, since detailed measurements of groundwater velocities are rarely feasible in practice, it seems particularly important to ascertain the validity of the spectral results concerning the correlation structure of the flux or velocity field. This question remains open in the case of stratified aquifers; however, encouraging results were obtained in the special case of statistically isotropic aquifers as explained below.

In the case of statistically isotropic aquifers, the groundwater velocity correlation functions (tensor) obtained numerically agreed very closely with the spectral results of Gelhar and Axness (1983) for moderate log-conductivity variability ($\sigma = 1$), and were still in reasonable agreement for

higher variability (up to $\sigma = 2.3$). However, the Gelhar-Axness solutions appeared to underestimate the velocity variances, especially for high variability ($\sigma > 1$). The discrepancy was milder for the "improved" velocity spectrum proposed in this work, although still significant. The numerical values obtained for the velocity variances suggested that the high order terms neglected in the standard and "improved" spectral solutions grow exponentially with the log-conductivity variance. Equations 6.13 give empirical expressions fitted to the numerical velocity variances. Finally, a visual inspection of the numerical velocity vector field also revealed that the longitudinal component had a positively skewed probability distribution, possibly close to a lognormal distribution.

These findings should motivate future research towards a higher order characterization of the random groundwater velocity field, as this may have consequences for stochastic solute transport. Our finding that the first order spectral solutions underestimate the velocity variance with respect to numerical solutions, also imply that contaminant macrodispersivity (over large time scale) will be higher than predicted by the spectral theory. Admittedly, more work is needed in order to assess more precisely the accuracy of our numerical evaluation of the variances of groundwater velocity. The effect of numerical noise was taken into account in our

comparisons of numerical/spectral solutions by using the previous results of truncation error analysis. It seems also important to evaluate the possible effects of the shape of the input log-conductivity (a Markov spectrum was used in the case at hand). The influence of the log-conductivity spectrum on stochastic flow and transport solutions was discussed in section 3.2 of Chapter 3 ("infrared" and "ultraviolet" divergences of Fourier integrals). At any rate, the simulation results of Chapter 6, section 6.3, clearly show that the "improved" spectral theory provides a reasonably accurate approximation of the groundwater velocity covariance for a wide range of conductivity variability, at least for the specific case of an isotropic Markov log-conductivity field with exponential covariance.

Overall, we may conclude that the single-realization approach to stochastic groundwater flow led to statistical results similar to those obtained by the infinite-domain spectral theory, at least for a choice of domain size and boundary conditions that guaranteed the approximate statistical homogeneity of second order moments of the flow field (after empirical detrending). This encouraging result seems to confirm the operational character of the homogeneity/ergodicity hypothesis on which the spectral theory depends, at least for steady state groundwater flow in sufficiently deep aquifers and

approximately constant "regional" hydraulic gradient. On the other hand, the limitations of the homogeneity/ergodicity hypothesis appeared to be much more severe in the case of complex nonlinear flow systems, such as infiltration in randomly heterogeneous unsaturated soils (Chapter 7). . The numerical single-realization solutions of infiltration are now being discussed.

In the case of transient infiltration from localized (strip) source in moderately dry random soils, it seemed quite obvious that no large three-dimensional flow region of approximate statistical homogeneity developed during the time scales of simulations (on the order of days or weeks). Nevertheless, visual inspection of the time-dependent three-dimensional pressure fields revealed some global features of evolving unsaturated plumes in heterogeneous soils. It was observed that maximum variability of the pressure field occured when the level and the slope of the unsaturated log-conductivity curve were both random and statistically independent. In the case of statistically isotropic soil, the shape of the wetted zone at early times of strip-source infiltration appeared to be extremely contorted in 3D space, but with little lateral spreading. On the other hand, there was a pronounced lateral spreading away from the strip source in the case of statistically stratified soils (vertical/horizontal anisotropy ratio equal to

1/4). Based on the spatial pattern of pressure contours observed during infiltration and drainage, the anisotropy of the flow field appeared to be pressure-dependent, with a more pronounced lateral spreading of the edges of the moisture plume (marginally wet) than inside the core of the plume (wet). This is qualitatively similar to the behavior predicted by Mantoglou and Gelhar (1987) based on their linearized spectral solutions of transient unsaturated flow (the anisotropy of the wetting effective conductivity is more pronounced in dry regions than in wet regions).

In spite of the large size of the grid (300,000 nodes) it seemed preposterous to attempt a quantitative statistical analysis of the above strip-source experiment, as the unsaturated plume remained too small to sample a sufficiently large "spectrum" of soil heterogeneities. Indeed, some of the features of the simulated moisture pattern seemed to be specifically related to the idiosyncracies of the heterogeneous environment (the particular random field realization of hydraulic parameters) and to boundary and initial conditions (strip width, input flux and initial pressure head). In view of these limitations, it may be useful to examine from a more general point of view the possibility of obtaining statistically meaningful realizations of transient unsaturated flow in typical situations.

The case of the accidental spill of a radioactive liquid at the Hanford site can be used here for illustration (see Chapter 1, and the report by Rouston et al. 1979 for details). As a first approximation - although admittedly a crude one - let us assume that the contaminant plume can be equated to the unsaturated plume. The source located near soil surface, can be assimilated to a disc with a diameter of a few meters. Due to the axi-symmetry of the source, we expect that the moisture or contamination pattern be more nearly statistically homogeneous tangentially around the axis of the source than along any other direction ("axi-symmetric homogeneity"). Finally, note that the time and length scales of interest could be a few decades and several tens or hundreds of meters, or perhaps much more. In comparison, the natural fluctuation scales of the formation heterogeneities could be on the order of a fraction of a meter or perhaps several meters.

The key question is whether the statistical properties of the three-dimensional unsaturated plume (real or simulated) will converge to some stable quantities as time goes on. Unfortunately, it seems clear from our example that a direct numerical simulation similar to the highly detailed simulations of strip source infiltration obtained in this work, will be extraordinarily prohibitive given the time and length scales of interest: perhaps tens of millions of mesh points, and hundreds

of hours of supercomputer time on a Cray 2 machine). Thus our hypothetical example leads us to conclude that some of the features of the current single realization approach may have to be altered before a meaningful and accurate characterization of evolving unsaturated plumes can be achieved for the very large time and length scales of interest. Essentially the same remarks apply to the similar problem of evolving contaminant plumes in groundwaters. To our knowledge, there exists at present no satisfactory simulation (high resolution — large time scale) of these types of phenomena that could be used for testing existing analytical theories.

On the other hand, in the case of a steady state unsaturated flow ("rainfall" infiltration), we have found a relatively good agreement between numerical results and the linearized spectral solutions of Mantoglou and Gelhar (1987) and Yeh et al. (1985). The steady state pressure field obtained for a statistically anisotropic soil was analyzed by the same spatial averaging method used in groundwater flow simulations, assuming a statistically homogeneous random field of pressure in all three space directions. The pressure head standard deviation and the vertical component of the effective unsaturated conductivity were both within 20% of the theoretical spectral solutions. This encouraging result is of interest for applications involving toxic wastes buried in dry formations characterized by a very

slow (downward?) flow of water, as in the hypothetical scenario discussed by Winograd (1981). In such cases, the simulated unsaturated water velocity field, if obtained on sufficiently large high-resolution grid, could be used to simulate the transport of a radioactive solute leaking from the buried source. Note that the present "rainfall" infiltration experiment on a 300,000 node grid involved a relatively "modest" domain size (5m x 15m x 15m) and a relatively high downward flux (213 mm/year) compared to only 2 mm/year at the Yucca Flat site in Nevada (approximate evaluation by Winograd, 1981). The time scale of interest for contaminant transport could be thousands of years or more.

It remains to be seen whether detailed simulations of very large steady state unsaturated flow fields in extremely dry heterogeneous formations can be obtained at reasonable costs with the present version of our unsaturated flow simulator. At any rate, the present results strongly suggest that the linearized spectral solutions of Mantoglou and Gelhar (1987) may provide an adequate characterization of pressure variability and effective conductivity in such cases. This is in contrast with the case of transient infiltration/drainage from localized sources, where the question of the validity of the homogeneity/ergodicity postulate remains open.

[b] Summary of contributions

It may be useful at this point to recapitulate in a compact form the main findings of this work, with a highlight on new approaches and results. For convenience, we follow the order of exposition adopted in this report; analytical results of Chapters 3 and 4, numerical analyses of Chapter 5, and statistical analyses and interpretation of single-realization simulations in Chapters 6 and 7. A header is used to indicate the nature of the results being summarized (analytical results, numerical analysis, simulation results):

Analytical Results: Explicit characterization of the stochastic hydraulic head and groundwater velocity fields by using the spectral solution method of Gelhar and Axness (1983) in the case of statistically stratified aquifers: new results concerning the statistical anisotropy of the flow field and the applicability of the theory for finite-thickness aquifers.

Analytical Results: Non-perturbative spectral relations for stochastic groundwater flow in statistically isotropic formulations. Test of first order spectral solutions: they satisfy all the non-perturbative

spectral relations between the flux and head spectra in 1,2,3 dimensions. In particular, an equation relating the flux and head spectra is shown to be "exact" in the 2D case.

Analytical Result: New closed form expression for the effective conductivity of stochastic groundwater flow systems in the general case of 3D statistical anisotropy. This conjectural expression fits most of previously established results (Matheron 1967; Gelhar and Axness 1983), including those known to be exact.

Analytical Result: "Improved" spectral approximation for the groundwater velocity spectrum based on a system of equations governing the velocity or flux vector. The velocity variances and the resulting macrodispersivity differ from the standard spectral results of Gelhar and Axness (1983). The behavior of both statistical properties appear more realistic with the new solutions. Numerical flow simulations also showed a better agreement with the new expressions for velocity variance.

Analytical Results: Self-similar model of randomness

and "spectral conditioning" approach for the characterization of stochastic flow and transport phenomena over finite and time dependent length scales. Quantification of effective flow and transport coefficients over finite size domains, and the uncertainty on these coefficients. For evolving phenomena such as a growing concentration plume in a 3D isotropic medium, the preliminary results suggest that macrodispersivity and effective conductivity increase while their uncertainty decreases.

Numerical Analysis: Truncation error analysis for the finite difference approximation of stochastic groundwater flow equation (a model of "random heat equation"). Explicit closed form evaluation of the root-mean-square error on the hydraulic head potential and on the water flux vector, for different types of random log-conductivity fields. The order of accuracy is fractional in the case of a "noisy" log-conductivity field such as the non-differentiable 3D isotropic

Markov field: 3/2 for the head and 1/2 for the flux, in terms of the mesh size resolution ($\Delta x/\lambda$).

Numerical Analysis: Evaluation of the true solution

error due to the approximate factorization and iterative solution of the finite difference system with the SIP solver. The residual error underestimate the true error in cases of slow convergence. Applications and numerical experiments for stochastic groundwater flow systems with grid size up to 1 million nodes. Analysis of convergence rate (inversely proportional to the unidirectional size of the grid).

Numerical Analysis: Non-standard stability analysis of the time-implicit finite difference approximation of the nonlinear unsaturated flow equation. A Peclet number constraint $Pe \leq 2$ is required for nonlinear stability. Note $Pe = \alpha \Delta x_1$, where α is the slope of the log-conductivity function of pressure, and Δx_1 the vertical mesh size. A severe constraint on the time step size could result if this Peclet condition was not satisfied everywhere, as may occur when α is a random field.

Simulation Results: Most of the spectral results of stochastic groundwater flow were confirmed by statistical analysis of single-realization flow fields, with random hydraulic conductivities generated by the 3D turning band method. The limitations of the

spectral results in the case of high variability and finite domains (shallow aquifers) were analyzed in detail. The simulations involved 3D grids of size 100,000 to 1 million nodes, and statistically isotropic as well as anisotropic random log-conductivities with standard deviations from $\sigma = 1$ up to 2.3. In the isotropic case, both the hydraulic head and the velocity field were thoroughly analyzed.

Simulation Results: The case of localized infiltration in three-dimensional heterogeneous soils with random unsaturated conductivity curves was explored by the single-realization approach with exceptionally fine grid resolution (from 25,000 up to 300,000 nodes). The wetting pattern appeared to be very sensitive to the variability and anisotropy of the conductivity parameters (especially the slope of the log-conductivity curve). The study includes in particular a comprehensive qualitative analysis of infiltration and drainage on a statistically stratified soil (20 days, 5m x 15m x 15m, and 300,000 nodes).

Simulation Results: Steady state "rainfall" infiltration (213 mm/year) on a statistically stratified soil (5m x 15m x 15m, and 300,000 nodes).

The results of statistical analysis were in agreement with the linearized spectral solutions of Mantoglou and Gelhar 1987 (pressure head variance, and unsaturated effective conductivity).

[c] Outlook of stochastic approaches:

Some of the new methods and results developed in this work, particularly the approach of "spectral conditioning" and the results obtained by single-realization simulations, suggest some possible modifications of current conceptual approaches of naturally heterogeneous subsurface flow and transport phenomena. Originally, one of the leitmotives of this work was that such phenomena can be represented by single spatial replicas of statistically homogeneous and ergodic random fields. At first sight, the single replica postulate seems to be a natural working hypothesis for the study of randomly heterogeneous phenomena, since events actually take place in a "single world" rather than through some hypothetical ensemble space. Furthermore, the homogeneity-ergodicity postulate can be justified intuitively by the observation that such physical phenomena, taking place in heterogeneous environments over large length scales, may become globally homogeneous after many natural fluctuations have been encountered. The idea of balanced compensation is in fact at the root of our intuitive understanding of the concept of "chance"

(law of large numbers: stable and equal frequencies for head or tail in a game of coin tossing).

Accordingly, the "ergodic" or "single realization" approach purports that spatially heterogeneous subsurface phenomena may be characterized uniquely by a few statistical parameters. These parameters describe spatial fluctuations in a synthetic manner, in the same sense that the mean, amplitude, and wavelength characterize entirely a sinusoidal signal. In the language of random fields, the equivalent statistical quantities are the mean, standard deviation, and correlation lengths. Similarly, the concept of cross-correlation between two random fields can be related to the phase difference between two periodic signals. This simple analogy illustrates the fact that deterministic (periodic) as well as random (ergodic) spatial fluctuations can be characterized in terms of spatial moments without any explicit recourse to a hypothetical ensemble space. In summary, the ergodic "single-world" approach focuses on a single flow/transport event, taking place in "infinite" physical space, and whose statistical properties describe uniquely the spatial structure and global transport properties of the phenomenon at hand.

However, the single-world approach might be challenged on the grounds that natural flow and transport phenomena take place over finite or evolving length scales rather than in

infinite space. A difficulty of this nature was encountered with some of the numerical single-realization simulations analyzed in this work, particularly for steady groundwater flow in *shallow* stratified aquifers, and for transient infiltration from *localized* sources (evolving moisture plume over a time scale of days or weeks). In the latter case in particular, it seemed clear that the assumptions of infinite domain, homogeneity and ergodicity, were not operational. In view of this crucial difficulty, it may be useful to consider alternative methodologies.

Some alternative stochastic approaches proposed in the literature do not have recourse to the postulate of homogeneity/ergodicity of subsurface flow/transport phenomena. Broadly speaking, these approaches are based on an ensemble characterizat ion of the statistical properties of random phenomena, and rely more or less explicitly on the notions of uncertainty and risk. The case of stochastic groundwater flow was tackled along these lines by Dagan (1982), Townley (1983), McLaughlin (1985), and Ma et al. (1987), using various mathematical methods (approximate Green functions, numerical solution of approximate moment equations, Monte-Carlo simulations). In these ensemble approaches, the concept of uncertainty seems to play a major role, particularly for phenomena of a local nature (e.g. uncertainty of drawdowns near a

pumping well). Nevertheless, there remains some ambiguity concerning the physical meaning of the statistical results obtained by the proponents of the ensemble approach in some applications (uncertainty or spatial variability ?). This question might be clarified by a simple hypothetical example in the area of groundwater contamination.

Consider the case of an evolving concentration plume due to the continuous release of a contaminant from a local source in a heterogeneous aquifer. Depending on the configuration of local heterogeneities near the source, the plume may initially take an extremely asymmetrical shape, or even split in two distinct parts. An example of plume splitting can be seen for instance in Figure 7.6 (bottom) in the case of a moisture plume during strip source infiltration. See also the very different moisture patterns observed in two distant vertical planes along a strip source (top and bottom parts of Figure 7.12). Now, it seems possible that some of the asymmetry and inhomogeneity observed at early times will persist as time goes on, despite increasing homogeneization and mixing with increasing travel distance. The peculiar features of the evolving plume are determined by the idiosyncracies of the heterogeneous formation in the neighborhood of the source, and depend on the exact location of the source in situ. With these considerations in mind, it seems clear that localized or evolving

flow and transport phenomena can be characterized by a certain degree of uncertainty. At the same time, the concept of "effective" or "large scale" transport properties (like effective conductivity and macrodispersivity) may still be relevant, provided that the particular length scale of interest be taken into account.

The analytical approach of *spectral conditioning*, developed in this work, may be one consistent way of combining the ensemble and single world approaches. The ensemble viewpoint enters into play by assigning uncertainty to the actual location of the contamination event in a single, randomly heterogeneous formation. The single world approach intervenes in the definition of global or effective transport properties at the scale of interest. Along these lines, it seems possible to design, in parallel to the spectral conditioning approach, a numerical simulation method somewhat similar to the single-realization approach implemented in this work. For instance, the fate of a contaminant released from a local source could be studied by solving numerically the flow and transport equations in a single realization of the random formation, using Monte-Carlo simulations to sample several possible locations of the source with respect to the detailed configuration of the heterogeneous porous formation.

REFERENCES

R. Ababou, (1981), "Modélisation Des Transferts Hydriques Dans Le Sol En Irrigation Localisée"; Dr.-Ing. Thesis, Inst. Nat. Polytech. and Univ. of Grenoble, France, (218 pp).

R. Ababou, D. McLaughlin, L. W. Gelhar, and A. F. B. Tompson, (1985), "Numerical Simulation of Saturated Flow Fields in Randomly Heterogeneous Porous Media"; in The Stochastic Approach to Subsurface Flow, pre-prints International Symposium, A.I.R.H., Montvillargennes, France, June, 1985.

R. Ababou, (1986), "Self-Similar Random Fields", Unpublished report (written under the advisorship of B. Mandelbrot), M.I.T. and Harvard University, 25 pp.

R. Ababou, D. McLaughlin, L. W. Gelhar, A. F. B. Tompson, (1987), "Numerical Simulation of Three-Dimensional Saturated Flow in Randomly Heterogeneous Porous Media", paper submitted to the *Journal of Transport in Porous Media*, J. Bear, ed.

R. J. Adler, (1981), The Geometry of Random Fields, Wiley, New York, 280 pp.

A. A. Bakr, (1976), "Stochastic Analysis of the Effect of Spatial Variations of Hydraulic Conductivity on Groundwater Flow," PhD Thesis, New Mexico Instit. of Mining and Technology, Socorro, New Mexico.

A. A. Bakr, L. W. Gelhar, A. L. Gutjahr, and R. J. McMillan, (1978), "Stochastic Analysis of Spatial Variability in Subsurface Flow (1) - Comparison of One and Three Dimensional Flows"; *Water Res. Res.* *14*(2).

F. Ballhaus, A. Jameson, and J. Albert, (1977), "Implicit Approximate-Factorization Schemes for the Efficient Solution of Steady Transonic Flow Problems," AIAA Paper, 77-634, 8 pp.

M. S. Bartlett, (1946), "On the Theoretical Specification and Sampling Properties of Autocorrelated Times Series", J. Royal Stat. Soc., Vol. 38, No. 27.

G. K. Batchelor, (1953), The Theory of Homogeneous Turbulence, Cambridge Univ. Press (197 pp.).

J. Bear, (1972), Dynamics of Fluids in Porous Media, American Elsevier, New York (746 pp).

C. M. Bender and S. A. Orszag, (1978), Advanced Mathematical Methods for Scientists and Engineers, McGraw-Hill, New York, (593 pp).

A. A. Binsariti, (1980), "Statistical Analyzes and Stochastic Modelling of the Contaro Aquifer in Southern Arizona", PhD dissertation, Dept. of Hydrol. and Water Resour., Univer. Ariz., Tucson.

G. Birkhoff and A. Schoenstadt, (1984), Elliptic Problem Solvers II, (*Proc. Elliptic Problem Solvers Conf.*, Monterey, California, January, 1983), Acad. Press, 573 pp.

J. Bjordammen and K. H. Coats, (1969), "Comparison of Alternative-Direction and Successive Overrelaxation Techniques in Simulation of Reservoir Fluid Flow", Trans. Soc. Petrol. Eng., March, 1969.

A. Brandt, (1977), "Multi-Level Adaptive Solutions for Boundary Value Problems"; *Mathematics of Computations*, 31,(138), 333-390 pp, April, 1977.

P. A. Burrough, (1981), "Fractal Dimensions of Landscapes and Other Environmental Data", *Nature*, Vol. 294, 238-242, 19 November, 1981.

H. S. Carslaw, and J. C. Jaeger, (1959), Conduction of Heat in Solids, Oxford Univ. Press (510 pp).

M. Celia and G. Pinder, (1985), "An Analysis of Alternate Directions Methods for Parabolic Equations," *Journal of Numerical Methods for Partial Differential Equations*, Vol. 1, 57-70 pp.

P. M. Clifton, S. P.Neuman, 1982, "Effects of Kriging and Inverse Modeling on Conditional Simulation of the Arra Valley Aquifer in Southern Arizona", *Water Res. Res.*, 18 (4), 1215-1234.

R. Cooley, (1974), "Finite Element Solutions for the Equations of Groundwater Flow"; Tech. Report series H-W, No. 18, Center for Water Res. Res., University of Nevada, Desert Research Institute, Nevada, 1974.

R. Cooley, (1983), "Some New Procedures for the Numerical Solution of Variably Saturated Flow Problems"; *Water Res. Res.* 19(5), 1271-1285 pp, 1983.

H. S. M. Coxeter, (1973), Regular Polytopes. Dover, 321 pp.

G. Dagan, (1981), "Analysis of Flow Through Heterogeneous Random Aquifers by the Method of Embedding Matrix, 1: Steady Flow"; *Water Res. Res.*, *17*(1), 107-121, 1981.

G. Dagan, (1982), "Stochastic Modeling of Groundwater Flow by Unconditional and Conditional Probabilities: (1) Conditional Simulation and the Direct Problem"; *Water Res. Res.* *18*(4), 813-833 pp, 1982.

G. Dagan, and E. Bresler, (1983), "Unsaturated Flow in Spatially Variable Fields, (1) Derivation of Models of Infiltration and Redistribution"; *Water Res. Res.* 19(2), 413-420 pp.

G. Dagan, (1985), "A Note on the Higher-Order Corrections of the Head Covariances in Steady Aquifer Flow", *Water Res. Res.* *21*(4), 573-578 pp.

G. Dagan, (1987), "Solute Transport in Groundwater", to be published in *Annual Review of Fluid Mechanics*, 19, 1987.

H. P. G. Darcy, (1856), "Les Fontaines Publiques de la Ville de Dijon, Exposition et Application des Principes à Suivre et des Formules à Employer dans les Questions de Distribution d'Eau", Victor Dalmont, Paris, 1856.

L. A. Davis and S. P. Neuman, (1983), "Documentation and User's Guide: UNSAT2-Variably Saturated Flow Model", Final Report WWL/TM-1791-1, W.W.L., Inc. (for U.S.N.R.C.) Fort-Collins, December, 1983.

J. P. Delhomme, (1979), "Spatial Variability and Uncertainty in Groundwater Flow Parameters: A Geostatistical Approach", *Water Res. Res.* *15*, 269-280 pp, 1979.

J. L. Devary, P. G. Doctor, 1982, "Pore Velocity Estimation Uncertainties", *Water Res. Res.*, *18*(4), 1157-1164.

J. Douglas, (1962), "Alternating Direction Methods for Three Space Variables", *Numerische Mathematik*, *4*, 411-463 pp.

T. DuPont, R. P. Kendall and H. H. Rachford, (1968), "An Approximate Factorization Procedure for Solving Self-Adjoint Elliptic Difference Equations", *SIAM J. Numer. Anal.*, Vol. 5, No. 3, September, 1968.

T. Dupont, (1968), "A Factorization Procedure for the Solution of Elliptic Difference Equations", *SIAM J. Numer. Anal.*, Vol. 5, No. 4, December, 1968.

D. J. Evans, (1981), "On Preconditioned Iterative Methods for Elliptic PDE's" in Elliptic Problem Solver I, Academic Press, New York.

D. J. Evans, (1983), Preconditioning Methods: Analysis and Applications, Ed. D. J. Evans, Gordon and Breach, New York, 1983.

D. J. Evans, (1984), "Implicit Block Explicit Overrelaxation Schemes" in Elliptic Problem Solver II, (*Proc. Elliptic Problem Solvers Conf.*, Monterey, Calif., Jan. 1983), Academic Press, 573 pp.

G. S. Fishman, L. R. Moore, (1986), "An Exhaustive Analysis of Multiplicative Congruential Random Number Generators with Modulus $2^{31}-1$", *SIAM J. Sci. Stat. Comput.*, Vol. 7, No. 1, January.

G. E. Forsythe and W. R. Wasow, (1960), Finite-Difference Methods for Partial Differential Equations, Wiley and Sons, New York.

R. A. Freeze, (1971), "Three-Dimensional Transient, Saturated Unsaturated Flow in a Groundwater Basin", *Water Res. Res.*, 7(2), 1971.

R. A. Freeze, (1975), "Stochastic-Conceptual Analysis of One Dimensional Groundwater Flow in Nonuniform Homogeneous Media", *Water Res. Res.* 11, 725-741 pp., 1975.

Y. M. Gajem, A. W. Warrick, and D. E. Myers, (1981), "Spatial Dependence of Physical Properties of a Typic Torrifluvent Soil", *Soil Sci. Soc. Am. J.*, Vol. 45, 709-715 pp.

G. Gambolati and A.M. Perdon, (1984), "The Conjugate Gradients in Subsurface Flow and Land Subsidence Modelling", in Fundamentals of Transport Phenomena in Porous Media, J. Bear and M. Y. Corapcioglu, Eds., The Hague, 1984.

L. W. Gelhar, (1976), "Stochastic Analysis of Flow in Aquifers", Advances in Groundwater Hydrology, *Proceedings, 1976 Symposium of the Amer. Water Resources Assoc.*, Minneapolis, Minnesota.

L. W. Gelhar, (1984), "Stochastic Analysis of Flow in Heterogeneous Porous Media" in Selected Topics in Mechanics of Fluids in Porous Media, *Proceedings NATO Symposium*, Eds. Bear and Corapcioglu, Martinus Nijhoff publishers, Dordrecht, The Netherlands, 673-718.

L. W. Gelhar, P. J. Wierenga, K. R. Rehfeldt, C. J. Duffy, M. J. Simonett, T.-C. Yeh, and W.R. Strong, (1982), "Irrigation Return Flow Water Quality Monitoring, Modeling, and Variability in the Middle Rio Grande Valley, New Mexico", EPA Report 600/2-83-072, New Mexico Inst. of Mining and Tech., Socorro, New Mexico.

L. W. Gelhar, and C. L. Axness, (1983), "Three Dimensional Stochastic Analysis of Macrodispersion in Aquifers", *Water Res. Res.* 19(1), 161-180 pp.

L. W. Gelhar, A. Mantoglou, C. Welty, and K. Rehfeldt, (1984), "A Review of Field Scale Subsurface Solute Transport Processes Under Saturated and Unsaturated Conditions", Report RP-22485-05, Electrical Power Research Institute.

L. W. Gelhar, (1986), "Stochastic Subsurface Hydrology from Theory to Applications", *Water. Res. Res.*, 22(99), 135-145 pp.

L. W. Gelhar, (1987), "Stochastic Analysis of Solute Transport in Saturated and Unsaturated Porous Media", Fundamentals of Transport in Porous Media, ed. J. Bear and M. Y. Corapcioglu, Martinus Nijhoff publishers, Dordrecht, The Netherlands, 657-700.

S. Godunov, (1973), Equations de la Physique Mathematique, ed. MIR, Moscow (French translation from Russian).

G. H. Golub and C. F. Van Loan, (1983), Matrix Computations, The John Hopkins Univ. Press, Baltimore

I. S. Gradshteyn and I. M. Ryzhik, (1980), Table of Integrals, Series, and Products, (ed. A. Jeffrey), Academic Press, New York (1160 pp).

I. Gustafsson, (1978), "A Class of First Order Factorization Methods," BIT (*Nordisk Tidskrift for Inform. Behandling*), 18, 1442-156 pp.

A. L. Gutjahr, L. W. Gelhar, A. A. Bakr, and R. J. MacMillan, (1978), "Stochastic Analysis of Spatial Variability in Subsurface Flows, (2) Evaluation and Application", *Water Res. Res.*, 14(5), 953-959 pp.

A. L. Gutjhar, and L. W. Gelhar, (1981), "Stochastic Models for Subsurface Flow; Infinite Versus Finite Domains and Stationarity", *Water Res. Res.* 17(2), 337-350 pp.

A. L. Gutjahr, (1984), "Stochastic Models of Subsurface Flow: Log Linearized Gaussian Models are Exact for Covariances", *Water Res. Res.*, 20, 1909-1912 pp.

L. A. Hageman and D. M. Young, (1981), Applied Iterative Methods, Acad. Press, New York.

R. Haverkamp and M. Vauclin, (1979), "A Note on Estimating Finite Difference Interblock Hydraulic Conductivity Value for Transient Unsaturated Flow Problems", *Water Res. Res.* 15(1).

M. R. Hestenes and E. Stiefel, (1952), "Method of Conjugate Gradients for Solving Linear Systems", Nat. Bureau of Standards, *J. Res.*, 49, 409-436.

R. J. Hoeksema, and P. K. Kitanidis, (1985), "Analysis of the Spatial Structure of Properties of Selected Aquifers", *Water Res. Res.* 21(4), 563-572 pp.

A. S. Householder, (1964), The Theory of Matrices in Numerical Analysis, Dover Publications, New York, 1964 and 1975.

P. Hufschmied, (1985), "Estimation of Three Dimensional Statistically Anisotropic Hydraulic Conductivity Field by Means of Single Well Pumping Tests Combined with Flowmeter Measurements", in The Stochastic Approach to Subsurface Flow, pre-prints International Symposium, A.I.R.H., Montvillargenne, France, June 1985.

P. S. Huyakorn and G. F. Pinder, (1983), Computational Methods in Subsurface Flow, Academic Press, New York

P. S. Huyakorn , .S. D. Thomas, and B. M. Thompson, (1984), "Techniques for Making Finite Elements Competitive in Modeling Flow in Variably Saturated Porous Media" , *Water Res. Res.*, 20(8), 1099-1115 pp.

C. P. Jackson and P. C. Robinson, (1985), "A Numerical Study of Various Algorithms Related to the Preconditioned Conjugate Gradient Method", *Int. J. Num. Methods in Eng.*, Vol. 21, 1315-1338.

D. A. H. Jacobs, (1981), "The Exploitation of Sparsity by Iterative Methods in Sparse Matrices and their Use, *Proceedings* edited by C. S. Duff, Academic Press, New York.

A. H. Jacobs, (1983), "Preconditioned Conjugate Gradient Algorithms for Solving Finite Difference Systems", in Preconditioning Methods: Analysis and Applications, Ed. D. J. Evans, Gordon and Breach, New York, 1983.

W. A. Jury, and L. H. Stolzy, (1982), "A Field Test of the Transfer Function Model for Predicting Solute Transport", *Water Res. Res.* 18(2), 369-375 pp., 1982.

W. A. Jury, G. Sposito, and White, (1986), " A Transfer Function Model of Solute Transport Thru Soil: (1)Fundamental Concepts", Water Res. Res. 22(2), 243-247 pp.

M. G. Kendall, A. Stuart, (1977), "The Advanced Theory of Statistics", Vol. 1, Distribution Theory, MacMillan, New York, 472 pp.

B. C. Kent, C. R. Mauldin, M. W. Cooper, (1982), "Evaluation of Subsurface Migration from Solar Ponds", *Underground Resource Management Report*, Austin, TX.

D. S. Kershaw, (1978), "The Incomplete Choleski-Conjugate Gradient Method for the Iterative Solution of Systems of Linear Equations", J. Comput. Physics, 2-6, 43-65 pp.

G. R. Kirchhoff, (1894), "Vorlesungen uber die Theorie der Warme".

G. A. Korn and T. M. Korn, (1968), Mathematical Handbook for Scientists and Engineers, McGraw-Hill, New York, 2nd Edition, (1130 pp).

L. K. Kuiper, (1981), "A Comparison of the Incomplete Choleski-Conjugate Gradient Method with the Strongly Implicit Method as Applied to the Solution of Two-Dimensional Groundwater Flow Equations", Water Res. Res. 17(6), pp 1082-1086.

L. K. Kuiper, (1987), "A Comparison of Iterative Methods as Applied to the Solution of the Nonlinear Three-Dimensional Groundwater Flow Equation" *SIAM Journal on Sci. Stat. Computing*, 8(4), July, 1987.

M. T. Landahl and E. Mollo-Christensen, (1986), Turbulence and Random Processes in Fluid Mechanics, Cambridge Univ. Press. (154 pp.).

M. Loève, (1963, 1978), Probability Theory, Vol. II; Springer-Verlag, 1978.

R. J. Luxmoore, B. P. Spaulding, I. M. Munro, (1981), "Areal Variation and Chemical Modification of Weathered Shale Infiltration Characteristics", *Soil Sci. Soc. Am. J.*, 45, 687-691.

F. Ma, M. S. Wei, W. H. Mills, (1987), "Correlation Structuring and the Statistical Analysis of Steady-State Groundwater Flow", SIAM J. Sci. Stat. Comput.,Vol. 8, No. 5, 848-867.

B. B. Mandelbrot and J. W. Van Ness, (1968), "Fractional Brownian Motions, Fractional Noises and Applications", *SIAM Review, Vol. 10*, No. 4, 422-437.

B. B. Mandelbrot and J. R. Wallis, (1969), "Some Long-Run Properties of Geophysical Records", *Water Resource Research, Vol.* 5, No. 2, pp. 321-340.

B. B. Mandelbrot, (1983), The Fractal Geometry of Nature, Freeman and Co., New York, (468 pp)

B. B. Mandelbrot, D. E. Passoja, A. J. Paullay, (1984), "Fractal Character of Fracture Surfaces of Metals," *Nature, Vol.* 308, No. 5961, pp. 721-722, 19 April 1984.

A. Mantoglou, and J. Wilson, (1982), "The Turning Bands Method for Simulation of Random Fields using Line Generation by a Spectral Method", *Water Res. Res.* 18(5), 1379-1394 pp.

A. Mantoglou, (1984), "Large-Scale Models of Transient Unsaturated Flow and Contaminant Transport Using Stochastic Methods", Ph.D. Thesis, M.I.T., Cambridge, Massachusetts.

A. Mantoglou, (1987), "Digital Simulation of Multivariate Two-and Three-Dimensional Stochastic Processes with a Spectral Turning Bands Method", *Mathemattcal Geology, Vol.* 19, No. 2, 129-149.

A. Mantoglou and L. W. Gelhar, (1987a), "Stochastic Modeling of Large-Scale Transient Unsaturated Flow Systems", *Water Res. Res.*, 23(1), 37-46.

A. Mantoglou and L. W. Gelhar, (1987b), "Capillary Tension Head Variance, Mean Soil Moisture Content, and Effective Specific Soil Moisture Capacity of Transient Unsaturated Flow in Stratified Soils", *Water Res. Res.*, 23(1), 47-56.

A. Mantoglou and L. W. Gelhar (1987c), "Effective Hydraulic Conductivities of Transient Unsaturated Flow in Stratified Soils", *Water Res. Res.*, 23(1), 57-67.

J. Marchant and R. Gabillard, (1975), Sur le calcul d'un réseau résistif aléatoire, Short Note in C.R.A.S.(Comptes-Rendus. Acad. Sci.), Paris, Vol. 281, Série B, 261-264, 6 Oct. 1975.

G. Matheron, (1967), Elements Pour une Théorie des Milieux Poreux, Masson et Cie, Paris, 1967 (164 pp).

G. Matheron, (1973), "The Intrinsic Random Functions and their Applications", *Adv. Appl. Prob.*, 5, 439-468 pp.

G. Matheron, (1984), "L'Emergence de la Loi de Darcy", *Annales des Mines*, No. 5-6, pp. 11-16, May-June, 1984, Paris School of Mines, France.

M. G. McDonald, and A. W. Harbaugh, (1984), "A Modular Three Dimensional Finite-Difference Groundwater Flow Model", U. S. Dept. Interior, and U. S. Geol. Survey, Nat. Center, Reston, Virginia (528 pp.).

D. McLaughlin, (1985), "A Distributed Parameter State Space Approach for Evaluating the Accuracy of Groundwater Predictions", Ph.D. thesis, Princeton Univ., Princeton, New Jersey.

J. A. Meijerink and H. A. Van der Vorst, (1977), "An Iterative Method for Linear Systems of which the Coefficient Matrix is a Symmetric M-Matrix", *Math. Comp.*, Jan. 1977.

P. C. D. Milly, (1985), "A Mass-Conservative Procedure for Time-Stepping in Models of Unsaturated Flow", *Adv. Water Resources*, Vol. 8, March, 32-36.

A. S. Monin and A. M. Yaglom, (1965), Statistical Fluid Mechanics: Mechanics of Turbulence (Volume 2), Ed. J. L. Lumley, The MIT Press, Cambridge, MA (874 pp).

R. L. Naff and A. V. Vecchia, (1986), "Stochastic Analysis of Three-Dimensional Flow in a Bounded Domain", *Water Resour. Res.*, 22(5), 695-704 pp.

D. R. Nielsen, J. W. Biggar, and K. T. Ehr, (1973), "Spatial Variability of Field-Measured Soil Water Properties", *Hilgardia*, 42, 215-260 pp., 1973.

S. A. Orszag, (1977), "Numerical Simulation of Turbulent Flows; Chapter 10" in Handbook of Turbulence, Vol. 1: Fundamentals and Applications, Plenum Press, Eds. Frost and Moulden, New York.

J. M. Ortega, and W. C. Rheinboldt, (1970), Iterative Solution of Nonlinear Equations in Several Variables, Academic Press, New York

J. Y. Parlange, (1972), "Theory of Water Movement in Soils: (5) Unsteady infiltration from Spherical Cavities", *Soil Sci.*, 113, 156-161 pp.

D. W. Peaceman, and H. H. Rachford, (1955), "The Numerical Solution of Parabolic and Elliptic Differential Equation", *J. SIAM*, 3, 1, 28-41 pp.

J. R. Philip, (1969) "Theory of Infiltration" in Advances in Hydroscience, 5, 1969, Acad. Press; N.Y.

P. A. C. Raats, (1971), "Some Properties of Flows in Unsaturated Soilds with an Exponential Dependence of Hydraulic Conductivity upon the Pressure Head", *J. of Hydrology*, 14, 129-138 pp.

A. E. Reisenauer, K. T. Key, T. N. Narasimhan and R. W. Nelson, (1982), "TRUST: A Computer Program for Variably Saturated Flow in Multidimensional, Deformable Media", Pacific Northwest Lab. Rep. NUREG/CR-2360, (for U.S. N.R.C.), Washington, D. C. January 1982.

I. Remson, G. M. Hornberger, and F. J. Molz, (1971), Numerical Methods in Subsurface Hydrology, Wiley-Interscience, New York.

R. C. Routson, W. H. Price, D. J. Brown, and K. R. Fecht, (1979), "High-Level Waste Leakage from the 241-T-106 Tank at Hanford"; Report RHO-ST-14, U. S. Department of Energy/Rockwell International, Richland, WA.

D. Russo, and E. Bresler, (1980), "Scaling Soil Hydraulic Properties of a Heterogeneous Field", *Soil Soc. Am. J.*, 44, 681-684.

D. Russo, and E. Bresler, (1981), "Soil Hydraulic Properties as Stochastic Processes. I: An Analysis of Field Spatial Variability", *Soil Soc. Am. J.*, 45, 682-687.

D. Russo, (1983), "A Geostatistical Approach to the Trickle Irrigation Design in Heterogeneous Soils, (1): Theory", *Water Res. Res.*, 19, 632-642 pp.

J. B. Scisson, and P. J. Wierenga, (1981), "Spatial Variability of Steady State Infiltration Rate as a Stochastic Process", *Soil Sci. Soc. Am. Journal*, 45 699-704 pp.

M. L. Sharma, G. A. Gander, C. G. Hunt, (1980), "Spatial Variability of Infiltration in a Watershed", *J. of Hydrology*, 45, 101-122.

M. Shinozuka, C. M. Jan, (1972), "Digital Simulation of Random Processes and its Applications" *J. Sound Vib.*, 25 (1), p. 111.

M. Shultz (editor), (1981), Elliptic Problem Solver, I, Acad. Press, New York.

C. S. Simmons, D. R. Nielsen, J. W. Biggar, (1979), "Scaling of Field-Measured Soil Water Properties", Hilgardia, 47 (4), 77-173, Sept. 1979.

M. Sivapalan, E. F. Wood, (1986), "Stochastic Description and Simulation of Nonstationary Space-Time Rainfall at the Catchment Scale", Chapman Conference on Modeling of Rainfall Fields, Proceedings, Caracas, 1986.

L. Smith, R. A. Freeze, (1979a), "Stochastic Analysis of Steady State Groundwater Flow in a Bounded Domain, 1: One-Dimensional Simulations", *Water Res.*, 15 (3), 521-528.

L. Smith, R. A. Freeze, (1979b), "Stochastic Analysis of Steady State Groundwater Flow in a Bounded Domain, 2: Two-Dimensional Simulations", *Water Res.*, 15(6), 1543-1559.

H. L. Stone, (1968), "Iterative Solution of Implicit Approximations of Multi-Dimensional Partial Differential Equations", *S.I.A.M. Journal Num. Anal.*, 5(3), Sept. 1968.

E. A. Sudicky, (1986), "A Natural Gradient Experiment on Solute Transport in a Sand Aquifer: Spatial Variability of Hydraulic Conductivity and its Role in the Dispersion Process", *Water Res. Res.*, 22 (13), 2069-2082.

A. F. B. Tompson, R. Ababou, and L. W. Gelhar, (1987), "Applications and Use of the Three-Dimensional Turning Band Random Field Generator in Hydrology: Single Realization Problems", Tech. Report. #313, Parsons Laboratory, M.I.T., Cambridge, MA (March, 1987).

L. Townley, (1983), "Numerical Models of Groundwater Flow: Prediction and Parameter Estimation in the Presence of Uncertainty", Ph.D. thesis, M.I.T., Cambridge, Mass., 1983.

S. J. Trauntwein, D. E. Daniel, and H. W. Cooper, (1983), "Case History Study of Water Flow Through Unsaturated Soils", in The Role of the Unsaturated Zone in Radioactive Hazardous Waste Disposal, Mercer et. al., Ann Arbor Science, Ann Arbor, MI.

P. C. Trescott, (1975),"Documentation of Finite-Difference Model for Simulation of Three-Dimensional Groundwater Flow", U.S. Geol. Survey, Open File Report 75-438 pp, Sept. 1975.

P. C. Trescott, and S. P. Larson, (1977), "Comparison of Iterative Methods of Solving Two-Dimensional Flow Equations", *Water Res. Res.* 13(1), 1977.

R. Van Genuchten, (1978), "Calculating the Unsaturated Hydraulic Conductivity with a New Closed-Form Analytical Model," Water Res. Program, Princeton University, (65 p)

M. Th. Van Genuchten, (1980), "A Closed Form Equation for Predicting the Hydraulic Conductivity of Unsatured Soils," *Soil Sci. Soc. Am., J., 44*, 892-898 pp.

E. Vanmarcke, (1983), Random Fields Analysis and Synthesis, The MIT Press, Cambridge, MA (382 pp).

R. Varga, (1962), Matrix Iterative Analysis, Prentice-Hall, Englewood Cliffs, N.J.

M. Vauclin, R. Haverkamp, and G. Vachaud, (1979), Résolution Numérique d'une Equation de Diffusion Nonlinéaire, P.U.G., Grenoble, 183 p.

M. Vauclin, J. Imbernon, and G. Vachaud, (1981), "Spatial Variability of Some Soil Physical Properties over One-Hectar Field Plot", AGU Chapman Conference, Fort-Collins, Colorado, July, 1981.

M. Vauclin, (1982), "Méthode d'étude de la Variabilité Spatiale des Propriétés d'un Sol", in Variabilité Spatiale des Processus de Transfert dans les Sols Avignon, France, June 1982, Ed. INRA publ., No. 15 9-43 pp.

S.R. Vieira, D. R. Nielsen and J. W. Biggar, (1981), "Spatial Variability of Field-Measured Infiltration Rate", *Soil Sci. Soc. Am. J.*, 45, 1040-1048.

E. Vomvoris, (1986). "Concentration Variability in Transport in Heterogeneous Aquifers: A Stochastic Analysis", Ph.D. thesis, Parsons Laboratory, M.I.T., Cambridge, MA.

A. W. Warrick, and D. O. Lomen, (1976), "Time Dependent Linearized Infiltration (III): Strip and Disc Sources)", *Soil Sci. Soc. Am. J.*, 40.

A. W. Warrick, G. J. Mullen and D. R. Nielsen, (1977), "Scaling Field-Measured Soil Hydraulic Properties Using a Similar Media Concept," *Water Res. Res.*, 13, 355-362.

A. W. Warrick, and Amoozegar-Fard, (1979), "Infiltration and Drainage Calculations Using a Similar Media Concept", *Water Res. Res.*, 13, 355-362 pp., 1977.

J. W. Watts, (1971), "An Iterative Matrix Solution Method Suitable for Anisotropic Problems", *Trans. Soc. Petrol. Eng.*, March 1971, 47-51 pp.

H. G. Weinstein, H. L. Stone, and T. V. Kwan, (1969), "Iterative Procedure for Solution of Systems of Parabolic and Elliptic Equations in Three Dimensions", *Industr. Engin. Chem., Fundamentals*, 8(2), 281-187 pp., 1969.

I. White and M. J. Sully, (1987), "Macroscopic and Microscopic Capillary Length and Time Scales from Field Infiltration", *Water Res. Res.*, 23, (8), 1516-1522.pp.

P. J. Wierenga, L. W. Gelhar, C. S. Simmons, G. W. Gee, and T. J. Nicholson (1986), "Validation of Stochastic Flow and Transport Models for Unsaturated Soils: A Comprehensive Field Study", Report NUREG/CR-4622 (U.S. Nuclear Regulatory Commission), Pacific Northwest Lab., Richland, WA.

P. J. Wierenga, I. Porro, W. Strong, J. Vinson, D. Hudson, M. Nash, and A. Schneeberger, (1986), "Validation of Stochastic Flow and Transport for Unsaturated Soils", Research Report 86-SS-01, Dept. Agronomy Agric., New Mexico State University, Las Cruces, NM.

K. G. Wilson and J. Kogut, (1974), "The Renormalization Group and the ϵ Expansion", *Physics Reports* (Section C of Physics Letters) 12 (2), 75-200.

K. G. Wilson, (1979) "Problems in Physics with Many Scales of Length", *Scientific American, Vol. 241, No. 2*, August, 1979.

K. G. Wilson, (1983), "The Renormalization Group and Critical Phenomena", *Review of Modern Physics*, 55(3), p. 583.

I. J. Winograd, (1981), "Radioactive Waste Disposal in Thick Unsaturated Zones," *Science, Vol. 212, No. 4502*, 1457-1464, June 26, 1981.

R. A. Wooding, (1968), "Steady Infiltration from a Shallow Circular Pond", *Water Res. Res.*, 4, No. 6, 1259-1273 pp.

G. T. Yeh and R. J. Luxmoore, (1983), "MATTUM: A Multidimensional Model for Simulating Moisture and Thermal Transport in Unsaturated Porous Media", *Env. Sci. Div. Publ. No.* 2009, Oak Ridge Nat. Lab. (for the U.S. Dept. of Energy).

G. T. Yeh (1985) "Comparisons of Successive Iteration and Direct Methods to Solve Finite Element Equations of Aquifer Contaminant Transport", *Water Res. Res.*, 21(3), 272-280 pp.

T.-C. Yeh, L. W. Gelhar, and A. L. Gutjhar, (1982), "Stochastic Analysis of Effects of Spatial Variability on Unsaturated Flow", Report No. H-11, New Mexico Institute of Mining and Technology, Socorro, N.M., July, 1982, (228 pp).

T.-C. Yeh, L. W. Gelhar, and A. L. Gutjhar, (1985a), "Stochastic Analysis of Unsaturated Flow in Heterogeneous Soils: (1) Statistically Anisotropic Media", Water Res. Res., 21(4), 447-456 pp., 1985.

T.-C. Yeh, L. W. Gelhar, and A. L. Gutjhar, (1985b), "Stochastic Analysis of Unsaturated Flow in Heterogeneous Soils: (2) Statistically Anisotropic Media with Variable α", Water Res. Res., 21((4), 457-464 pp.

T.-C. Yeh, L. W. Gelhar, and A. L. Gutjhar, (1985c), "Stochastic Analysis of Unsaturated Flow in Heterogeneous Soils: (3): Observations and Applications", Water Res. Res., 21(4), 465-471 pp.

D. M. Young, (1971), Iterative Solution of Large Linear Systems, Academic Press, New York.

APPENDIX 2A:
UNCERTAINTY OF SAMPLE STATISTICS FOR RANDOM VARIABLES AND RANDOM FIELDS

This appendix gives a brief overview of finite sample statistics for random variables, and adds further indications in the more general case of random fields. This may serve as a reference for parts of chapters 2 and 6 where some of the sample statistics are used to evaluate confidence intervals on spatial moments of single replicas of random fields. However, the present review is not meant to be a complete summary of available results in the literature.

1. Random variables:

The statistics of finite size samples of a random variable (y) are themselves random variables, whose variances quantify the uncertainty of finite size sample statistics. In the case where the sample size is reasonably large (say $n > 50$) the sample mean and the sample variance are defined, respectively, by:

$$\hat{\mu} = \frac{1}{n} \sum_i y_i$$

$$\hat{\sigma}^2 = \frac{1}{n-1} \sum_i (y_i - \hat{\mu})^2$$

and follow approximately the normal distributions:

$$\hat{\mu}: N(\mu, \sigma^2/n)$$
$$\hat{\sigma}^2: N(\sigma^2, 2\sigma^4/n)$$

Moreover, the sample standard derivation $\hat{\sigma}$ also follows approximately a normal distribution for sufficiently large n, as shown below:

$$\hat{\sigma}: N(\sigma, \sigma^2/2n)$$

These results can be found in many textbooks, for instance Kendall and Stuart (1977). Note that all three estimators are unbiased and convergent.

For practical applications, it may be useful to quantify the uncertainty of these sample statistics by defining a "relative error" (ϵ) as follows:

$$\epsilon(\mu) = \frac{(\mathrm{Var}(\hat{\mu}))^{1/2}}{\sigma}$$

$$\epsilon(\sigma^2) = \frac{(\mathrm{Var}(\hat{\sigma}^2))^{1/2}}{\sigma^2}$$

$$\epsilon(\sigma) = \frac{(\mathrm{Var}(\hat{\sigma}))^{1/2}}{\sigma}$$

Plugging the previous results in these expressions gives the relative errors on the sample mean, variance, and standard deviation as follows:

$$\epsilon(\mu) = \sqrt{1/n}$$
$$\epsilon(\sigma^2) = \sqrt{2/n}$$
$$\epsilon(\sigma) = \sqrt{1/2n}$$

As suggested in chapters 2 and 6, these formulas can be used also to evaluate (crudely) the uncertainty of sample statistics of finite size realizations of correlated random functions, with an appropriate definition of the "equivalent" number of independent samples (e.g. $n = L/\lambda$ for one-dimensional space).

2. Correlated random variables and random functions:

Let us point out other results of interest in the case of correlated random functions or discrete random processes (sequence of correlated random variables). Beginning with the case of two correlated random variables (y_1, y_2) following a bivariate normal distribution, Kendall and Stuart (1977) show that the variance of the sample correlation coefficient ($\hat{\rho}$) is given by:

$$\text{Var } (\hat{\rho}) = \frac{1}{n} (1-\rho)^2$$

However, Kendall and Stuart also point out that the sampling distribution of $\hat{\rho}$ tends very slowly to normality as n increases, so that using this formula to estimate confidence intervals on the true value (ρ) may be misleading.

For a discrete random process or a sequence of random variables, the sample correlation coefficient:

$$\hat{\rho}_i = \frac{1}{n-j} \sum_{i=1}^{n-j} Y_i \, Y_{i+j} \Big/ \frac{1}{n} \sum_{i=1}^{n} U_i^2$$

is unbiased for sufficiently large n, and its variance is given by:

$$\text{Var}(\hat{\rho}_i) = \frac{1}{n} \sum_{i=-\infty}^{+\infty} [\rho_i^2 + \rho_{i-j}\rho_{i+j} - 4\rho_i\rho_j\rho_{i+j} + 2\rho_i^2\rho_j^2].$$

The latter formula is due to Bartlett (1946).

Finally, for a stationary random function Y(x) of one-dimensional space (or time), the sample covariance function could be evaluated as:

$$\hat{R}(\xi) = \frac{1}{L}\int_{0}^{L-\xi} (Y(x) - \hat{\mu})(Y(x+\xi)-\hat{\mu})dx$$

for lag distance $\xi \leq L$, where L is the size of the available sample. The above estimator is unbiased. Bartlett (1946) gave the ensemble covariance between two values of the estimated covariance function at different lags (see also Vanmarcke, 1983). In particular, this yields the variance of the estimated covariance function:

$$\mathrm{Var}(\hat{R}(\xi)) = \frac{1}{L^2} \cdot \int_{0}^{L-\xi}\int_{0}^{L-\xi} \mathrm{Cov}(Y(x_1-\xi)\cdot Y(x_1), Y(x_2-\xi)\cdot Y(x_2))dx_1 dx_2$$

Alternatively, the domain of integration $(L-\xi)$ could be replaced by (L) to obtain unbiased estimates. With this modification and some further manipulations, it is easily shown that:

$$\boxed{\mathrm{Var}(\hat{R}(\xi)) = \frac{1}{L}\int_{-L}^{+L} (1 - \frac{|s|}{L})(R(s+\xi)\cdot R(s-\xi) + R^2(s))ds}$$

The latter formula gives explicitly the ensemble variance of the estimated covariance function at any lag distance $\xi \leq L$. Note

that an a-priori knowledge of the true covariance function is required.

It may be useful to illustrate the above formula in a simple case. Let $Y(x)$ be a one-dimensional random function with exponential covariance function:

$$R(\xi) = \sigma^2 \, e^{-|\xi|/\lambda}$$

where σ^2 is the variance and λ the integral correlation scale of $Y(x)$. After some tedious but straightforward integrations, we obtained a closed-form expression for the squared relative error defined as:

$$\epsilon^2(\xi) = \mathrm{Var}(\hat{R}(\xi))/R(\xi)^2.$$

In particular, that expression could be simplified in the case $L >> \lambda$ (large number of equivalent independent samples). The result is given below:

$$\epsilon^2(\xi) \simeq \frac{2\lambda}{L} \cdot [1 - \frac{1}{2}\frac{\xi}{L} - \frac{1}{4}\frac{\lambda}{L} + \frac{\xi}{\lambda}(1 - \frac{\xi}{2L})].$$

At zero lag ($\xi = 0$) this gives the relative error on the estimated variance:

$$\epsilon^2(0) \simeq 2\frac{\lambda}{L}\left(1 - \frac{1}{4}\frac{\lambda}{L}\right)$$

which, by comparison with the result obtained for the estimated variance of a single random variable ($\epsilon^2 = 2/n$), illustrates that for $\lambda/L \ll 1$ the number of independent samples becomes $n = L/\lambda$. For intermediate lag distances, say $\xi = \lambda$, the relative error is approximately (using $\lambda \ll L$):

$$\epsilon^2(\lambda) \simeq 4\frac{\lambda}{L}.$$

Finally, at large lag distances $\xi \gg \lambda$, one obtains a large relative error that goes to unity (100%) as ξ goes to L. These simple results could probably be generalized to treat the case of discrete finite realizations of three-dimensional fields.

APPENDIX 3.A

CLOSED FORM EVALUATION OF THE HEAD GRADIENT VARIANCES FOR THE 3D ISOTROPIC MARKOV SPECTRUM

Assuming for convenience that the mean hydraulic gradient J is aligned with the x_i axis, and denoting $h_i = \frac{\partial h}{\partial x_i}$ the gradient of head perturbation, the spectrum of the head gradient field is, from Section 3.1:

$$S_{h_i,h_j}(\underline{k}) = k_i k_j \frac{J_i^2 k_i^2}{k^4} S_{ff}(\underline{k}).$$

In particular, this gives:

$$\sum_i S_{h_i,h_i}(\underline{k}) = \frac{J_i^2 k_i^2}{k^2} S_{ff}(\underline{k})$$

$$\sum_i \sigma_{h_i}^2 = \sigma_{h_1}^2 + \sigma_{h_2}^2 + \sigma_{h_3}^2 = \iiint_{-\infty}^{+\infty} \frac{J_i^2 k_i^2}{k^2} S_{ff}(\underline{k}) \, d\underline{k}.$$

Plugging this expression in the 3D Markov isotropic spectrum, one obtains:

$$\sum_i \sigma_{h_i}^2 = \frac{\sigma_f^2 \lambda^3 J_1^2}{\pi^2} \iiint_{-\infty}^{+\infty} \frac{k_1^2}{k^2} \frac{1}{(1+\lambda^2 k^2)^2} \, d\underline{k}.$$

Using spherical coordinates, this gives:

$$\sum_i \sigma_{h_i}^2 = \frac{\sigma_f^2 \lambda^3}{\pi^2} J_1^2 \int_{\theta=0}^{\theta=2\pi} \int_{\varphi=0}^{\varphi=\pi} \int_{k=0}^{k=+\infty} \frac{\cos^2\theta \, \sin^2\varphi \cdot k^2 \sin\varphi}{(1+\lambda^2 k^2)^2} \, d\theta \, d\varphi \, dk$$

$$= \frac{\sigma_f^2 \lambda^3 J_1^2}{\pi^2} \cdot \int_{\theta=0}^{\theta=2\pi} \cos^2\theta \, d\theta \int_{\varphi=0}^{\varphi=\pi} \sin^3\varphi \, d\varphi \int_{k=0}^{k=+\infty} \frac{k^2}{(1+\lambda^2 k^2)^2} \, dk$$

$$= \frac{4}{3} \frac{\sigma_f^2 J_1^2}{\pi} \int_{-\infty}^{+\infty} \frac{u^2}{(1+u^2)} \, du$$

The integral above, is equal to $\pi/4$, whence the final result:

$$\sum_{i=1,2,3} \sigma_{h_i}^2 = \frac{1}{3} \sigma_f^2 J^2 \Rightarrow \boxed{\sqrt{\sigma_{h_1}^2 + \sigma_{h_2}^2 + \sigma_{h_3}^2} = \frac{1}{\sqrt{3}} \sigma_f J}$$

On the other hand, the transverse head gradient variance can be

obtained directly as follows:

$$\sigma_{h_2}^2 = \iiint S_{h_2 h_2}(\underline{k})\, d\underline{k}$$

$$= J_1^2 \iiint \frac{k_1^2 k_2^2}{k^4} S_{ff}(\underline{k})\, d\underline{k}$$

Plugging the 3D isotropic Markov spectrum above and integrating yields finally:

$$\boxed{\sigma_{h_2}^2,\ \sigma_{h_3}^2 = \frac{1}{15} J_1^2\ \sigma_f^2}$$

The longitudinal head variance obtains readily from previous results, using the fact $\sigma_{h_2} = \sigma_{h_3}$ by symmetry. Whence:

$$\sigma_{h_1}^2 = \sum_1 \sigma_{h_1}^2 - (\sigma_{h_2}^2 + \sigma_{h_3}^2)$$

$$= \frac{1}{3} \sigma_f^2\ J^2 - \frac{2}{15} \sigma_f^2\ J^2$$

$$= \frac{3}{15} \sigma^2 J^2$$

$$\Rightarrow \boxed{\sigma_{h_1}^2 = \frac{1}{5} \sigma_f^2 \cdot J^2}$$

In summary, the head gradient standard deviations are:

$$\boxed{\sigma_{h_1} = \frac{1}{\sqrt{5}}\ \sigma_f\ J} \quad \text{and} \quad \boxed{\sigma_{h_2} = \sigma_{h_3} = \frac{1}{\sqrt{15}}\ \sigma_f\ J}$$

APPENDIX 3.B

CLOSED FORM EVALUATION OF FLUX VARIANCES AND CROSS-COVARIANCES AT LAG ZERO, FOR THE 3D ISOTROPIC MARKOV SPECTRUM

In order to evaluate $R_{q_i q_j}(\underline{0})$, we use the flux spectrum of the standard first order spectral theory, given by equation (3.18):

$$S_{q_i q_j}(\underline{k}) = K_G^2 J_i^2 \left[\delta_{i1} - \frac{k_i k_1}{k^2}\right] \left[\delta_{j1} - \frac{k_j k_1}{k^2}\right] S_{ff}(\underline{k})$$

where S_{ff} is the 3D isotropic Markov spectrum:

$$S_{ff}(\underline{k}) = \frac{\sigma_F^2 \lambda^3}{\pi^2} \cdot \frac{1}{(1+\lambda^2 k^2)^2}$$

and k is the radial wavenumber:

$$k^2 = k_1^2 + k_2^2 + k_3^2.$$

The cross-covariances are given by

$$R_{q_i q_j}(\underline{0}) = \iiint_{-\infty}^{+\infty} S_{q_i q_j}(\underline{k})\, d\underline{k}. \quad (i=1,2,3 \text{ and } j=1,2,3)$$

By using certain symmetry properties of the flow as explained in Section 4.2, only the following spectra need to be integrated:

$$S_{q_1q_1}(\underline{k}) = K_G^2 J_1^2 \sigma_f^2 \left[1 - \frac{k_1^2}{k^2}\right]^2 \cdot \frac{\lambda^3}{\pi^2(1+\lambda^2k^2)^2}$$

$$j \neq 1: \quad S_{q_1q_j}(\underline{k}) = K_G^2 J_1^2 \sigma_f^2 \left[1 - \frac{k_1^2}{k^2}\right] \cdot \left[-\frac{k_1k_j}{k^2}\right] \frac{\lambda^3}{\pi^2(1+\lambda^2k^2)^2}$$

$$S_{q_2q_3}(\underline{k}) = K_G^2 J_1^2 \sigma_f^2 \frac{k_1^2k_2k_3}{k^4} \frac{\lambda^3}{\pi^2(1+\lambda^2k^2)^2}$$

$$j \neq 1: \quad S_{q_jq_j}(\underline{k}) = K_G^2 J_1^2 \sigma_f^2 \frac{k_1^2k_j^2}{k^4} \frac{\lambda^3}{\pi^2(1+\lambda^2k^2)^2}$$

1. Transverse Flux Variance:

$\sigma_{q_T}^2 = R_{q_jq_j}(0)$ $(j = 2,3)$:

$$\frac{\sigma_{q_T}^2}{K_G^2J_1^2\sigma_f^2} = \int_{-\infty}^{+\infty}\int\int\int \frac{k_1^2k_2^2}{k^4} \frac{\lambda_3}{\pi^2(1+\lambda^2k^2)^2} \, dk_1 \, dk_2 \, dk_3$$

$$\cdots = \frac{\lambda^3}{\pi^2} \int_{\varphi=0}^{\pi} \int_{\theta=0}^{2\pi} \int_{k=0}^{+\infty} dk \, d\theta \, d\varphi \cdot k^2 \sin\varphi.$$

$$\cdot \quad \frac{\sin^2\varphi \cos^2\theta \cdot \sin^2\varphi \sin^2\theta}{(1+\lambda^2 k^2)^2}$$

$$\cdots = \frac{\lambda^3}{\pi^2} \int_{\varphi=0}^{\pi} \sin^5\varphi d\varphi \cdot \int_{\theta=0}^{2\pi} \cos^2\theta \sin^2\theta \, d\theta \cdot \int_{k=0}^{+\infty} \frac{k^2}{(1+\lambda^2 k^2)^2} dk$$

$$\cdots = \frac{\lambda^3}{\pi^2} \cdot \frac{16}{5} \cdot \frac{\pi}{4} \frac{\pi}{4\lambda^3}$$

$$\cdots = \frac{1}{15} \Rightarrow \qquad \boxed{\sigma^2_{q_T} = \frac{1}{15} K_G^2 J_1^2 \sigma_f^2}$$

2. Longitudinal Flux Variance:

$\sigma^2_{q_L} = R_{q_1 q_1}(0)$:

$$\frac{\sigma_{q_L^2}}{K_G^2 J_1^2 \sigma_f^2} = \frac{\lambda^3}{\pi^2} \iiint_{-\infty}^{+\infty} \frac{(1-k_1^2/k^2)^2}{(1+\lambda^2 k^2)^2} \, dk_1 \, dk_2 \, dk_3$$

$$\cdots = \frac{\lambda^3}{\pi^2} \int_{\varphi=0}^{\pi} \int_{\varphi=0}^{2\pi} \int_{k=0}^{+\infty} [1 - \sin^2\varphi \cos^2\theta]^2 \cdot \frac{k^2 \sin\varphi}{(1+\lambda^2 k^2)^2} dk \, d\theta \, d\varphi.$$

Expanding:

$$(1-\sin^2\varphi \cos^2\theta)^2 \cdot \sin\varphi \equiv \sin\varphi - 2 \sin^3\varphi \cos^2\theta + \sin^5\varphi \cdot \cos^4\theta$$

and plugging this in the integral gives:

$$\cdots = \frac{\lambda^3}{\pi^2} \cdot \left\{ \int_0^{2\pi} d\theta \times \int_0^{\pi} \sin\varphi d\varphi - 2 \int_0^{2\pi} \cos^2\theta d\theta \times \int_0^{\pi} \sin^3\varphi d\varphi \right.$$

$$\left. + \int_0^{2\pi} \cos^4\theta d\theta \times \int_0^{\pi} \sin^5\varphi d\varphi \right\} \times \left\{ \int_0^{+\infty} \frac{k^2}{(1+\lambda^2 k^2)^2} \, dk \right\}$$

$$\cdots = \frac{\lambda^3}{\pi^2} \cdot \left\{ 2\pi \times 2 - 2 \times \pi \times 4/3 + \frac{3\pi}{4} \times \frac{16}{15} \right\} \times \left\{ \frac{\pi}{4\lambda^3} \right\}$$

$$\cdots = \frac{8}{15} \Rightarrow \qquad \boxed{\sigma^2_{q_L} = \frac{8}{15} K_G^2 \, \sigma_f^2 \, J_i^2} \; .$$

3. Cross-Covariances Between Different Flux Components at Lag Zero:

These cross-variances vanish due to the fact that the spectral integrand is odd. Precisely, $Rq_2q_3(\underline{0})$ vanishes since $S_{q_2q_3}(\underline{k})$ is odd in k_2 and k_3; similarly, $R_{q_1q_2}(\underline{0})$ vanishes because $S_{q_1q_2}(\underline{k})$ is odd in k_1 and k_2. Whence the result:

$$\boxed{R_{q_i q_j}(\underline{0}) \text{ is } 0 \text{ for } i \neq j.}$$

APPENDIX 3.C

CLOSED FORM EVALUATION OF CERTAIN CORRELATION FUNCTIONS OF THE FLUX AND HEAD GRADIENT VECTORS, FOR THE 3D ISOTROPIC MARKOV SPECTRUM

1. Transverse Flux Correlation Function

Here, we focus on the correlation of the transverse flux component q_2 along the other transverse direction x_3. This correlation function is defined as:

$$\tilde{R}_{q_2q_2}(\xi_3) = \frac{R_{q_2q_2}(0,0,\xi_3)}{\sigma^2_{q_2}}.$$

From (3.18) and (3.24) we have:

$$S_{q_iq_j}(\underline{k}) = K_G^2 J_i^2 \left[\delta_{i1} - \frac{k_i k_1}{k^2}\right] \left[\delta_{j1} - \frac{k_j k_1}{k^2}\right] S_{ff}(k)$$

$$\sigma^2_{q_2} = \frac{1}{15} K_G^2 \sigma_f^2 J_i^2$$

which gives for the correlation function:

$$\tilde{R}_{q_2q_2}(\xi_3) = \frac{15}{\sigma_f^2} \iiint e^{jk_3\xi_3} \frac{k_1^2 k_2^2}{k^4} S_{ff}(\underline{k}) d\underline{k}.$$

Plugging the 3D isotropic Markov spectrum:

$$S_{ff}(\underline{k}) = \frac{\sigma_f^2 \lambda^3}{\pi^2} \frac{1}{(1+\lambda^2 k^2)^2}$$

in the integral above yields:

$$\tilde{R}_{q_2 q_2}(\xi_3) = \frac{15\lambda^3}{\pi^2} \iiint e^{jk_3\xi_3} \frac{k_1^2 k_2^2}{k^4} \frac{1}{(1+\lambda^2 k^2)} d\underline{k}.$$

Using spherical coordinates we obtain finally the double-integral:

$$\tilde{R}_{q_2 q_2}(\xi_3) = \frac{15\lambda^3}{4\pi} \int_0^{\pi} \sin^5\varphi \, d\varphi \int_0^{\infty} \frac{k^2 \cos(k\xi_3 \cos\varphi)}{(1+\lambda^2 k^2)^2} dk.$$

Equivalently, by letting $u = \lambda k$ and $a = \xi_3/\lambda$ this gives:

$$\tilde{R}_{q_2 q_2}(\xi_3) = \frac{15}{4\pi} \int_0^{\pi} \sin^5\varphi \, d\varphi \int_0^{\infty} \frac{u^2 \cos(ua \cos\varphi)}{(1+u^2)^2} du$$

Finally, taking symmetries into account and letting $v = \sin\varphi$ or $\cos\varphi$, and $\sqrt{1-v^2} = \cos\varphi$ or $\sin\varphi$, with $0 \leq \varphi \leq \pi/2$, we obtain:

$$\tilde{R}_{q_2 q_2}(\xi_3) = \frac{15}{2\pi} \cdot \int_0^{1} (1-v^2)^2 \, dv \int_0^{\infty} \frac{u^2 \cos(uv\, a)}{(1+u^2)^2} du$$

From Gradshtein and Rhyzik (3.728.3), we have for the inner

integral:

$$\int_0^\infty \frac{x^2 \cos Ax}{(1+x^2)^2}\,dx = \frac{\pi}{4}(1-A)e^{-A} \ .$$

Note that as $A \to 0$ the result above converges to $\pi/4$ as expected (good check). Plugging this result in the double-integral above yields:

$$\tilde{R}_{q_2q_2}(\xi_3) = \frac{15}{8}\int_0^1 [1-av-2v^2+2av^3+v^4-av^5]e^{-av}\,dv$$

where $a = \xi_3/\lambda$ is the dimensionless separation distance. After integration, this gives:

$$\tilde{R}q_2q_2(a) = \frac{15}{8}\left\{\frac{1}{a}(1-e^{-a}) + e^{-a}(1+\frac{1}{a}) - \frac{1}{a}\right.$$

$$+ 2e^{-a}\left[\frac{1}{a} + \frac{2}{a^2} + \frac{2}{a^3}\right] - \frac{4}{a^3}$$

$$- 2e^{-a}\left[1 + \frac{3}{a} + \frac{6}{a^2} + \frac{6}{a^3}\right] + \frac{12}{a^3}$$

$$- e^{-a}\left[\frac{1}{a} + \frac{4}{a^2} + \frac{12}{a^3} + \frac{24}{a^4} + \frac{24}{a^5}\right] + \frac{24}{a^5}$$

$$\left. - e^{-a}\left[\frac{1}{a} + \frac{5}{a} + \frac{20}{a^2} + \frac{60}{a^3} + \frac{120}{a^4} + \frac{120}{a^5}\right] - \frac{120}{a^5}\right\}$$

This expression finally reduces to:

$$\tilde{R}_{q_2q_2}(0,0,\xi_3) = \frac{15}{a^2} \cdot \left\{ \frac{1}{a}\left(1 - \frac{12}{a^2}\right) + e^{-a} \cdot \left(1 + \frac{5}{a} + \frac{12}{a^2} + \frac{12}{a^3}\right) \right\}$$

where $a \equiv \xi_3/\lambda$. It can be checked that this correlation function goes to one as $a \to 0$, as it should. This can be shown by using a Taylor development of e^{-a} up to fifth order.

2. Head Gradient Correlation Functions:

The correlation functions $\tilde{R}_{h_ih_j}(\underline{\xi})$ for the head gradient vector $h_i = \partial h/\partial x_i$ can be obtained similarly by integrating the spectrum $S_{h_ih_j}(\underline{k})$ given in Chapter 3. It turns out that some of the directional correlations thus obtained are identical to certain flux correlations. In particular, we obtain:

$$\boxed{\tilde{R}_{h_1h_1}(0,0,\xi_3) = \tilde{R}_{q_2q_2}(0,0,\xi_3).}$$

A more general closed form expression for $\tilde{R}_{h_ih_j}(\underline{\xi})$ could be obtained directly by differentiating the known head correlation $\tilde{R}_{hh}(\underline{\xi})$ as explained in Chapter 3:

$$R_{h_i h_j}(\xi) = - \frac{\partial^2 R_{hh}(\xi)}{\partial \xi_i \partial \xi_j}.$$

By carrying out differentiation with respect to ξ_1 and to $r = \sqrt{\xi_2^2 + \xi_3^2}$, one obtains equation (4.14) in the text. The final closed form result, not reproduced here, would obtain by plugging $R_{hh}(\xi)$ of equation (3.22) into equation (4.14).

APPENDIX 3.D
HEAD COVARIANCE FUNCTION FOR THE 3D ANISOTROPIC MARKOV SPECTRUM (INDICATIONS FOR NUMERICAL INTEGRATION)

In this appendix, we explain how the head covariance functions shown in Figure 3.4 were obtained for arbitrary anisotropy ratio, in the form of double Fourier integrals to be integrated numerically.

Assume $\ell_1 = \ell_2 = \ell$ and let $\epsilon = \ell_3/\ell$ be the arbitrary, anisotropy ratio in the 3D anisotropic Markov spectrum of log-conductivity S_{ff} (Table 1 of Chapter 3). The relation between the head and log-conductivity spectra is:

$$S_{hh}(\underline{k}) = J_1^2 \frac{k_1^2}{k^4} S_{ff}(\underline{k})$$

The head covariance function is just the Fourier Transform of S_{hh}:

$$R_{hh}(\underline{\xi}) = \iiint e^{j\underline{k}\underline{\xi}} S_{hh}(\underline{k}) \, d\underline{k}$$

which finally leads to an expression of the form:

$$\boxed{R_{hh}(\underline{\xi}) = \frac{\pi}{8}\sigma_f^2\, J_1^2\, \ell\ell_3 \cdot I(\underline{\xi})}$$

where $I(\underline{\xi})$ is the triple integral:

$$I(\underline{\xi}) = \left(\frac{2}{\pi\ell}\right)^3 \iiint_{-\infty}^{+\infty} \frac{k_1^2 \cdot \cos(\underline{k}\,\underline{\xi})}{k^4[\ell^{-2}+k_1^2+k_2^2+\epsilon^2 k_3^2]^2}\, d\underline{k}.$$

We now express $I(\underline{\xi})$ by using spherical coordinates in Fourier space:

$$\begin{aligned} k &= \sqrt{k_1^2+k_2^2+k_3^2} && 0 \le k \le +\infty \\ k_1 &= k\cos\theta\sin\phi && 0 \le \phi \le 2\pi \\ k_2 &= k\sin\theta\sin\phi && 0 \le \phi \le \pi \\ k_3 &= k\cos\phi. \end{aligned}$$

The Jacobian of the transformation (from Cartesian to spherical coordinates) is:

$$\frac{\partial(k_1,k_2,k_3)}{\partial(k,\theta,\phi)} = k^2 \cdot \sin\phi.$$

After some manipulations, this gives:

$$I(\xi) = \left(\frac{2}{\pi\ell}\right)^3 \cdot \int_0^{2\pi} \cos^2\theta \cdot d\theta \int_0^{\pi} \sin^3\phi d\phi \int_0^{+\infty} \frac{\cos(k\cdot A)}{[k^2B^2+\ell^{-2}]^2}\, dk$$

where:

$$A(\theta,\phi) = (\xi_1 \cos\theta + \xi_2 \sin\theta)\sin\phi + \xi_3 \cdot \cos\phi$$

$$B(\phi) = \sqrt{\sin^2\phi + \epsilon^2 \cdot \cos^2\phi}.$$

Generalizing a formula given by Gradshteyn and Rhyzik (3.729.1) we obtained for the k-integral above:

$$\int_0^{+\infty} \frac{\cos(k\cdot A)}{[k^2B^2+\ell^{-2}]^2}\, dk = \frac{\pi}{4\ell^{-3}} \frac{1+C}{B} e^{-C}$$

where:

$$C = \ell^{-1} \cdot \left|\frac{A}{B}\right|.$$

This leads to the expression given in the text:

$$I(\underline{\xi}) = \frac{2}{\pi^2} \cdot \int_0^{2\pi} \cos^2\theta \cdot d\theta \int_0^{\pi} F(\theta,\phi)d\phi$$

$$F(\theta,\phi) = \sin^3\phi \cdot \left[\frac{1+C(\theta,\phi)}{B(\phi)}\right] e^{-C(\theta,\phi)}$$

which was finally integrated numerically as explained in the text.

The head variance in particular obtains by letting the separation vector go to zero:

$$\sigma_h^2 = R_{hh}(\underline{0}) \ .$$

In this case, the integral $I(\underline{0})$ above comes much simpler:

$$I(\underline{0}) = \frac{2}{\pi^2} \cdot \int_0^{2\pi} \cos^2\theta \cdot d\theta \int_0^{\pi} \frac{\sin^3\phi \ d\phi}{\sqrt{\sin^2\phi+\epsilon^2 \cdot \cos^2\phi}} \ .$$

This integral (or another equivalent integral) has already been evaluated by Naff and Vecchia (1986). The resulting head variance is given in close form in the text (equation 3.26).

APPENDIX 3.E

QUASI-ANALYTICAL EVALUATION OF THE HEAD COVARIANCE $R_{hh}(0,0,\xi_3)$ FOR THE 3D ANISOTROPIC MARKOV SPECTRUM WITH SMALL ANISOTROPY RATIO

In this appendix, we compute the vertical head covariance function in the anisotropic case with small anisotropy ratio ($\epsilon \ll 1$), in order to check the more general results obtained by numerical integration. The result given in Section 3.4 for the 3D anisotropic Markov spectrum was:

$$R_{hh}(\underline{\xi}) = \frac{\pi}{8} \sigma_f^2 \, J^2 \, \ell\ell_3 \cdot I(\underline{\xi})$$

where $I(\underline{\xi})$ had to be evaluated numerically.

In the case $\epsilon \ll 1$, we let $\epsilon = 0$ in $I(\underline{\xi})$ and restrict the analysis to the case of a vertical separation vector $(0,0,\xi_3)$. This gives a more tractable integral as shown below (for $\xi_3 \geq 0$):

$$I(\xi_3) = \frac{2}{\pi^2} \int_0^{2\pi} \cos^2\theta \cdot d\theta.$$

$$\cdot \left\{ \int_0^{\pi/2} \sin^2\phi \cdot \left[1 + \frac{\xi_3}{\ell} \operatorname{cotg}\, \phi\right] \exp\left[- \frac{\xi_3}{\ell} \operatorname{cotg}\, \phi\right] d\phi \right.$$

$$\left. + \int_{\pi/2}^{\pi/2} \sin^2\phi \cdot \left[1 + \frac{\xi_3}{\ell} \operatorname{cotg}\, \phi\right] \exp\left[- \frac{\xi_3}{\ell} \operatorname{cotg}\, \phi\right] d\phi \right\}.$$

Now, let:

$$u = \pm \operatorname{cotg}\, \phi$$

$$a = \xi_3/\ell$$

After some manipulations, we obtain:

$$I(\xi_3) = \frac{4}{\pi} \left\{ \int_0^{+\infty} \frac{e^{-au} du}{(1+u^2)^2} + a \cdot \int_0^{+\infty} \frac{u e^{-au}}{(1+u^2)^2} du \right\}$$

where $a = \xi_3/\ell$ is the dimensionless separation distance in the vertical. We now use a result from Gradshteyn and Rhyzik (3.355.1 and 2):

$$\int_0^\infty \frac{e^{-au}du}{(1+u^2)^2} = \frac{1}{2}\{ci(a)\cdot\sin(a) - si(a)\cdot\cos(a) - a\cdot[ci(a)\cdot\cos(a)+si(a)\cdot\sin(a)]\}$$

$$\int_0^\infty \frac{ue^{-au}du}{(1+u^2)^2} = \frac{1}{2}\{1-a\cdot[ci(a)\cdot\sin(a) - si(a)\cdot\cos(a)]\}$$

The special functions si(x) and ci(x) are the sine and cosine integrals:

$$si(x) = -\int_x^\infty \frac{\sin t}{t}\,dt = -\frac{\pi}{2} + \int_0^x \frac{\sin(t)}{t}\,dt$$

$$ci(x) = -\int_x^\infty \frac{\cos t}{t}\,dt = C + \ell n\, x + \int_0^x \cos(t) - 1\,dt$$

where C is the Euler constant:

$$C = 0.577215\cdots$$

Using a Table of sine-cosine integrals (Korn and Korn, 1968, Appendix F.6) we obtain in particular:

$$I(0,0,\xi_3) = \frac{4}{\pi} \cdot 0.6717 \text{ for } \xi_3 = \ell$$

$$I(0,0,\xi_3) = \frac{4}{\pi} \cdot 0.2529 \text{ for } \xi_3 = 7\ell.$$

Plugging these values into the relation given on top of this appendix gives the head correlation for two different separation distances in the vertical:

$$\frac{R_{hh}(0,0,\ell)}{\sigma_h^2} \simeq 0.8552$$

$$\frac{R_{hh}(0,0,7\ell)}{\sigma_h^2} \simeq 0.3220.$$

The results obtained by numerical integration agreed closely with these analytical values (see Figure 3.4 with $\epsilon \ll 1$).

APPENDIX 3.F

CLOSED FORM EVALUATION OF THE FLUX VARIANCE FOR THE 3D ANISOTROPIC MARKOV SPECTRUM WITH SMALL ANISOTROPY RATIO

In this Appendix, we compute the variance of the flux vector components for a small anisotropy ratio ($\epsilon << 1$), using the 3D anisotropic Markov spectrum of Table 3.1 (Chapter 3). For completeness, we also compute the *macrodispersivity* according to Gelhar and Axness (1983), for arbitrary anisotropy ratio.

The flux spectrum obtained by the standard first order spectral theory is given generally by equation (3.18) in the text. For the case at hand, we define for convenience a rescaled flux spectrum as follows:

$$\tilde{S}_{q_i q_i} = S_{q_i q_i} / \{ \frac{\ell^2 \ell_3}{\pi^2} \cdot \sigma_f^2 \, K_G^2 \, J^2 \}.$$

The resulting expression for the rescaled flux spectrum is:

$$\tilde{S}_{q_i q_i}(\underline{k}) = \left[\delta_{i1} - \frac{k_i k_1}{k^2} \right]^2 \cdot \frac{1}{[1+\ell^2(k_1^2+k_2^2+\epsilon^2 k_3^2)]^2}$$

where $\epsilon = \ell_3/\ell$ is the (small) anisotropy ratio. The flow statistics of interest can now be expressed as:

$$\tilde{\sigma}^2_{q_i} = \iiint \tilde{S}_{q_i q_i}(\underline{k})\, d\underline{k}$$

$$\tilde{A}_{ii} = \frac{\pi}{\bar{Q}^2} \cdot \iint \tilde{S}_{q_i q_i}(0, k_2, k_3)\, dk_2\, dk_3$$

where $\tilde{\sigma}^2_{q_i}$ is a scaled flux variance, and $\tilde{A}_{ii}$ a scaled macrodispersivity for solute transport at large times in the absence of local dispersion (see Gelhar and Axness, 1983, and Gelhar, 1985).

Using spherical coordinates in Fourier space (see for instance Appendix 3.D), we obtain the scaled flux variances in the form:

$$\tilde{\sigma}^2_{q_i} = \int_0^{2\pi} d\theta \int_0^{\pi} B_i'(\theta,\phi)\, d\phi \int_0^{\infty} \frac{k^2\, dk}{[1+\ell^2(\sin^2\phi+\epsilon^2\cos^2\phi)k^2]^2}.$$

The k-integral can be worked out by using a formula given in Gradshtein and Rhyzik (3.241.5):

$$\int_0^{\infty} \frac{x^2\, dx}{(1+x^2)^2} = \pi/4.$$

This gives finally:

$$\tilde{\sigma}^2_{q_i} = \frac{\pi}{4\ell^3} \int_0^{2\pi} d\theta \int_0^{\pi} B_i(\theta,\phi)d\phi$$

where the integrand B_i takes the form:

$$i=1: \; B_1(\theta,\phi) = (1-2\cos^2\theta \sin^2\phi + \cos\theta^4 \sin^4\phi) \frac{\sin\phi}{(\sin^2\phi+\epsilon^2\cos^2\phi)^{3/2}}$$

$$i=2: \; B_2(\theta,\phi) = \cos^2\theta \cdot \sin^2\phi \frac{\sin^5\phi}{(\sin^2\phi+\epsilon^2\cos^2\phi)^{3/2}}$$

$$i=3: \; B_3(\theta,\phi) = \cos^2\theta \cdot \cos^2\phi \frac{\sin^3\phi}{(\sin^2\phi+\epsilon^2\cos^2\phi)^{3/2}}$$

For $\epsilon \ll 1$, it turns out that the approximation $\epsilon \simeq 0$ can be used in the integrals involving B_2 and B_3, but not in the integral involving B_1 (this would lead to an indeterminacy of the type "zero divided by zero"). Beginning with the components $i = 2$, and $i = 3$, we plug $\epsilon \simeq 0$ in B_2 and B_3 to obtain, after some simple integrations:

$$\tilde{\sigma}^2_{q_2} \simeq \frac{\pi^3}{32\ell^3} \qquad (\epsilon \simeq 0)$$

$$\tilde{\sigma}^2_{q_3} \simeq \frac{\pi^3}{8\ell^3} \qquad (\epsilon \simeq 0)$$

For the longitudinal flux component, we obtain after integrating over θ and keeping $\epsilon \neq 0$ in some of the intermediate expressions:

$$\tilde{\sigma}^2_{q_1} \simeq \frac{\pi}{4\ell^3}\left\{4\pi \int_0^{\pi/2} \frac{\sin\phi\, d\phi}{(\sin^2\phi+\epsilon^2\cos^2\phi)^{3/2}} - \frac{13}{8}\pi^2\right\}.$$

However note that we used $\epsilon \simeq 0$ to evaluate an intermediate expression (ϕ-integral) that resulted in the term $13\pi^2/8$.

To evaluate the remaining ϕ-integral above, let us take $u = \cos\phi$ as the new variable of integration and use a result by Gradshtein and Rhyzik (2.271.5). This yields for the ϕ-integral above:

$$\int_0^{\pi/2} \cdots d\phi = \int_0^1 \frac{du}{(1-(1-\epsilon^2)u^2)^{3/2}}$$

$$= \left[\frac{u}{\sqrt{1-(1-\epsilon^2)u^2}}\right]_0^1$$

$$= \frac{1}{\epsilon}.$$

This leads finally to a close form expression for the scaled

longitudinal flux variance:

$$\tilde{\sigma}^2_{q_1} \simeq \frac{\pi^2}{\ell^3}\left(\frac{1}{\epsilon} - \frac{13}{32}\pi\right)$$

Finally, the flux variances are readily obtained by observing that:

$$\sigma^2_{q_i} = \tilde{\sigma}^2_{q_i} \cdot \left\{\frac{\ell^2 \ell_3}{\pi}\sigma_f^2 \, K_G^2 \, J_i^2\right\}$$

This gives finally:

$$\boxed{\begin{aligned} \sigma^2_{q_1} &\simeq \sigma_f^2 \, K_G^2 \, J_1^2\left(1 - \frac{13}{32}\pi\epsilon\right) \\ \sigma^2_{q_2} &\simeq \sigma_f^2 \, K_G^2 \, J_1^2 \, \frac{\pi}{32}\,\epsilon \\ \sigma^2_{q_3} &\simeq \sigma_f^2 \, K_G^2 \, J_1^2 \, \frac{\pi}{8}\,\epsilon \end{aligned}}$$

provided that $\epsilon \ll 1$. This result was given in equation 3.31. Note that σ_{q_1} tends to a non-zero constant value as $\epsilon \to 0$, while σ_{q_2} and σ_{q_3} vanish as $\epsilon \to 0$..

The scaled macrodispersivity $\tilde{A}_{ii}$ defined at the beginning of this appendix is easily computed for arbitrary values of the anisotropy ratio ($\epsilon \leq 1$), as shown below:

$$\frac{\pi}{\bar{Q}_1^2}\,\tilde{A}_{ii} = \int_{-\infty}^{+\infty}\int \frac{\delta_{i1}}{[1+\ell^2(k_2^2+\epsilon^2 k_3^2)]^2}\,dk_2\,dk_3 \ .$$

This gives immediately:

$$\boxed{A_{22} = A_{33} = 0} \ .$$

For the longitudinal component of macrodispersing, let us use circular coordinates in the transverse plane (k_2, k_3):

$$k_2 = k_o \cos\theta$$

$$k_3 = k_o \sin\theta$$

$$k_o = \sqrt{k_2^2+k_3^2}$$

$$\text{Jacobian} = k_o$$

This yields:

$$\tilde{A}_{11} = \frac{\pi}{\bar{Q}_1^2} \int_0^{2\pi} d\theta \int_0^{\infty} \frac{k_o\,dk_o}{[1+B(\theta)\cdot k_o^2]^2}$$

$$B(\theta) = \ell^2\cdot[1-(1-\epsilon^2)\sin^2\theta] \geq 0$$

The k_o-integral is easily worked out by using the variable of

integration:

$$W = 1 + B(\theta) \cdot k_0^2$$

We obtained after integration:

$$\tilde{A}_{11} = \frac{2}{\ell^2} \frac{\pi}{\bar{Q}_1^2} \cdot \int_0^{\pi/2} \frac{d\theta}{1-\gamma \cdot \sin^2\theta}$$

where $\gamma = 1 - \epsilon^2$ $(0 \leq \gamma < 1)$. From Gradshtein and Rhyzik (2.562.1) we get for θ-integral:

$$\int^{x} \frac{d\theta}{1-\gamma \sin^2\theta} = \frac{1}{\sqrt{1-\gamma}} \operatorname{arctg} (\sqrt{1-\gamma} \operatorname{tg} x) .$$

This gives:

$$\tilde{A}_{11} = \frac{2}{\ell^2} \frac{\pi}{\bar{Q}_1^2} \frac{1}{\epsilon} . [\operatorname{arctg}(\epsilon \operatorname{tg} x)]_0^{\pi/2}.$$

After rescaling $\tilde{A}_{11}$, we obtain finally the dimensional macrodispersivity:

$$\boxed{A_{11} = \left[\frac{K_G J}{\bar{Q}_1} \right]^2 \cdot \sigma_f^2 \cdot \ell}$$

It is worth mentioning that a correction to the

standard first order spectral method was proposed in Section 4.3 of this work. Accordingly, the term $(K_G J)$ should be replaced by $(\overline{Q}_1)$ in all the results obtained in this Appendix. In particular, the macrodispersivity becomes

$$\boxed{A_{11} = \sigma_f^2 \cdot \ell}$$

The major difference between this and the previous expression is that A_{11} increases monotonously with σ_f in the modified result just above. In addition, note that A_{11} is independent of the anisotropy ratio $(0 \leq \epsilon \leq 1)$. However, A_{11} becomes indeterminate if $\epsilon = 0$.

APPENDIX 3.G
CLOSED FORM EVALUATION OF THE HEAD VARIANCE AND COVARIANCE FUNCTION FOR THE 3D HOLE-MARKOV SPECTRUM (ISOTROPIC AND ANISOTROPIC CASES)

In this Appendix, we evaluate the head variance for the Hole-Markov spectrum with arbitrary anisotropy ratio. In addition, we also evaluate in closed form the head correlation function along the vertical direction (in the isotropic case only). These results are used in the text for comparison with the standard Markov spectrum without a "hole". Note that the effect of the "hole" is to decrease the low-wavenumber content of the log-conductivity spectrum.

The head covariance $R_{hh}(\xi)$ is proportional to a certain triple Fourier integral $I(\xi)$, given in Section 3.6. By using spherical wavenumber coordinates as in Appendix 3.D, we obtain after some manipulations:

$$R_{hh}(\xi) = (\frac{\pi}{8}\sigma_f^2 J_i^2 \ell\ell_3)\cdot I(\xi)$$

$$I(\xi) = (\frac{\pi}{2\ell})^3 \cdot \int_0^{+\infty} \cos^2\theta \cdot d\theta \int_0^{\pi} \frac{\sin^3\phi\cdot K(\theta,\phi)\ d\phi}{[\sin^2\phi+\epsilon^2\cos^2\phi]^2}$$

$$K(\theta,\phi) = \int_0^{+\infty} \frac{k^2 \cos(ak)dk}{(k^2+b^2)^3}$$

$$a = \left|(\xi_1 \cos\theta + \xi_2 \sin\theta) \sin\phi + \xi_3 \cos\phi\right|$$

$$b = \frac{1}{\ell \cdot \sqrt{\sin^2\phi+\epsilon^2\cos^2\phi}}$$

By using a number of intermediate results from Gradshteyn and Rhyzik (3.737.1) we obtained a closed form expression for the $K(\theta,\phi)$ integral as shown below. First, let us define a class of integrals of the form:

$$J_n = \int_0^{+\infty} \frac{\cos(ak)dk}{(k^2+b^2)^n}$$

Then we have:

$$K(\theta,\phi) = J_2 - b^2 \cdot J_3$$

On the other hand, the J_n integrals are known in closed form:

$$J_n = \frac{\pi \ e^{-ab}}{(2b)^{2n-1} \cdot (n-1)!} \cdot \sum_{k=0}^{n-1} \frac{(2n-k-2)!(2ab)^k}{k!(n-k-1)!}$$

Plugging J_n into K finally leads to

$$\boxed{K(\theta,\phi) = \frac{\pi}{16} \cdot \frac{1+ab-(ab)^2}{b^3} \cdot e^{-ab}}$$

Plugging $K(\theta,\phi)$ in $I(\underline{\xi})$ above leaves a fairly complicated double integral to be evaluated in the general anisotropic case with arbitrary separation vector $\underline{\xi}$. To arrive at a useful close form result for the correlation function, let us focus on the isotropic case, and let $\underline{\xi}$ be a vertical separation vector $(0,0,\xi_3)$. The anisotropic case will also be considered later for variance calculations.

1. Isotropic Case: Covariance $R_{hh}(0,0,\xi_3)$:

Letting $\epsilon = \ell_3/\ell = 1$ and $\xi_1 = \xi_2 = 0$, the expression for the $I(\underline{\xi})$ integral reduces to:

$$I(\xi_3) = \frac{\pi}{16} \cdot (\frac{\pi}{2})^3 \cdot \int_0^{2\pi} \cos^2\theta \cdot d\theta \cdot L(\xi_3)$$

$$L(\xi_3) = 2 \int_0^1 (1-u^2)\ (1+s_3u-(s_3 \cdot u)^2)\ e^{-au} du$$

where $s_3 = \xi_3/\ell$ is the dimensionless separation distance in the vertical. Note that the integral L was obtained after changing a variable of integration ($u = \sin\phi$). This integral can be worked out without difficulty (the details are tedious and will

not be shown here):

$$L(\xi_3) = \frac{16}{s_3}\left\{\frac{2}{s_3}\left[\frac{1-e^{-s_3}}{s_3} - e^{-s_3}\right] - \left[1+\frac{s_3}{4}\right]e^{-s_3}\right\}.$$

Eventually, we find that the head covariance can be related directly to $L(\xi_3)$ via:

$$R_{hh}(0,0,\xi_3) = \frac{1}{16}\left(\frac{\pi}{2}\right)^6 \sigma_f^2 \, J^2 \ell^2 \cdot L(\xi_3) \ .$$

In particular, taking $\xi_3 = 0$ gives the head variance in the isotropic case. The value of $L(0)$ can be found by using a Taylor development of $L(\xi_3)$ as $\xi_3 \to 0$; the result is:

$$L(0) = 4/3.$$

This gives immediately the *head variance for the isotropic case*:

$$\boxed{\sigma_h^2 = \frac{1}{12}\left(\frac{\pi}{2}\right)^6 \cdot \sigma_f^2 \, J^2 \ell^2} \quad (\epsilon=1)$$

The *head correlation function* in the vertical direction can now be expressed as:

$$\boxed{\frac{R_{hh}(0.0.\xi_3)}{\sigma_h^2} = \frac{12}{s^3}\left\{\frac{2}{s^3}\left[\frac{1-e^{-s_3}}{s_3} - e^{-s_3}\right] - \left[1 - \frac{s_3}{4}\right]e^{-s_3}\right\}} \quad (\epsilon = 1)$$

where $s_3 = \xi_3/\ell$. These two equations, taken together, give in closed form the head covariance in the cross-flow direction for the isotropic Hole-Markov spectrum.

2. Anisotropic Case: Head Variance σ_h^2:

In the general anisotropic case, the head variance obtains by taking $\underline{\xi} = \underline{0}$ in the general expression given for $I(\underline{\xi})$ at the beginning of this appendice. The integral $K(\theta,\phi)$ now becomes more tractable since the term cos(ak) is eliminated from the integrand:

$$K(\theta,\phi) = \int_0^{+\infty} \frac{k^2}{(k^2+b^2)^3}\, dk$$

After Gradshetyn and Rhyzik (3.241.4) we obtain:

$$K(\theta,\phi) = \frac{\pi}{16.b^3}$$

where b is a function of ϕ alone, as defined earlier.

Plugging this expression into the integral $I(\underline{\xi})$ evaluated at zero spearation distance gives finally:

$$I(\underline{0}) = \frac{1}{4}\left(\frac{\pi}{2}\right)^5 \int_0^{\pi} \frac{\sin^3\phi \, d\phi}{\sqrt{\sin^2\phi+\epsilon^2\cos^2\phi}}$$

$$\sigma_h^2 = \frac{\pi}{8}\sigma_f^2 \, J^2\ell^2 \cdot I(\underline{0}).$$

It turns out that the ϕ-integral above can be computed in closed form, separately, for $\epsilon > 1$, $\epsilon = 1$ and $\epsilon < 1$. For the simplest case $\epsilon = 1$, we obtain the same head variance as already found above (isotropic case). For $\epsilon < 1$, the ϕ-integral can be rewritten as:

$$\frac{1}{\epsilon} \cdot \int_0^{\pi} \frac{\sin^3\phi \, d\phi}{\sqrt{1+\gamma^2\sin^2\phi}}$$

where $\gamma^2 = (1-\epsilon^2)/\epsilon^2$. This integral can be evaluated from two results of Gradshteyn and Rhyzik (2.584.7 and 2.598). We give below the final result for σ_h^2:

$$\boxed{\begin{aligned} &\sigma_h^2 = \frac{\pi}{8}\sigma_f^2 \, J^2\ell\ell_3 \cdot I(0) \\ &I(\underline{0}) = \frac{1}{4}\left(\frac{\pi}{2}\right)^5 \frac{1}{\sqrt{1-\epsilon^2}} \left\{ \frac{\epsilon}{\sqrt{1-\epsilon^2}} + \frac{1-2\epsilon^2}{1-\epsilon^2} \cdot \arcsin\left(\sqrt{1-\epsilon^2}\right) \right\} \end{aligned}} \quad (\epsilon < 1)$$

For $\epsilon > 1$ the ϕ-integral can be expressed as:

$$\int_0^{\pi} \frac{\sin^3\phi \; d\phi}{\sqrt{1-\omega^2 \cdot \sin^2\phi}}$$

where $\omega^2 = (\epsilon^2-1)/\epsilon^2$. Using again a few intermediate results of Gradshteyn and Rhyzik, we obtain finally:

$$\sigma_h^2 = \frac{\pi}{8}\,\sigma_f^2\, J^2 \ell \ell_3 \cdot I(0)$$

$$I(\underline{0}) = \frac{1}{4}\left(\frac{\pi}{2}\right)^5 \frac{\epsilon^2}{\epsilon^2-1}\left\{ -\frac{1}{\epsilon} + \frac{2\epsilon^2-1}{\epsilon^2\sqrt{\epsilon^2-1}} \cdot \ell n \left[\frac{\epsilon+\sqrt{\epsilon^2-1}}{\epsilon-\sqrt{\epsilon^2-1}}\right]\right. \qquad (\epsilon > 1)$$

It is interesting to note that σ_h^2 tends to a non-zero constant as $\epsilon \to 0$ if the geometric mean correlation scale $\ell_G = \sqrt{\ell \ell_3}$ is held fixed. On the other hand, the last equation above shows that $\sigma_h^2 \to 0$ as $\epsilon \to \infty$ while ℓ_G is held fixed.

APPENDIX 5.A

CLOSED FORM EVALUATION OF THE NUMERICAL HEAD ERROR $\sigma(\delta H)$ FOR THE 3D MARKOV SPECTRUM OF LOG-CONDUCTIVITY

In this Appendix, we describe in some detail the analytical integrations needed to obtain the root-mean-square norm of then numerical head error $\delta H(\underline{x})$ (truncation error) in the case where the log-conductivity is an isotropic 3D Markov random field. The final result was given in the text (equation 5.63 top: "noisy input"). The next appendix (5.B) presents similar calculations in the case of a Gaussian log-conductivity spectrum ("smooth input"). Recall that these results were obtained by a stochastic analysis of the *truncature errors* arising from the finite difference discretization of the groundwater flow equation.

Our starting point is equation (5.59) in the text, which gives the variance of $\delta H(\underline{x})$ obtained by Fourier integration of the δH-spectrum up to wavenumbers $|k| \simeq \pi/\Delta x$. That equation is reproduced below for convenience:

$$\mathrm{Var}(\hat{\delta H}i) \simeq \left[J_1 \frac{\Delta x^2}{24}\right]^2 \cdot I$$

where I is the 3D integral:

$$I = \int_{0 \le k \le \pi/\Delta x} k_i^2 \left[\frac{3k_i^2}{k^2} + \frac{(k_m^2 \cdot k_m^2)}{k^4}\right]^2 \cdot \frac{S_{ff}(\underline{k})}{\sigma_f^2} \, d\underline{k}.$$

Note that k is the radial wavenumber $(k_i \cdot k_i)^{1/2}$, and that summation over repeated indices is implicit, unless stated otherwise.

In the case of the isotropic 3D Markov spectrum, the last term in the integrand of I takes the form:

$$\frac{S_{ff}(\underline{k})}{\sigma_f^2} = \frac{\lambda^3}{\pi^2} \cdot \frac{1}{(1+\lambda^2 k^2)^2} .$$

By using spherical coordinates as defined, for instance, in Appendix 3D, we obtain:

$$I = I' \cdot I''$$

where the integrals I' and I'' are respectively:

$$I' = \frac{\lambda^3}{\pi^2} \int_0^{\pi/\Delta x} \frac{k^4}{(1+\lambda^2 k^2)^2}\, dk$$

$$I'' = \int_0^{2\pi} d\theta \cdot \int_0^{\pi} A(\theta,\phi)\, d\phi$$

$$A(\theta,\phi) = \cos^2\theta \cdot \sin^3\phi \cdot [3\cos^2\theta \cdot \sin^2\phi + \cos^4\theta \cdot \sin^4\phi + \sin^4\theta \cdot \sin^4\phi + \cos^4\phi]^2$$

Now, the first integral I' can be rewritten by using the transformation $u = \lambda k$ as follows:

$$I' = \frac{1}{(\lambda\pi)^2} \cdot \int_0^{\frac{\lambda\pi}{\Delta x}} \frac{u^4}{(1+u^2)^2}\, du.$$

This integral was already computed in the text by using identities from Gradshteyn and Rhyzik 1980 (2.174 and 2.175): see above equations (5.61) in the text for details. The resulting expression for the I' integral is finally:

$$I' = \frac{1}{(\lambda\pi)^2} \cdot \frac{1}{R} \cdot \left[\frac{1}{1+R^2} + \frac{3}{2} \cdot \frac{R^2}{1+R^2} - \frac{3}{2} R \operatorname{arctg}\left(\frac{1}{R}\right)\right]$$

where R is the radial grid resolution parameter defined as:

$$\boxed{R = \frac{\Delta x}{\lambda \pi}}.$$

For the second integral I'', the integrand $A(\theta,\phi)$ can be decomposed in the form:

$$A(\theta,\phi) = [a+b+c+d]^2 = a^2+b^2+c^2+d^2+2(ab+bc+cd+da+ac+bd)$$

This gives $A(\theta,\phi)$ in the form:

$$\begin{aligned} A(\theta,\phi) = {} & 9\cos^6\theta\cdot\sin^7\phi + \cos^{10}\theta\cdot\sin^{11}\phi \\ & + \cos^2\theta\cdot\sin^8\theta\cdot\sin^{11}\phi + \cos^2\theta\cdot\sin^3\phi\cdot\cos^8\phi \\ & + 6\cos^8\theta\,\sin^9\phi + 2\cos^6\theta\cdot\sin^4\theta\cdot\sin^{11}\phi \\ & + 6\cos^4\theta\cdot\sin^5\phi\cdot\cos^4\phi + 6\cos^4\theta\,\sin^4\theta\cdot\sin^9\phi \\ & + 2\cos^6\theta\cdot\sin^7\phi\cdot\cos^4\phi + 2\cos^2\theta\cdot\sin^4\theta\cdot\sin^7\phi\cdot\cos^4\phi \end{aligned}$$

To obtain a close-form expression for the double-integral of $A(\theta,\phi)$, we used the following identities from Gradshteyn and Rhyzik, 1980 (2.510 - 511-512-513):

$$\int_0^{2\pi} \cos^{2p}\theta \cdot d\theta = 2\pi \cdot \frac{(2p-1)!!}{p!2^p}$$

$$\int_0^{2\pi} \cos^{P}\theta \cdot \sin^{2n}\theta \cdot d\theta = \frac{(2n-1)!!}{(2n+p)(2n+p-2)\cdots(p+2)} \cdot \int_0^{2\pi} \cos^{P}\theta . d\theta$$

$$\int_0^{\pi} \sin^{2n+1}\phi \cdot d\phi = \frac{2^{n+1}}{2n+1} \cdot \frac{n!}{(2n-1)(2n-3)\cdots 1} \quad (n \geq 1)$$

$$\int_0^{\pi} \cos^{P}\phi \cdot \sin^{2n+1}\phi \cdot d\phi = 0 \quad (n \geq 1,\ p \text{ odd})$$

$$\int_0^{\pi} \cos^{P}\phi \cdot \sin^{2n+1}\phi \cdot d\phi = \quad (n \geq 1,\quad p \text{ even})$$

$$\frac{1}{2n+p+1} \cdot \left[\frac{4n}{2n+p-1} \cdot \delta_{1n} + 2^{n+1} \cdot \frac{n!}{(2n+p-1)(2n+p-3)\cdots(p+1)}\right]$$

In these expressions, we used the following notations:

$$(2n-1)!! = (2n-1)\ (2n-3)\cdots 1$$

$$\delta_{1n} = 1 \text{ if } n = 1$$

$$\delta_{1n} = 0 \text{ if } n \neq 1.$$

Using these identities finally led to a closed form (exact) expression for $I'' = \iint A(\theta,\phi)d\theta\ d\phi$ in the form of a sum of ten rational numbers (fractions) multiplied by the number π. The

approximate value of I'' is finally:

$$I'' \simeq 3.85\pi \simeq 4\pi.$$

This gives immediately the desired result for $\mathrm{Var}(\delta H)$. Multiplying I' by I'' above and using the first equation of this appendix gives a closed form expression for $\mathrm{Var}(\delta H)$. Furthermore, to obtain the *relative* root-mean-square error:

$$\epsilon(\delta H) = \frac{\sigma(\delta H)}{\sigma_H}$$

we also need the following result already obtained in the text (equation 3.21 or Bakr et al. 1978):

$$\sigma_H = \frac{1}{\sqrt{3}} \sigma_f \, J_1 \, \lambda$$

This gives finally the desired result for the relative root-mean-square error on the head, as follows:

$$\boxed{\frac{\sigma(\delta H)}{\sigma(H)} \simeq \frac{\sqrt{3}}{12} \cdot \left(\frac{\Delta x}{\lambda}\right)^{3/2} \cdot G\left(\frac{\Delta x}{\pi\lambda}\right)}$$

where the function $G(y)$ is defined by:

$$G(y) = \left[\frac{1}{1+y^2} + \frac{3}{2} \cdot \frac{y^2}{1+y^2} - \frac{3}{2}\, y \,\mathrm{arctg}\, \left(\frac{1}{y}\right)\right]^{1/2}$$

Note that, for $y = \frac{\Delta x}{\lambda \pi} << 1$ we obtain:

$$G(\frac{\Delta x}{\lambda \pi}) \simeq \sqrt{1+0\ (\frac{\Delta x}{\lambda \pi})} \simeq 1 + 0\ (\frac{\Delta x}{\lambda \pi}).$$

Therefore, replacing the term $G(\frac{\Delta x}{\lambda \pi})$ by one in the above result gives the leading order term of the relative head error, as shown in the text.

APPENDIX 5.B

CLOSED FORM EVALUATION OF THE NUMERICAL HEAD ERROR $\sigma(\delta H)$ FOR THE 3D HOLE-GAUSSIAN SPECTRUM OF LOG-CONDUCTIVITY

This Appendix follows a development parallel to that of Appendix 5A, but with a Hole-Gaussian spectrum rather than a Markov spectrum for the 3D isotropic log-conductivity field. Therefore, we will refer to some of the notations used in Appendix 5A in the sequel. However, let us first define the Hole-Gaussian spectrum, since it was not used anywhere else in this work.

The Hole-Gaussian ellipsoidal log-conductivity spectrum, with "rational hole" of order m, was defined and used by Vomvoris (1986) to obtain spectral solutions of stochastic solute transport. The general form of this spectrum is:

$$S_{ff}(\underline{k}) = \sigma_f^2 \frac{\ell_1 \ell_2 \ell_3}{(2\pi)^{3/2}} \cdot \frac{(\ell_i^2 k_i^2)^m}{(2m+1)!!} \cdot \exp(-\frac{1}{2} \ell_i^2 k_i^2)$$

with implicit summation on repeated indices, and:

$$(2m+1)!! = 1.3.5 \cdots (2m+1).$$

In the particular case at hand, we used the isotropic

Hole-Gaussian spectrum of order one (m = 1):

$$\boxed{S_{ff}(\underline{k}) = \frac{\sigma_f^2\ \ell^3}{3(2\pi)^{3/2}} \cdot \ell^2 k^2 \cdot e^{-\ell^2 k^2/2}}$$

Now, in order to evaluate the *relative* head error $\sigma(\delta H)/\sigma(H)$, we need to evaluate the standard deviation $\sigma(H)$ of the head solution by using the results of the spectral theory of stochastic flow (equations 3.18 of Chapter 3). The head spectrum is related to the log-conductivity spectrum by:

$$S_{hh}(\underline{k}) = \frac{J_i^2 k_i^2}{k^4} S_{ff}(\underline{k}).$$

The head variance σ_H^2 obtains by integrating the head spectrum in Fourier space ($-\infty \leq k_i \leq +\infty$). Plugging the Hole-Gaussian S_{ff} spectrum on the right-hand side gives:

$$\sigma_H^2 = \frac{\sigma_f^2\ J_i^2\ \ell^5}{3(2\pi)^{3/2}} \cdot I_1$$

$$I_1 = \iiint_{-\infty}^{+\infty} \frac{k_i^2}{k^2} e^{-\ell^2 k^2/2}\ d\underline{k}\ .$$

The I_1 integral is easily worked out by using spherical coordinates. We obtained after some manipulations:

$$I_1 = \frac{4\pi}{3} \cdot \int_0^{+\infty} k^2 \, e^{-\ell^2 k^2/2} dk$$

$$= \frac{4\pi}{3\ell^3} \cdot \int_0^{+\infty} u^2 e^{-u^2/2} \, du$$

$$= \frac{4\pi}{3\ell^3} \cdot \sqrt{\frac{\pi}{2}}$$

where we used the identity:

$$\boxed{\int_0^{\infty} u^{2n} \, e^{-pu^2} du = \frac{(2n-1)!!}{2(2p)^n} \cdot \sqrt{\frac{\pi}{p}}}$$

after Gradshteyn and Rhyzik 1980 (3.461.2). This gives finally the first order spectral solution for the head variance in the case of a Hole-Gaussian isotropic log-conductivity field in 3D space:

$$\boxed{\sigma_H^2 = \frac{1}{9} \sigma_f^2 \, J_1^2 \, \ell^2}$$

Let us now evaluate the standard deviation of the head

error, $\sigma(\delta H)$, as in Appendix 5A. Briefly, our starting point is the relation:

$$\sigma(\delta H)^2 \simeq \frac{\sigma_f^2 \; J_i^2 \; \ell^6}{3(2\pi)^{3/2}} \left[\frac{\Delta x^2}{24}\right]^2 \cdot I$$

$$I = \int_{0 \leq k \leq \pi/\Delta x} \left[\frac{3k_i^3}{k} + \frac{k_i(k_m^2 \cdot k_m^2)}{k^3}\right]^2 \cdot e^{-\ell^2 k^2/2} \cdot d\underline{k} \; .$$

Note that the exponential term in the integrand above resulted from plugging the Hole-Gaussian spectrum in equation (5.59) given in the text. Now, by using spherical coordinates, the I-integral above takes the form:

$$I = I' \cdot I''$$

where the I' integral is:

$$I' = \int_0^{\pi/\Delta x} k^6 \cdot e^{-\ell^2 k^2/2} \, dk$$

and the I'' integral is the same as that of Appendix 5A:

$$\boxed{I'' = \int_0^{2\pi} d\theta \int_0^{\pi} d\phi \; A(\theta,\phi) \simeq 4\pi}$$

For the I''-integral, we use the transformation $u = k\ell$ to obtain, after some manipulation:

$$I' = \frac{4\pi}{\ell^7} \cdot \left[\int_0^{\infty} u^6 \cdot e^{-u^2/2} du - \int_{\frac{\pi\ell}{\Delta x}}^{\infty} u^6 \cdot e^{-u^2/2} du \right]$$

Using again the Gradshteyn-Rhyzik identity given above, we obtain by taking n = 3 and p = 1/2:

$$\int_0^{\infty} u^6 \cdot e^{-u^2/2} \, du = \frac{15}{2} \sqrt{2\pi} \quad .$$

Now, the second integral intervening in I' is always positive, and goes to zero as the radial resolution:

$$\boxed{R = \frac{\Delta x}{\pi \ell}}$$

goes to zero. This gives a relatively tight upper bound on the I' integral:

$$I' \leq \frac{4\pi}{\ell^7} \cdot \frac{15}{2}\sqrt{2\pi} \quad .$$

Using intermediate results above finally leads to a similar upper bound estimate of the variance of δH:

$$\boxed{\sigma(\delta H)^2 \leq \frac{5\sigma_f^2 J_1^2 \ell^2}{(24)^2} \cdot \left(\frac{\Delta x}{\ell}\right)^4}$$

with equality in the limit as the grid resolution R goes to zero. Combining this result with the previous equation for σ_H^2 finally gives a tight upper bound for the *relative* error on the head in the case of a Hole-Gaussian log-conductivity spectrum:

$$\boxed{\frac{\sigma(\delta H)}{\sigma(H)} \leq \frac{\sqrt{5}}{8}\left(\frac{\Delta x}{\ell}\right)^2} \quad .$$

This inequality was given in the text in equation (5.63) under the designation "smooth input". Recall that the inequality becomes equality asymptotically as the radial grid resolution $R = \Delta x/(\pi\ell)$ goes to zero. In practice, approximate equality holds for $R \ll 1$, say $\Delta x \leq 0.5\lambda$.

APPENDIX 5.C

CLOSED FORM EVALUATION OF THE NUMERICAL ERROR ON THE FLUX VECTOR AND HEAD GRADIENT FOR THE 3D MARKOV SPECTRUM OF LOG-CONDUCTIVITY

In this Appendix, we evaluate the root-mean-square error on the flux vector q_m and the head gradient G_m, using equations (5.73) and (5.77) in the text. Recall that Appendix 5.A evaluated the error on the hydraulic head in the case of the isotropic 3D Markov log-conductivity spectrum. The same spectrum is used here to evaluate $\sigma(\delta q_m)$ and $\sigma(\delta G_m)$.

According to equations (5.73) and (5.77), the expression for $\mathrm{Var}(\delta q_m)$ will involve a sum of three sets of integrals $L_m^{(1)}$, $L_m^{(2)}$, $L_m^{(3)}$. The L_1 integral taken alone will also give the value of $\mathrm{Var}(\delta G_m)$. These integrals are three-dimensional Fourier space integrals, with domain of integration $0 \leq |k_m| \leq \pi/\Delta x$. For simplicity, we will approximate this rectangular domain as the sphere $0 \leq k \leq \pi/\Delta x$, where k is the three-dimensional radial wavenumber.

More precisely, we have:

$$\mathrm{Var}(\delta q_m) = \left[\frac{K_G \sigma_f J_1 \Delta x^2}{24}\right]^2 \cdot \left(L_m^{(1)} + L_m^{(2)} + L_m^{(3)}\right)$$

$$\mathrm{Var}(\delta G_m) = \left[\frac{J_1 \sigma_f \Delta x^2}{24}\right]^2 \cdot L_m^{(1)}$$

where the $L_m^{(1)}$, $L_m^{(2)}$, $L_m^{(3)}$ integrals are defined as follows for each component m = 1,2,3 of the flux or head gradient vectors:

$$L_m^{(1)} = \frac{1}{\sigma_f^2} \cdot \iiint I_m^2(\underline{k})\, S_{ff}(\underline{k})\, d\underline{k}$$

$$L_m^{(2)} = \frac{1}{\sigma_f^2} \cdot \iiint \frac{2k_1 k_m^3}{k^2} \cdot I_m(\underline{k})\, S_{ff}(\underline{k})\, d\underline{k}$$

(no summation implied over m)

$$L_m^{(3)} = \frac{1}{\sigma_f^2} \cdot \iiint \frac{k_1^2 k_m^6}{k^4}\, S_{ff}(\underline{k})\, d\underline{k}$$

and the $I_m(\underline{k})$ terms appearing in the integrand are of the form:

$$I_m(\underline{k}) = k_1\, k_m \cdot \left[\frac{3k_1^2}{k^2} + \sum_{i=1,2,3} k_i^4/k^4\right]$$

We now proceed to evaluate these integrals after plugging the 3D isotropic Markov spectrum:

$$S_{ff}(\underline{k}) = \sigma_f^2 \frac{\lambda^3}{\pi^2} \frac{1}{(1+\lambda^2 k^2)^2} .$$

Let us focus first on the $L_m^{(1)}$ integral. By using spherical coordinates, we obtained after some manipulation a tractable expression for the first "component" of $L_m^{(1)}$ (i.e., with m = 1) as follows:

$$L_1^{(1)} = L_o \cdot L_1^{(1)''}$$

$$L_o = \frac{1}{\pi^2 \lambda^4} \cdot \int_0^{\frac{\pi\lambda}{\Delta x}} \frac{u^6}{(1+u^2)^2} \, du$$

$$L_1^{(1)''} = \int_0^{2\pi} d\theta \int_0^{\pi} d\phi \cdot A(\theta,\phi)$$

$$\begin{aligned} A(\theta,\phi) = {} & 9 \cos^8\theta \cdot \sin^9\phi + \cos^{12}\theta \cdot \sin^{13}\phi \\ & + \cos^4\theta \cdot \sin^8\theta \cdot \sin^{13}\phi \\ & + 2 \cos^8\theta \cdot \sin^4\theta \cdot \sin^{13}\phi \\ & + \cos^4\theta \cdot \sin^5\phi \cdot \cos^8\phi \\ & + 2 \cos^8\theta \cdot \sin^9\phi \cdot \cos^4\phi \\ & + 2 \cos^4\theta \cdot \sin^4\theta \cdot \sin^9\phi \cdot \cos^4\phi \\ & + 6 \cos^{10}\theta \cdot \sin^{11}\phi \\ & + 6 \cos^6\theta \cdot \sin^4\theta \cdot \sin^{11}\phi \\ & + 6 \cos^6\theta \cdot \sin^7\phi \cdot \cos^4\phi \end{aligned}$$

For L_o, we obtained by using identities from Gradshteyn and Rhyzik 1980 (2.174 and 2.175):

$$L_o = \frac{1}{\pi^2\lambda^4} \cdot \left[\frac{1}{1+R^{-2}}\left(\frac{R^{-5}}{3} - \frac{5R^{-3}}{3} - \frac{5R^{-1}}{2}\right) + \frac{5}{2}\,\mathrm{arctg}\,(R^{-1})\right]$$

in terms of the radial resolution ratio:

$$\boxed{R = \frac{\Delta x}{\pi\lambda}}$$

For $R \ll 1$ (say $R \lesssim 0.2$ or so) this gives approximately:

$$\boxed{L_o \simeq \frac{1}{3\pi^2\lambda^4 R^3}}$$

On the other hand, evaluating the double integral $L_i^{(1)\cdot\cdot}$ requires some straightforward but tedious trigonometric integrations, similar to those developed in Appendix 5.A. Without going into details, we give below the final result.

$$\boxed{L_i^{(1)\cdot\cdot} \simeq 7.35\pi \simeq \frac{22\pi}{3}}$$

Combining the two previous results gives finally, for a

resolution $R = \Delta x/(\lambda\pi)$ reasonably smaller than unity (say $R \leq 0.2$ or $\Delta x/\lambda \leq 0.5$):

$$\boxed{\underline{m = 1}: \quad L_1^{(1)} \simeq \frac{22}{9\pi} \frac{1}{\lambda^4 R^3}}$$

For $m = 2$, the evaluation of $L_2^{(1)}$ requires integrations similar to those developed above. Briefly, this integral can be cast into the form:

$$L_2^{(1)} = L_o \cdot L_2^{(1)\cdot\cdot}$$

where L_o was defined and evaluated previously, and $L_2^{(1)\cdot\cdot}$ is a double trigonometric integral similar (but not identical) to the previous $L_1^{(1)\cdot\cdot}$. The final result is written below for the case $R \ll 1$ (as explained previously):

$$\boxed{\underline{m = 2}: \quad L_2^{(1)} \simeq \frac{2}{15\pi\lambda^4 R^3}}$$

where we used for convenience the approximation $0.41 \simeq 2/5$.

We now focus on the second set of integrals, $L_m^{(2)}$. Using again spherical coordinates, we obtained these integrals in the form:

$$L_m^{(2)} = L_o \cdot L_m^{(2)..}$$

where L_o was defined (and evaluated) previously, and the $L_m^{(2)..}$ are trigonometric integrals similar in form to the $L_m^{(1)..}$ integrals, but simpler. They are given below:

$$\underline{m = 1:}\ L_1^{(2)..} = \int_0^{2\pi} d\theta \int_0^{\pi} d\phi$$
$$[\cos^8\theta\cdot\sin^9\phi + \cos^{10}\theta \cdot \sin^{11}\phi$$
$$+ \cos^6\theta\cdot\sin^4\theta \cdot \sin^{11}\phi + \cos^6\theta \cdot \sin^7\phi \cdot \cos^4\phi]$$

$$\underline{m = 2:}\ L_2^{(2)..} = \int_0^{2\pi} d\theta \int_0^{\pi} d\phi$$
$$[\cos^4\theta\cdot\sin^4\theta \cdot \sin^9\phi$$
$$+ \cos^8\theta\cdot\sin^2\theta \cdot \sin^{11}\phi + \cos^4\theta \cdot \sin^6\theta \cdot \sin^{11}\phi$$
$$+ \cos^4\theta\cdot\sin^2\theta\cdot\sin^7\phi\cdot\cos^4\phi]$$

This gives finally:

$$L_1^{(2)..} \simeq 0.84\pi$$
$$L_2^{(2)..} \simeq 0.10\pi.$$

Multiplying by L_o and using again the approximation $R = \Delta x/(\lambda\pi) << 1$ as explained previously gives finally the $L_m^{(2)}$

integrals:

$$\boxed{L_1^{(2)} \simeq \frac{2}{3}\frac{0.84}{\pi}\frac{1}{\lambda^4 R^3}}$$

$$\boxed{L_2^{(2)} \simeq \frac{2}{3}\frac{0.10}{\pi}\frac{1}{\lambda^4 R^3}}$$

For the $L_m^{(3)}$ integrals, we use again spherical coordinates to obtain after some manipulations:

$$\underline{m = 1}: \quad \boxed{L_1^{(3)}} = L_o \cdot \int_0^{\pi} \sin^9\phi \, d\phi \cdot \int_0^{2\pi} \cos^8\theta \cdot d\theta$$

$$\simeq \frac{1}{3\pi^2\lambda^4 R^3} \cdot \frac{8}{9}\frac{32}{35} \cdot \frac{35}{64}\pi$$

$$\simeq \boxed{\frac{4}{27\pi}\frac{1}{\lambda^4 R^3}} \quad (\text{for } R \ll 1)$$

and:

$$\underline{m = 2}: \quad \boxed{L_2^{(3)}} = L_o \cdot \int_0^{\pi} \sin^9\phi \cdot \int_0^{2\pi} \cos^2\theta \, \sin^5\theta \, d\theta$$

$$\simeq \frac{1}{3\pi^2\lambda^4 R^3} \cdot \frac{8}{9}\frac{32}{35} \cdot \frac{5\pi}{64}$$

$$\simeq \boxed{\frac{1}{49\pi}\frac{28}{27}\frac{1}{\lambda^4 R^3}} \quad (\text{for } R \ll 1)$$

We have therefore obtained closed form expressions for the three sets of integrals $L_m^{(1)}$, $L_m^{(2)}$ and $L_m^{(3)}$ involved in the variance of the flux error and head gradient error, as defined at the beginning of this Appendix. Note that each set of integral was evaluated for the longitudinal component (m = 1) and for the transverse component (m = 2). The result for m = 3 is identical to m = 2 by symmetry, due to the statistical isotropy of the flow in the cross-flow plane. The final results given in the text (equations 5.78 - 5.79) were obtained as follows:

- Assemble the integrals above to compute $Var(\delta Y_m)$ as indicated on top of this Appendix (Y_m stands for the components of the flux vector or of the head gradient).
- Use the known spectral solutions $Var(Y_m)$ to evaluate the ratio $Var(\delta Y_m)/Var(Y_m)$.
- Take the square-root of the above expression to obtain the final result $\sigma(\delta Y_m)/\sigma(Y_m)$, which gives the root-mean-square norm of the error *relative* to the root-mean-square norm of the variable itself.

APPENDIX 5.D
"BIGFLO" CODE ABSTRACT

A High Resolution, Three Dimensional, Saturated/Unsaturated Flow Simulator

1. Program Name: BIGFLO

2. Auxiliary Programs:

   -- Combig (Set of common blocks for BIGFLO.)

   -- Floproc (Large set of Data Processing Routines)

   -- Cturn or TB3 (Turning Band Generator of 3D Random Fields)

3. Programming Language: Fortran 77

4. Computers and Operating Systems:

   BIGFLO has been developed on a Microvax minicomputer running the VMS operating system; it was subsequently modified to run on a Cray 2 supercomputer running the UNICOS (UNIX) operating system, and the CFT77 Fortran compiler. These modifications eliminated a few minor non-standard features, such as instructions with more than 20 continuation lines, and the "INCLUDE" statement used on the Microvax to include the set of common blocks COMBIG (same for all subroutines).

5. Machine Requirements:

BIGFLO contains about 12,000 lines of instructions and comments. Most of the storage required at execution time is taken up by the master array ABIG defined in the main program MAINFLO. The size of this array can be modified as needed in the main program; the parameter LPAR located just below the dimension statement must take exactly the same value as the dimension (otherwise the results could be unpredictable). No other modification will be needed in the BIGFLO code in order to run a particular problem.

The actual size of the master array required to solve a particular problem is proportional to the size (N) of the three-dimensional grid: typically about 12 N for a saturated flow problem with spatially variable conductivity. On a Microvax 2, a practical limit for the size of the master array is about 1 -1.5 Million; on the four-quadrant Cray 2, the size could be as large as 250 Million words in principle. The code will issue an error message and stop execution if the prescribed size of the master array is insufficient to solve the problem.

6. Program Description:

BIGFLO is a three-dimensional porous medium flow simulator, handling steady, transient saturated, and partially saturated or unsaturated flow, with spatially variable or randomly distributed hydraulic coefficients.

The code is based on a finite difference approximation of the equation governing the hydraulic head (saturated flow) or the pressure head (partially saturated or unsaturated flow). The governing flow equation was obtained from the (generalized) Darcy equation and the continuity equation without source terms. The computational flow domain is a three-dimensional parallelepiped rectangle, discretized into an orthogonal grid of mesh points.

For transient unsaturated flow in dry soils, or any similar evolution problems, the actual size of the computational domain can be time-dependent (automatically controlled by the code). For one and two-dimensioanl problems, the size of the grid can be shrinked to just 5 nodes (3 internal nodes and 2 boundary nodes) along the unmodeled directions.

The boundary conditions accepted by the code are, respectively, a fixed flux normal to the boundary, a fixed head, or a zero head gradient. The prescribed fluxes and heads can vary arbitrarily over the boundaries, as well as the type of boundary condition (flux, head, or zero head gradient). In the case of unsaturated or partially saturated flow, the direction of the gravity vector with respect to the axes of the flow domain can be arbitrary, as prescribed by the user.

The hydraulic properties of the porous medium required for saturated flow problems are the saturated hydraulic conductivity (K_s) and the specific storativity (S_s). Both can vary arbitrarily in space as needed. For partially saturated or unsaturated flow, the hydraulic conductivity (K) is assumed to be an exponential function of pressure head (h) with a given slope (α), up to a given bubbling pressure (h_b) where K reaches the saturation value K_s. All three coefficients, K_s, and h_b can be spatially variable over the 3D grid of mesh points. The soil moisture retention curve $\theta(h)$ can be an arbitrary function with several parameters (two of which can be spatially variable). The current version of the code includes subroutines for $\theta(h)$

piecewise linear, exponential, and "Van Genuchten function". The soil moisture capacity is computed by a chord slope (finite difference) differentiation of the $\theta(h)$ function. Finally, the specific storativity S_s is taken into account in regions of positive pressures (partially saturated flow). In this case, unlike the case of purely saturated flow, S_s must be assumed constant in space.

7. Solution Method:

The governing equation is discretized by a seven-point centered finite difference scheme in 3D space, and a fully implicit backwards Euler finite difference scheme in time. The code accomodates both transient and steady solution algorithms for the linear saturated flow problem. A steady state option also exists for the nonlinear unsaturated flow problem, however the best strategy in this case seems to obtain the steady state by running the transient solution algorithm for large times.

The nonlinear flow problem is approximately linearized by a modified Picard iteration scheme. Thus, an approximate linear system has to be solved for each

iteration step, and this is repeated several times at each time step.

The linear or linearized finite difference system is solved iteratively by using a preconditioned iterative method. For the nonlinear case, this gives a doubly iterative loop: outer iteration loop for linearization, and inner iteration loop for solution of the linear system. The available matrix solvers used in this code are variants of the Strongly Implicit Procedure (SIP solver), based on an approximate LU factorization, and on a modified Picard iteration scheme to converge to the exact solution. Other routines corresponding to the ICCG solver (Incomplete Choleski-Conjugate Gradients) have been introduced in the code, but are not fully debugged at this time.

8. **Problem Restrictions:**

Some of the limitations of the BIGFLO simulator are listed below:

-- Geometry: The 3D domain must be a parallelepiped rectangle.

-- Source terms: There are no source terms in the interior of the domain.

-- Water table: The familiar 2D equation of unconfined flow with a water table is not included (use instead the partially saturated flow option).

9. I/O Data Processing:

Most of the inputs/outputs of the BIGFLO code can be processed interactively by using the companion code FLOPROC, a special-purpose data processor for creating the basic input file of BIGFLO and processing 1D, 2D, 3D data fields (including statistical analysis). The generation of random field parameters inputs is handled separately by using the 3D Turning Band code (CTURN or TB3). BIGFLO can be run as a batch process (non-iteractively). The required input files required have the logical names INPUTj (j=1,...9). The basic input file INPUT1 contains the actual names chosen by the user for all the other input files, as well as the basic description of the flow problem and a number of numerical options. INPUT1 can be created interactively by using the data processor FLOPROC.

The numerical outputs from the BIGFLO code can be quite large. A short file containing basic information on the simulation is created at the start (OUT10) as well as a short error file named OUTBAD. The output files

OUT11 and OUT12 contain numerical information such as the residual iteration errors; the output file OUT13 contains mass balance errors and other information required at each time step (depending on options). The three-dimensional head field (solution) is stored in a data file named HEAD-TO for steady flow, or in several data files named HEAD_Tn or H_Tnnn for transient flow problems (at selected times prescribed by the user).

The format of these files can be either ASCII (formatted) or BINARY (unformatted). The latter option is strongly recommended in the case of large simulations. However, binary data files are not easily transportable among different operating systems. It is recommended to rename all output files after completion of a BIGFLO run, since the code uses always the same file names for its outputs.

The data processor FLOPROC can be used to obtain other information from the 3D head field, such as: 3D flux vector field, 3D head gradient field, transects and plane sections of three-dimensional fields, and statistical properties (mean, variance, covariance functions).

10. Practical Implementation:

The tasks required to execute the BIGFLO code are summarized below:

(a) Create basic input data file INPUT1 by using the interactive FLOPROC code.

(b) Find out which other input files are needed. The FLOPROC processor can be used to generate the initial condition (INPUT2) and the boundary conditions (INPUT3) if they are spatially variable. The other input files INPUT4-INPUT9 correspond to spatially variable hydraulic properties. In certain simple cases, only the INPUT1 file is required. Example: saturated or unsaturated flow with uniform initial condition, uniform boundary conditions, on each face of the domain, and spatially constant hydraulic coefficients.

(c) If necessary, specify the names of the additional input files in the basic input file INPUT 1 created previously.

(d) Run BIGFLO: for complex problems, it is advised to execute the code with the option LRUN = 0 as a test; a full simulation LRUN = 1 can then be launched after inspection of the output (OUT10) of the previous test.

(e) Error messages from the BIGFLO code will appear in the output file OUTBAD in cases of abnormal termination. Three types of errors (usually detected after a short time of execution) will cause the program to stop executing:

-- Insufficient dimension of the master array ABIG

-- Erroneous or incompatible set of data in the basic input file INPUT 1; the error code LBAD = -n will help locate the cause of the problem, e.g. by scanning the source code for the string "LBAD = ".

-- Erroneous or non-existent data file INPUTj($2 \leq j \leq 9$); the first digit of the error code LBAD will help locate the problem (e.g., LBAD = - 52 indicates a problem with INPUT5).

11. Author and Reference:

R. Ababou, "Three-Dimensional Flow in Random Porous Media", PhD Thesis, Parsons Laboratory, MIT, Cambridge, Massachusetts, January 1988.